

# **Defined and Functional Materials for Microtissue Engineering Applications**

Dissertation

zur Erlangung des Grades

„Doktor der Naturwissenschaften“

im Promotionsfach Chemie

am Fachbereich Chemie, Pharmazie, Geographie und Geowissenschaften  
der Johannes Gutenberg-Universität Mainz

**Elena Stengelin**

geb. in Frankfurt am Main

Mainz, 2022



Die vorliegende Dissertation wurde im Zeitraum von März 2018 bis Januar 2022 in der Arbeitsgruppe von [REDACTED] im Department Chemie der Johannes Gutenberg-Universität Mainz angefertigt.

Dekanin: [REDACTED]

1. Berichterstatter: [REDACTED]

2. Berichterstatter: [REDACTED]

Datum der mündlichen Prüfung: 28.03.2022



## **Eigenständigkeitserklärung**

Ich, Elena Stengelin, versichere, dass ich die vorliegende Arbeit selbstständig verfasst und keine anderen als die angegebenen schriftlichen und elektronischen Quellen sowie andere Hilfsmittel benutzt habe. Alle Ausführungen, die anderen Schriften wörtlich oder sinngemäß entnommen wurden, habe ich kenntlich gemacht.

Mainz, 10.01.2022

---

(Ort, Datum)

---

(Unterschrift)



## Danksagung

Ein großer Dank geht an dieser Stelle an [REDACTED] für die Betreuung und wissenschaftliche sowie persönliche Unterstützung während meiner Promotion und die Möglichkeit der freien und kreativen Gestaltung meines interdisziplinären Forschungsthemas. Ein weiterer Dank geht an [REDACTED] für das Amt des Zweitgutachters, und die hilfreichen Tipps und Gespräche während der gesamten Promotion.

Ein herzliches Dankeschön geht zudem an alle aktuellen und ehemaligen Mitglieder der Arbeitsgruppe [REDACTED]. Besonders möchte ich mich hier bei den drei guten Seelen des Arbeitskreises [REDACTED], [REDACTED] und [REDACTED] für die intensive Unterstützung, die vielen guten Gespräche und die sehr schöne Zeit zusammen bedanken. An dieser Stelle geht auch ein Dankeschön an [REDACTED] für den administrativen Support und an [REDACTED] für den wissenschaftlichen Rat zu Beginn meiner Promotion. Ein herzliches Dankeschön geht weiterhin an [REDACTED], [REDACTED], [REDACTED], [REDACTED], [REDACTED], [REDACTED], [REDACTED], [REDACTED] sowie den drei Berlinern [REDACTED], [REDACTED] und [REDACTED]. Den wissenschaftlichen Austausch, die gemeinsamen Mensabesuche, die Pausen in der Kaffeecorner, die Grillerevents, die Weihnachtsfeiern und die Ausflüge mit euch allen habe ich sehr genossen.

Zusätzlich bedanke ich mich bei meinen Kooperationspartnern für die erfolgreiche Zusammenarbeit. Besonders möchte ich mich hier bei [REDACTED] für den persönlichen und wissenschaftlichen Austausch sowie für die Messungen zur konfokalen Raman-Mikroskopie bedanken. Ein weiteres Dankeschön geht an [REDACTED] für die Festkörper-NMR Messungen, an [REDACTED] für den intensiven Austausch zur Zellkultivierung und an [REDACTED] für die gute Zusammenarbeit beim Schreiben des Reviews. Ein weiteres Dankeschön geht an die Arbeitsgruppen von [REDACTED], [REDACTED], [REDACTED], [REDACTED] und [REDACTED]. Besonders möchte ich hier [REDACTED], [REDACTED], [REDACTED], [REDACTED] und [REDACTED] hervorheben. Bei den Mitgliedern der Arbeitsgruppe von [REDACTED] bedanke ich mich für den Support im Zelllabor sowie dem Chemikalienlager- und Werkstatt-Team für die umfangreiche Unterstützung im Laboralltag. Herzlich möchte ich mich zudem bei [REDACTED] und [REDACTED] für das Korrekturlesen dieser Arbeit bedanken.

Weiterhin bedanke ich mich bei meinen Bachelor- und Masterstudierenden [REDACTED], [REDACTED], [REDACTED], [REDACTED] und [REDACTED] für ihre Motivation und ihren Fleiß im Labor. Ein großer Dank geht hierbei besonders an [REDACTED] für seinen ehrgeizigen Einsatz im Forschungsmodul und in der Masterarbeit. Die Zusammenarbeit mit euch allen hat mir immer sehr viel Freude bereitet.

Ein sehr großer Dank gebührt meiner Familie und meinen Freunden. Besonders möchte ich mich bei meinem viel zu früh verstorbenen Vater, meiner Mutter sowie meiner Schwester und meiner Patenfamilie für die mentale Unterstützung und den unermüdlichen Glauben an mich bedanken. Und bei Dir [REDACTED] möchte ich mich für die sehr schönen gemeinsamen Jahre, die Motivation und die vielen aufbauenden Gespräche in kniffligen Momenten bedanken. Dein liebevoller Rückhalt hat vieles einfacher gemacht.



## Allgemeine Anmerkungen

Die nachfolgende Arbeit gliedert sich in einer theoretischen Einleitung zur Beschreibung des wissenschaftlichen Hintergrundes, einer Zielsetzung, einem wissenschaftlichen Hauptteil mit drei Kapiteln und einer Zusammenfassung. Wie unten aufgeführt wurden die Inhalte der Einleitung und der drei Kapitel des Hauptteils in verschiedenen Fachjournalen im Peer-Review Verfahren veröffentlicht. Das dritte Kapitel wurde durch einen Exkurs ergänzt.

Einleitung: E. Stengelin, [REDACTED], *Adv. Sci.* **2022**, 2105319.

<https://doi.org/10.1002/advs.202105319>

Kapitel 1: E. Stengelin, [REDACTED], [REDACTED], *Adv. Healthc. Mater.* **2020**, *9*, 1901820.

Kapitel 2: E. Stengelin, [REDACTED], [REDACTED], *Macromol. Biosci.* **2021**, *21*, 2100209.

Kapitel 3: [REDACTED], E. Stengelin, [REDACTED], [REDACTED], *Macromol. Rapid Commun.* **2021**, 2100505.

Zur Einordnung in den Gesamtkontext der Arbeit wird den jeweiligen Publikationen eine kurze spezifische Zusammenfassung mit Bezug auf die Eigenleistung vorangestellt. Zusätzliche und ergänzende Informationen der einzelnen Kapitel („Supporting Information“) sind dem Anhang zu entnehmen. Weitere Projekte werden in einem separaten Kapitel als Kurzzusammenfassung dargestellt. Die Einführung von Abkürzungen, sowie die Zitation der Literaturstellen erfolgt kapitelweise.



## Zusammenfassung

Die vorliegende Arbeit thematisiert die Entwicklung von funktionalen Materialien mit definierten Strukturprofilen und deren Anwendung im Bereich des *Microtissue Engineering*. Das übergeordnete Ziel besteht darin, alternative und biologisch aktive, mimetische Modellsysteme bereitzustellen, um den übermäßigen Einsatz von Tierversuchen im biotechnologischen Bereich zu vermeiden. Neben der Wahl der Ausgangsmaterialien wird der Fokus auf das Materialdesign und die Aufklärung von Struktur–Eigenschaftsbeziehungen gelegt. Speziell werden dabei Materialeigenschaften wie Prozessierbarkeit, Adaptivität, Biokompatibilität und Stabilität/Abbaubarkeit betrachtet und den physiologischen Anforderungen entsprechend eingestellt. Die Formgebung der Materialien erfolgt zusätzlich zu makroskopischen Verfahren mittels der Tröpfchen-basierten Mikrofluidik. Zur Bestimmung der Materialeigenschaften werden neben den physikochemischen Analysen auch biologische Zellstudien durchgeführt.

In einer ersten Studie werden Zell- und Vaterit-beladene, Polyethylenglykol-basierte Mikrogelsysteme zur Anwendung in der Knochenregeneration durch das Mikrofluidik-Verfahren synthetisiert. Dabei werden die mechanischen Eigenschaften und die Gelierungszeiten der Systeme gezielt eingestellt und ihr Einfluss auf das Verhalten der verkapselten Zellen analysiert. Zusätzlich wird die Umwandlung des Calciumlieferanten Vaterit in Hydroxylapatite untersucht. Die Hydrolyse-Empfindlichkeit der Mikrogele wird zudem in Abbaustudien gezeigt. Insgesamt wird eine vielversprechende *in vitro* Plattform für die Untersuchung von metabolischen Prozessen in der Knochenbildung sowie für die Entwicklung neuer Knochenregenerationstherapien präsentiert.

Eine zweite Studie befasst sich mit langzeitstabilen, Volumenschaltbaren Kern–Schale Mikrogeltemplaten zur Nachahmung von mikroskopischen *in vivo* Gewebestrukturen, wie der Blastula in der Embryogenese, Brustdrüsen oder dem Alveolarepithel in der Lunge. Zur Nachahmung dieser komplexen *in vivo* Strukturen werden thermoresponsive Mikrogele aus Poly(*N*-isopropylacrylamid) mithilfe der Tröpfchen-basierten Mikrofluidik synthetisiert und ihre mechanischen Eigenschaften über verschiedene Comonomer-Anteile (*N*-Hydroxyethylacrylamid) eingestellt. Die Zelladhäsion wird durch die Oberflächenbeschichtung der Mikrogele mit Polydopamin in Kombination mit Kollagen oder Fibronectin verbessert. Die so erreichte größere Affinität der Zellen zur Mikrogeleoberfläche sowie deren homogene Verteilung wird zudem über Zellstudien bestätigt.

Eine dritte Studie thematisiert Polyurethan-basierte Biomaterialien für den potenziellen Einsatz im *Microtissue Engineering*. Dabei wird der Fokus auf die Synthese von thermoresponsiven, fotovernetzbaren Polymerketten gelegt, aus denen Hydrogele mit variabel einstellbaren physikalischen und mechanischen Eigenschaften hergestellt werden können. Die Biokompatibilität der Hydrogele wird zudem durch den kovalenten Einbau von Catechol-basierten Biolinkern signifikant erhöht, was durch Zellstudien gezeigt werden kann. Um ein stabiles Fundament für den zukünftigen Einsatz im *Microtissue Engineering* bereitzustellen zu können, werden Mikrogele über die Tröpfchen-basierte Mikrofluidik synthetisiert.

## Abstract

The present thesis addresses the development of functional materials with defined structural profiles and their application in the field of microtissue engineering. The overall goal is to provide alternative and biologically active mimetic systems to avoid the excessive use of animal testing in the biotechnological field. In addition to the selection of starting materials, the focus of this work is on material design and the elucidation of structure–property relationships. In particular, material properties such as processability, adaptivity, biocompatibility, and stability/degradability are considered and optimized according to the requirements. In addition to macroscopic methods, the materials are shaped via droplet-based microfluidics. Besides the physicochemical analyses, the materials are also examined biologically by cell culture experiments.

In a first study, cell- and vaterite-laden poly(ethylene glycol)-based microgel systems, for potential application in bone regeneration, are synthesized via the microfluidic method. The mechanical properties and gelation times of the systems are specifically tuned and their influence on the behavior of the encapsulated cells is analyzed. Additionally, the conversion of the meta-stable calcium supplier vaterite into hydroxyapatite is investigated. The hydrolysis sensitivity of the microgels is further demonstrated in degradation studies. In summary, a promising *in vitro* platform for future studies of metabolic processes in bone formation as well as for the development of new therapies regarding the bone regeneration is presented.

A second study focuses on long-term stable and volume-switchable core–shell microgel templates that can be used to mimic microscopic *in vivo* tissue structures such as the blastula in embryogenesis, mammary glands, or the alveolar epithelium. To mimic these complex *in vivo* structures, thermoresponsive microgels of poly(*N*-isopropylacrylamide) are synthesized using droplet-based microfluidics and their mechanical properties are tuned by different amounts of the comonomer *N*-hydroxyethylacrylamide. In addition, cell adhesion is improved by surface coating of the microgels with polydopamine in combination with collagen or fibronectin. The resulting increased cell affinity to the microgel surface as well as their homogeneous distribution is also confirmed via cell studies.

A third study addresses polyurethane-based biomaterials in terms of their applicability in microtissue engineering. The focus is on the synthesis of thermoresponsive, photocrosslinkable polymer chains, used to prepare hydrogels with tunable physical and mechanical properties. The biocompatibility of the hydrogels is significantly improved by the covalent incorporation of catechol-based biolinkers, which has been demonstrated by cellular studies. In

order to provide a solid platform for future microtissue engineering applications, microgels are synthesized using droplet-based microfluidics.

## Table of Contents

EIGENSTÄNDIGKEITSERKLÄRUNG.....	III
DANKSAGUNG .....	V
ALLGEMEINE ANMERKUNGEN.....	VII
ZUSAMMENFASSUNG .....	IX
ABSTRACT.....	XI
<b>1. THEORY.....</b>	<b>1</b>
1.1. SPECIFIC SUMMARY .....	1
1.2. INTRODUCTION .....	3
1.3. FABRICATION TECHNIQUES.....	6
1.4. RELEVANT MATERIALS.....	10
1.5. MULTIPARAMETRIC MATERIAL FUNCTIONALITY.....	14
1.6. CONCLUSION.....	32
1.7. LITERATURE .....	33
<b>2. SCIENTIFIC GOAL .....</b>	<b>46</b>
<b>3. CHAPTER I .....</b>	<b>49</b>
3.1. SPECIFIC SUMMARY .....	49
3.2. INTRODUCTION .....	52
3.3. RESULTS & DISCUSSION .....	55
3.4. CONCLUSION.....	77
3.5. EXPERIMENTAL SECTION .....	78
3.6. LITERATURE .....	85
<b>4. CHAPTER II.....</b>	<b>88</b>
4.1. SPECIFIC SUMMARY .....	88
4.2. INTRODUCTION .....	90
4.3. RESULTS & DISCUSSION .....	93
4.4. CONCLUSION.....	112
4.5. EXPERIMENTAL SECTION .....	113
4.6. LITERATURE .....	118
<b>5. CHAPTER III .....</b>	<b>120</b>
5.1. SPECIFIC SUMMARY .....	120
5.2. INTRODUCTION .....	122
5.3. RESULTS & DISCUSSION .....	124
5.4. CONCLUSION.....	133
5.5. LITERATURE .....	134
<b>6. SUMMARY &amp; CONCLUSION.....</b>	<b>136</b>
<b>7. ADDITIONAL PROJECTS.....</b>	<b>138</b>
<b>8. INDEXES.....</b>	<b>141</b>
<b>9. APPENDIX .....</b>	<b>144</b>
9.1. CHAPTER I.....	144
9.2. CHAPTER II .....	148
9.3. CHAPTER III .....	164
9.4. LITERATURE .....	209





# 1. Theory

## ●●● “Multiparametric Material Functionality of Microtissue-Based In Vitro Models as Alternatives to Animal Testing”

The content of the following chapter (p. 1–45) has been accepted for publication by *Advanced Science* on December 29, 2021.

**Elena Stengelin,<sup>1</sup>** [REDACTED]\*, *Adv. Sci.* **2022**, 2105319.  
<https://doi.org/10.1002/advs.202105319>

<sup>1</sup>Johannes Gutenberg-University Mainz, Department of Chemistry, Duesbergweg 10–14, Mainz D-55128, Germany

<sup>2</sup> [REDACTED]

\* Corresponding author

Reprinted with permission from *Adv. Sci.* **2022**, 2105319. <https://doi.org/10.1002/advs.202105319>

© 2022 The Authors. *Advanced Science* published by Wiley-VCH GmbH

## 1.1. Specific Summary

Since the definition of the 3R principle by Russel and Burch in 1959, the scientific community has increasingly focused on finding replacements for animal testing, not only for ethical reasons, but also for scientific, economic, and legal considerations. For these reasons, the following review explores and discusses in vitro platforms as potential replacements for animals. It focuses on microtissue-based systems whose microscopic size allows a simplified representation of the complex in vivo environment. However, to push this development forward, the functionality of the material basis must be continuously improved. From this point of view, fabrication techniques, relevant materials, and the multiparametric material functionalities in terms of processability, adaptivity, biocompatibility, and stability/degradability are discussed. In this context, the review provides the theoretical basis, scientific

## THEORY

framework, and motivation for this thesis, which aims to develop defined and functional materials for the use in microtissue engineering as a sustainable alternative to animal testing.

The personal contribution to this review was the conceptualization, literature research, illustration design, and writing the sections “1.2. *Introduction*”, “1.4. *Relevant Materials*” (“1.4.1. *Natural Materials*” and “1.4.2. *Synthetic Materials*”), “1.5. *Multiparametric Material Functionality*” (“1.5.1. *Materials Requirements*” with the subsections “1.5.1.1. *Processability: How to get gelation under control?*”, “1.5.1.2. *Adaptivity: Tunability of mechanical material properties*”, “1.5.1.3. *Biocompatibility: Cell viability versus material functionality*”, “1.5.1.4. *Stability/degradability: Influences of physiological parameter space*”, and “1.5.2. *Advanced Materials*”), and “1.6. *Conclusion*”.

### **Acknowledgements**

A project related to this review has received funding from the European Research Council (ERC) under the European Union’s Horizon 2020 research and innovation program (grant agreement No. 852065). [REDACTED] also thanks the Volkswagen Foundation for generous support by “Experiment!” and “Change of Course” grants.

## 1.2. Introduction

Animal testing is a common approach in industry and academia to classify the risks and effects of pharmaceuticals, pesticides, biocides, and food additives on the environment and humans.<sup>[1]</sup> However, their use simultaneously raises questions as well as pros and cons of moral and ethical nature that have been the subject of controversy over decades.<sup>[2,3]</sup>

Pro-voices argue based on the physiological similarity of animals and humans. As a result, conclusions are drawn regarding the effect of tested substances in animal experiments on the human organism, which has already made it possible to classify a large number of substances in terms of danger and benefit to the society.<sup>[4]</sup> By contrast, voices against animal experiments argue from an ethical as well as scientific and economic point of view. Ethically, the question generally arises as to why human welfare should have a higher priority than animal welfare. This topic is not the subject of this review, and we refer to more detailed accounts in this regard, such as those by Petetta et al. and Ferdowsian et al.<sup>[2,5]</sup> From a scientific point of view, animal experiments are often considered a black box whose results are based on functions and mechanisms that are challenging to understand.<sup>[3,6]</sup> This lack of knowledge may result in erroneous transferability to the human organism, especially because influencing factors such as gender, age, occupation, lifestyle, and disease are not taken into account, which is one of the reasons why only few substances successfully pass the clinical phase.<sup>[3,7]</sup> Moreover, the inter-laboratory reproducibility of animal studies is low.<sup>[7]</sup> From an economic standpoint, animal experiments are resource-intensive (time-consuming and costly) and require skilled labor.<sup>[8]</sup> For example, drug approval takes 10–15 years.<sup>[7,9]</sup>

Based on that controversy, Russel and Burch took up the issue of animal testing in 1959 and wrote *The Principles of Humane Experimental Technique* to improve the situation of animals in animal experiments as well as the quality and reproducibility of scientific and medical research.<sup>[10]</sup> Since then, especially in the last two to three decades, there have been significant developments on political and legal levels that have taken up and further optimized Russel and Burch's ideas into internationally accepted ethical frameworks.<sup>[11]</sup> In Europe, for example, the *EU Directive 86/609/EEC* was founded in 1986 to which each member state has to comply.<sup>[12]</sup> In 2010 it was revised, resulting in the currently valid guideline *EU Directive 2010/63/EU*, which is a basis for regulations in the individual EU states.<sup>[2,13]</sup> In the United States, animal testing is controlled by the Animal Welfare Act since 1966.<sup>[2]</sup> At the heart of all these regulations, Russel and Burch's so named 3R principle forms the benchmark for scientific quality and ethical considerations. In that abbreviation, 3R stands for Refinement,

## THEORY

Reduction, and Replacement of animal experiments.<sup>[14]</sup> Based on that premise, when animal experiments are necessary, inhumane procedures should be avoided and animal welfare should be improved (Refinement), while the number of experimental animals should be reduced to a minimum (Reduction).<sup>[11]</sup> In addition, intensive research should be carried out on alternatives to replace animal experiments involving living vertebrates (Replacement).<sup>[8]</sup>

Overall, the 3R principle covers many disciplines and areas. Refining and reducing animal testing primarily focuses on medical and regulatory areas, whereas replacing animal testing focuses on a broader range of research topics, as illustrated in **Figure 1-1** using the branches of a tree to illustrate the spreading of this concept.<sup>[1,8,15]</sup> In branch (i), ex vivo procedures are situated, which focus on animal organs (e.g., skin) outside the living organism, while in (ii), alternative organisms such as the invertebrates (e.g., *Drosophila*) and the fish embryo test are listed.<sup>[16–20]</sup> Other alternatives are based on (iii) computer-assisted in silico methods for drug discovery, (iv) cell-free tissue models (e.g., imitation of complex organisms as cells), and (v) cell-based tissue or in vitro models (2D and 3D cell cultivation).<sup>[21–28]</sup> In this article, we focus on cell-based tissue alternatives, as highlighted in **Figure 1-1**, whereas we refer to selected reviews for the others, as quoted just before.

An excellent path towards cell-based tissue models is microtissue engineering, as it addresses the complexity of natural tissues on a microscopic level, but in a simplified form.<sup>[29,30]</sup> Appropriately engineered models aim to replicate only specific areas and functions of the human organism, enabling new, intelligent and specific preclinical testing methods applicable to any specific human situation and also allowing for precisely monitoring system processes.<sup>[3,31]</sup> The foundation of such microtissue engineered models is based on suitable cells and well-designed scaffold structures, with the chemical and structural composition of the shaping materials in particular guiding the model systems. The more functional the materials are, the more complex and intelligent alternatives can be achieved. Hence, this review presents research on the multiparametric material properties of cell-based microtissue models as a substitute for animal testing. It includes (1) an overview of fabrication techniques, (2) a selection of relevant hydrogel-based materials, and (3) their multiparametric material functionality. The latter focuses on the main hydrogel requirements that are *processability*, *adaptivity*, *biocompatibility*, and *stability/degradability* (**Figure 1-1**). In many of the publications covered in this article, the original context is actually more on aspects like tissue engineering and drug delivery, whereas they in fact often not explicitly refer to the replacement of animal testing; nevertheless, despite their originally different designation, these studies may also address aspects of 3R as well. This review aims at reflecting these studies in view of this topic.

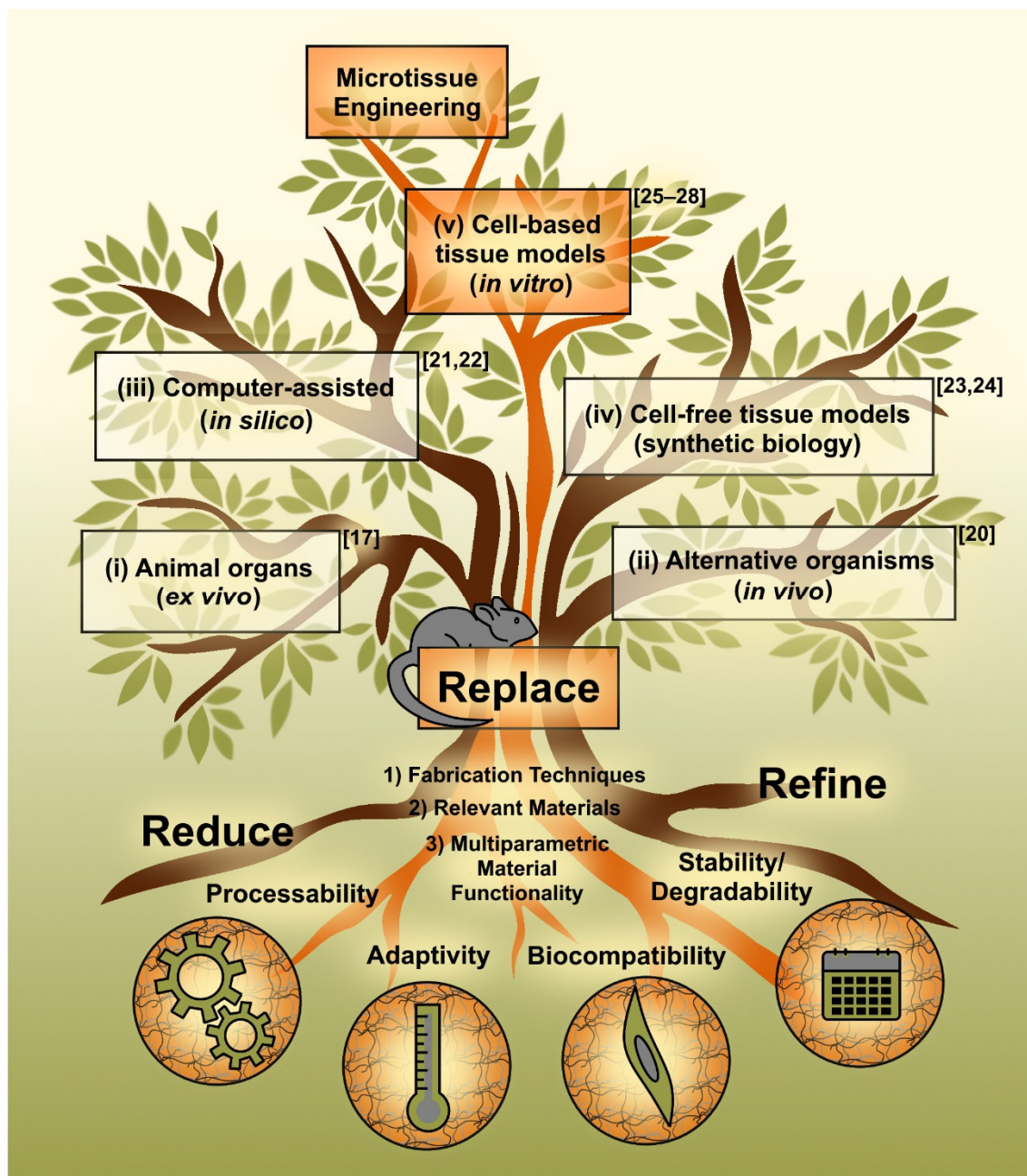


**Figure 1-1.** Schematic of a tree with a key pathway highlighted in orange starting at the roots and ending in the crown to illustrate the theme and story line of this review. Based on the 3R principles (reduce, replace, refine), the review’s focus is on the replacement of animal experiments through cell-based microtissue models. Accordingly, fabrication techniques (1), relevant hydrogel-based materials (2), and multiparametric material functionality (3) are addressed as the main foundation for the cell-based microtissue alternatives (“crown”) with particular focus on material processability, adaptivity, biocompatibility and stability/degradability (“roots”). In addition, other potential alternatives to animal testing are highlighted through the branches of the tree, such as animal organs, alternative organisms, computer-assisted technologies, and cell-free tissue models. Since these will not be discussed in detail in the remainder of this review, reference is made to selected literature collections.

### 1.3. Fabrication Techniques

The increasing complexity in structure and function of artificial microtissue is closely related to the advancements in design and engineering of materials processing strategies and methods. The following section will discuss a selection of these processes based on *bioprinting*, *spheroids*, *microfluidics*, and *organ-on-a-chip*, that have advanced the design of functional co-cultures, microtissues, and organoids (**Table 1-1**).

*Bioprinting* is an additive-manufacturing process that make use of cells in media as well as in to-build-up tissue structures in a bottom-up approach. The material basis of bioprinting is commonly known as bioinks.<sup>[32]</sup> Bioinks are usually based on bioprintable hydrogels with shear thinning properties, fast gelation times, and shape retention properties, that are also capable of entrapping cells.<sup>[33]</sup> The broader application of bioprinting for microtissue design requires two major foundations: suitable cell material and bioprinters at an advanced level of engineering, e.g., to not harm living cells during bioink processing by mechanical forces induced by the printing process itself.<sup>[34]</sup> Only then we can sufficiently address the complex parameter space of minimal feature size (resolution), vascularization, perfusion, automation, cost, diffusion of molecules, growth factors and nutrients as well as the supply of mechanical and biochemical stimuli. Although bioprinting has been shown to be able to create microstructures with embedded cells, it requires more than that. The key properties of an in vivo environment - (multi-)cellular assemblies with dense cell-cell or cell-extracellular matrix (ECM) interactions - are additionally required to approximate the structure and biochemistry of the native environment of cells and tissues. Only these have the potential to provide a new set of tools for understanding diseases and the effectiveness of patient-specific therapies, while being based on human cells, such models may be eventually more predictive than animal models, thus reducing or even replacing the need for animal testing.

A key element in designing such multiparametric, multicellular platforms could involve the use of *spheroids*.<sup>[35]</sup> These densely packed microtissue units can be formed template-free or engineered by the support of microparticles, e.g., polymer microgels, which have also emerged as individual engineered cell scaffolds themselves (cf. below).<sup>[36]</sup> While traditional tissue scaffolding follows a top-down approach, e.g., based on implants or transplants,<sup>[37]</sup> the concept of bottom-up construction of microtissue by spheroids holds great promises for the design of multiphasic cell matrices with tissue-specific structures across scales.<sup>[38]</sup> Exemplarily, Torisawa et al. utilized a continuous-flow microfluidic device equipped with a semi-porous membrane to regulate culture media flow towards distinct geometric compartments,

which then filled with co-cultures. In there, weeks-long culturing yielded self-aggregated, individual spheroids with microtrap-controlled size and shape.<sup>[39]</sup> And Mekhileri et al. precisely placed spherical microstructures into 3D-plotted scaffolds (bottom-up approach) using computer-assisted layer-by-layer bioprinting and promoted the growth of large and complex tissues with improved architectural control. Compared to the top-down approach, this strategy has advantages in cell-cell interaction and natural cell arrangement in the tissue due to the pre-programmed composition.<sup>[40]</sup> While the design of single cell line-based spheroids is rather straight-forward, the orchestration of multiple cell lines requires platforms that provide compartmentalization *and* spatial control over matrix conditions for optimal co-culturing. A solution to that could be the usage of core-shell (polymer) microstructures. For instance, the groups of Park, Shin and coworkers established the sequential seeding of mesenchymal stem cells (MSCs) and endothelial cells on individual hydrogel patches made from a thermoresponsive hydrogel. Upon thermal actuation, these hydrogel structures transitioned into core-shell spheroids that, after an additional fusion step, lead to the formation of vascularized microtissue.<sup>[41]</sup>

Spheroids can be utilized as building blocks in tissue design due to the large parameter space of potential template (e.g., material basis, size, shape, functionalization, elasticity) and tissue properties (e.g., cell line, cell density). However, for fabricating physiological microtissue constructs based on human cells, some of the above-discussed methods lack material uniformity (e.g., of spheroids and their templates). They also do not provide the necessary fabrication rates and ability to validate and characterize these in a high-throughput fashion.<sup>[42]</sup> On this account, Matsunaga et al. established the *microfluidic* high-throughput production of uniform collagen microparticles via axisymmetric flow-focusing devices as templates for cell overgrowth and spheroid formation.<sup>[43]</sup> Using NIH 3T3 cells, HepG2 cells, human umbilical endothelial cells (HUVECs), primary neurons, primary rat hepatocytes, and MIN6m9 cells, the versatility of this template-mediated spheroid formation was highlighted. Microgels with seeded cells adhered to each other and eventually fused via cell-cell interactions coated on the collagen gel beads. The cells also grew into the collagen gel beads, which eventually lead to gel decomposition and macroscopic tissue formation. In fact, microfluidics generally is the most-established method for producing microemulsions that act as templates for uniform hydrogel-based microstructures.<sup>[44,45]</sup> The power of microfluidics-based material design lies in its ability to tune the size of biocompatible soft microtissue from a few to hundreds of micrometers, whose physicochemical and mechanical properties can be approximated to that of the native ECM. Yet, for closely mimicking mechanobiological cues of the ECM as

## THEORY

well as regulating the ECM's effect on cell differentiation and migration, artificial microtissue design also requires the processing of ECM molecule mixtures or ECM-derived materials. In continuous- and segmented-flow (droplet-based) microfluidics, this task is often challenging, as mixtures of polysaccharides and proteins (containing collagen, fibronectin, laminin, hyaluronic acid, among others), that are essential ingredients of the natural ECM, may exhibit complex flow behavior. Exemplarily, shear-thinning of these multi-component mixtures may exacerbate the throughput of material in microfluidic devices as, in the case of droplet formation, only low flow rates will provide stable droplet formation.<sup>[46]</sup>

Microfluidic devices do not only serve as enabling technology for the design of tissue building blocks and artificial niches, as discussed above, but their exact control over flow pattern formation in microchannels with tailored-made architecture and integrated functional units (e.g., valves, micropumps, membranes, vents, hydrodynamic traps) is most suitable to control cell attachment (e.g., in microstructured niches), cell agglomeration with spatiotemporal control, nutrient and gas flow. Based on well-established manufacturing methods of microfluidic devices including combined photo- and soft lithography, additive manufacturing based on Fused Deposition Modeling and projection-microlithography, and glass microcapillaries, such platforms have evolved as experimental platform in cell biology, e.g., for mimicking tissue organization and its physiological environment. Researchers have pushed this development towards so-called *organs-on-a-chip*, which contain human-derived cells preserved with biophysical and chemical cues to mimic the structure and function of single human organs and even interconnected organs embedded in microfluidic systems. Functioning as simplified organ models, they enable a wide range of in vitro toxicity and efficacy testing. Such microfluidic devices can be used in place of animals or animal-derived tissue models to replicate human physiology in disease research, testing of drug safety or the effect of chemicals, cosmetics, and consumer products on human tissue in the admission process. For example, Purtscher et al. have integrated a dual cell culture bioassay into a common lab-on-a-chip platform for evaluating the safety of pharmaceutical products.<sup>[47]</sup> Key examples of these microfluidics-based experimental platforms for microtissue design have made the transition into commercialization. For instance, AlveoliX's platform emulates the complexity of the human lung, named lung-on-a-chip, or tissue barriers, and MIMETAS' microfluidic cell culture plates provide perfused tubular tissues in a parallelized fashion without the presence of artificial membranes. Beyond microfluidic platforms, Swedish Fluicell has developed a 3D bioprinting system with micrometer precision for medical research models in cell dish and



microtiter plates that potentially complement and decrease animal testing, e.g., in intermediate stages of drug development.

**Table 1-1.** Comparison of bioprinting and microfluidic technology.

	Properties <sup>a)</sup>	current research challenges	application examples
<b>bioprinting</b>	<p>basis: hydrogels, suitable cells/spheroids, and bioprinters</p> <p>shear-thinning, fast gelling, form and mechanically stable, biocompatible hydrogels/bioinks desirable<sup>[33]</sup></p> <p><math>\mu\text{m}</math>-mm-cm scaling; low throughput</p>	<p>multi-material printing; adaptive and responsive culture systems; vascularization of tissue; bioprintable material availability; on-demand production<sup>[48]</sup></p>	<p>printing of microstructures with embedded cells/spheroids for, e.g., the imitation of in vivo tissues<sup>[40]</sup></p>
<b>microfluidics</b>	<p>basis: hydrogels, suitable cells/spheroids, and microfluidic devices</p> <p>simple flow behavior of hydrogels desirable; form and mechanically stable, biocompatible hydrogels desirable; oxygen and nutrient exchange by flow cells</p> <p><math>\mu\text{m}</math> scaling; size tunability and uniformity; direct characterization; low throughput</p>	<p>high throughput fabrication; automation, integration, and intelligent synthesis of biomaterials<sup>[49]</sup></p>	<p>template-mediated spheroid synthesis for, e.g., tissue formation<sup>[43]</sup></p> <p>organ-on-the-chip applications for, e.g., toxicity and efficacy testing<sup>[47]</sup></p>

<sup>a)</sup> The table is intended to provide an exemplary overview but does not claim to be complete.

## 1.4. Relevant Materials

In addition to the material design, the materials themselves are also an important building block (or even the most important one) for the design of *in vitro* model systems. Materials commonly used in this context are hydrogels, e.g., physically or chemically crosslinked 3D polymers that swell in aqueous media.<sup>[50,51]</sup> In the following, a selection of natural and synthetic materials is presented and explained in terms of their structural composition, accessibility and origin, as schematically shown in **Figure 1-2**. There are many more bio-based hydrogel types and we refer to much more detailed reviews by Thiele et al., Van Vlierberghe et al., Caliani et al., and Rice et al.<sup>[52–55]</sup>

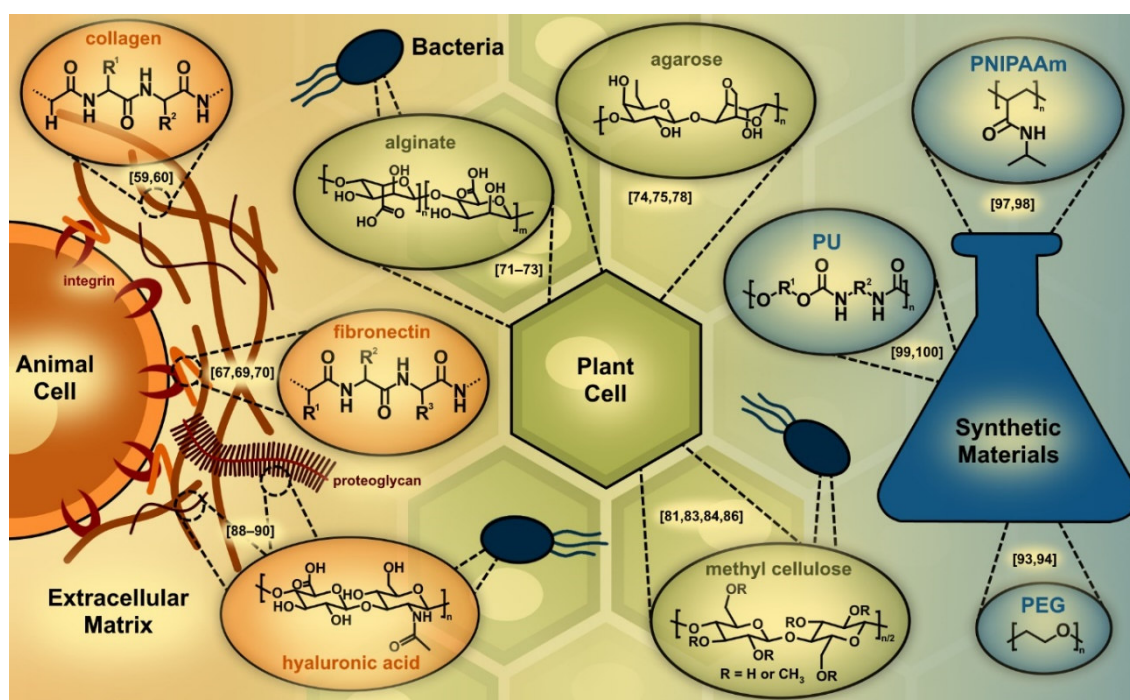


**Figure 1-2.** Schematic overview of some relevant natural materials obtained from animal, plant, and bacterial sources, as well as some representative synthetic materials.

### 1.4.1. Natural Materials

The main representatives of natural materials are based on proteins and polysaccharides derived from animal, plant, and bacterial sources. Proteins and polysaccharides are commonly part of the ECM where they are scaffold and promoter of cell-cell/cell-matrix interactions and of cellular activities.<sup>[56,57]</sup>

An essential natural protein of the ECM is *collagen type I*, which is composed of  $n$ -alternating amino acid sequences  $[-Gly-X-Y-]_n$  with glycine (Gly) and any amino acid X and Y linked by amide bonds  $[-CO-NH-]$ .<sup>[58–60]</sup> In natural ECM tissue, three such polypeptide chains

arrange in a triple helix and connect to each other by hydrogen bonding. These triple helices stack together and connect covalently by lateral interactions to form fibrils, which in turn aggregate to larger fibers.<sup>[52,61]</sup> Through solubilization of collagen fibers (e.g., collagen type I from rat-tail tendons) at enzymatic and salt/acid conditions, collagen fibrils are extracted and become applicable for in vitro experiments.<sup>[54,62,63]</sup> By hydrolysis or denaturation of collagen type I, *gelatin*, an alternative protein based on single-strand molecules, can be obtained.<sup>[53,55,64–66]</sup> Another type of ECM proteins are multi-adhesive glycoproteins (a combination of proteins and polysaccharides), that contain several binding domains for interacting with the ECM matrices, cell surface receptors, and other glycoproteins.<sup>[67]</sup> A prominent representative is *fibronectin*, which primarily connects ECM matrices to cell adhesion receptors (integrins).<sup>[68]</sup> It consists of two similar, intramolecularly linked polypeptide subunits (230–270 kDa), whose assembly of type I, type II, and type III repeating units is responsible for collagen/gelatin and integrin specificity.<sup>[67,69,70]</sup>

Beside proteins, polysaccharides are also part of the ECM. They are based on a high number of glycosidically linked monosaccharides and obtained from plant, bacterial, and animal sources. A relevant representative, frequently used in food and pharmaceutical industry is *alginate*, a linear polysaccharide, which can be obtained from brown algae (Phaeophyceae) through the treatment with an alkaline solution, or by bacterial synthesis.<sup>[54,71]</sup> Alginate is composed of several (1,4)-linked  $\beta$ -D-mannuronic acid (M block) and  $\alpha$ -L-guluronic acid (G block) units, based on [–OH] and [–COOH] functionality, whose molecular weight depends on the source and the fabrication process, typically varying between 10–1000 kDa.<sup>[53,72,73]</sup> An alternative polysaccharide is *agarose*, which is obtained from agar, an posed of (1,3) linked  $\beta$ -D-galactose and (1,4) linked  $\alpha$ -L-3,6-anhydrogalactose, primarily equipped with [–OH] functionality and molecular weight of almost 12 kDa.<sup>[74–78]</sup>

The most naturally occurring biomaterial is cellulose, which can be obtained from bacterial and plant sources by chemical treatment.<sup>[79,80]</sup> On a molecular level cellulose is composed of linear (1,4)-linked  $\beta$ -D-glucopyranosyl molecules with [–OH] functionality.<sup>[81]</sup> These polysaccharides stack parallel during biosynthesis to fibrils, which in turn aggregate to larger microfibrils with crystalline and amorphous regions, promoted by intermolecular physical interactions.<sup>[79,82]</sup> In general, cellulose is insoluble in water, but this can be overcome by etherification of hydroxyl groups.<sup>[79]</sup> A corresponding known and Food and Drug Administration (FDA)-approved derivative is *methyl cellulose*, a partially methylated [–O–CH<sub>3</sub>] derivative of cellulose at its hydroxy functionalities with a degree of substitute between 1.7–2.0.<sup>[81,83–85]</sup> The

## THEORY

non-polar methoxy groups disturb hydrogen bonding between other hydroxy molecules, allowing water molecules to enter the polysaccharide structure, resulting in increased water solubility.<sup>[86]</sup>

Considering the ECM environment, there exists a further special linear type of polysaccharides (glycosaminoglycans), which are based on the repeating disaccharides uronic acid and D-galactosamine or D-glucosamine.<sup>[87]</sup> *Hyaluronic acid* is its most prominent representative, commercially available and widely used in industry since 1970.<sup>[88–90]</sup> It is composed of  $\beta$ -1,4-D-glucuronic acid and  $\beta$ -1,3-N-acetyl-D-glucosamine and contains three functional groups [–COOH], [–OH], and [–NHCOCH<sub>3</sub>].<sup>[88]</sup> Hyaluronic acid can be extracted from animal sources or synthesized through bacterial fermentation (*Escherichia coli*), which provides high reproducibility of molecular weight (100–8,000 kDa).<sup>[54,88,91]</sup> If the glycosaminoglycans are bound to proteins, proteoglycans are obtained, which serve as further stabilizing components of the ECM.<sup>[92]</sup>

### 1.4.2. Synthetic Materials

Despite practicable properties such as cell adhesion and biodegradability, animal-derived materials often have poor mechanical properties and batch-to-batch variations.<sup>[66,92]</sup> Since their use is also controversial in terms of replacing animal testing, the research is focusing on the development of synthetic materials that cover the entire spectrum of tunable chemical, physical, mechanical, and biological properties. Some synthetic materials are already widely used in microtissue engineering, and three prominent examples are briefly described below.

One of them is *poly(ethylene glycol)* (PEG), a FDA-approved polymer, based on repeating ethylene glycol units [–(CH<sub>2</sub>CH<sub>2</sub>O)<sub>n</sub>].<sup>[93]</sup> PEG polymers can be generated by ring-opening polymerization, starting from ethylene oxide. It is commercially available in various molecular weights. In addition, a variety of PEG-polymer structures are known, such as linear, multi-armed and hyperbranched. Thereby, the designation of PEG usually changes to poly(ethylene) oxide (PEO) above a molecular weight of 30 kDa.<sup>[94]</sup> Thus, with appropriate end-group functionalization, PEG-based hydrogels with diverse mechanical properties are accessible, making them ideal candidates for in vitro applications.<sup>[92]</sup>

A second prominent synthetic polymer is *poly(N-isopropylacrylamide)* (PNIPAAm), first reported in 1968.<sup>[95]</sup> It is composed of N-isopropylacrylamide monomer units, which are based on hydrophilic amide [–CO–NH–] and hydrophobic isopropyl [–CH(CH<sub>3</sub>)<sub>2</sub>] moieties.<sup>[96]</sup> It has thermoresponsive properties and therefore finds versatile use in tissue engineering, bio-

sensing and drug delivery applications.<sup>[97]</sup> Additionally, PNIPAAm polymers and 3D networks are accessible via numerous synthesis routes as described in detail by Doberenz et al.<sup>[98]</sup>

A third type of relevant synthetic materials is based on *polyurethanes (PU)*, which are widely used in industry since 1937, developed by Otto Bayer and co-workers. Their characteristic repeating unit is the urethane group  $[-NH-CO-O-]$ , which classically results from the polyaddition reaction between polyols and polyisocyanates with at least two or more hydroxyl  $[-OH]$  and isocyanate groups  $[-N=C=O]$ .<sup>[99,100]</sup> There are two PU families, thermoplastics and thermosets, which differ in structural design. Thermoplastic PUs have a linear structure and are based on diols, diisocyanates, and chain extenders (low molecular weight diol components), while thermoset PUs form 3D networks based on polyols and polyisocyanates.<sup>[99]</sup> Depending on the application, versatile materials with a wide range of mechanical properties can be obtained.

## 1.5. Multiparametric Material Functionality

Microtissue-derived in vitro models are promising candidates to replace animal testing, as they aim to replicate small compartments of the host organ for preclinical studies, rather than focusing on the entire, highly complex organism. The models are based on simply constructed platforms whose components can mimic the extensive tissue properties such as 3D anatomy, functionality, and physiology (e.g., oxygen and nutrient exchange, vascularization, etc.). Because of these properties, they provide an excellent basis for modeling specific organ diseases, modular tissue engineering, and drug delivery studies – all applications where animal testing can potentially be avoided in the future. In addition, due to their microscopic size and synthetic background, the model systems enable the performance of many parallel experiments, a high degree of reproducibility, and the simultaneous performance of analyses during experiments. These features are mainly applied in high-throughput drug screening and in the analysis of natural processes. Overall, the potential applications of microtissue-based in vitro model systems are very diverse and require different shapes, as well as a different material base depending on the objectives. Accordingly, different fabrication techniques for providing microtissue platforms, as well as hydrogel-based materials have been described in the previous sections. To gain a deeper insight into the requirements of hydrogels for microtissue applications, they are discussed in the following sections in terms of their processability, adaptivity, biocompatibility and stability/degradability (**Table 1-2**). Finally, an outlook on advanced materials is given and their potential use in in vitro models as a substitute for animal testing is discussed.

### 1.5.1. Materials Requirements

#### 1.5.1.1. Processability: How to get gelation under control?

The multiparametric functionality of hydrogels is based, among other factors, on their processability, which in the broadest sense refers to their application in manufacturing techniques for shaping. Depending on their intended application, spheroids, microstructures, and modular tissues need to be formed by different manufacturing methods, the use of which depends on the processability of the hydrogels. Extrusion-based bioprinting, for example, requires shear-thinning, fast gelling, and form stable materials, as illustrated by the example of Kang et al., who synthesized spheroidal and tubular microstructures by one-step bioprinting to create human tissue analogs.<sup>[101]</sup> In contrast, the preparation of cell-loaded microgels

by microfluidics requires precursor materials that covalently bond with each other in a time-delayed manner, e.g. by external stimuli such as UV irradiation, to ensure homogeneous droplet formation.<sup>[102]</sup> Overall, these two technologies show how different and diverse the requirements for the processability of hydrogels are. Accordingly, a selection of natural and synthetic materials will be discussed below regarding their gelling properties, which have a significant influence on their processability. In addition, possible control elements will be addressed.

In general, most materials gel and form either physically or covalently crosslinked hydrogels as shown schematically in **Figure 1-3**. However, for the physically crosslinked hydrogels, external parameters such as temperature, pH and ion concentration often affect the stability of the corresponding gels, which then degrade. This often limits applications in in vitro models due to limited control of gelation time, gel stability, and handling. To overcome this limitation and extend processing options, chemical modification of individual materials is a versatile approach to enable covalent and controllable gelation.

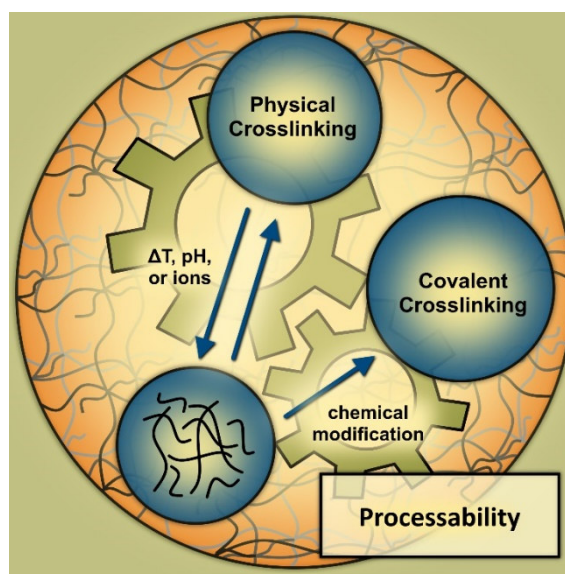


**Figure 1-3.** Processability of materials with emphasis on gelling properties and potential control.

A reversible gelation process of polymers in water is based on temperature and pH changes and depends on the solubility of these polymers in water, as conceptually described by Seiffert et al.<sup>[103]</sup> The temperature at which this solubility changes is either referred to as the Lower Critical Solution Temperature (LCST) or to the Upper Critical Solution Temperature (UCST). In the former case polymers intermolecularly interact with water molecules at low temperatures through hydrogen bonding and dipole-dipole interactions. However, as the temperature increases, these bonds break, and the polymer chains precipitate in a coil-to-

## THEORY

globule transition.<sup>[103]</sup> An appropriate example is *PNIPAAm*, whose polar amide groups interact by hydrogen bonding with water molecules below the LCST (32 °C) and precipitate above this temperature.<sup>[95]</sup> Due to that property and the LCST being close to the physiological temperature range, PNIPAAm polymers are widely used as drug delivery materials and beyond.<sup>[104]</sup> To overcome the temperature-dependent stability of PNIPAAm polymers, they can be copolymerized with functional monomers (e.g., crosslinkers) that make stable hydrogels accessible through chemical or physical interactions.<sup>[105]</sup> Exemplary, Kim et al. have developed multi-stimuli-responsive microfibers and microtubes as potential cell scaffolds for tissue engineering applications. These scaffolds are based on NIPAAm molecules, the crosslinker *N,N'*-methylenebis(acrylamide), and the comonomers allylamine or sodium acrylate, which connect covalently by UV irradiation in a microfluidic approach.<sup>[106]</sup>

Another thermoreversibly gelling polymer is *methyl cellulose* (LCST = 40–50 °C), whose hydrophobic methyl groups [–CH<sub>3</sub>] self-assemble into fibrils with increasing temperature and percolate into networks.<sup>[84,107]</sup> Due to that reason, methyl cellulose is usually fluidic at physiological conditions and hence useful as a thickening agent for spheroid synthesis.<sup>[108]</sup> Accordingly, Wang et al. have developed core–shell microgels for organoid synthesis using microfluidics. The microgels consisted of a core based on liquid methyl cellulose and encapsulated liver cells (HepG2) or a coculture of liver and endothelial cells (HepG2/HUVECs) with a stabilizing shell of gelatin methacrylate (GelMA).<sup>[109]</sup> Due to the good printability of methyl cellulose at room temperature but the lack of crosslinking ability, it is also frequently used with polymers such as GelMA and alginate in blend-based bioinks with high dimensional stability and fidelity.<sup>[110,111]</sup>

In contrast, in other polymer systems, such as agarose and gelatin, intra- and intermolecular polymer–polymer interactions are promoted for enthalpic reasons, which counteract polymer dissolution at low temperatures. By increasing the temperature, these interactions can be overcome, and the polymers dissolve in water at the UCST.<sup>[103,112,113]</sup> For example, *agarose* assembles into double helices and aggregates into ordered structures below its UCST of 20 to 70 °C and liquefies at higher temperatures.<sup>[53,114,115]</sup> Hence, stable agarose gels for microtissue applications can be obtained at physiological conditions, as described by Struzyna et al. In the corresponding study, agarose-based microcolumns were filled with proteins and dopaminergic neuronal aggregates to mimic the nigrostriatal pathway for the treatment of Parkinson's disease.<sup>[116]</sup> *Gelatin*, in turn, assembles into triple helices from random coil chains at about 25 to 30 °C and associates into 3D networks.<sup>[50,53,114]</sup> Since its UCST is below the physiological temperature, they do not form stable gels at 37 °C. Because of this property, it is



often used as a sacrificial substrate. For example, Hwang et al. have prepared cell-laden porous alginate hydrogels by incorporating gelatin microspheres (150–300  $\mu\text{m}$ ) that are stable at low temperatures and liquify under physiological conditions.<sup>[117]</sup> To provide temperature-stable gelatin hydrogels, they are usually functionalized with crosslinking moieties, e.g., with methacrylate groups (known as GelMA).<sup>[118]</sup> A relevant example was provided by Zoratto et al. who developed thermostable microporous scaffolds based on photocrosslinked GelMA microgels, to better mimic the ECM and facilitate nutrient and oxygen transport of in vitro models.<sup>[119]</sup> Alternatively, crosslinkers such as glutaraldehyde and genipin can be incorporated and stabilize gelatin networks.<sup>[120,121]</sup>

Protonation or deprotonation of pH-sensitive polymers can further impair the intermolecular polymer–water interaction, which also affects solubility.<sup>[103]</sup> Accordingly, acidic *collagen type I* solutions must be neutralized, causing the triple-helical fibrils to self-assemble into fibrillar matrices at about 37 °C within a slow gelation time of half an hour.<sup>[54,114]</sup> A related approach was used by Ugolini et al., who separately confined cell-laden type I collagen and fibrin gels in PDMS-based templates to mimic complex biological compartments.<sup>[122]</sup> Further, the gelation of collagen type I is reversible below the denaturation temperature of approximately 37 °C, but gels still remain statically stable for extended periods of time.<sup>[123]</sup> However, to make gelation temperature-independent and to accelerate the gelation time, chemical modifications are possible that correspond to those described for gelatin.

In turn, gelation of *alginate* occurs with multivalent cations such as  $\text{Ca}^{2+}$ ,  $\text{Ba}^{2+}$ , and  $\text{Fe}^{3+}$ , with mainly G-block elements associating with these to form tight junctions in an egg carton pattern due to negatively charged  $[-\text{COOH}]$  groups.<sup>[63,72]</sup> This association occurs instantaneously by cations diffusing from the external environment into the alginate precursor solution.<sup>[72]</sup> Agarwal et al. used this approach by preparing cell-laden core–shell microgels (collagen–alginate) as a biomimetic platform for high-throughput drug screening. For this purpose, microgels were synthesized by microfluidics, where  $\text{Ca}^{2+}$  ions (from  $\text{CaCl}_2$ ) diffused from the oil phase into the alginate precursor droplets and initiate gelation.<sup>[124]</sup> Because alginate gelation is fast, the rate can be slowed down by cations released into the system in a controlled manner, which is called the internal gelation method.<sup>[72,125]</sup> Accordingly, Weitz and coworkers encapsulated MSCs in alginate microgels as possible in vitro model systems for drug testing. For this purpose, they used a precursor solution of alginate and calcium-ethylenediaminetetraacetic acid (EDTA), which released  $\text{Ca}^{2+}$  ions at acidic conditions (pH 5) and initiated controlled alginate gelation.<sup>[126]</sup> Alternatively, also  $\text{CaCO}_3$  could be used.<sup>[127]</sup>

## THEORY

There are also polymers that do not naturally gel due to external stimuli. Therefore, they must be functionalized to be interesting for microtissue applications. A relevant example is *hyaluronic acid*, which at very low concentrations assumes a rigid helical configuration due to intermolecular hydrogen bonding. These chains entangle randomly, resulting in jelly-like solutions.<sup>[128]</sup> Chemical modification at the side groups [–COOH], [–OH], and [–NHCOCH<sub>3</sub>] is the basis to form stable covalent-crosslinked hydrogels. A corresponding example is based on microstranded bioinks by Kessel et al., where gel formation was achieved by photocross-linking of hyaluronan methacrylate. The resulting hydrogels were extruded through a lattice with an aperture size of 40 and 100 μm, resulting in microstrands with shear-thinning properties that mimic key ECM features.<sup>[129]</sup> For more chemical modifications of hyaluronic acid, we refer to Collins et al. and Khunmanee et al.<sup>[130,131]</sup>

Another polymer that also requires pre-functionalization for crosslinking is *PEG*, as it has an LCST of ~100 °C in water and therefore does not self-assemble naturally below that temperature.<sup>[132]</sup> A well-known modification of PEG precursor polymers used in microtissue engineering is the functionalization with acrylates, which enables fast, UV-induced crosslinking.<sup>[133,134]</sup> Slightly slower and controlled gelation times, in turn, can be achieved by strain-promoted alkyne azide cycloaddition (SPAAC) and thiol-ene Michael addition reaction between thiols and vinylsulfones, acrylates/methacrylates, or norbornene-functionalized PEG polymers.<sup>[135–141]</sup>

*PU*s (usually thermoplastic PUs) are very versatile in their composition and form gels both covalently and physically. Exemplarily, covalently crosslinking has been studied by Jung et al., who provided cell-adhesive Janus PU microfibers for tissue engineering applications. For this purpose, a commercially available, photocurable PU oligomer solution with crosslinker (NOA63) is used, that solidify via radical polymerization through UV irradiation.<sup>[142]</sup> Physical crosslinking in turn has been mainly utilized in bioprinting applications. For instance, Lin et al. have synthesized a biodegradable and thermo-sensitive PU/soy protein hybrid bioprinting ink for direct 3D cell printing, which undergo a sol gel transition with increasing temperature up to 37 °C.<sup>[143]</sup> And Hsieh et al. synthesized a bioink based on PU nanoparticles and gelatin, which form a double-network in two-stages through chelation of both components at room temperature (using Ca<sup>2+</sup> ions) and subsequent thermal gelation of gelatin at 37 °C.<sup>[144]</sup> A combination of both, physical and covalent gelation, was provided by Hsiao et al., who synthesized a UV- and thermo-sensitive bioink based on PU nanoparticles with acrylate functionalization and thermosensitive oligodiols.<sup>[145]</sup> The wide range of further gelation strategies cannot be covered completely in this review and reference is made to previous work.<sup>[146]</sup>

### 1.5.1.2. Adaptivity: Tunability of mechanical material properties

Another important requirement of materials for microtissue engineering applications is their mechanical adaptivity and tunability to the different structural conditions of in vivo tissues to ensure the best possible mimicry of host structures and thus increase the success rate with respect to animal avoidance. In vivo tissues are naturally subject to a wide range of mechanical strengths. For example, brain tissue exhibits a relatively small elastic modulus of  $< 0.1$  kPa, whereas tendons exhibit a relatively large elastic modulus of  $\sim 1.4$  MPa.<sup>[147]</sup> To account for this diversity, the influence of nanoscopic material structure on the resulting macroscopic properties must be considered. Accordingly, the focus in the following is on nanoscopic material structures, their effects on mechanical strength and their potential tunability, which will be discussed in terms of mesh size  $\xi$ , comonomer composition, molar mass, concentration, degree of swelling and crosslink density (Figure 1-4).

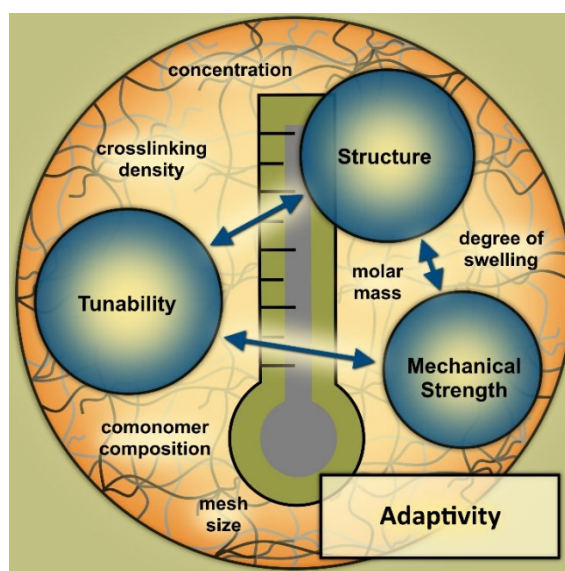


**Figure 1-4.** Adaptivity of materials described by the triangular relationship between nanoscopic material structure, mechanical strength, and potential tunability.

Since the material strength is often provided in the literature as shear storage modulus  $G'$  [Pa] or elastic (Young's) modulus  $E$  [Pa], this review will focus on exactly these two mechanical parameters. Both quantities are related by the Poisson's ratio  $\nu$  ( $E = 2G(1+\nu)$ ). In case of incompressible materials such as hydrogels, the Poisson's ratio is usually 0.5. Hence, the shear storage and elasticity modulus can be transformed into each other according to the relationship  $E \sim 3G$ .<sup>[148]</sup>

The mesh size  $\xi$  (distance between two network points) of a polymer network is crucial for tuning its mechanical properties. Its relationship to the mechanical material strength can be

## THEORY

derived from the phantom network model, described by  $\xi = ((RT)/(G \cdot N_A))^{1/3}$ , with  $R$  being the gas constant,  $T$  the temperature,  $N_A$  the Avogadro constant, and  $G$  the storage modulus.<sup>[148–151]</sup> Exemplarily, PEG enables easy tuning of the mesh size and mechanical strength of a corresponding hydrogel by varying the molar mass, geometric composition (linear-, 4arm-, 8arm-, star-PEG), and concentration of precursor polymers. In one example, degradable vaterite/PEG-composite microgels were developed as in vitro models for bone tissue engineering applications. Herein, the molar mass of precursor polymers was varied to obtain shear storage moduli between 20.9 and 30.3 kPa.<sup>[138]</sup> A second example was given by de Laporte and coworkers, encapsulating cells in rod-like (anisometric) PEG-based microgels for mimicking elongated tissue architectures such as musculoskeletal tissues. Thereby, the microgels differ in the concentration (2–5% (w/v)) of initially used precursor polymers and show storage moduli between 0.1 to 7.2 kPa.<sup>[137]</sup>

The mechanical strength of covalently crosslinked *PNIPAAm* hydrogels is temperature dependent, since *PNIPAAm* hydrogels have a Volume Phase Transition Temperature (VPTT) of 34 °C, which corresponds to the LCST of *PNIPAAm* polymers as described in the previous section.<sup>[96]</sup> Therefore, as the temperature increases, the hydrogel displaces water for thermodynamic reasons, resulting in a decrease in hydrogel volume. This leads to a higher density of network strands per unit volume and thus to an increasing mechanical strength of *PNIPAAm* hydrogels with increasing temperature.<sup>[152]</sup> Möhwald and coworkers for example have developed *PNIPAAm* microgel films for bio-applications, which show an increase of elastic modulus from 86 to 330 kPa with increasing temperature from 25.3 to 37.2 °C.<sup>[153]</sup> To further shift the VPTT of *PNIPAAm* and hence decrease or increase its mechanical strength at a given temperature (e.g., at physiological temperature) hydrophilic or hydrophobic comonomers can be incorporated into the *PNIPAAm* network.<sup>[50,95]</sup> Additional influences on the VPTT as pH and salt ions of the cell culture medium need to be considered as well.<sup>[50]</sup>

Thermoplastic and thermoset *PU*s contain hard (diisocyanate and chain extender) and soft (polyol) segments that micro-segregate due to physical interactions between urethane groups and affect the mechanical properties of *PU*s.<sup>[99]</sup> Correspondingly, by varying the portion of hard and soft segments in *PU* polymer networks, different elastic moduli could be obtained. For example, Mi et al. have synthesized soft and hard thermoplastic electrospun scaffolds for bone tissue applications and investigated the effects of incorporated hydroxyapatite (HA) particles on the mechanical strength of the polymers. In case of soft thermoplastic *PU*s, HA particles show no effect on the mechanical stiffness, which remains at about  $E = 0.01$  MPa. By contrast, hard thermoplastic *PU*s exhibit a larger elastic modulus of 0.4 MPa, which,

however, decreases with the incorporation of HA particles.<sup>[154]</sup> Much softer PU polymers were obtained by Hill et al. who prepared PEG-based colloidal microgel particles by self-assembly and obtained elastic moduli between 7.5 to 2525 Pa by varying the molar mass of the soft segment PEG (2,000 down to 600 g mol<sup>-1</sup>).<sup>[155]</sup> These both examples demonstrate the wide range of possible mechanical strengths that PUs simply achieve by the composition and ratio of soft and hard segments in the polymer backbone.

By contrast, most natural materials have usually weak and less tunable mechanical properties, such as *collagen* ( $G' = 0.5\text{--}429.7$  Pa for 0.5–5.0 mg mL<sup>-1</sup>), *gelatin* ( $E = 179$  Pa at a concentration of 10%), and *agarose* ( $E = 3.6$  kPa at a concentration of 1%), which can be improved by increasing the molar mass and the concentration of precursor polymers.<sup>[124,156,157]</sup> The mechanical strength can further be improved through the formation of interpenetrating networks with mechanical stronger polymers, as described by Ort et al. For this purpose, they have synthesized collagen/alginate-based microgels and analyzed the influence of increasing alginate concentration (0–1.6 mg/mL) on the storage modulus (0.5–2.3 kPa) of microgels.<sup>[158]</sup> The mechanical properties can be further improved by chemical crosslinking. Lee et al. for example have encapsulated MCF-7 cells and cocultures of MCF-7 and macrophages in covalently crosslinked gelatin (GelMA)-based microgels to provide a strategy to design tumor spheroids. They varied the precursor concentration (6–14% (w/v)) and analyzed the effect of mechanical properties ( $G' = 1.8\text{--}18.5$  kPa) on the spheroid growth.<sup>[159]</sup> The stiffness of agarose can further be reduced by aldehyde-functionalization as described by Yamada et al. for tissue engineering applications. Without aldehyde functionalization agarose-based microgels show a storage modulus of 11.1 kPa, whereby CHO functionalization reduce the storage modulus to 0.5 kPa (both 1 wt%).<sup>[76]</sup>

Also *hyaluronic acid* has weak mechanical properties ( $E = 1.5$  kPa at a concentration of 1%) that can be improved by chemical crosslinking.<sup>[157]</sup> For example, Jooybar et al. developed hyaluronic acid-based microgels embedded in a hydrogel for the delivery of platelet lysate (a blood product with a high concentration of growth factors). In this process, hyaluronic acid was modified with tyramine, which enzymatically crosslinks in the presence of hydrogen peroxide and horseradish peroxidase, resulting in microgels with a mechanical strength of 5.4 kPa.<sup>[160]</sup> In addition, hyaluronic acid has another special feature at pH 7: At this pH, the [–COOH] units are deprotonated, resulting in a strongly hydrophilic polymer character and a water absorption up to 1000 times its solid volume.<sup>[128,131]</sup> In these cases, it is obvious that a high water content reduces the mechanical strength of hydrogels. A general characteristic parameter describing the water content in a hydrogel beyond the scope of hyaluronic acid is

## THEORY

the degree of swelling. It is defined as the mass-swelling ratio  $Q_M = m_s/m_d$  between the mass of the swollen  $m_s$  and the dried hydrogel  $m_d$ .<sup>[161]</sup> Or it is defined as the volumetric swelling ratio  $Q_V = 1 + \rho_d/\rho_s (Q_M - 1)$  with  $\rho_d$  and  $\rho_s$  the density of the dried and the swollen hydrogels.<sup>[161,162]</sup> Corresponding thermodynamic studies have been performed, for example, by Bystroňová et al. who created a 3D microenvironment based on gelatin and hyaluronic acid hydrogels suitable for in vitro microtissue modeling applications. By varying the ratio of polymer components and the crosslinking mode, different degrees of swelling and, accordingly, different mechanical strengths between 10 and 20 kPa (4% (w/v)) could be obtained.<sup>[163]</sup> To relate the swelling behavior or the mechanical strength of hydrogels to the structural composition of the nanoscopic network, the Flory-Rehner equation can further be used. From this, the expression  $\xi = 0.1748 (M_c)^{1/2} (Q_V)^{1/3}$  can be derived, which relates the mesh size of hyaluronic acid-based hydrogels ( $\xi$ ) to the strand molar mass between two crosslinking points ( $M_c$ ) and the volumetric swelling ratio ( $Q_V$ ). This expression applies specifically to hyaluronic acid-based systems, but can be adapted to other materials by considering the derivation of Collins et al.<sup>[162]</sup>

In turn, the mechanical strength of *alginate* ( $E = 3.6$  kPa at a concentration of 1%) can further be improved by surface modification with positively charged polyelectrolytes as poly(ethylene imine), chitosan or poly-(L-lysine) (PLL), which adhere to the negatively charged alginate backbone.<sup>[157]</sup> The change of the total surface charge restricts its swelling behavior and promotes the mechanical polymer strength.<sup>[164,165]</sup> Pasqua et al. for example have synthesized cell-laden alginate-PLL-based microbeads for extracorporeal liver supply. Herein, PLL reinforced the mechanical stability of pure alginate microbeads, whereby the elastic module increased from  $\sim 1$  to 5 kPa with PLL modification.<sup>[166]</sup>

Due to its LCST slightly above the physiological temperature range (LCST = 40–50 °C), *methyl cellulose* is usually viscous at physiological conditions and has a correspondingly low mechanical strength.<sup>[107]</sup> An increase in viscosity could be improved by increasing the polymer concentration and the molar mass of the polymer strands.<sup>[86]</sup> Additionally, to promote conversion of the methyl cellulose solution into a gel-like state under physiological conditions, precursor polymers with a higher proportion of methyl groups in the polymer backbone could be used. These cause an increase in hydrophobicity of the material shifting the LCST to lower temperatures.<sup>[167]</sup> In combination with other polymers like alginate, methyl cellulose also forms stable hydrogels. For example, Babu et al. synthesized alginate-methyl cellulose microspheres for drug delivery applications, whereby alginate and methyl cellulose were connected to each other by glutaraldehyde.<sup>[168]</sup>

### 1.5.1.3. **Biocompatibility: Cell viability versus material functionality**

Another important parameter is the biocompatibility of the materials used. These materials must actively support cell viability in the experiments through their microscopic structure and chemical functionality. Regarding the microscopic structure, access to oxygen and nutrients plays a particularly important role. Without these components, cell viability is considerably reduced, which can result in necrotic tissues and, correspondingly, the validity of the in vitro models is considerably diminished.<sup>[169]</sup> Hydrogels are generally accessible to diffusible species due to their swelling behavior and porosity. However, there is often a lack of oxygen and nutrients because their diffusion is restricted in the tissue to be imitated. Usually, such diffusion occurs over a tissue thickness of 100–200  $\mu\text{m}$ , beyond which it is limited.<sup>[169]</sup> Due to this fact, microscopic-scale model systems are particularly suitable for in vitro applications, as they allow oxygen and nutrient exchange by simple diffusion. In contrast, diffusion in larger constructs is limited, which can be compensated by active vascularization in the hydrogel systems. Agarwal et al. demonstrated corresponding studies by assembling microscopic tissue building blocks, together with vessel-specific cells into macroscale vascularized 3D tumors for anticancer studies.<sup>[170]</sup> Other experiments address oxygen and nutrient exchange through precise and controlled mass transport.<sup>[171]</sup> For example, Ahmeda et al. cultured spheroids in bioreactors exposed to a fluid flow to enable continuous oxygen and nutrient exchange.<sup>[172]</sup> A combination of both, mass transport and vascularization, is offered by Hsu et al. who have developed an organ-on-a-chip assembly based on connected microtissues exposed to fresh fluid via a controlled circuit.

In addition to good oxygen and nutrient supply, adherent cells are essential for cell viability, proliferation, and differentiation in in vitro models. For this reason, the relationship between cell adhesion and chemical functionality of materials requires special attention. To enable cell adhesion, cells present integrins on their cell membrane that enable cells to bind to specific ligands of materials and other cells through physical and (bio-)chemical interactions, which actively control the cell morphology, as sketched in **Figure 1-5**.<sup>[98]</sup> If a material is rich in ligands, cells will predominantly adhere to that material (A). These materials are accessible in two ways: via materials with the molecular structure of the ligands (“direct” cell adhesion), or via materials to which ligand-rich materials adsorb by physical interactions (“indirect” cell adhesion). Conversely, cells exhibit a spherical morphology when a material has few cell-binding ligands. In this case, cell-cell interactions are favored, leading to the formation of cell agglomerates and spheroids (B).<sup>[173,174]</sup>

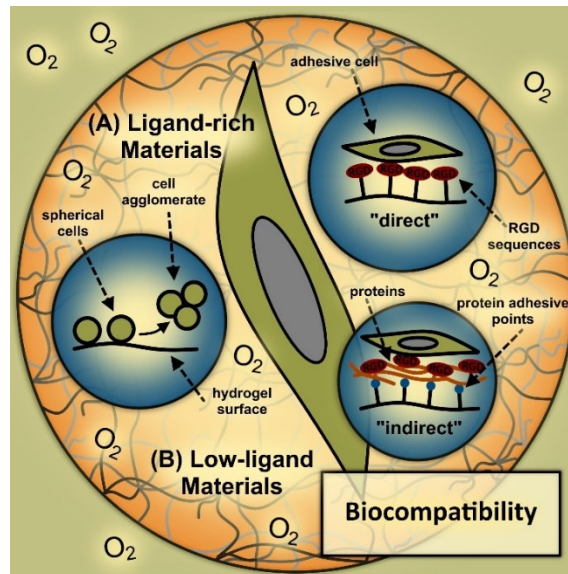


**Figure 1-5.** Biocompatibility of materials in microtissue engineering, with emphasis on oxygen/nutrient exchange and cell adhesion to (A) ligand-rich ("direct" versus "indirect") and (B) low-ligand materials.

Proteins from the ECM with specific amino acid sequences as for example the Arg-Gly-Asp (RGD) sequence in fibronectin, or the Gly-Phe-Hyp-Gly-Glu-Arg (GFOGER) sequence found in collagen, are ligand-rich materials that enable “direct” cell adhesion.<sup>[55,175]</sup> Cell surface integrins link to these ligand-rich domains by physical interactions, which is why cells adhere well to *fibronectin*, *collagen type I*, and *gelatin* based materials.<sup>[55]</sup> Hence, they are widely used in in vitro models, especially in lab-on-the-chip applications. According to 3R regulations, Sfriso et al. studied the interplay between endothelial cells and the plasma cascade system for cardiovascular research. Here, they used a closed microfluidic circulation system with cells cultured as monolayers in round printed polydimethylsiloxane (PDMS) microchannels that had been treated with fibronectin or type I collagen to imitate blood vessels.<sup>[176]</sup> Wang et al. used a decellularized liver matrix/gelatin methacryloyl-laden microfluidic device to mimic continuous 3D metastatic cancer cell growth as a platform for effectively testing therapeutic strategies.<sup>[177]</sup>

However, the structure of many materials does not allow for "directly" adhering cells due to the lack of cell-adhesive ligands; instead, cell adhesion sometimes occurs "indirectly" through ligand-rich components such as proteins and polypeptides that adsorb to materials with low ligand content due to their net positive or negative charge.<sup>[98]</sup> Protein adsorption to these materials is usually achieved by incubation in protein-rich cell culture medium (e.g., by adding fetal bovine serum) or by cells that actively secrete proteins.<sup>[178]</sup> A corresponding ligand-poor material to which proteins and polypeptides adsorb in a temperature-dependent manner is *PNIPAAm* with  $[-CO-NH-]$  functionality. Above the VPTT of 34 °C, PNIPAAm materials



are in the collapsed state with low water content and high protein adsorption, resulting in good cell adhesiveness. However, with decreasing temperature, the PNIPAAm material becomes more hydrated, which counteracts protein adsorption and leads to cell detachment.<sup>[179]</sup> Takahashi et al. took advantage of this property to enable scaffold-free microtissues by culturing astrocytes and neurons on PNIPAAm-based substrates at 37 °C. After several days of cultivation, the temperature was lowered to room temperature, enabling the growth of microtissues with diameters of 50, 100, and 200  $\mu\text{m}$  to detach from the PNIPAAm substrate.<sup>[180]</sup> The temperature-dependent cell attachment character of PNIPAAm hydrogels can also be rendered temperature-independent and be stabilized by additional surface modification, e.g., with polydopamine (PDA), since PDA (a component consisting of catechol and amino groups) physically binds to both, proteins and PNIPAAm hydrogels. Accordingly, PDA-coated PNIPAAm-based microgel templates were fabricated as in vitro models to allow for homogeneous and temperature-independent cell coating and adhesion on microgel surfaces to potentially mimic the blastula in embryogenesis, mammary glands, or alveolar epithelium.<sup>[152]</sup> Also, some types of *PU* materials enable protein adsorption due to hydrogen-bonding between urethane groups and proteins as described by Sheikholeslam et al. and Chernonosova et al.<sup>[181,182]</sup> Both references included PU/gelatin composite materials for tissue engineering applications prepared by electrospinning, which showed good cell adhesion on these materials.

In turn, materials based on ethylene glycol  $[-(\text{CH}_2\text{CH}_2\text{O})_n]$  units as *PEG* are low-ligand materials without the potential to bind physically to ligand-rich proteins and polypeptides, which is why they are also referred to as bioinert.<sup>[173,174]</sup> Accordingly, the cells do not adhere to these materials and form cell agglomerates. This property is often deliberately exploited, for example, to generate cell spheroids, as by Siltanen et al. who encapsulated hepatocytes in PEG-based microgels by the droplet-based microfluidic technique to generate spheroids for hepatotoxicity screening in the preclinical drug development.<sup>[150]</sup> However, to further increase the cell adhesive properties of these materials, bioactivation via covalent modification with RGD or peptide sequences is possible.<sup>[55,92,183]</sup> Corresponding RGD-treated hollow PEG-based micromodules were fabricated by Wang et al., where PEG diacrylate components were photopolymerized with acryloyl-PEG-Arg-Gly-Asp-Ser sequences. These micromodules were then assembled to form a tissue-specific morphology (e.g., liver lobules) with a vessel-like lumen for tissue regeneration.<sup>[133]</sup> Similar low-ligand properties apply to most polysaccharides due to their hydrophilic nature.<sup>[184,185]</sup> In particular, *agarose* hydrogels are frequently used as a bioinert template for the synthesis of cell spheroids and organoids, as described by Gong et

## THEORY

al., Janjić et al., and Oberoi et al.<sup>[186–188]</sup> To improve cell adhesion to these materials, RGD or polypeptide units need to be incorporated into these networks as well.<sup>[76]</sup> The same applies to other polysaccharide-based hydrogels such as *alginate* and *hyaluronic acid*.<sup>[189–191]</sup>

### 1.5.1.4. Stability/degradability: Influences of physiological parameter space

Long-term stable materials are an important prerequisite for many in vitro models to achieve reproducible results without changes in the microenvironment and without the risk of toxic degradation products. Cullen and coworkers have worked exemplarily on the development of axonal pathways to modulate neuronal circulation. Here, the columnar hydrogel template must be stable until the axonal pathways have connected to host neurons via synapses.<sup>[192]</sup> In contrast, there a large number of in vitro applications exist that require targeted material degradation, e.g., for the release of cells and drugs.<sup>[193]</sup> Accordingly, the natural stability and degradability of materials to enzymes, hydrolysis or solubilization, as well as potential control elements for (de-)stabilization, are presented below (**Figure 1-6**).

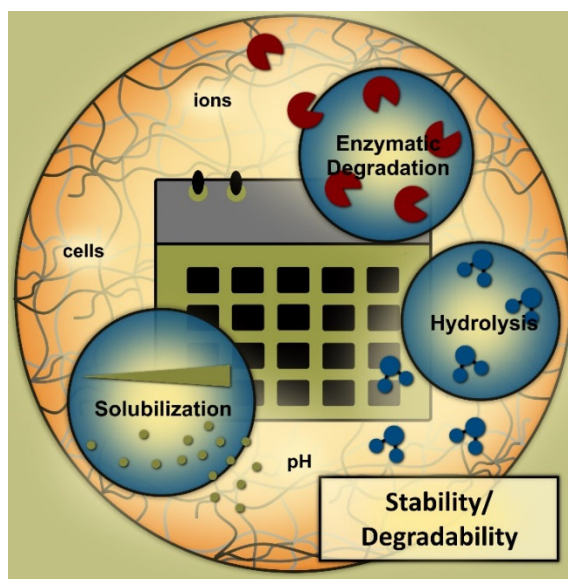


**Figure 1-6.** Natural stability/degradability of hydrogels to enzymes, hydrolysis, and solubilization, and key elements for control.

Proteins such as *collagen* and *gelatin* are enzymatically degradable by cleavage of C–O, C–N, and C–C bonds.<sup>[194]</sup> A corresponding enzymatic degradation of modified cell-laden collagen type I microgels was analyzed by Thomas et al. by adding the enzyme collagenase. Here, the physically crosslinked microgels (~1 mm diameter) were completely degraded within 24 hours. They also analyzed PEG- and glutaraldehyde-crosslinked microgels, which degrade more slowly compared to the physical crosslinked microgels, indicating a stabilizing effect of covalent bonds.<sup>[195]</sup> However, even without the addition of enzymes, protein gels could be

degraded by cellular secretion enzymes, which needs to be taken into account if long-term stable materials are desired.<sup>[196,197]</sup> However, because cells also produce proteins at the same time, hydrogels are often biologically remodeled, which is hugely important for cell organization, alignment, and migration in microtissues and for mimicking the natural ECM.<sup>[198]</sup> Such remodeling of cell-coated collagen microgels, for example, has been investigated by Crampton et al. as potential in vitro high-throughput platforms. They analyzed the difference in collagen remodeling between physically ("soft") and covalently ("stiff") crosslinked microgels and found significant remodeling of "soft" by second harmonic generation but little to no remodeling of "stiff" microtissues.<sup>[199]</sup> A corresponding dependence of materials degradation or remodeling on crosslinking density was also shown by Nichol et al. The authors synthesized GelMA-based microgel units and analyzed the cell behavior as a function of polymer concentration (5, 10, and 15%), while cell migration and microgel remodeling decreased with increasing gel concentration.<sup>[198]</sup> In summary, physical crosslinking promotes the degradation and remodeling of proteins, while covalent crosslinks often slows down these processes. The more covalent crosslinking units, the slower the degradation process and the more stable are the materials.

Enzymatic degradation is also a suitable tool for material manipulation of polysaccharides, whereby glycosidic bonds between sugar units are cleaved. Correspondingly, microtissues based on *methyl cellulose*, *agarose*, and *hyaluronic acid* are degradable in the presence of enzymes (such as cellulase, agarase, and hyaluronidase). These processes can be influenced and slowed down by their molar mass, the type of chemical modification and the degree of functionalization.<sup>[86,200–202]</sup> In addition to enzymatic degradation (e.g., by lyase), *alginate* (and other physically cross-linked polysaccharides and proteins) solubilizes in water due to its physical crosslinking nature, which can be controlled among others by the pH of the surrounding solvent (alginate is stable between pH 5 and 10).<sup>[72,203]</sup> The addition of complexing agents such as citric acid or EDTA, can further promote the liquefaction of alginate, by chelating the calcium ions of the alginate network and dissolving alginate strands.<sup>[165,204]</sup> Because of this property, it is often used as a sacrificial template, such as described by Nadine et al. who liquefied cell-laden microcapsules for various tissue engineering applications using EDTA.<sup>[165]</sup> By contrast, the long-term stability of alginate can be significantly improved by covalent incorporation of crosslinkers or physical interaction with cationic polymers (e.g., chitosan).<sup>[52]</sup> Yao et al. for example fabricated stable alginate-based multicomponent fibers for cell co-culture. Here, the microfibers were stabilized over a period of 21 days in cell culture medium by the addition of positively charged chitosan.<sup>[205]</sup>

## THEORY

Without the intentional incorporation of hydrolytic cleavable groups, synthetic hydrogels such as PEG and PNIPAAm are in general stable and suitable for long-term in vitro studies of synthetic microtissues. For example, Haag and coworkers have synthesized non-degradable polyglycerol-based microcapsules by combining the SPAAC click reaction with droplet-based microfluidics. These platforms are used as potential cell therapeutics for long-term isolation and protection of encapsulated cells from immune responses of potential hosts.<sup>[206]</sup> In contrast, for a controlled degradation of these synthetic materials, they must be modified. For example, the chemical incorporation of peptides or polysaccharide units into these hydrogels enables enzymatic degradation. Accordingly, Rose et al. have resembled the ECM by embedding anisometric PEG-based microgels into PEG/peptide hydrogels, which are sensitive to metalloproteinases and hence enzymatic degradation.<sup>[207]</sup> Furthermore, Sattari et al. have synthesized micro-/nanohydrogel composites based on PNIPAAm graphene oxide and starch as biodegradable crosslinker for biocompatible drug delivery.<sup>[208]</sup> Another possibility to tune network degradability is the deliberate incorporation of hydrolysis-sensitive ester groups, which can degrade into carboxylic acid and alcohol units. Accordingly, Steinhilber et al. have synthesized a hydrolysis-sensitive PEG-based microgel construction kit for the pH-controlled release of living cells.<sup>[136]</sup> And Sivakumaran et al. have prepared hydrolytic degradable thermoresponsive PNIPAAm-based microgels via the microfluidic technology, using aldehyde- and hydrazide-functionalized PNIPAAm precursor polymers.<sup>[209]</sup> Overall, synthetic materials such as PEG and PNIPAAm in particular are easily and specifically adaptable in terms of degradability and long-term stability through chemical modification, which makes them particularly interesting as materials for in vitro model systems from this point of view.

PU-based materials, in turn, inherently contain hydrolytically labile groups in their polymer backbone, which generally makes them susceptible to degradation.<sup>[99]</sup> In this context, the degradability of these materials, or conversely their stability, depends on the hydrophilicity of the hard and soft segments of the PU structure. The more hydrophilic the structure is overall, the more aqueous medium can be absorbed (increasing degree of swelling) and the faster the material degrades. Accordingly, the stability of the material can be promoted by increasing the hydrophobic content in the materials. Relevant studies were performed, for example, by Nair et al., who incubated poly(ester-urethane)urea-based microfiber structures in PBS (pH 7.4) at 37 °C and analyzed their degradation rate over a period of 180 days.<sup>[210]</sup> Depending on the structural composition of the PU backbone, pH-assisted degradation is also feasible, as described by Bachelder et al.<sup>[211]</sup> In this work, they prepared PU microparticles

for protein-based vaccines with dimethyl acetal moieties in the polymer backbone that hydrolyze under acidic conditions.

**Table 1-2.** Characteristic chemical groups of selected natural and synthetic materials relevant to the field of microtissue engineering and their multiparametric functionality in terms of processability, adaptivity, biocompatibility, and stability/degradability.

	Structure <sup>a)</sup>	processability	adaptivity	biocompatibility	stability/degradability
	chemical functionality	self-assembly	modulus $G'$ or $E$	cell adhesion	natural degradation
<b>collagen</b>	[-CO-NH-] [-H, -R]	physical: pH = 7 (37 °C)	$G' = 0.5\text{--}429.7$ Pa (0.5–5.0 mg/mL) <sup>[124]</sup> $E = 5\text{--}25$ kPa (1.0–2.5 mg/mL) <sup>[212]</sup>	(+) “direct”	enzymatic (collagenase)
<b>gelatin</b>	[-CO-NH-] [-H, -R]	physical: $T_{UCST} = 25\text{--}30$ °C	$E = 179$ Pa (10%) <sup>[156]</sup> $E \sim 10$ Pa (5%) <sup>[213]</sup>	(+) “direct”	enzymatic (collagenase)
<b>fibronectin</b>	[-CO-NH-] [-R]	no relevance	no relevance	(+) “direct”	enzymatic
<b>alginate</b>	[-OH] [-COOH]	physical: $\text{Ca}^{2+}$ , $\text{Ba}^{2+}$ , $\text{Fe}^{3+}$	$E = 3.6$ kPa (1%) <sup>[157]</sup>	(-)	enzymatic (lyase); solubilization
<b>agarose</b>	[-OH]	physical: $T_{UCST} = 20\text{--}70$ °C	$E = 3.6$ kPa (1%) <sup>[157]</sup> $E = 20.2 \pm 0.5$ kPa (5 wt%) <sup>[214]</sup>	(-)	enzymatic (agarase); solubilization
<b>methyl cellulose</b>	[-OH] [-O-CH <sub>3</sub> ]	physical: $T_{LCST} = 40\text{--}50$ °C	no relevance	(-)	enzymatic (cellulase); solubilization
<b>hyaluronic acid</b>	[-COOH] [-OH] [-NHCOCH <sub>3</sub> ]	physical: entangle	$E = 1.5$ kPa (1%) <sup>[157]</sup>	(-)	enzymatic (hyaluronidase); solubilization
<b>PEG</b>	[-(CH <sub>2</sub> CH <sub>2</sub> O) <sub>n</sub> ]	no relevance	$G' = 20.9\text{--}30.3$ kPa <sup>[138]</sup> $G' = 0.1\text{--}7.2$ kPa 2–5% (w/v) <sup>[137]</sup>	(-)	(-)
<b>PNIPAAm</b>	[-CO-NH-] [-CH(CH <sub>3</sub> ) <sub>2</sub> ]	physical: $T_{LCST} = 32$ °C	$E = 86\text{--}330$ kPa (25.3–37.2 °C) <sup>[153]</sup>	$T > T_{VPTT}$ (+) $T < T_{VPTT}$ (-) “indirect”	(-)
<b>PU</b>	[-NH-CO-O-]	(physical)	$E \sim 0.01\text{--}0.40$ MPa <sup>[154]</sup> $E = 7.5\text{--}2525$ Pa <sup>[155]</sup>	(-)/(+) “indirect”	hydrolysis; enzymatic

<sup>a)</sup> The table is intended to provide an exemplary overview but does not claim to be complete.

### 1.5.2. Advanced Materials

To further advance the diversity and quality of in vitro model systems as a basis to replace animal experiments with high-quality and reproducible alternatives, materials will have to become even more intelligent in the future. Building on the multiparametric material requirements discussed so far, pre-programmable material properties such as *self-assembly*, *self-healing*, and *4D structure* will play an increasingly important role in enabling predefined and material response functions. Often referred to as smart materials, these polymers respond in a self-determined manner to external influences and selectively change their composition, structure, and mechanical properties. They dynamically adapt to external conditions, enabling even more concrete mimicry of in vivo tissues than general multiparametric materials.<sup>[215–217]</sup> The more precisely synthetic materials adapt to natural structures and processes, the better the informative value of in vitro model systems will ultimately be and the faster animal testing can be replaced by artificial alternatives.

In this context, especially functional, synthetic, supramolecular polymers and their application in tissue regeneration are increasingly being explored.<sup>[218]</sup> Modeled after natural materials, they are capable of *self-assembly* through physical interactions, enabling the construction of complex structures with sophisticated geometric and architectural control over the entire scale. For example, Khademhosseini and coworkers have developed pre-programmable and controllable PEG-/DNA-based hydrogel cuboids that self-assemble into complex microstructures through supramolecular binding interactions between complementary DNA strands.<sup>[219]</sup> These microstructures form cleverly and complex assembled tissue imitations whose physicochemical and mechanical properties are comparable to those of conventional multifunctional polymer materials.<sup>[215]</sup> Further insights to that topic can be found in a review article by Ouyang et al. that addresses various bottom-up strategies for assembling building blocks in tissue engineering.<sup>[220]</sup>

Similar, pre-programmed properties are also exhibited by *self-healing* materials, which can self-heal independently and automatically to return to their normal state. This capability enables the restoration or maintenance of the original material properties and accordingly leads to an increase in the lifetime as well as the reliability of in vitro model systems.<sup>[221]</sup> Mealy et al. have presented exemplary injectable, shear-thinning, and self-healing hyaluronic acid-based granular hydrogels for biomedical applications, whose self-healing properties enable rapid material stabilization after bioprinting.<sup>[222]</sup> Self-healing is mostly based on non-covalent

interactions and occurs in the example through guest-host bonding between adamantane-modified hyaluronic acid hydrogels and linear cyclodextrin-modified hyaluronic acid strands. The transition from static 3D materials to adaptive and responsive materials is further enabled by dynamic, pre-programmed *4D structures*, where form, function, and properties change over time due to external factors.<sup>[223–225]</sup> These materials adapt to the environment during their life cycle and can be broadly described as 3D materials, taking time into account as a fourth dimension.<sup>[226,227]</sup> In this context, cells and materials are not considered as separate components (as it is the case in 3D structures), but as a whole, living construct that communicates with each other during cell growth and material adjustment. A relevant example is provided by Apsite et al. who used a 4D biofabrication method to produce microtissues for skeletal muscles. Herein, electrospinning is applied to develop two-layer mats of anisotropic methacrylated alginate fibers (outer layer) and polycaprolactone nanofibers (inner layer) that self-fold into tubes in aqueous buffer solutions. Depending on the orientation of the polycaprolactone nanofibers and the concentration of calcium ions in the buffer solution, the tubes can be oriented differently, controlling cell growth accordingly.<sup>[228]</sup> Another possibility is 4D shape memory materials (materials that return to their original shape after mechanical deformation).<sup>[229]</sup> For example, cell-loaded hollow tubular microstructures based on chemically cross-linked alginate-methacrylate hydrogels were fabricated through bioprinting by Kirillova et al. In the presence of calcium ions, the structure of the microtubes twisted due to complex formation between alginate and buffer ions. By removing calcium ions from the hydrogel matrix by EDTA, they regained their permanent structure.<sup>[230]</sup> Overall, the development of 4D material-cell composites represents another important step to further close the gap between synthetic in vitro model systems and natural in vivo tissues. Through intelligent communication between synthetic tissues and cells, they are visibly approaching the complexity of natural tissues. Together with the other pre-programmable materials, they thus ultimately drive progress in the field of in vitro model systems, and thus also in the field of animal testing avoidance.

## 1.6. Conclusion

The aim of the review is to discuss the increasing importance of in vitro models as a substitute for animal testing, focusing on materials properties in microtissue applications. The more defined and functional the materials are, the more likely they are to mimic similar co-cultures, microtissues, and organoids in vivo. Accordingly, potential processes based on bioprinting, spheroids, microfluidics, and organ-on-a-chip are addressed, as well as the origin and chemical composition of relevant materials. Another focus is on multiparametric material functionality as an important basis for the successful development of in vitro models. To this end, natural and synthetic materials are discussed in terms of their processability, adaptivity, biocompatibility and stability/degradability. In addition, advanced "smart" materials that can self-assemble and heal through pre-programming and form 4D structures are addressed. As the abundance of materials with versatile properties has become increasingly dense in recent decades, the question now arises as to what synthetic possibilities will result from this in the future, and what significance they may have for replacing animal experiments. A correspondingly promising answer can be found in the field of synthetic biology, which has gained enormous importance in recent years. In addition to the synthesis of living bio-machines for the autonomous recognition of disease states in vivo and appropriate treatment, designer cells (hybrids of living cells and artificial biological units) with adjustable properties are being targeted.<sup>[23,24]</sup> Their independent and agile ability to act enables personalized medicine to take a major step towards the future and hence also forms one of the many promising alternatives for the replacement of animal experiments.



## 1.7. Literature

- [1] S. Scholz, E. Sela, L. Blaha, T. Braunbeck, M. Galay-Burgos, M. García-Franco, J. Guinea, N. Klüver, K. Schirmer, K. Tanneberger, M. Tobor-Kaplon, H. Witters, S. Belanger, E. Benfenati, S. Creton, M. T. D. Cronin, R. I. L. Eggen, M. Embry, D. Ekman, A. Gourmelon, M. Halder, B. Hardy, T. Hartung, B. Hubesch, D. Jungmann, M. A. Lampi, L. Lee, M. Léonard, E. Küster, A. Lillicrap, T. Luckenbach, A. J. Murk, J. M. Navas, W. Peijnenburg, G. Repetto, E. Salinas, G. Schüürmann, H. Spielmann, K. E. Tollefsen, S. Walter-Rohde, G. Whale, J. R. Wheeler, M. J. Winter, *Regul. Toxicol. Pharmacol.* **2013**, *67*, 506.
- [2] F. Petetta, R. Ciccocioppo, *Addict. Biol.* **2020**, *26*, e12991.
- [3] M. Balls, *Altern. to Lab. Anim.* **2020**, *48*, 40.
- [4] S. Garattini, G. Grignaschi, *Eur. J. Intern. Med.* **2017**, *39*, 32.
- [5] H. R. Ferdowsian, N. Beck, *PLoS One* **2011**, *6*, e24059.
- [6] L. Robinson, *Alternative Methods to Animal Testing. A Practical Guide to Toxicology and Human Health Risk Assessment*, Hoboken, USA, Wiley **2019**.
- [7] D. Peneda Pacheco, N. Suárez Vargas, S. Visentin, P. Petrini, *Biomater. Sci.* **2021**, *9*, 70.
- [8] S. K. Doke, S. C. Dhawale, *Saudi Pharm. J.* **2015**, *23*, 223.
- [9] G. A. Van Norman, *JACC Basic to Transl. Sci.* **2016**, *1*, 170.
- [10] J. Tannenbaum, B. T. Bennett, *J. Am. Assoc. Lab. Anim. Sci.* **2015**, *54*, 120.
- [11] R. C. Hubrecht, E. Carter, *Animals* **2019**, *9*, 754.
- [12] Council of the European Union, Council Directive 86/609/EEC of 24 November 1986 on the approximation of laws, regulations and administrative provisions of the Member States regarding the protection of animals used for experimental and other scientific purposes, **1986**. <https://eur-lex.europa.eu/legal-content/EN/ALL/?uri=CELEX:31986L0609> (11/2021)
- [13] European Parliament, Council of the European Union, Directive 2010/63/EU of the European Parliament and of the Council of 22 September 2010 on the protection of animals used for scientific purposes Text with EEA relevance, **2010**. <https://eur-lex.europa.eu/legal-content/EN/ALL/?uri=CELEX:32010L0063&qid=1641284199175> (11/2021)

- [14] R. G. W. Kirk, *Sci. Technol. Hum. Values* **2018**, *43*, 622.
- [15] I. A. Freires, J. de C. O. Sardi, R. D. de Castro, P. L. Rosalen, *Pharm. Res.* **2017**, *34*, 681.
- [16] E. Abd, S. A. Yousef, M. N. Pastore, K. Telaprolu, Y. H. Mohammed, S. Namjoshi, J. E. Grice, M. S. Roberts, *Clin. Pharmacol. Adv. Appl.* **2016**, *8*, 163.
- [17] D. E. Ingber, *J. Exp. Med.* **2021**, *218*, e20201756.
- [18] A. K. Yadav, S. Srikrishna, S. C. Gupta, *Trends Pharmacol. Sci.* **2016**, *37*, 789.
- [19] T. Braunbeck, B. Kais, E. Lammer, J. Otte, K. Schneider, D. Stengel, R. Strecker, *Environ. Sci. Pollut. Res.* **2015**, *22*, 16247.
- [20] S. Majdi, L. Ren, H. Fathali, X. Li, A. G. Ewing, *Analyst* **2015**, *140*, 3676.
- [21] X. Yang, Y. Wang, R. Byrne, G. Schneider, S. Yang, *Chem. Rev.* **2019**, *119*, 10520.
- [22] A. B. Raies, V. B. Bajic, *WIREs Comput Mol Sci* **2016**, *6*, 147.
- [23] Y. Elani, *Angew. Chemie - Int. Ed.* **2021**, *60*, 5602.
- [24] S. Ausländer, D. Ausländer, M. Fussenegger, *Angew. Chemie - Int. Ed.* **2017**, *56*, 6396.
- [25] K. H. Benam, S. Dauth, B. Hassell, A. Herland, A. Jain, K. J. Jang, K. Karalis, H. J. Kim, L. MacQueen, R. Mahmoodian, S. Musah, Y. S. Torisawa, A. D. Van Der Meer, R. Villenave, M. Yadid, K. K. Parker, D. E. Ingber, *Annu. Rev. Pathol. Mech. Dis.* **2015**, *10*, 195.
- [26] S. A. Langhans, *Front. Pharmacol.* **2018**, *9*, 1.
- [27] M. R. Ebrahimkhani, C. L. Young, D. A. Lauffenburger, L. G. Griffith, J. T. Borenstein, *Drug Discov. Today* **2014**, *19*, 754.
- [28] Z. Li, *Drug Discov. Today* **2011**, *19*, 754.
- [29] P. Zorlutuna, N. Annabi, G. Camci-Unal, M. Nikkhah, J. M. Cha, J. W. Nichol, A. Manbachi, H. Bae, S. Chen, A. Khademhosseini, *Adv. Mater.* **2012**, *24*, 1782.
- [30] A. Khademhosseini, R. Langer, *Biomaterials* **2007**, *28*, 5087.
- [31] J. Rouwkema, S. Gibbs, M. P. Lutolf, I. Martin, G. Vunjak-Novakovic, J. Malda, *J. Tissue Eng. Regen. Med.* **2011**, *5*, e164.
- [32] M. Mobaraki, M. Ghaffari, A. Yazdanpanah, Y. Luo, D. K. Mills, *Bioprinting* **2020**, *18*, e00080.
- [33] S. Heid, A. R. Boccaccini, *Acta Biomater.* **2020**, *113*, 1.

- [34] A. Elemoso, G. Shalunov, Y. M. Balakhovskiy, A. Y. Ostrovskiy, Y. D. Khesuani, *Int. J. Bioprinting* **2020**, *6*, 62.
- [35] S. Kim, E. M. Kim, M. Yamamoto, H. Park, H. Shin, *Adv. Healthc. Mater.* **2020**, *9*, 2000608.
- [36] D. Rana, T. S. S. Kumar, M. Ramalingam, *J. Biomater. Tissue Eng.* **2014**, *4*, 507.
- [37] R. Langer, J. P. Vacanti, *Science (80-. )*. **1993**, *260*, 920.
- [38] S. Kühn, J. Sievers, A. Stoppa, N. Träber, R. Zimmermann, P. B. Welzel, C. Werner, *Adv. Funct. Mater.* **2020**, *30*, 1908857.
- [39] Y. Torisawa, B. Mosadegh, G. D. Luker, M. Morell, K. S. O'Shea, S. Takayama, *Integr. Biol.* **2009**, *1*, 649.
- [40] N. V Mekhileri, K. S. Lim, G. C. J. Brown, Mutreja, B. S. Schon, G. Hooper, T. B. F. Woodfield, *Biofabrication* **2018**, *10*, 024103.
- [41] E. M. Kim, Y. Bin Lee, S. Kim, J. Park, J. Lee, S. W. Kim, H. Park, H. Shin, *Acta Biomater.* **2019**, *100*, 158.
- [42] H. Zhang, R. D. Whalley, A. M. Ferreira, K. Dalgarno, *Prog. Biomed. Eng.* **2020**, *2*, 022001.
- [43] Y. T. Matsunaga, Y. Morimoto, S. Takeuchi, *Adv. Healthc. Mater.* **2011**, *23*, H90.
- [44] S. Seiffert, *Macromol. Chem. Phys.* **2017**, *218*, 1600280.
- [45] S. Ma, N. Mukherjee, *Adv. Biosyst.* **2018**, *2*, 1800119.
- [46] A. R. Abate, J. Thiele, D. A. Weitz, *Lab Chip* **2011**, *11*, 253.
- [47] M. Purtscher, M. Rothbauer, S. R. A. Kratz, A. Bailey, P. Lieberzeit, P. Ertl, *Lab Chip* **2021**, *21*, 1364.
- [48] S. Chameettachal, S. Yeleswarapu, S. Sasikumar, P. Shukla, P. Hibare, A. K. Bera, S. S. R. Bojedla, F. Pati, *J. Indian Inst. Sci.* **2019**, *99*, 375.
- [49] R. Dong, Y. Liu, L. Mou, J. Deng, X. Jiang, *Adv. Mater.* **2019**, *31*, 1805033.
- [50] L. Klouda, A. G. Mikos, **2008**, *68*, 34.
- [51] M. W. Tibbitt, K. S. Anseth, *Biotechnol. Bioeng.* **2009**, *103*, 655.
- [52] J. Thiele, Y. Ma, S. M. C. Bruckers, S. Ma, W. T. S. Huck, *Adv. Mater.* **2014**, *26*, 125.
- [53] S. Van Vlierberghe, P. Dubruel, E. Schacht, *Biomacromolecules* **2011**, *12*, 1387.
- [54] S. R. Caliarì, J. A. Burdick, *Nat. Methods* **2016**, *13*, 405.

- [55] J. J. Rice, M. M. Martino, L. De Laporte, F. Tortelli, P. S. Briquez, J. A. Hubbell, *Adv. Healthc. Mater.* **2013**, *2*, 57.
- [56] C. Frantz, K. M. Stewart, V. M. Weaver, *J. Cell Sci.* **2010**, *123*, 4195.
- [57] A. D. Theocharis, S. S. Skandalis, C. Gialeli, N. K. Karamanos, *Adv. Drug Deliv. Rev.* **2016**, *97*, 4.
- [58] T. H. Barker, *Biomaterials* **2011**, *32*, 4211.
- [59] M. G. Patino, M. E. Neiders, S. Andreana, B. Noble, R. E. Cohen, *Implant Dent.* **2002**, *11*, 280.
- [60] A. Sionkowska, S. Skrzyński, K. Śmiechowski, A. Kołodziejczak, *Polym. Adv. Technol.* **2017**, *28*, 4.
- [61] J. Darnell, H. Lodish, D. Baltimore *Molecular Cell Biology 2*, New York, Scientific American Books, **1990**.
- [62] M. Achilli, D. Mantovani, *Polymers (Basel)*. **2010**, *2*, 664.
- [63] W. Zhao, X. Jin, Y. Cong, Y. Liu, J. Fu, *J. Chem. Technol. Biotechnol.* **2013**, *88*, 327.
- [64] C. F. Marques, G. S. Diogo, S. Pina, J. M. Oliveira, T. H. Silva, *J. Mater. Sci. Mater. Med.* **2019**, *30*, 32.
- [65] K. Yue, X. Li, K. Schrobback, A. Sheikhi, N. Annabi, J. Leijten, W. Zhang, Y. S. Zhang, D. W. Hutmacher, T. J. Klein, A. Khademhosseini, *Biomaterials* **2017**, *139*, 163.
- [66] K. Y. Lee, D. J. Mooney, *Chem. Rev.* **2001**, *101*, 1869.
- [67] P. Singh, C. Carraher, J. E. Schwarzbauer, *Annu. Rev. Cell Dev. Biol.* **2010**, *26*, 397.
- [68] J. D. Humphries, A. Byron, M. J. Humphries, *J. Cell Sci.* **2006**, *119*, 3901.
- [69] J. E. Schwarzbauer, D. W. DeSimone, *Cold Spring Harb. Perspect. Biol.* **2011**, *3*, a005041.
- [70] A. J. Zollinger, M. L. Smith, *Matrix Biol.* **2017**, *60*, 27.
- [71] K. Y. Lee, D. J. Mooney, *Prog. Polym. Sci.* **2012**, *37*, 106.
- [72] S. N. Pawar, K. J. Edgar, *Biomaterials* **2012**, *33*, 3279.
- [73] M. I. Neves, L. Moroni, C. C. Barrias, *Front. Bioeng. Biotechnol.* **2020**, *8*, 16.
- [74] P. Zarrintaj, S. Manouchehri, Z. Ahmadi, M. R. Saeb, A. M. Urbanska, D. L. Kaplan, M. Mozafari, *Carbohydr. Polym.* **2018**, *187*, 66.

- [75] M. Khodadadi Yazdi, A. Taghizadeh, M. Taghizadeh, F. J. Stadler, M. Farokhi, F. Mottaghitalab, P. Zarrintaj, J. D. Ramsey, F. Seidi, M. R. Saeb, M. Mozafari, *J. Control. Release* **2020**, *326*, 523.
- [76] Y. Yamada, C. Yoshida, K. Hamada, Y. Kikkawa, M. Nomizu, *Biomacromolecules* **2020**, *21*, 3765.
- [77] R. Suntornnond, J. An, C. K. Chua, *Macromol. Mater. Eng.* **2017**, *302*, 1600266.
- [78] M. A. Salati, J. Khazai, A. M. Tahmuri, A. Samadi, S. Habibzadeh, F. Seidi, M. R. Saeb, M. Mozafari, *Polymers (Basel)*. **2020**, *12*, 1150.
- [79] S. Kamel, N. Ali, K. Jahangir, S. M. Shah, *eXPRESS Polym. Lett.* **2008**, *2*, 758.
- [80] R. J. Hickey, A. E. Pelling, *Front. Bioeng. Biotechnol.* **2019**, *7*, 1.
- [81] P. L. Nasatto, F. Pignon, J. L. M. Silveira, M. E. R. Duarte, M. D. Nosedá, M. Rinaudo, *Polymers (Basel)*. **2015**, *7*, 777.
- [82] R. J. Moon, A. Martini, J. Nairn, J. Youngblood, A. Martini, J. Nairn, *Chem. Soc. Rev.* **2011**, *40*, 3941.
- [83] S. Ghorbani, H. Eyni, S. R. Bazaz, H. Nazari, L. S. Asl, H. Zaferani, V. Kiani, A. A. Mehrizi, M. Soleimani, *Polym. Sci. - Ser. A* **2018**, *60*, 707.
- [84] S. Morozova, *Polym. Int.* **2020**, *69*, 125.
- [85] K. Kobayashi, C. I. Huang, T. P. Lodge, *Macromolecules* **1999**, *32*, 7070.
- [86] T. Ahlfeld, V. Guduric, S. Duin, A. R. Akkineni, K. Schütz, D. Kilian, J. Emmermacher, N. Cubo-Mateo, S. Dani, M. V. Witzleben, J. Spangenberg, R. Abdelgaber, R. F. Richter, A. Lode, M. Gelinsky, *Biomater. Sci.* **2020**, *8*, 2102.
- [87] N. S. Gandhi, R. L. Mancera, *Chem. Biol. Drug Des.* **2008**, *72*, 455.
- [88] J. A. Burdick, G. D. Prestwich, *Adv. Healthc. Mater.* **2011**, *23*, H41.
- [89] G. D. Prestwich, *J. Control. Release* **2011**, *155*, 193.
- [90] X. Xu, A. K. Jha, D. A. Harrington, M. C. Farach-Carson, X. Jia, *Soft Matter* **2012**, *8*, 3280.
- [91] J. H. Sze, J. C. Brownlie, C. A. Love, *3 Biotech* **2016**, *6*, 67.
- [92] J. Zhu, *Biomaterials* **2010**, *31*, 4639.
- [93] A. A. D'souza, R. Shegokar, *Expert Opin. Drug Deliv.* **2016**, *13*, 1257.

## THEORY

- [94] J. Herzberger, K. Niederer, H. Pohlitz, J. Seiwert, M. Worm, F. R. Wurm, H. Frey, *Chem. Rev.* **2016**, *116*, 2170.
- [95] S. Lanzalaco, E. Armelin, *Gels* **2017**, *3*, 36.
- [96] M. A. Haq, Y. Su, D. Wang, *Mater. Sci. Eng. C* **2017**, *70*, 842.
- [97] Y. Guan, Y. Zhang, *Soft Matter* **2011**, *7*, 6375.
- [98] F. Doberenz, K. Zeng, C. Willems, K. Zhang, T. Groth, *J. Mater. Chem. B* **2020**, *8*, 607.
- [99] S. Wendels, L. Avérous, *Bioact. Mater.* **2021**, *6*, 1083.
- [100] J. O. Akindoyo, M. D. H. Beg, S. Ghazali, M. R. Islam, N. Jeyaratnam, A. R. Yuvaraj, *RSC Adv.* **2016**, *6*, 114453.
- [101] B. Kang, Y. Park, D. G. Hwang, D. Kim, U. Yong, K. S. Lim, J. Jang, *Adv. Mater. Technol.* **2021**, 2100947.
- [102] M. G. A. Mohamed, S. Kheiri, S. Islam, H. Kumar, A. Yang, K. Kim, *Lab Chip* **2019**, *19*, 1621.
- [103] S. Seiffert, *Physical Chemistry of Polymers*, De Gruyter, Berlin/Boston, **2020**.
- [104] H. Wei, S. X. Cheng, X. Z. Zhang, R. X. Zhuo, *Prog. Polym. Sci.* **2009**, *34*, 893.
- [105] Z. M. O. Rzaev, S. Dinçer, E. Pişkin, *Prog. Polym. Sci.* **2007**, *32*, 534.
- [106] D. Kim, A. Jo, K. B. C. Imani, D. Kim, J. W. Chung, J. Yoon, *Langmuir* **2018**, *34*, 4351.
- [107] C. C. Huang, Z. X. Liao, D. Y. Chen, C. W. Hsiao, Y. Chang, H. W. Sung, *Adv. Healthc. Mater.* **2014**, *3*, 1133.
- [108] N. Kojima, S. Takeuchi, Y. Sakai, *Biomaterials* **2012**, *33*, 4508.
- [109] H. Wang, H. Liu, H. Liu, W. Su, W. Chen, J. Qin, *Adv. Mater. Technol.* **2019**, *4*, 1800632.
- [110] H. Rastin, R. T. Ormsby, G. J. Atkins, D. Losic, *ACS Appl. Bio Mater.* **2020**, *3*, 1815.
- [111] H. Li, Y. J. Tan, K. F. Leong, L. Li, *ACS Appl. Mater. Interfaces* **2017**, *9*, 20086.
- [112] J. Seuring, S. Agarwal, *Macromol. Rapid Commun.* **2012**, *33*, 1898.
- [113] J. Seuring, S. Agarwal, *ACS Macro Lett.* **2013**, *2*, 597.
- [114] H. Li, C. Tan, L. Li, *Mater. Des.* **2018**, *159*, 20.
- [115] T. A. Ulrich, A. Jain, K. Tanner, J. L. MacKay, S. Kumar, *Biomaterials* **2010**, *31*, 1875.

- [116] L. A. Struzyna, K. D. Browne, Z. D. Brodnik, J. C. Burrell, J. P. Harris, H. I. Chen, J. A. Wolf, K. V. Panzer, J. Lim, J. E. Duda, R. A. España, D. K. Cullen, *J. Tissue Eng. Regen. Med.* **2018**, *12*, 1702.
- [117] C. M. Hwang, S. Sant, M. Masaeli, N. N. Kachouie, B. Zamanian, S. H. Lee, A. Khademhosseini, *Biofabrication* **2010**, *2*, 035003.
- [118] B. J. Klotz, D. Gawlitta, A. J. W. P. Rosenberg, J. Malda, F. P. W. Melchels, *Trends Biotechnol.* **2016**, *34*, 394.
- [119] N. Zoratto, D. Di Lisa, J. de Rutte, M. N. Sakib, A. R. Alves e Silva, A. Tamayol, D. Di Carlo, A. Khademhosseini, A. Sheikhi, *Bioeng. Transl. Med.* **2020**, *5*, e10180.
- [120] C. Zhang, Z. Zhao, N. A. Abdul Rahim, D. Van Noort, H. Yu, *Lab Chip* **2009**, *9*, 3185.
- [121] B. Sung, J. Krieger, B. Yu, M. H. Kim, *J. Biomed. Mater. Res. - Part A* **2018**, *106*, 2753.
- [122] G. S. Ugolini, R. Visone, A. Redaelli, M. Moretti, M. Rasponi, *Adv. Healthc. Mater.* **2017**, *6*, 1601170.
- [123] K. E. Drzewiecki, A. S. Parmar, I. D. Gaudet, J. R. Branch, D. H. Pike, V. Nanda, D. I. Shreiber, *langmuir* **2014**, *30*, 11204.
- [124] P. Agarwal, J. K. Choi, H. Huang, S. Zhao, J. Dumbleton, J. Li, X. He, *Part. Part. Syst. Charact.* **2015**, *32*, 809.
- [125] E. Tumarkin, E. Kumacheva, *Chem. Soc. Rev.* **2009**, *38*, 2161.
- [126] S. Utech, R. Prodanovic, A. S. Mao, R. Ostafe, D. J. Mooney, D. A. Weitz, *Adv. Healthc. Mater.* **2015**, *4*, 1628.
- [127] B. W. Tan, S. Takeuchi, *Adv. Mater.* **2007**, *19*, 2696.
- [128] J. Necas, L. Bartosikova, P. Brauner, J. Kolar, *Vet. Med. (Praha)*. **2008**, *53*, 397.
- [129] B. Kessel, M. Lee, A. Bonato, Y. Tinguely, E. Tosoratti, M. Zenobi-Wong, *Adv. Sci.* **2020**, *7*, 001419.
- [130] M. N. Collins, C. Birkinshaw, *Carbohydr. Polym.* **2013**, *92*, 1262.
- [131] S. Khunmanee, Y. Jeong, H. Park, *J. Tissue Eng.* **2017**, *8*, 1–16.
- [132] S. Hocine, M. H. Li, *Soft Matter* **2013**, *9*, 5839.
- [133] H. Wang, J. Cui, Z. Zheng, Q. Shi, T. Sun, X. Liu, Q. Huang, T. Fukuda, *ACS Appl. Mater. Interfaces* **2017**, *9*, 41669.

## THEORY

- [134] K. A. Heintz, M. E. Bregenzer, J. L. Mantle, K. H. Lee, J. L. West, J. H. Slater, *Adv. Healthc. Mater.* **2016**, *5*, 2153.
- [135] A. S. Caldwell, G. T. Campbell, K. M. T. Shekiri, K. S. Anseth, *Adv. Healthc. Mater.* **2017**, *6*, 1700254.
- [136] D. Steinhilber, T. Rossow, S. Wedepohl, F. Paulus, S. Seiffert, R. Haag, *Angew. Chemie - Int. Ed.* **2013**, *52*, 13538.
- [137] L. P. B. Guerzoni, J. C. Rose, D. B. Gehlen, A. Jans, T. Haraszti, M. Wessling, A. J. C. Kuehne, L. De Laporte, *Small* **2019**, *15*, 1900692.
- [138] E. Stengelin, A. Kuzmina, G. L. Beltramo, M. F. Koziol, L. Besch, R. Schröder, R. E. Unger, W. Tremel, S. Seiffert, *Adv. Healthc. Mater.* **2020**, *9*, 1901820.
- [139] T. Rossow, J. A. Heyman, A. J. Ehrlicher, A. Langhoff, D. A. Weitz, R. Haag, S. Seiffert, *J. Am. Chem. Soc.* **2012**, *134*, 4983.
- [140] C. Siltanen, M. Yaghoobi, A. Haque, J. You, J. Lowen, M. Soleimani, A. Revzin, *Acta Biomater.* **2016**, *34*, 125.
- [141] S. Xin, O. M. Wyman, D. L. Alge, *Adv. Healthc. Mater.* **2018**, *7*, 1800160.
- [142] J. Jung, C. Choi, S. Chung, Y. Chung, C. Lee, *Lab Chip* **2009**, *9*, 2596.
- [143] H. Lin, F. Hsieh, C. Tseng, S. Hsu, *J. Mater. Chem. B* **2016**, *4*, 6694.
- [144] C. Hsieh, S. Hsu, *ACS Appl. Mater. Interfaces* **2019**, *11*, 32746.
- [145] S. Hsiao, S. Hsu, *ACS Appl. Mater. Interfaces* **2018**, *10*, 29273.
- [146] S. Kim, S. Liu, *ACS Biomater. Sci. Eng.* **2018**, *4*, 1479.
- [147] M. Levy, H. Bass, R. Stern, Handbook of Elastic Properties of Solids, Liquids and Gases, Academic Press, **2001**.
- [148] H. M. James, E. Guth, *J. Chem. Phys.* **1943**, *11*, 455.
- [149] H. M. James, E. Guth, *J. Chem. Phys.* **1953**, *21*, 1039.
- [150] C. Siltanen, M. Diakataou, J. Lowen, A. Haque, A. Rahimian, G. Stybayeva, A. Revzin, *Acta Biomater.* **2017**, *50*, 428.
- [151] M. Rubinstein, R. H. Colby, *Polymer Physics*, Oxford University Press, **2003**.
- [152] E. Stengelin, B. Nzigou Mombo, M. Mondeshki, G. L. Beltramo, M. A. Lange, P. Schmidt, H. Frerichs, S. V Wegner, S. Seiffert, *Macromol. Biosci.* **2021**, *21*, 2100209.



- [153] B. S. Schmidt, M. Zeiser, T. Hellweg, C. Duschl, A. Fery, H. Möhwald, *Adv. Funct. Mater.* **2010**, *20*, 235.
- [154] H. Mi, S. Palumbo, X. Jing, L. Turng, W. Li, X. Peng, *Biomed Mater Res Part B* **2014**, *102B*, 1434.
- [155] M. J. Hill, D. Sarkar, *Langmuir* **2017**, *33*, 6167.
- [156] E. P. Broderick, D. M. O'Halloran, Y. A. Rochev, M. Griffin, R. J. Collighan, A. S. Pandit, *J. Biomed. Mater. Res. - Part B Appl. Biomater.* **2005**, *72B*, 37.
- [157] C. D. Markert, X. Guo, Z. Wang, *J. Mech. Behav. Biomed. Mater.* **2013**, *27*, 115.
- [158] C. Ort, Y. Chen, A. Ghagre, A. Ehrlicher, C. Moraes, *ACS Biomater. Sci. Eng.* **2021**, *7*, 2814.
- [159] D. Lee, K. Lee, C. Cha, *Adv. Biosyst.* **2018**, *2*, 1800236.
- [160] E. Jooybar, M. J. Abdekhodaie, M. Karperien, A. Mousavi, M. Alvi, P. J. Dijkstra, *Int. J. Biol. Macromol.* **2020**, *144*, 837.
- [161] G. T. Gold, D. M. Varma, P. J. Taub, S. B. Nicoll, *Carbohydr. Polym.* **2015**, *134*, 497.
- [162] M. N. Collins, C. Birkinshaw, *J. Appl. Polym. Sci.* **2008**, *109*, 923.
- [163] J. Bystroňová, I. Ščigalková, L. Wolfová, M. Pravda, N. E. Vrana, V. Velebný, *RSC Adv.* **2018**, *8*, 7606.
- [164] F. He, T. Tao, H. Liu, Y. Wang, K. Cui, Y. Guo, J. Qin, *ACS Appl. Bio Mater.* **2021**, *4*, 1584.
- [165] S. Nadine, S. G. Patrício, C. C. Barrias, I. S. Choi, M. Matsusaki, C. R. Correia, J. F. Mano, *Adv. Biosyst.* **2020**, *4*, 2000127.
- [166] M. Pasqua, U. Pereira, C. De Lartigue, J. Nicolas, P. Vigneron, Q. Dermigny, C. Legallais, *Biotechnol. Bioeng.* **2021**, *118*, 453.
- [167] N. Contessi, L. Altomare, A. Filipponi, S. Farè, *Mater. Lett.* **2017**, *207*, 157.
- [168] V. Ramesh Babu, M. Sairam, K. M. Hosamani, T. M. Aminabhavi, *Carbohydr. Polym.* **2007**, *69*, 241.
- [169] A. Asthana, W. S. Kisaalita, *Drug Discov. Today* **2012**, *17*, 810.
- [170] P. Agarwal, H. Wang, M. Sun, J. Xu, S. Zhao, Z. Liu, K. J. Gooch, Y. Zhao, X. Lu, X. He, *ACS Nano* **2017**, *11*, 6691.
- [171] Y. H. Hsu, M. L. Moya, P. Abiri, C. C. W. Hughes, S. C. George, A. P. Lee, *Lab Chip* **2013**, *13*, 81.

## THEORY

- [172] H. M. M. Ahmed, S. Salerno, A. Piscioneri, S. Khakpour, L. Giorno, L. De Bartolo, *Colloids Surfaces B Biointerfaces* **2017**, *160*, 272.
- [173] O. Guillame-Gentil, O. Semenov, A. S. Roca, T. Groth, R. Zahn, J. Vörös, M. Zenobi-Wong, *Adv. Mater.* **2010**, *22*, 5443.
- [174] N. Faucheux, R. Schweiss, K. Lützow, C. Werner, T. Groth, *Biomaterials* **2004**, *25*, 2721.
- [175] W. M. Zhang, J. Käpylä, J. S. Puranen, C. G. Knight, C. F. Tiger, O. T. Pentikäinen, M. S. Johnson, R. W. Farndale, J. Heino, D. Gullberg, *J. Biol. Chem.* **2003**, *278*, 7270.
- [176] R. Sfriso, S. Zhang, C. A. Bichsel, O. Steck, A. Despont, O. T. Guenat, R. Rieben, *Sci. Rep.* **2018**, *8*, 5898.
- [177] Y. Wang, D. Wu, G. Wu, J. Wu, S. Lu, J. Lo, Y. He, C. Zhao, X. Zhao, H. Zhang, S. Q. Wang, *Theranostics* **2020**, *10*, 300.
- [178] H. Brotchie, D. Wakefield, *Australas. J. Dermatol.* **1990**, *31*, 47.
- [179] H. Liu, S. Wang, *Sci. China Chem.* **2014**, *57*, 552.
- [180] H. Takahashi, K. Itoga, T. Shimizu, M. Yamato, *Adv. Healthc. Mater.* **2016**, *5*, 1931.
- [181] M. Sheikholeslam, M. E. E. Wright, N. Cheng, H. H. Oh, Y. Wang, A. K. Datu, J. P. Santerre, S. Amini-Nik, M. G. Jeschke, *ACS Biomater. Sci. Eng.* **2020**, *6*, 505.
- [182] V. S. Chernonosova, A. A. Gostev, Y. Gao, Y. A. Chesalov, A. V. Shutov, E. A. Pokushalov, A. A. Karpenko, P. P. Laktionov, *Biomed Res. Int.* **2018**, *2018*, 1.
- [183] F. Berthiaume, T. J. Maguire, M. L. Yarmush, *Annu. Rev. Chem. Biomol. Eng.* **2011**, *2*, 403.
- [184] A. J. Steward, Y. Liu, D. R. Wagner, *JOM* **2011**, *63*, 74.
- [185] D. Gupta, C. H. Tator, M. S. Shoichet, *Biomaterials* **2006**, *27*, 2370.
- [186] X. Gong, C. Lin, J. Cheng, J. Su, H. Zhao, T. Liu, X. Wen, P. Zhao, *PLoS One* **2015**, *10*, e0130348.
- [187] K. Janjić, B. Lilaj, A. Moritz, H. Agis, *Int. Endod. J.* **2018**, *51*, e146.
- [188] G. Oberoi, K. Janjić, A. S. Müller, B. Schädli, O. Andrukhov, A. Moritz, H. Agis, *Front. Physiol.* **2018**, *9*, 1683.
- [189] B. Abecasis, P. G. M. Canhão, H. V. Almeida, T. Calmeiro, E. Fortunato, P. Gomes-Alves, M. Serra, P. M. Alves, *Front. Bioeng. Biotechnol.* **2020**, *8*, 580744.

- [190] H. F. Chan, Y. Zhang, Y. P. Ho, Y. L. Chiu, Y. Jung, K. W. Leong, *Sci. Rep.* **2013**, *3*, 3462.
- [191] A. M. Porrás Hernández, H. Pohlit, F. Sjögren, L. Shi, D. Ossipov, M. Antfolk, M. Tenje, *J. Mater. Sci. Mater. Med.* **2020**, *31*, 89.
- [192] M. D. Serruya, J. P. Harris, D. O. Adewole, L. A. Struzyna, J. C. Burrell, A. Nemes, D. Petrov, R. H. Kraft, H. I. Chen, J. A. Wolf, D. K. Cullen, *Adv. Funct. Mater.* **2017**, *28*, 1701183.
- [193] J. Wang, R. C. Cooper, H. He, B. Li, H. Yang, *Macromolecules* **2018**, *51*, 6111.
- [194] K. R. Kamath, K. Park, *Adv. Drug Deliv. Rev.* **1993**, *11*, 59.
- [195] D. Thomas, G. Fontana, X. Chen, C. Sanz-Nogués, D. I. Zeugolis, P. Dockery, T. O'Brien, A. Pandit, *Biomaterials* **2014**, *35*, 8757.
- [196] R. Parenteau-bareil, R. Gauvin, F. Berthod, *Materials (Basel)*. **2010**, *3*, 1863.
- [197] K. Mladenovska, E. F. Kumbaradzi, G. M. Dodov, L. Makraduli, K. Goracinova, *Int. J. Pharm.* **2002**, *242*, 247.
- [198] J. W. Nichol, S. T. Koshy, H. Bae, C. M. Hwang, S. Yamanlar, A. Khademhosseini, *Biomaterials* **2010**, *31*, 5536.
- [199] A. L. Crampton, K. A. Cummins, D. K. Wood, *Integr. Biol. (United Kingdom)* **2018**, *10*, 555.
- [200] C. Mulas, A. C. Hodgson, T. N. Kohler, C. C. Agle, P. Humphreys, H. Kleine-Brüggeney, F. Hollfelder, A. Smith, K. J. Chalut, *Lab Chip* **2020**, *20*, 2580.
- [201] T. Ma, X. Gao, H. Dong, H. He, X. Cao, *Appl. Mater. Today* **2017**, *9*, 49.
- [202] W. J. Chi, Y. K. Chang, S. K. Hong, *Appl. Microbiol. Biotechnol.* **2012**, *94*, 917.
- [203] H. S. Kim, C. G. Lee, E. Y. Lee, *Biotechnol. Bioprocess Eng.* **2011**, *16*, 843.
- [204] A. M. Compaan, K. Song, W. Chai, Y. Huang, *ACS Appl. Mater. Interfaces* **2020**, *12*, 7855.
- [205] K. Yao, W. Li, K. Li, Q. Wu, Y. Gu, L. Zhao, Y. Zhang, X. Gao, *Macromol. Biosci.* **2020**, *20*, 1900395.
- [206] E. Kapourani, F. Neumann, K. Achazi, J. Dervede, R. Haag, *Macromol. Biosci.* **2018**, *18*, 1800116.
- [207] J. C. Rose, D. B. Gehlen, T. Haraszti, J. Köhler, C. J. Licht, L. De Laporte, *Biomaterials* **2018**, *163*, 128.

- [208] M. Sattari, M. Fathi, M. Daei, H. Erfan-Niya, J. Barar, A. A. Entezami, *BioImpacts* **2017**, *7*, 167.
- [209] D. Sivakumaran, E. Mueller, T. Hoare, *Soft Matter* **2017**, *13*, 9060.
- [210] P. A. Nair, P. Ramesh, *Biomed Mater Res Part A* **2013**, *101A*, 1876.
- [211] E. M. Bachelder, T. T. Beaudette, K. E. Broaders, S. E. Paramonov, J. Dashe, J. M. J. Fréchet, *Mol. Pharm.* **2008**, *5*, 876.
- [212] W. R. Legant, A. Pathak, M. T. Yang, V. S. Deshpande, R. M. McMeeking, C. S. Chen, *Proc. Natl. Acad. Sci. U. S. A.* **2009**, *106*, 10097.
- [213] A. Tijore, S. A. Irvine, U. Sarig, P. Mhaisalkar, V. Baisane, S. Venkatraman, *Biofabrication* **2018**, *10*, 025003.
- [214] A. Kumachev, E. Tumarkin, G. C. Walker, E. Kumacheva, *Soft Matter* **2013**, *9*, 2959.
- [215] M. Palma, J. G. Hardy, G. Tadayyon, M. Farsari, S. J. Wind, *Adv. Healthc. Mater.* **2015**, *4*, 2500.
- [216] M. Vázquez-González, I. Willner, *Angew. Chemie - Int. Ed.* **2020**, *59*, 15342.
- [217] N. Ghareeb, M. Farhat, *Nanotechnol. Appl.* **2018**, *1*, 1.
- [218] O. J. G. M. Goor, S. I. S. Hendrikse, P. Y. W. Dankers, E. W. Meijer, *Chem. Soc. Rev.* **2017**, *46*, 6621.
- [219] H. Qi, M. Ghodousi, Y. Du, C. Grun, H. Bae, P. Yin, A. Khademhosseini, *Nat. Commun.* **2013**, *4*, 2275.
- [220] L. Ouyang, J. P. K. Armstrong, M. Salmeron-sanchez, M. M. Stevens, *Adv. Funct. Mater.* **2020**, *30*, 1909009.
- [221] D. L. Taylor, M. in het Panhuis, *Adv. Mater.* **2016**, *28*, 9060.
- [222] J. E. Mealy, J. J. Chung, H. H. Jeong, D. Issadore, D. Lee, P. Atluri, J. A. Burdick, *Adv. Mater.* **2018**, *30*, 1705912.
- [223] X. Li, J. Shang, Z. Wang, *Assem. Autom.* **2017**, *37*, 170.
- [224] S. Tibbits, *Archit. Des.* **2014**, *84*, 116.
- [225] J. Lai, X. Ye, J. Liu, C. Wang, J. Li, X. Wang, M. Ma, M. Wang, *Mater. Des.* **2021**, *205*, 109699.
- [226] C. A. Deforest, K. S. Anseth, *Annu. Rev. Chem. Biomol. Eng.* **2012**, *3*, 421.

- [227] M. Quanjin, M. R. M. Rejab, M. S. Idris, N. Manoj, M. H. Abdullah, G. Ramakrishna, *Procedia Comput. Sci.* **2020**, *167*, 1210.
- [228] I. Apsite, J. M. Uribe, A. F. Posada, S. Rosenfeldt, S. Salehi, *Biofabrication* **2020**, *12*, 15016.
- [229] L. Sun, W. M. Huang, Z. Ding, Y. Zhao, C. C. Wang, H. Purnawali, C. Tang, *Mater. Des.* **2012**, *33*, 577.
- [230] A. Kirillova, R. Maxson, G. Stoychev, C. T. Gomillion, L. Ionov, *Adv. Mater.* **2017**, *29*, 1703443.

## 2. Scientific Goal

### ●●● “Defined and Functional Materials for Microtissue Engineering Applications”

In accordance with Russel and Burch's 3R principle (replace, reduce, refine), the development of sustainable alternatives to animal testing has become increasingly urgent in recent decades. To contribute to this need, the following thesis explores the development of defined and functional materials for microtissue engineering applications to replace animal testing. In separate studies, different aspects of designing suitable materials and understanding their structure–property relationships will be investigated. Consistent with the previously described notion of well-designed microtissues (*Theory Chapter: “Multiparametric Material Functionality of Microtissue-based in vitro Models as Alternatives to Animal Testing”*), particular attention will be paid to the fabrication of microgel platforms using the droplet-based microfluidic method, the selection of ideal materials, and the tunability of material properties such as processability, adaptivity, biocompatibility, and stability/degradability. To complete these studies, additional material-oriented cell culture experiments will be performed (**Figure 2-1**).

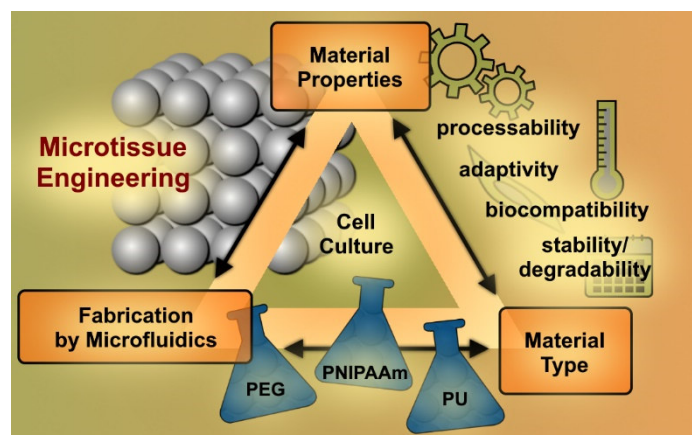


**Figure 2-1.** Schematic overview of the scientific goal. The topic includes the rational design of defined and functional materials for microtissue engineering applications with special emphasis on microgel fabrication by droplet-based microfluidics, proper material selection, and tuning of material properties such as processability, adaptivity, biocompatibility, and stability/degradability. In addition, cell experiments are performed (E. Stengelin, [REDACTED], *Adv. Sci.* **2022**, 2105319. <https://doi.org/10.1002/advs.202105319>).

In this context, the first study addresses the development of composite microgels based on poly(ethylene glycol) (PEG) loaded with living cells and vaterite. These injectable microgels are expected to provide a new and promising platform for patients with osteoporosis who are at particularly high risk for fractures and poorly healing bone injuries. Since bones have different mineral compositions depending on their location in the body, a regenerative therapy approach is used. Based on this, microgels are rationally designed by varying the molar mass of precursor polymers and using droplet-based microfluidics while encapsulating vaterite particles as calcium providers. In addition, cells are embedded in the microgels to enable (i) an in vitro platform for further investigation of the metabolic processes involved in bone formation and (ii) an in vitro basis for novel regenerative therapies. Overall, a complete system is investigated in terms of microgel production, assembly of composite structures, and cell activity/interaction, that serves as an important basis for further studies.

The second study, in turn, addresses the rational design of volume-switchable core-shell patterned platforms with thermoresponsive and cell-adhesive properties that can potentially mimic the blastula in embryogenesis, mammary glands, or the alveolar epithelium. Considering the complex and hierarchical structure of the in vivo tissue that needs to be replicated, the thermoresponsive poly(*N*-isopropylacrylamide) is chosen as the material base, being tuned in three steps with respect to functionality, shape, and mechanical properties. Step one focuses on the design and synthesis of microgels, paying closer attention to the processability and adaptivity of the materials. In the second step, the surface of the microgels is coated with polydopamine in combination with collagen or fibronectin to improve their biocompatibility to promote cell adhesion. In the third step, cell growth experiments are performed on these microgels. In combination, these three steps lead to cell-coated and long-term stable microcarriers to form a viable basis for complex and advanced 3D in vitro cell culture systems.

The third project aims to provide a toolbox of polyurethane (PU)-based, biocompatible materials with tunable thermoresponsive and mechanical properties as a novel basis for future microtissue engineering studies. The project focus is on the synthesis and analysis of PEG-based PU precursor polymers whose physical properties can be tuned by the amphiphilic balance of the comonomers and the amount of dimethylmaleimide crosslinking units. UV irradiation can covalently crosslink these precursor polymers to form hydrogels with physical and mechanical properties similar to those of the precursor polymers. Further improvement of the biocompatibility is intended by incorporating catechol-based biolinkers into the polymer network. Since the material structure is an essential cornerstone of a biomaterial, a

## SCIENTIFIC GOAL

separate excursus presents the synthesis of microgel particles to provide a basis for further research on applications in the field of microtissue engineering.

In short, three different defined and functional microgel platforms will be provided that can potentially replace animal testing. The first project aims to provide a model system to mimic processes from nature and presents an in vitro platform for bone regeneration. The second project shifts the focus to mimicking complex in vivo tissue functionality and provides a well-designed in vitro 3D cell culture platform. Finally, the third project combines the experiences of the first and second project and provides a new polymer system from scratch for microtissue applications.



# 3. Chapter I

## ●●● “Bone Scaffolds Based on Degradable Vaterite/PEG-Composite Microgels”

The results of the following chapter (p. 49–87) and the Supporting Information (p. 144–147) were published at *Advanced Healthcare Materials* on May 6, 2020.

**Elena Stengelin**,<sup>1</sup> [REDACTED]  
[REDACTED],  
*Adv. Healthc. Mater.* **2020**, *9*, 1901820.

<sup>1</sup> Johannes Gutenberg University Mainz, Department of Chemistry, Duesbergweg 10–14, D-55128 Mainz, Germany

<sup>2</sup> [REDACTED]  
[REDACTED]

<sup>3</sup> [REDACTED]

\* Corresponding author

Reprinted with permission from *Adv. Healthc. Mater.* **2020**, *9*, 1901820.

© 2020 The Authors. Published by WILEY-VCH Verlag GmbH & Co. KGaA, Weinheim

### 3.1. Specific Summary

The rational design of microtissue-based in vitro models makes it possible to replicate specific areas and functions of the human body in the simplest possible way, while still considering the complexity of natural tissue. Depending on the material composition and intrinsic properties, such in vitro systems not only represent potential tools for the development of bioactive materials in medicine, they also provide a new and intelligent approach for preclinical testing that, in the best case, can avoid the need for animal testing.

## CHAPTER I

In this context, a defined and functional *in vitro* platform is provided, specifically for the study of cellular metabolic processes in bone regeneration. Focusing on material design, poly(ethylene glycol) (PEG)-based microgels are prepared via droplet-based microfluidics. Their material properties in terms of processability and adaptivity are analyzed and adjusted to the requirements of the bone regeneration process. Additionally, the biocompatibility of microgels and the influence of their gelation time and mechanical strength on the cell viability are investigated by encapsulating osteoblasts inside the microgels. The degradability of the hydrolysis-sensitive microgels is also demonstrated under physiological conditions. Besides the material design, this study additionally focuses on mimicking metabolic processes during bone regeneration. For this purpose, vaterite particles are encapsulated as metastable calcium sources in the flexible microgel packaging and their transformation into the bone-like hydroxycarbonate apatite is analyzed. To extend the system, cells as well as vaterite particles are encapsulated within monodisperse, submillimeter microgels to provide a powerful *in vitro* platform as a starting point for further studies on bone tissue regeneration.

The personal contribution to the publication was the project development, interdisciplinary project coordination, lab work (polymer basis development; rheology measurements to analyze the mechanical material properties and gelation times of the polymer systems; microgel synthesis by droplet-based microfluidics; synthesis and analysis (FT-IR and Raman) of vaterite particles; encapsulation of vaterite particles into microgels by microfluidics; FT-IR spectroscopy measurements to analyze the vaterite transformation to hydroxycarbonate apatite in the gel system; fluorescence correlation spectroscopy measurements to analyze the mesh size of the hydrogel systems; cell experiments (encapsulation of cells and cells/vaterite particles in microgels by microfluidics); confocal laser scanning microscopy and light microscopy for imaging of cell- and vaterite-laden microgels; degradation studies; sample preparation for SEM measurements, light scattering experiments, confocal Raman microscopy, and endotoxin and toxicity testing), data analysis, writing and illustration of the manuscript, design of the cover picture (E. Stengelin, [REDACTED], [REDACTED], *Adv. Healthc. Mater.* **2020**, *9*, 2070030.).

### **Acknowledgements**

Parts of the results of this study were acquired with a confocal laser scanning microscope funded in part by the Major Research Instrumentation Program of the German Research Foundation under grant No. INST 247/878-1 FUGG. The authors wish to thank [REDACTED], [REDACTED], [REDACTED], [REDACTED], and [REDACTED].

██████████ for initial support in cellular biology. Further thanks go to ██████████ and ██████████ for SEM measurements. The authors also thank ██████████ ██████████ for the design of photomasks, as well as ██████████ and ██████████ ██████████ for their printing. We gratefully acknowledge general support and assistance by ██████████.

## 3.2. Introduction

Bone injuries have become an increasing health problem due to increasing life expectancy of the population.<sup>[1,2]</sup> In the United States, for example, more than 6 million fractures and 500,000 bone grafts occur every year, and worldwide, there are more than 20 million patients affected by bone-tissue loss due to trauma and degenerative diseases.<sup>[1,3]</sup> The skeleton is a central component for body stability, force distribution, and protection of organs, and bone lesions are accompanied by pain and physical limitations. This is accompanied by a loss of personal life quality and considerable costs for the health system and society.<sup>[1,4]</sup>

Patients with osteoporosis are at particularly high risk for fractures and poorly healing bone injuries.<sup>[5]</sup> This metabolic disease causes a low bone mineral density and structural bone loss due to an imbalance in the bone remodeling process.<sup>[5]</sup> Conventional osteoporosis therapies with drugs, such as bisphosphonates, estrogen agonists/antagonists, or teriparatide, primarily aim at inhibiting bone resorption or promoting bone formation, but they do not enable restoration of vanished bone mass.<sup>[5,6]</sup> Therefore, despite good availability of antiresorptive and anabolic medications, bone fractures are common in patients with osteoporosis and are often the cause of the problems described above.<sup>[6]</sup> As a result, there is an increasing need for novel therapeutic approaches that promote bone regeneration within a reasonable period of time.<sup>[1,6]</sup>

A promising regenerative approach might consist of a restorative therapy using a combination of scaffold-based biomaterials and bioactive agents, into which endogenous cells can migrate to build new bone material.<sup>[1,7]</sup> In addition to ceramics, polymers of synthetic and natural origin are the most popular scaffolding matrix for tissue regeneration, as they allow the three-dimensional (3D) structure and biochemical properties of tissue to be mimicked.<sup>[1,8-12]</sup> Moreover, they enable the integration of additional bone-regenerating components to obtain mechanically stable and biocompatible composites. Accordingly, Shi et al. developed artificial polymer-hydroxyapatite framework structures to promote bone growth, based on the premise that hydroxyapatite ( $\text{Ca}_{10}(\text{PO}_4)_6(\text{OH})_2$ ) is the most prevalent component in inorganic bone.<sup>[13-16]</sup> However, natural, non-stoichiometric hydroxyapatite is composed of a multitude of ions such as  $\text{Mg}^{2+}$ ,  $\text{Na}^+$ , and  $\text{CO}_3^{2-}$ , and depending on the specific bone location and function, there is a wide spectrum of bone mineral variants with regard to structure, composition, and biological behavior.<sup>[1,17]</sup> As a result, synthetically produced stoichiometric hydroxyapatite has only a limited capability of reaching the versatility of its natural counterpart.<sup>[18]</sup>

To overcome such limitations, an alternative approach is to provide a suitable form of a calcium precursor to support bone mineralization *in situ*. Vaterite, which is a metastable modification of calcium carbonate, is such a promising calcium precursor, as it is easily convertible to bone-like hydroxycarbonate apatite (HCA).<sup>[17,19,20]</sup> When provided in the form of micrometer-sized particles, it is highly biocompatible with human osteoblasts and endothelial cells, and hence, it may represent a suitable platform for rapid *in situ* bone regeneration.<sup>[17,19,20]</sup> Vaterite in combination with endogenous cells and in a flexible packaging form with adjustable mechanical properties, functionality, and biocompatibility might be a powerful starting point for tissue regeneration.<sup>[21–24]</sup>

To accomplish this, certain conditions must be met. Any preclinical development of a biotherapeutic material is generally characterized by a sequence of *in vitro* and *in vivo* optimization cycles, where the *in vivo* phase is complex, time consuming, and expensive. In contrast, the preceding *in vitro* phase is generally less time consuming and expensive. Thus, the introduction of living cells to the *in vitro* phase would allow for a rational, early-stage optimization of the biocompatibility of all materials and the entire therapeutic process. This, in turn, would reduce the time and cost for the subsequent *in vivo* phase. Moreover, exposing composite bone-promoting matrix materials to bone-derived living cells would also allow for a detailed study of bone formation processes *in vitro*.

A suitable method to combine vaterite particles and living cells homogeneously in a flexible packing form is droplet-based microfluidic technology. This method enables the synthesis of monodisperse and uniform micrometer-sized hydrogels with exquisite control over their geometry. It also enables the controlled micro- and nanoencapsulation of further additives such as cells and drugs.<sup>[25]</sup>

To provide a basis for such rational materials engineering, this paper aims to (i) introduce a convenient *in vitro* platform for the study of metabolic processes in bone formation and (ii) provide an *in vitro* foundation for novel tissue-regenerative therapies. We report on the development of system where a model matrix composed of osteoblast cells and vaterite particles are co-embedded within three-dimensional hydrogel-based structures designed and produced by droplet-based microfluidics (**Figure 3-1**). Our approach includes the development of monodisperse, sub-millimeter-sized hydrogel scaffolds, directed by a systematic parameter control. On a macroscopic level, microfluidic droplet templating enables the production of size- and shape-defined specimens with the option of controlled cell- and vaterite encapsulation. On a microscopic level, key requirements for the polymer system, such as the absence

of cytotoxicity as well as good biocompatibility and biodegradability are achieved by the use of functionalized poly(ethylene glycol) (PEG).<sup>[21,26]</sup> Harmful radicals and toxic catalysts are avoided by the use of bio-orthogonal and cytocompatible thiol–ene Michael addition chemistry to induce droplet gelation.<sup>[27–29]</sup> On a mesoscopic level, the microgel properties, such as their mechanical stiffness and gelation time, are adjusted to obtain high cellular viabilities by control of the polymer concentration, precursor polymer size, and the reaction conditions during gelation. Based on this systematic approach, physicochemically tailored scaffolding structures with bone matrix-specific properties are designed to eventually degrade under physiological conditions.

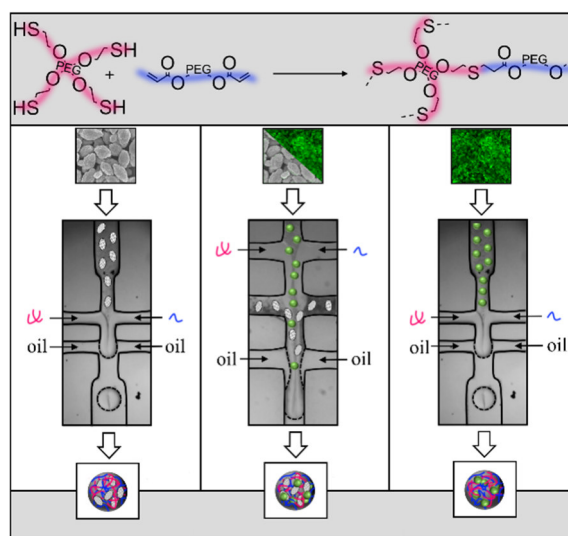


**Figure 3-1.** Production scheme for the encapsulation of vaterite particles (left), osteoblast cells (right), as well as a combination of both (middle) in a uniform sub-millimeter-sized microgel package formed by droplet-based microfluidics. Gelation of the precursor polymers is carried out by a biocompatible Michael addition between PEG-based thiol- and acrylate functionalized precursor polymers.

## 3.3. Results & Discussion

### 3.3.1. Polymer Scaffold

#### 3.3.1.1. Basis

Biocompatible PEG is chosen as the starting material for generating microgels containing living cells and vaterite particles since it is FDA approved and commercially available in a variety of pre-functionalized forms, architectures, molar masses, and narrow distribution of the latter. As a result, this polymer provides a suitable model platform in which key parameters for tailored hydrogel generation can be controlled and explored. Based on this material, the production of polymer-network gels is performed by using PEG building blocks with star-shaped and linear topologies. Thiol-functionalization of the star-shaped precursors (4-arm PEG-thiol) and acrylate-functionalization of the linear precursors (linear PEG-acrylate) allows the precursors to be linked by radical-free and biocompatible Michael addition (see reaction scheme in **Figure 3-1**). Since the Michael addition reaction generally takes place in alkaline medium, the precursor polymers are dissolved in a slightly alkaline, biocompatible phosphate buffer at pH 7.2. Due to subsequent experiments involving living cells, the precursor polymers are also dissolved in Dulbecco's Modified Eagle Medium (DMEM) as a culture medium for cells with a pH at physiological conditions (37 °C and 5% CO<sub>2</sub>) of 7.2–7.4.

For comparative analyses of the precursor-polymer solution gelation time in phosphate buffer and in DMEM, time-dependent rheology measurements are performed. For this purpose, a [4-arm PEG-thiol 10000 g mol<sup>-1</sup> (10K)/linear PEG-acrylate 5000 g mol<sup>-1</sup> (5K)] composition with a mean mass concentration of 160 g L<sup>-1</sup> is used. The evolution of the storage modulus,  $G'$ , and the loss modulus  $G''$  is monitored as a function of time  $t$ , as shown in **Figure 3-2**. In these experiments, the crossing point of  $G'$  and  $G''$  indicates gelation. In phosphate buffer ( $G'$  (□),  $G''$  (■)), gelation occurs after approximately twenty minutes at room temperature. By contrast, gelation occurs after less than one minute in DMEM ( $G'$  (▽),  $G''$  (▼)) at room temperature. The reasons for the fast gelling in DMEM are probably additional ingredients as salts and amino acids in the cell culture medium and also the slightly higher pH value of the medium as compared to that of the phosphate buffer: since the Michael addition preferably occurs in alkaline solutions, an increased basicity leads to an increased reaction rate.

In addition, the influence of additives to the medium, such as GlutaMAX (Gl), fetal bovine serum (FBS), and penicillin/streptomycin (P/S), on the reaction rate is studied by time-dependent rheology. The resulting curves ( $G'$  and  $G''$  as a function of time  $t$ ), are shown in **Figure 3-2b**. Gelation in DMEM (1% Gl) ( $G'$  (●),  $G''$  (○)) as well as DMEM (1% Gl, 10% FBS) ( $G'$  (◆),  $G''$  (◇)) and DMEM (1% Gl, 10% FBS, 1% P/S) ( $G'$  (▲),  $G''$  (△)) leads to crossing of  $G'$  and  $G''$  within one minute and is therefore similar to the reaction in pure DMEM ( $G'$  (▼),  $G''$  (▽)). Major influences of these additives on the gelling time are therefore considered to be negligible.

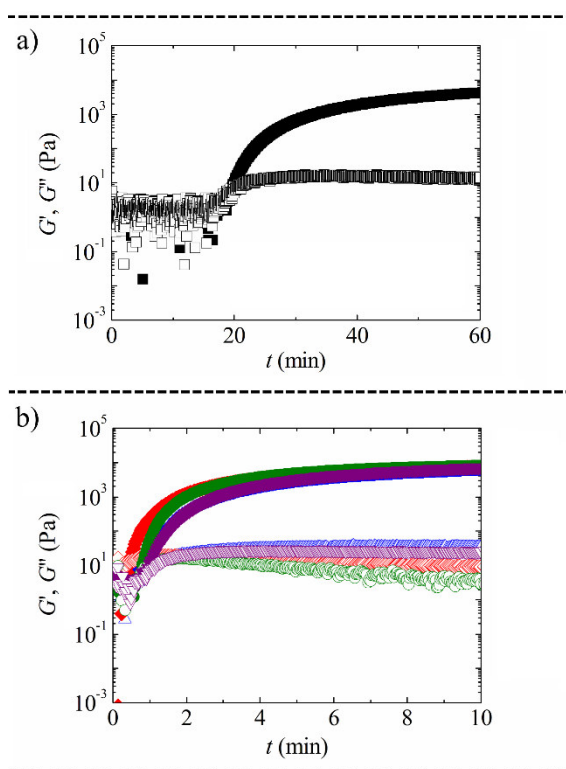


**Figure 3-2.** Time-dependent rheology measurements of the [4-arm PEG-thiol  $10000 \text{ g mol}^{-1}$  (10K)/linear PEG-acrylate  $5000 \text{ g mol}^{-1}$  (5K)] composition with a mean mass concentration of  $160 \text{ g L}^{-1}$  in (a) phosphate buffer and (b) in cellular medium DMEM. Herein, the crossing point of storage modulus,  $G'$ , and loss modulus  $G''$  indicates gelation. In phosphate buffer ( $G'$  (■),  $G''$  (□)), gelation occurs after approximately twenty minutes, whereas it occurs in less than a minute in DMEM ( $G'$  (▼),  $G''$  (▽)). Additional time-dependent rheology measurements of the same precursor polymers under cross-linking conditions in DMEM with several supplements (1% Gl ( $G'$  (●),  $G''$  (○)), 1% Gl + 10% FBS ( $G'$  (◆),  $G''$  (◇)), 1% Gl + 10% FBS + 1% P/S ( $G'$  (▲),  $G''$  (△)) show no influence of these on the gelling time: they all exhibit an increase of the complex viscosity within about 1 minute.

Due to the use of thiol-functionalized building blocks, oxidative disulfides can be formed in a competing side reaction to the Michael addition. To estimate the rate of this side reaction, time-dependent rheology measurements of the 4-arm PEG-thiol 10K precursor (mass



concentration of  $160 \text{ g L}^{-1}$ ) dissolved in physiological phosphate buffer as well as in DMEM (1% GI, 10% FBS, 1% P/S) are performed in the absence of the Michael-reactive linear PEG-acrylate precursor. Again, the crossing point of  $G'$  and  $G''$  indicates gelation. It appears that the disulfide formation and the subsequent gelation in cell culture medium DMEM (1% GI, 10% FBS, 1% P/S) occurs within a few hours. The reasons for the fast gelling in DMEM are probably a high oxygen level in the solution as well as a high amount of nutrients and salts in the medium. Furthermore, 4-arm PEG-thiol 10K precursor linkages to thiol-containing components in the culture medium DMEM, such as amino acids (e.g., cysteine) and proteins, have to be considered as well. In comparison, we observe a longer gelation in phosphate buffer. Depending on the batch of the polymers, the gelation time varies between approximately 10 to 48 hours. Since disulfides are formed faster in the cell culture medium DMEM (1% GI, 10% FBS, 1% P/S) than in phosphate buffer, further microfluidic experiments are done using phosphate buffer as the solvent, or a mixture of both.

### 3.3.1.2. Droplet-Based Microfluidics

Droplet-based microfluidic devices are used to form microgel particles from the heterofunctional PEG precursors. These devices can also be simultaneously used to embed cells and vaterite particles as bone-regeneration supporting supplements into the microgels. We employ two different poly(dimethylsiloxane) (PDMS) devices fabricated by soft lithography, that are shown in **Figure 3-1**. The devices displayed on the left and on the right side are designed for the preparation of either vaterite- or cell containing microgels, whereas the device shown in the middle of the scheme is designed for the simultaneous preparation of vaterite- and cell containing microgels (for details see Supporting Information (SI) **Figure S9-1** and **Figure S9-2**).

The microfluidic device for the encapsulation of either vaterite particles or cells exhibits a rectangular cross-section of  $100 \mu\text{m}$  diameter, intersecting at two sequential cross-junctions. At the first junction, aqueous solutions or suspensions of the two precursor polymers (4-arm PEG-thiol and linear PEG-acrylate), cells, or vaterite particles combine to form a laminar co-flowing stream. At the second junction, addition of an immiscible carrier fluid (HFE fluorinated oil/PFPE–Tris surfactant) serves to break the stream into monodisperse droplets with a uniform size of  $150\text{--}200 \mu\text{m}$  in diameter, depending on the flow rates and the precursor solution viscosities. In these droplets, surrounded by oil, the two polymeric building blocks react in a radical-free, biocompatible thiol–ene Michael addition and form a three-dimensional polymer network within a few minutes.

The microfluidic device designed for the simultaneous encapsulation of vaterite particles and cells is composed of channels that exhibit rectangular cross-sections of 100  $\mu\text{m}$  diameter, intersecting at three sequential cross-junctions. In the first junction, aqueous solutions of the two precursor polymers (4-arm PEG-thiol and linear PEG-acrylate) and the cell suspension are injected and combined. In the second junction, a water miscible vaterite/ethylene glycol suspension is injected. At the third junction, addition of an immiscible carrier fluid (HFE fluorinated oil/ PFPE–Tris surfactant) serves to break this fluid stream into monodisperse droplets with a uniform size of 160  $\mu\text{m}$  in diameter.

In a subsequent purification step, the resulting microgel particles synthesized using both microfluidic devices are freed from the oil and transferred to an aqueous environment. Depending on the microgel composition and the aqueous environment (phosphate buffer or DMEM), they swell to uniform sizes in the range of 200–300  $\mu\text{m}$  in these media.

### 3.3.2. Vaterite-Containing Microgels

#### 3.3.2.1. Vaterite Synthesis and Analytics

Vaterite is a meta-stable modification of calcium carbonate and converts to bone-like HCA under physiological conditions.<sup>[19,30]</sup> In combination with a PEG-based packaging form, this could be a useful compound for *in situ* bone regeneration.

The synthesis of vaterite particles is carried out by sonification of a mixture of calcium chloride dihydrate and sodium bicarbonate in ethylene glycol until a precursor vaterite solution is obtained.<sup>[19,30]</sup> The particle size of vaterite in the precursor solution is monitored by dynamic light scattering (DLS), which denotes polydisperse particles in the range of diameters between 200 and 600 nm (for details see SI **Figure S9-3**). Since vaterite particles are more stable in the dry state than in suspension, they are precipitated from the precursor vaterite/ethylene glycol mixture by addition of water and then dried under high vacuum. The precipitated nanoparticles agglomerate to micrometer-sized clusters, as shown by scanning-electron microscopy imaging (SEM) (**Figure 3-3a**). The nanoparticles as well as their larger agglomerates have characteristic ellipsoidal morphologies. Further particle characterization is performed by Fourier-transform infrared spectroscopy (FT-IR) and Raman spectroscopy (**Figure 3-3b, c**). The resulting spectra show characteristic  $\text{CO}_3^{2-}$  vibrational frequencies of vaterite and verify its identity (antisymmetric  $\nu_3$  stretching mode at 1487–1411  $\text{cm}^{-1}$ ,

symmetric  $\nu_1$  stretching mode at  $1090\text{ cm}^{-1}$ , out-of-plane bending motion  $\nu_2$  at  $877\text{ cm}^{-1}$ , and in-plane bending motion  $\nu_4$  at  $744\text{ cm}^{-1}$ ).<sup>[17,19]</sup>

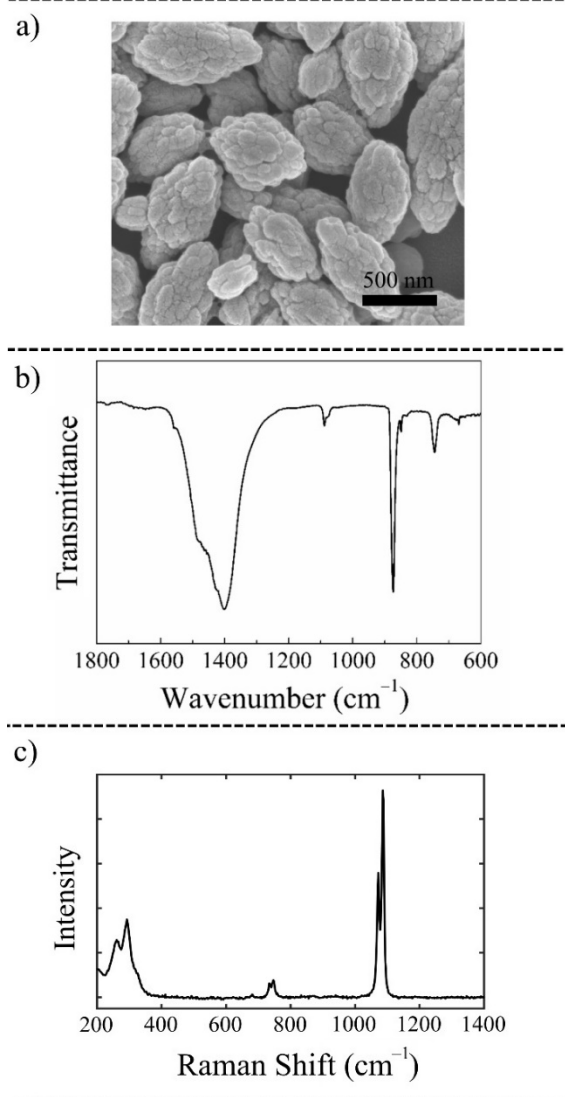


**Figure 3-3.** Characterization of vaterite particles. (a) Scanning electron microscopy (SEM) image of vaterite particles. (b) FT-IR and (c) Raman spectra show the characteristic  $\text{CO}_3^{2-}$  vibrational bands of vaterite ( $1487\text{--}1411\text{ cm}^{-1}$ : antisymmetric  $\nu_3$  stretching mode;  $1090\text{ cm}^{-1}$ : symmetric  $\nu_1$  stretching mode;  $877\text{ cm}^{-1}$ : out-of-plane bending mode  $\nu_2$ ;  $744\text{ cm}^{-1}$ : in-plane bending motion  $\nu_4$ ).

### 3.3.2.2. Encapsulation of Vaterite Particles

Vaterite particles are encapsulated into microgels using the microfluidic device depicted in **Figure 3-4a**. The four sections are passed by the droplets at different dwell times in the channel system. The section framed in blue shows the two rectangular cross-sections of the microfluidic device that are overlaid by schematics of the injected linear PEG-acrylate

precursors (blue), star-shaped 4-arm PEG-thiols (red), and vaterite particles (gray). The sections framed in red, green, and yellow show the droplets a few seconds after their formation.

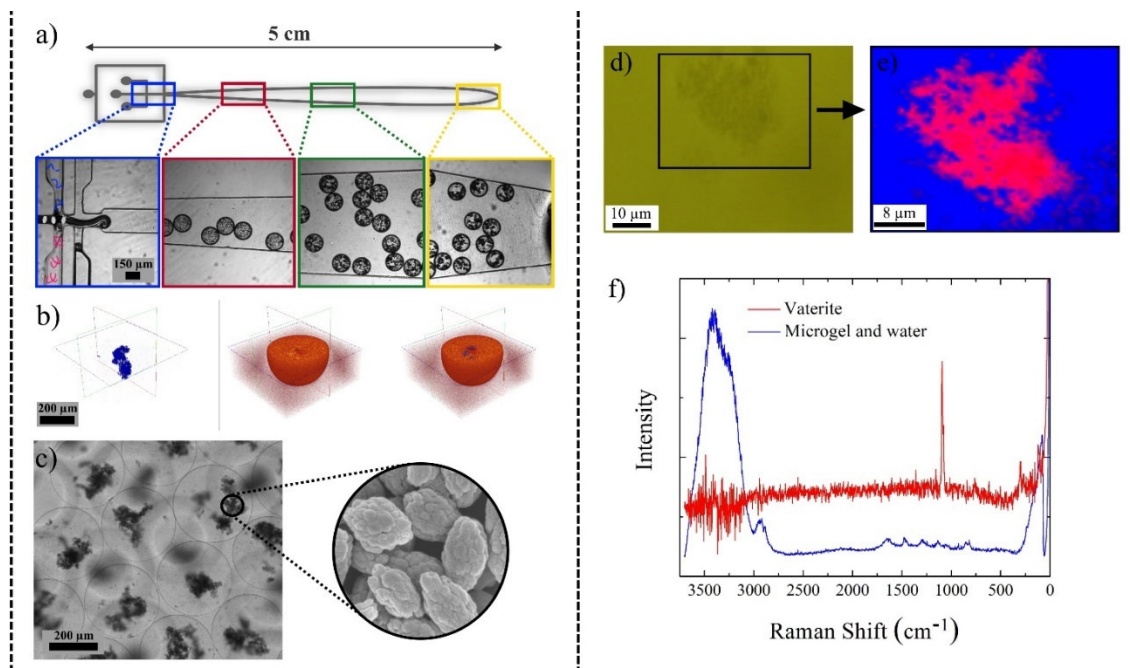


**Figure 3-4.** Images and analysis of vaterite-containing microgels. (a) Schematic representation of the microfluidic device used for this experiment, including four sections (framed in blue, red, green, and yellow, respectively) displaying the droplets at different second-scale dwell times in the channel system. Vaterite particles in the droplets agglomerate increasingly to clusters after encountering the aqueous building block solution in the first cross-section, as is depicted in the sequence of the four sections. (b) The resulting vaterite-containing microgels are analyzed by 3D confocal laser scanning microscopy and selective staining with sulforhodamine B and calcium-selective tetracycline, (c) as well as by the transmission path of the confocal laser scanning microscope. (d) Bright-field image of vaterite particles located in a microgel, whereby a small section of the microgel is depicted. (e) Confocal Raman image from the black squared area of the bright-field image. The red area shows the vaterite agglomerates, and the blue area shows the microgel fragment, stored in water. (f) Raman spectrum from the vaterite agglomerates (red) and the combined spectrum of the microgel fragment and water (blue). The spectra are obtained by hyperspectral analysis of the confocal Raman image.

Microgel formation occurs after injection of aqueous 4-arm PEG-thiol  $10000 \text{ g mol}^{-1}$  (10K) and linear PEG-acrylate  $5000 \text{ g mol}^{-1}$  (5K) precursor polymer solutions (dissolved in phosphate buffer) with a mean mass concentration of  $300 \text{ g L}^{-1}$  each at the first junction of the microfluidic device, along with vaterite particles resuspended in ethylene glycol (5% (w/v)) by ultrasonic mixing. Droplets of the mixture of these components are formed at the second junction by flow-focusing with a non-miscible fluorinated oil. In these droplets, the precursor polymers react in a radical-free, biocompatible Michael addition, while vaterite particles agglomerate to clusters within a few seconds after encountering the aqueous building block solution in the first cross-section. An increasing agglomeration of the vaterite particles in the

droplets is demonstrated in **Figure 3-4a** progressing from the red section to the green and finally the yellow section. After gelation of the droplets occurs, the resulting vaterite-containing microgels are transferred into phosphate buffer or water.

Vaterite agglomerates in the microgels are characterized by 3D confocal laser scanning microscopy. By incubation in a dye solution of sulforhodamine B and calcium-selective tetracycline, the vaterite particles and the microgels are distinguishable due to the special affinity of sulforhodamine B to the polymer scaffold and tetracycline to the vaterite particles. In **Figure 3-4b**, vaterite clusters stained in blue and microgels stained in red and an overlay of the two images is shown. By confocal laser scanning microscopy (transmission path), vaterite particles are also recognizable as dark spots in the microgels (**Figure 3-4c**).

Meta-stable vaterite may transform to the thermodynamically more stable calcite or aragonite during the microfluidics studies. To determine if this is the case, the stability of vaterite in the microgels is confirmed by confocal Raman spectroscopy, since vaterite and the other calcium carbonate modifications as calcite and aragonite are Raman active compounds. The successful verification of the vaterite modification is depicted in **Figure 3-4**, where in (d) a bright-field image of a microgel section containing vaterite agglomerates, stored in water is shown. The image shown is made 48 hours after gelation of the microgel. In (e) the confocal Raman image from the black squared area of the bright-field image is shown. The red area shows the vaterite agglomerates, and the blue area shows the microgel fragment, stored in water. The Raman spectrum obtained after hyperspectral analysis of the measured microgel section including vaterite agglomerates is shown in (f). The blue spectrum corresponds to the combined signals of the microgel PEG backbone and water. Due to the high impact of water in the microgels, a separation into two single spectra is not possible. The red spectrum presents the characteristic bands of vaterite, which corresponds to the symmetric stretching mode  $\nu_1$  at  $1090\text{ cm}^{-1}$  and  $1075\text{ cm}^{-1}$ , the in-plane bending motion  $\nu_4$  at around  $744\text{ cm}^{-1}$ , and the lattice modes at  $305\text{ cm}^{-1}$  and  $120\text{ cm}^{-1}$ .<sup>[17,19]</sup> This spectrum is obtained after subtracting the combined spectrum of PEG and water from the mean spectra of the red area and shows the meta-stable vaterite modification, successfully encapsulated in the microgels (for details see SI **Figure S9-4**).

### 3.3.2.3. Transformation of Vaterite to HCA

For the assessment of the in vitro bone-like HCA forming ability of vaterite embedded in the polymer matrix, vaterite-containing gels are immersed in Dulbecco's phosphate-buffered

saline (DPBS) and analyzed by FT-IR spectroscopy. The same measurements are also performed with the polymer matrix and with pure vaterite particles as a control. Respective IR-spectra are depicted in **Figure 3-5**, where measurements before the immersion in phosphate buffer and after 48 hours of immersion are shown. The IR-spectra of the polymer matrix (**Figure 3-5a**) show no changes after 48 hours of incubation in DPBS, while the spectra of vaterite particles (**Figure 3-5b**) record an increase of  $\text{PO}_4^{3-}$  band intensity (non-degenerate symmetric P–O stretching mode at  $963\text{ cm}^{-1}$  and the triply degenerate antisymmetric P–O stretching mode at  $1024\text{ cm}^{-1}$ ).<sup>[19,30]</sup> Additionally, the typical vibrational frequencies of the  $\text{CO}_3^{2-}$  bands at  $1487\text{--}1411\text{ cm}^{-1}$ ,  $1090\text{ cm}^{-1}$ ,  $877\text{ cm}^{-1}$ , and at  $744\text{ cm}^{-1}$ , are shown in both spectra. These results indicate the transformation of vaterite to HCA and agree to previous findings of Schröder et al.<sup>[19,30]</sup>

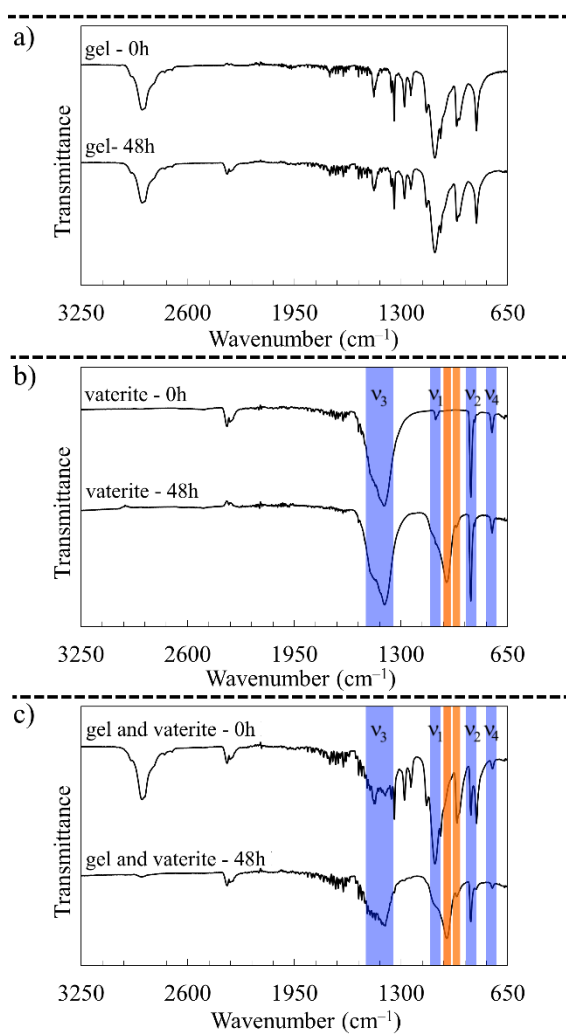


**Figure 3-5.** Transformation of vaterite particles embedded within the polymer matrix to HCA at physiological conditions. FT-IR-spectra of (a) the PEG polymer matrix, (b) pure vaterite particles (normalized to  $\nu_2$ ), and (c) vaterite particles embedded in the polymer matrix, each before and after 48 hours incubation in DPBS.

The IR-spectra of vaterite-containing gels (25 wt%) are shown in **Figure 3-5c**, whereby the spectra of the sample before immersion in DPBS mainly display the frequencies of the polymer scaffold, but also two characteristic bands of vaterite at  $877\text{ cm}^{-1}$  and at  $744\text{ cm}^{-1}$ . After 48 hours of incubation in DPBS, the spectra change. The intensity of the polymer frequencies is mainly decreased, which is caused by hydrolysis sensitive ester groups in the polymer network. Due to the vaterite-caused increased basicity of DPBS, the polymer degradation is accelerated and makes a view of the mineral spectra possible, which is comparable to that of pure vaterite after 48 hours of incubation in DPBS. This analysis indicates a vaterite transformation in the polymer matrix to HCA and makes the vaterite/PEG composite material a suitable candidate for further investigations on the mineral level.

### 3.3.3. Gel Composition vs. Cellular Viability

#### 3.3.3.1. Endotoxin and Toxicity Testing of Gels

To determine the cell- and biocompatibility of the gels, endotoxin and toxicity tests are done. For the endotoxin assay, gels and extracts from gels ([4-arm PEG-thiol  $10000\text{ g mol}^{-1}$  (10K)/linear PEG-acrylate  $5000\text{ g mol}^{-1}$  (5K)] composition with a mean mass concentration of  $160\text{ g L}^{-1}$ ) are added to HUVEC cells in culture, whereby no induction of E-selectin is observed. Based on previous studies showing that the induction of the cell-adhesion molecule E-selectin by endotoxin is a highly sensitive method for the detection of endotoxin in biomaterials, it is clear that the precursor polymer synthesis methods used for the formation are sufficient for the production of endotoxin-free gels.<sup>[31,32]</sup> In **Figure 3-6a** respective images of HUVEC cells cultured on plastic are shown, and the dye Hoechst 33342 is used to stain the cell nuclei (blue). In (1), cells are exposed to  $1\text{ }\mu\text{g mL}^{-1}$  endotoxin (LPS), which results in an intensely green stain that indicates the presence of E-selectin. (2) is an untreated control of HUVEC cells, while (3) and (4) are cells exposed to the gel or extracts from the gel. The absence of green staining in (3) and (4) indicates no induction of E-selectin and therefore the absence of endotoxin in the test sample.

The viability of cells growing on two gels ([4-arm PEG-thiol  $10000\text{ g mol}^{-1}$  (10K)/linear PEG-acrylate  $5000\text{ g mol}^{-1}$  (5K)] composition with a mean mass concentration of  $300\text{ g L}^{-1}$ ) is compared to the same amount of cells growing on plastic (control experiment). GFP-marked osteoblast cells (MG-63 GFP) are used since osteoblasts are responsible for the production of extracellular matrix (e.g. collagen) in metabolic bone regeneration processes and

has been extensively used as a model cell line for osteoblast studies on biomaterials.<sup>[19]</sup> The metabolic activity of the cells is assayed after 24 hours by examining the conversion of resazurin to resorufin. Only viable, metabolically active cells can carry out this conversion. As can be seen in **Figure 3-6b**, cells on the gels exhibit nearly the same amount of metabolic activity after 24 hours as the cells on plastic, and therefore, the gels exhibit no toxic effect on the cells.

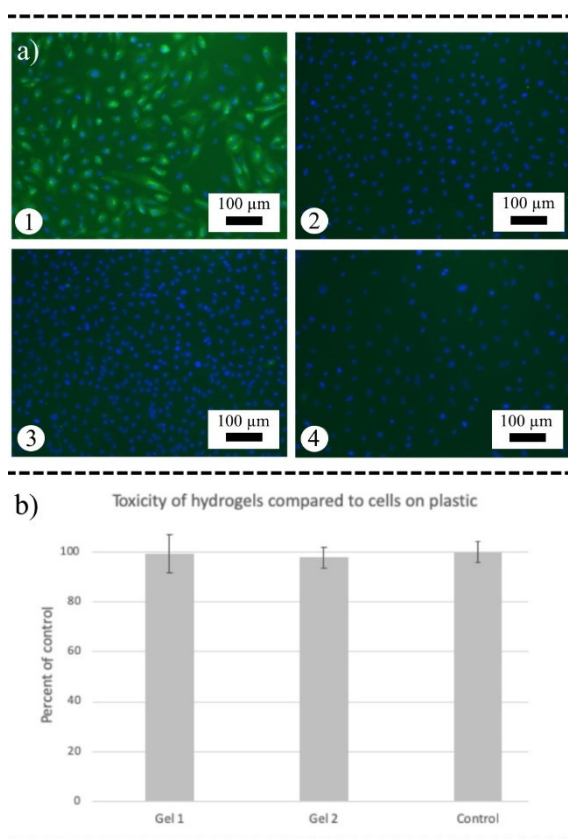


**Figure 3-6.** Endotoxin and toxicity testing of gels of type [4-arm PEG-thiol 10000 g mol<sup>-1</sup> (10K)/linear PEG-acrylate 5000 g mol<sup>-1</sup> (5K)]. (a) Evidence of endotoxin by E-selectin staining of HUVEC cells cultured on plastic (1, 2) and exposed to gels (3) or supernatant extract from the gels (4). A positive control is shown in (1), where HUVEC cells are exposed to 1 μg mL<sup>-1</sup> endotoxin (LPS) after 24 hours incubation on plastic. The intense green fluorescence indicates the presence of E-selectin (using E-selectin as a first antibody and anti-mouse Alexa Fluor 488 as a second antibody), whereby the dye Hoechst 33342 is used to stain the cell nuclei (blue). The control, (2), as well as cells exposed to the gel or extracts from the gel (3 and 4, respectively) show no green staining and indicate endotoxin-free materials. Similar results are observed with two different donors of HUVECs. (b) Relative metabolic activity of cells growing on gels compared to cells growing on cell culture plastic (control), by examining the conversion of resazurin to resorufin. The cells growing on two gels exhibited nearly an identical metabolic activity for the reduction of resazurin after 24 hours compared to the control cells growing on cell culture plastic set to 100%. Two different donors for HUVEC are used (mean ± SD (n = 8)).



### 3.3.3.2. Gel Elasticity

In most cases, endogenous cells will grow into implanted biomaterials, but the preclinical development requires an optimization of the materials that is usually accomplished with *ex vivo* and *in vivo* experiments. Since *in vivo* experiments are complex, time consuming, and expensive, the *in vivo* studies can be mimicked *ex vivo* by examining cells. This requires that the gel elasticity be optimized to maximize the viability of the cells.

To achieve a general understanding of the cell behavior in different polymer-network mesh-sized scaffolds, GFP-marked osteoblast cells (MG-63 GFP) are encapsulated by microfluidics in three different polymer networks that differ from each other in terms of the polymer-network mesh size and consequently in the gel stiffness or softness. A focus is placed on the influence of the gel mechanical strength and gelation time on the cell viability.

To examine the influence of the variation of the polymer-network mesh size, the molar mass of the 4-arm PEG-thiol precursor polymer is kept constant at  $10000 \text{ g mol}^{-1}$  (10K), whereas the molar masses and thereby the length of the linear PEG-acrylate precursor polymers are varied from  $2000 \text{ g mol}^{-1}$  (2K) over  $5000 \text{ g mol}^{-1}$  (5K) to  $7500 \text{ g mol}^{-1}$  (7.5K) (**Table 3-1**). The molar concentration of the precursor polymers in diverse solvents (and thus the molar concentration of their reactive end groups) is kept constant at a ratio of 1:2 (4-arm PEG-thiol to linear PEG-acrylate), whereas their respective mass concentrations increase within the three systems.

**Table 3-1.** Composition of three specific networks, are compared based on their respective precursor polymer molar mass ( $M$ ) as well as molar and mass concentrations ( $\rho_{\text{prec}}$ ) in diverse solvents. Storage and loss modulus crossing points in buffer ( $t_{\text{g,buffer}}$ ) and in a mixture of phosphate buffer/DMEM (1% GI, 10% FBS, 1% P/S) at a ratio of 6:1 ( $t_{\text{g,mixture}}$ ) as well as the final network storage moduli after five hours of reaction time ( $G'_{\text{g,buffer}}$  and  $G'_{\text{g,mixture}}$ ) are obtained by rheology. Respective polymer-network mesh sizes ( $\xi_{\text{buffer}}$  and  $\xi_{\text{mixture}}$ ) are calculated by the phantom network model.

	$M$ (kDa)	$\rho_{\text{prec}}$ (mol L <sup>-1</sup> )	$\rho_{\text{prec}}$ (g L <sup>-1</sup> )	$t_{\text{buffer}}$ (min)	$G'_{\text{buffer}}$ (kPa)	$\xi_{\text{buffer}}$ (nm)	$t_{\text{mixture}}$ (min)	$G'_{\text{mixture}}$ (kPa)	$\xi_{\text{mixture}}$ (nm)
4-arm PEG-thiol	10	0.03	300	29	15.7±0.8	6.4	11	20.9±3.6	5.8
linear PEG-acrylate	2	0.06	120						
4-arm PEG-thiol	10	0.03	300	15	29.9±3.1	5.2	4	26.6±3.9	5.4
linear PEG-acrylate	5	0.06	300						
4-arm PEG-thiol	10	0.03	300	11	28.7±1.4	5.2	4	30.3±3.9	5.2
linear PEG-acrylate	7.5	0.06	450						

The network stiffness and gelation times of the three systems are analyzed by time-dependent rheology measurements of macrogels. The resulting curves are shown in **Figure 3-7**, where the storage modulus,  $G'$ , and the loss modulus  $G''$ , are plotted against time. The crossing points serve as an indication of the gelation time ( $t_g$ ), and the terminal storage modulus ( $G'_g$ ) denotes the polymer gel stiffness, whereby the plateau storage modulus  $G'$  is generally connected to the number density of elastically effective chains in the gel,  $\nu_{\text{eff},1}$ , by the phantom network model ( $\mathcal{A} \cdot \nu_{\text{eff},1} = G' / (RT)$ ). In this formula,  $R$  is the gas constant,  $T$  the temperature, and  $\mathcal{A} = 1 - (2 / f)$  is a structure factor, with  $f$  the functionality of the cross-links (here,  $f = 4$ ).<sup>[33]</sup>

Measurements are performed in a phosphate buffered solution as a standard, as well as in a mixture of phosphate buffer and DMEM (1% Gl, 10% FBS, 1% P/S) at a ratio of 6:1. Since disulfide formation as a side reaction to the Michael addition is more dominant in the DMEM culture medium than in the phosphate buffer, experiments are performed in a mixture of phosphate buffer and DMEM (1% Gl, 10% FBS, 1% P/S). The respective values are listed in **Table 3-1**, where *buffer* and *mixture* represent the measurements in phosphate buffer or in the mixture medium.

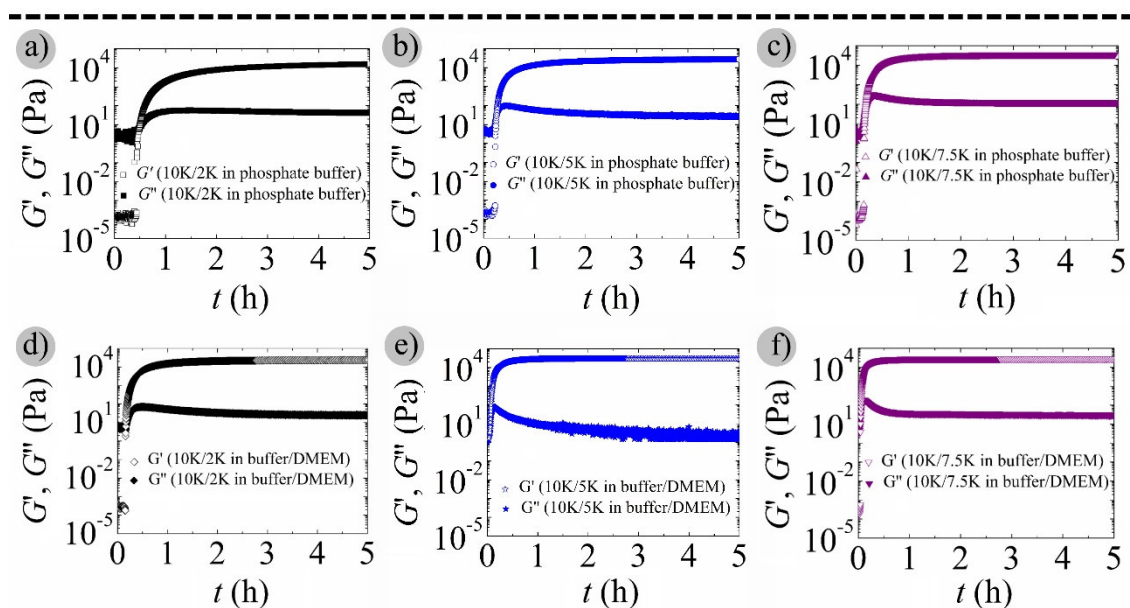


**Figure 3-7.** Dependency of cell viability on the scaffolding gel elasticity: Time-dependent storage and loss moduli over time for selected 4-arm PEG-thiol/linear PEG-acrylate network compositions in phosphate buffer (a–c, at the top) and in a phosphate buffer/DMEM mixture at a ratio of 6:1 (d–f, at the bottom). Black symbols: 10K/2K composition ( $G'$  ( $\square$ ),  $G''$  ( $\blacksquare$ ) and  $G'$  ( $\diamond$ ),  $G''$  ( $\blacklozenge$ )); blue symbols: 10K/5K composition ( $G'$  ( $\circ$ ),  $G''$  ( $\bullet$ ) and  $G'$  ( $\star$ ),  $G''$  ( $\blackstar$ )); purple symbols: 10K/7.5K composition ( $G'$  ( $\triangle$ ),  $G''$  ( $\blacktriangle$ ) and  $G'$  ( $\nabla$ ),  $G''$  ( $\blacktriangledown$ )).

### ***Discussion of the Gelation Time***

In phosphate buffer, the 4-arm PEG-thiol/linear PEG-acrylate 10K/2K (**Figure 3-7a**) ( $G'$  (□),  $G''$  (■)) composition gels after 29 minutes. In contrast, the 10K/5K (**Figure 3-7b**) ( $G'$  (○),  $G''$  (●)) composition gels within 15 minutes and is thus twice as fast as the 10K/2K composition. Furthermore, the 10K/7.5K (**Figure 3-7c**) ( $G'$  (△),  $G''$  (▲)) composition gels within just 11 minutes. Therefore, the gelation time decreases with increasing molar mass of the linear PEG-acrylate (2K, 5K up to 7.5K). This is because the hydrodynamic radius increases in the same row, making the reactive ends of the precursor polymers more likely to find and react with the reactive groups of the PEG-thiol components at increasing size of the linear PEG-acrylate.<sup>[33]</sup> Also, a greater hydrodynamic radius comes along with a lower probability of loop-type reaction of both ends of the same linear precursor with two extremities of the same star precursor, which consumes these precursors without contributing to actual network formation and this delays the formation of a percolated network. Almost the same sequence is observed in the phosphate buffer/DMEM mixtures, although at a faster rate. The 4-arm PEG-thiol/linear PEG-acrylate 10K/2K (**Figure 3-7d**) ( $G''$  (◇),  $G'$  (◆)) composition gels after 11 minutes, whereas the 10K/5K (**Figure 3-7e**) ( $G'$  (☆),  $G''$  (★)) composition and the 10K/7.5K (**Figure 3-7f**) ( $G'$  (▽),  $G''$  (▼)) composition gels within just 4 minutes. Here, the more alkaline pH value of the phosphate buffer/DMEM mixture in comparison to the pH of the pure phosphate buffer is most likely responsible for the overall accelerated reaction rate. It is also possible that there is an overall larger radius of gyration of the linear building block in the phosphate buffer/DMEM mixture than in phosphate buffer, due to the additional salts and amino acids in DMEM, thereby leading to the faster gelation.

### ***Discussion of the Gel Stiffness***

Comparison of the terminal storage moduli  $G'$  indicates differences between the networks. In phosphate buffer, the 10K/2K (**Figure 3-7a**) ( $G'$  (□),  $G''$  (■)) composition shows the lowest storage modulus ( $(15.7 \pm 0.8)$  kPa) and is therefore the softest network compared to the others. The 10K/5K (**Figure 3-7b**) ( $G'$  (○),  $G''$  (●)) and the 10K/7.5K (**Figure 3-7c**) ( $G'$  (△),  $G''$  (▲)) compositions show storage moduli of  $(29.9 \pm 3.1)$  kPa and  $(28.7 \pm 1.4)$  kPa. The increase in the network strength between these three systems from  $(15.7 \pm 0.8)$  kPa to  $(29.9 \pm 3.1)$  and  $(28.7 \pm 1.4)$  kPa is due to the different size of the PEG-acrylate building blocks. The smaller the radius of gyration, the more likely is the occurrence of looping defects in the network, and hence, these networks are softer. This agrees with the longer time it takes for these precursors to actually form a gel, as just discussed above. Similar

results are obtained with the phosphate buffer/DMEM mixture (10K/2K:  $(20.9 \pm 3.6)$  kPa, 10K/5K:  $(26.6 \pm 3.9)$  kPa, 10K/7.5K:  $(30.3 \pm 3.9)$  kPa) (**Figure 3-7(d–f)**) and demonstrates that the culture medium has little effect on the final gel stiffness.

The nanoscopic mesh sizes,  $\xi$  of the polymer networks are calculated using the number density of elastically effective chains from the phantom network model  $\mathcal{A} \cdot \nu_{\text{eff},1} = G' / (RT)$  from the moduli. The product of the structure factor  $\mathcal{A}$  and the number density of elastically effective chains on the left side,  $\mathcal{A} \cdot \nu_{\text{eff},1}$ , equals the number density of elastically effective cross-links  $\nu_{\text{eff},2}$  [ $\text{mol} \cdot \text{L}^{-1}$ ]. Multiplication of  $\nu_{\text{eff},2}$  with the Avogadro constant  $N_A$  yields the absolute number of effective cross-links per liter, and the mean distance of these cross-links, that is, the mesh size  $\xi$ , is obtained from the cube-root of the inverse of that value:  $\xi = (1 / (\nu_{\text{eff},2} \cdot N_A))^{1/3} = (RT / (G' \cdot N_A))^{1/3}$ . In this calculation,  $R$  is the gas constant,  $T$  the temperature at which  $G'$  is measured,  $N_A$  the Avogadro constant, and  $G'$  the measured storage modulus of each network, here at a measurement frequency of  $6.28 \text{ rad s}^{-1}$  (**Table 3-1**). Altogether, the mesh sizes calculated in this manner do not differ from each other: both in the phosphate buffer and in the phosphate buffer/DMEM mixture, the mesh sizes of the 10K/5K and 10K/7.5K systems are estimated to be approximately 5.2 nm or 5.4 nm, whereas the mesh sizes of the 10K/2K system are slightly larger in the phosphate buffer (6.4 nm) and in the phosphate buffer/DMEM mixture (5.8 nm). This is a reflection of the same trends in the moduli, from which the mesh sizes are actually calculated.

In summary, the three polymer systems show storage moduli of similar magnitude, corresponding to similar network mesh sizes, but differences in the cross-linking time of the precursor polymers.

### 3.3.3.3. Gel Permeability

To independently probe the polymer-network meshes, fluorescence correlation spectroscopy (FCS) is used to measure the permeability of small and mesoscopic probes through the gels. This study also mimics the diffusive permeation of nutrients and metabolites in the gels in cases where cells are encapsulated in order to determine how efficient the transport of species of this size and molar mass occurs to and from cells. To determine this, gel samples of type 10K/2K, 10K/5K, and 10K/7.5K are prepared and incubated in a dye solution for several hours. The FCS measurements are performed on macrogels rather than on microgels. Since the reaction conditions in the production of the micro- and macrogels are similar, it is

predicted that the very similar network structures will be generated in either form. Therefore, the diffusion coefficients measured in the macrogels can be applied to the microgels as well. Sulforhodamine B is chosen as a surrogate for low-molar-mass components of the culture medium (e.g., salts and amino acids). Rhodamine has a diffusion coefficient  $D$  of  $440 \mu\text{m}^2 \text{s}^{-1}$  in aqueous solutions,<sup>[34]</sup> and this is used to calculate the hydrodynamic radius  $R_H$  of 0.5 nm using the Stokes–Einstein equation ( $R_H = k_B T / 6\pi\eta D$ ), with  $k_B$  the Boltzmann constant,  $T$  the room temperature, and  $\eta$  the viscosity of the medium (essentially, identical to water). In contrast, bovine serum albumin (BSA) labeled with tetramethyl rhodamine is chosen as a surrogate for larger molecules in the culture medium (e.g., proteins), as BSA is a major protein in cell culture medium with a measured diffusion coefficient  $D$  of  $204 \mu\text{m}^2 \text{s}^{-1}$  in aqueous solutions and a calculated hydrodynamic radius of 1.1 nm. In the three specific networks, FCS measurements show diffusion coefficients of similar magnitude for both sulforhodamine B and dye-labeled BSA. Compared to free sulforhodamine B in phosphate buffer ( $440 \mu\text{m}^2 \text{s}^{-1}$ ),<sup>[34]</sup> the diffusion coefficients in the networks are 4–5 times slower ( $D_{10K/2K} = (105 \pm 15) \mu\text{m}^2 \text{s}^{-1}$ ,  $D_{10K/5K} = (93 \pm 8) \mu\text{m}^2 \text{s}^{-1}$ ,  $D_{10K/7.5K} = (88 \pm 10) \mu\text{m}^2 \text{s}^{-1}$ ), whereas compared to free dye-labelled BSA ( $204 \mu\text{m}^2 \text{s}^{-1}$ ), the diffusion coefficients are two times slower in the networks ( $D_{10K/2K} = (120 \pm 27) \mu\text{m}^2 \text{s}^{-1}$ ,  $D_{10K/5K} = (118 \pm 19) \mu\text{m}^2 \text{s}^{-1}$ ,  $D_{10K/7.5K} = (76 \pm 6) \mu\text{m}^2 \text{s}^{-1}$ ). These lowered diffusion coefficients indicate an inhibited diffusion of the substrate due to the network cross-linkings and chains. Nevertheless, a sufficient nutrient exchange between the gels and the surrounding medium up to a substrate hydrodynamic radius of 1.1 nm is possible.

#### 3.3.3.4. Encapsulation of Cells

The influence of the gel properties on the viability of a human osteoblast cell line expressing GFP (line MG-63) is analyzed by encapsulation into microgels. For this purpose, the microfluidic device shown in **Figure 3-1** (on the left and on the right side) is used. Microgel production occurs after injection of aqueous 4-arm PEG-thiol and linear PEG-acrylate precursor polymer solutions (dissolved in phosphate buffer) each at the first junction of the microfluidic device, along with cells suspended in DMEM (1% Gl, 10% FBS, 1% P/S) and 15% OptiPrep acting as a density-increasing compound to avoid deposition of the cells in the microfluidic experiment. After gelation and purification, cell-containing microgels of the 10K/5K type are incubated in DMEM (1% Gl, 10% FBS, 1% P/S) at physiological conditions (37 °C, 5% CO<sub>2</sub> and humidity) over a period of two weeks (**Figure 3-8a**). During the first seven days, cells are centered in the microgels and form clusters, while the polymer-gel

specimen swells due to the hydrolysis of ester groups in the polymer network. The increase of the degree of network swelling is illustrated by white dashed lines around the microgels.

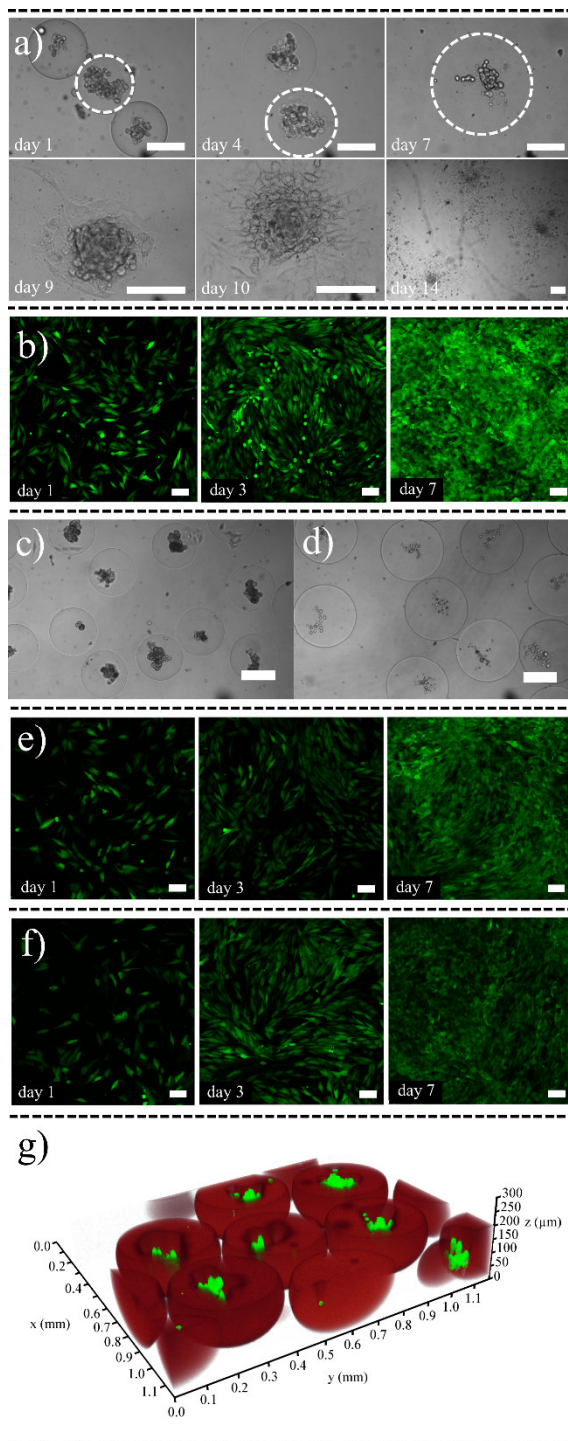


**Figure 3-8.** Cell-containing microgels. (a) Monitoring of the cell viability in 10K/5K microgels is performed by light microscopy imaging over a period of two weeks. (b) Control test of the experiment with 10K/5K microgels monitored by 2D confocal microscopy. Increasing green fluorescence of GFP expressing cells indicates cell proliferation. (c) Light microscopy imaging of type 10K/2K and (d) 10K/7.5K microgels containing cells. (e) Control test of the experiment with 10K/2K microgels and (f) 10K/7.5K microgels. (g) 3D confocal

microscopy of MG-63 GFP cells (green fluorescence) in microgels of type 10K/2K, incubated in a sulforhodamine B/ phosphate buffer solution (red fluorescence). Scale bars: 100  $\mu\text{m}$ .

After complete degradation of the microgels (after about 7–8 days), cloud-like cell clusters are observed in the culture medium. These clusters eventually settle at random points on the culture dish surface, adhere, and proliferate, seen as cells growing out of the clusters (day 9). With time, cells continue to increase in numbers until at least day 14. This observation demonstrates a high viability of cells that are encapsulated for at least 7 days within the 10K/5K polymer network, and these cells are able to attach and proliferate after gel degradation, as evidenced by their growth on the cell culture dish surface.

In parallel to the microfluidic experiment, the viability of the cells is monitored in control experiments. For this purpose, the cells are seeded on plastic, and their growth is followed over a period of 7 days. The visualization of the cell growth is performed by 2D confocal microscopy, whereby an increasing intensity of green fluorescence indicates increasing cell growth. **Figure 3-8b** shows one experiment at days 1, 3, and 7.

Cells are also encapsulated in the 10K/2K and 10K/7.5K networks. Cells in the 10K/2K microgels behave similar to cells encapsulated in the 10K/5K system (**Figure 3-8c**). These cells form cellular clusters that adhere to the cell culture dish after gel degradation. In contrast, the encapsulated cells in the 10K/7.5K network (**Figure 3-8d**) do not survive. In this experiment, cellular clusters are not observed after degradation of the microgels, however, some isolated, rounded-up single cells are observed that do not adhere to the cell culture dish. The viability of the cells is also monitored in control experiments (**Figure 3-8e,f**)

Differences in the cellular viability between both polymer systems 10K/2K and 10K/7.5K are probably based on differences in the ability of the cells to form cell–cell contacts. Since PEG is an antifouling material and resistant against protein adsorption from the environment, cells are not able to adhere to that material.<sup>[35]</sup> Instead, they form a round sphere-like morphology and aggregate to cell clusters through specialized protein complexes, like E-cadherin, integrin, or ECM proteins.<sup>[36,37]</sup> This can be observed in the 10K/2K and 10K/5K networks, where the cells interact spatially and form clusters, whereas the cells in the 10K/7.5K system remain isolated over the entire encapsulation period. As cell–cell interaction is an important parameter of cellular viability,<sup>[38]</sup> this might be the cause for survival differences in the networks.

The inhibition of cell–cell contacts in the 10K/7.5K microgels may be based on differences in the gelling time, the elasticity of the polymer network, and the viscosity of the precursor

polymer solution. The 10K/5K system and the 10K/7.5K system both require approximately 4 minutes to gel in the hybrid mixture of phosphate buffer and DMEM respectively, and the elasticity of both polymer gel systems has been found to differ only marginally ( $(26.6 \pm 3.9)$  kPa and  $(30.3 \pm 3.9)$  kPa). Despite this similarity, however, the cell viability in these two systems differ substantially. The reason may be due to the different viscosities of the precursor polymer solutions. In the 10K/5K system, the cells are embedded in a  $300 \text{ g L}^{-1}$  precursor solution with a linear-precursor polymer molar mass of  $5000 \text{ g mol}^{-1}$ , whereas in the 10K/7.5K system, they are embedded in a  $375 \text{ g L}^{-1}$  solution with a linear-precursor polymer molar mass of  $7500 \text{ g mol}^{-1}$ . Both the higher concentration and polymer molar mass in the 10K/7.5K system as compared to the 10K/5K entails a higher solution viscosity, which impairs cellular motion. If the gelation is then faster than the time that it takes for cells to come into physical contact with one another in that viscous surrounding, they are fixed at isolated positions in the polymer network, as it is the case in the 10K/7.5K system, thereby preventing them from forming cell-clusters.

Next to the precursor polymer viscosity, the gelling time is more influential in the 10K/2K system compared to the 10K/5K and the 10K/7.5K systems. In the 10K/2K system, the low precursor polymer concentration of only  $210 \text{ g L}^{-1}$ , along with the lower linear-polymer molar mass of  $2000 \text{ g mol}^{-1}$  entails a low viscosity and therefore promotes cell migration in the precursor–gel droplets. In addition, the 11-minute gelling time in the phosphate buffer/DMEM mixture is two and a half times longer than the gelling times of the 10K/5K and the 10K/7.5K systems, which also allows for more distant cell migration in the pre-gel stage. As a result, the cells have more time and can migrate with a higher mobility in the pre-gel droplets to form clusters by the expression of junction proteins before gelation occurs.

**Figure 3-8g** shows the encapsulated cells in a microgel network of the 10K/2K type, visualized by 3D confocal imaging. For this purpose, the cell containing microgels are incubated in a solution of red-fluorescent sulforhodamine B. The red dye molecules adhere to the polymer network allowing visualization of the microgels and the green fluorescence stems from the GFP expressing cells. As can be seen, the cells are located in the center of the microgels. This is achieved by shaking of the cell containing droplets during the microfluidic steps, thereby preventing sedimentation of the cells in the templates.



### 3.3.4. Cell- and Vaterite-Containing Microgels

As a next step towards material development for ex vivo tests, co-encapsulation of both cells and vaterite particles is performed, using the modified microfluidic device shown in **Figure 3-1** (middle scheme). Besides the injection of the two polymeric building blocks (4-arm PEG-thiol and linear PEG-acrylate, solved in phosphate buffer), the independent encapsulation of both, vaterite particles suspended in ethylene glycol (3.42%(w/v)) as well as the cell suspension of osteoblasts (MG-63 GFP) and DMEM in droplets, is made possible. While the two polymeric building blocks react in a thiol–ene Michael addition and form three-dimensional polymer networks, the injected cells form cell clusters and vaterite particles agglomerate to larger granules distributed in these networks. Respective cell- and vaterite-containing microgels are observed with 2D confocal microscopy over a period of several days as shown in **Figure 3-9a** (above). Since the [4-arm PEG-thiol  $10000 \text{ g mol}^{-1}$  (10K)/linear PEG-acrylate  $2000 \text{ g mol}^{-1}$  (2K)] polymer composition is chosen, a high cell viability is ensured, which is investigated by microgel incubation in DMEM (1% Gl, 10% FBS, 1% P/S) at physiological conditions (37 °C, 5% CO<sub>2</sub> and humidity). The images of day 1 and day 5, respectively, show microgels with vaterite agglomerates visible as dark spots (transmission path), superimposed with the green fluorescence of cells expressing GFP (fluorescence path). Since the degree of microgel swelling increases with time due to hydrolysis sensitive ester groups in the polymer network, the microgel diameter increases from day 1 to day 5, until the complete gel degradation after about 7 days. Additionally, cells in the microgels form clusters by cell–cell interactions and settle after degradation of microgels at random points on the culture dish surface and adhere and proliferate. This is shown in the image of day 8, where the green fluorescence indicates high viable layer of adherent cells.

In comparison, the same number of cells as in the experiment above are encapsulated in the [4-arm PEG-thiol  $10000 \text{ g mol}^{-1}$  (10K)/linear PEG-acrylate  $2000 \text{ g mol}^{-1}$  (2K)] polymer system, using the microfluidic device shown in **Figure 3-1** (left and right side of the scheme) without further vaterite encapsulation. The respective microgels are also observed with 2D confocal microscopy, while incubating in DMEM (1% Gl, 10% FBS, 1% P/S) at physiological conditions (37 °C, 5% CO<sub>2</sub> and humidity) over a period of several days, as shown in **Figure 3-9b** (above). While the microgel diameters increase during the incubation period (day 1 to day 8) comparable to these of vaterite- and cell-containing microgels, cell clusters are formed by cell–cell interactions as well. Microgels degrade after approximately 7 days, and the released cell clusters adhere to the plastic and proliferate, which indicates a high cell viability (day 8).

In parallel to both microfluidic experiments, the general viability of the cells is monitored in triple control experiments over a period of three days. In **Figure 3-9a, b** (below), one experiment is shown each after 24 hours, 48 hours, and 72 hours of incubation. Visualization of the cell growth is achieved by 2D confocal microscopy, and the increasing intensity of green fluorescence indicates increasing cell growth.

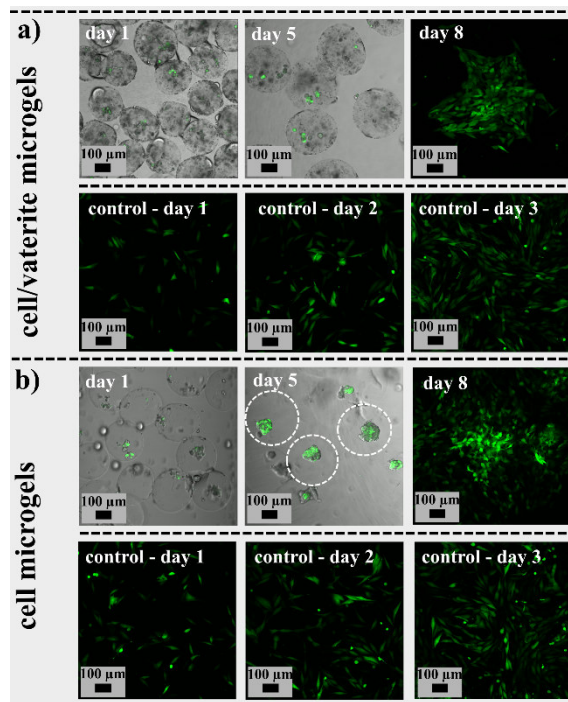


**Figure 3-9.** Viability of cells in vaterite-containing and vaterite-free microgels. (a) MG-63 GFP cells encapsulated in vaterite-containing microgels of the 10K/2K type and (b) in microgels of the 10K/2K type without further vaterite particle encapsulation. Cell viability is monitored in both experiments by 2D confocal microscopy over a period of eight days. Depicted are the days 1 and 5, where a superposition of transmission and fluorescence paths is shown, while day 8 is only shown in the fluorescence path. A control experiment is also performed by 2D confocal microscopy over a period of three days. Scale bars: 100  $\mu\text{m}$ .

In summary, cells encapsulated in both microgels with and without vaterite particles survive the microfluidic experiments and remain in the gels over a period of 7 days. This indicates that the polymer model system described in this study is highly suitable for further studies of bone tissue regeneration. Differences of cell growth are marginal, most likely due to differences in the gelation time of precursor polymers in droplets. In vaterite-free microgels, encapsulated cells are present as agglomerates in the microgels from day 1 and grow into large clusters during the 8-day incubation period in culture medium. These agglomerates consist of many cells. In vaterite- and cell-containing microgels, encapsulated cells are mostly present as smaller agglomerates up to single cells beginning at day 1. When vaterite particles are encapsulated, a slight increase of pH is observed in the reaction solution in the droplets,

which decreases the reaction time of polymer-network formation. Cells in the droplets are therefore impaired to form contacts and such remain as small agglomerates or single cells. Nevertheless, with increasing incubation time in culture medium, the cells grow into larger clusters. This is probably enabled by the small modulus of the (10K/2K) system ( $20.9 \pm 3.6$  kPa), which also decreases with increasing incubation time due to hydrolysis sensitive ester groups in the network. The resulting lower constriction to the encapsulated cells enables them to grow more easily. An additional favorable influence will probably have vaterite particles in the gels, since they are highly compatible for osteoblasts and promote cell growth as proven in previous studies.<sup>[19]</sup>

### 3.3.5. Microgel Degradation

An additional feature of the polymer networks used in this study are the hydrolysis-sensitive ester groups that promote polymer degradation in aqueous environments. After cleavage of these ester groups, there is a loss of network points in the polymer network and thereby an increase in the degree of swelling over time until complete degradation of the microgels occurs.

Investigation of the pH dependence of the polymer degradation is performed with microgels of the 10K/5K type by incubation in phosphate buffer at pH 5.0, 7.2, and 9.0 at room temperature. At acidic and neutral pH, no swelling is observed for 40 days ( $\Delta$ ,  $\circ$ ). By contrast, microgels in alkaline buffer solution (pH 9.0) show a marked ongoing swelling ( $\square$ ) and decompose completely after approximately one month. The increase of the degree of swelling of the gels in alkaline buffer solution is also illustrated by the white dashed outlines in **Figure 3-10a** (at days 0, 18, and 32). The respective swelling curves are depicted in **Figure 3-10b**. Since the goal is to use the gel capsules for biomedical applications, swelling measurements are also carried out in culture medium (DMEM with 1% Gl, 10% FBS and 1% P/S) at physiological conditions (5% CO<sub>2</sub> and 37 °C). Therefore, microgels of type 10K/2K, 10K/5K, and 10K/7.5K are incubated in the cell culture medium for several days. The respective swelling curves are depicted in **Figure 3-10c**. Compared to microgels stored in alkaline phosphate buffer at room temperature, microgels stored in cell culture medium at physiological conditions decompose at a higher rate (within one week). Reasons for the faster decomposition of the microgels in the culture medium at physiological conditions compared to phosphate buffer at room temperature are most likely due to the elevated temperature (37 °C instead of room temperature) and additional substances such as amino acids and proteins in

the cell culture medium. The accelerated degradation kinetics of microgels in the cell culture medium is considered to be an advantage, as it enables a rapid *in situ* vaterite particle release in pharmacological experiments. All three polymer systems (10K/2K, 10K/5K and 10K/7.5K) show similar degradation kinetics (■, ●, ▲), as their number of network points and thus the number of hydrolysis-sensitive ester groups are equal.

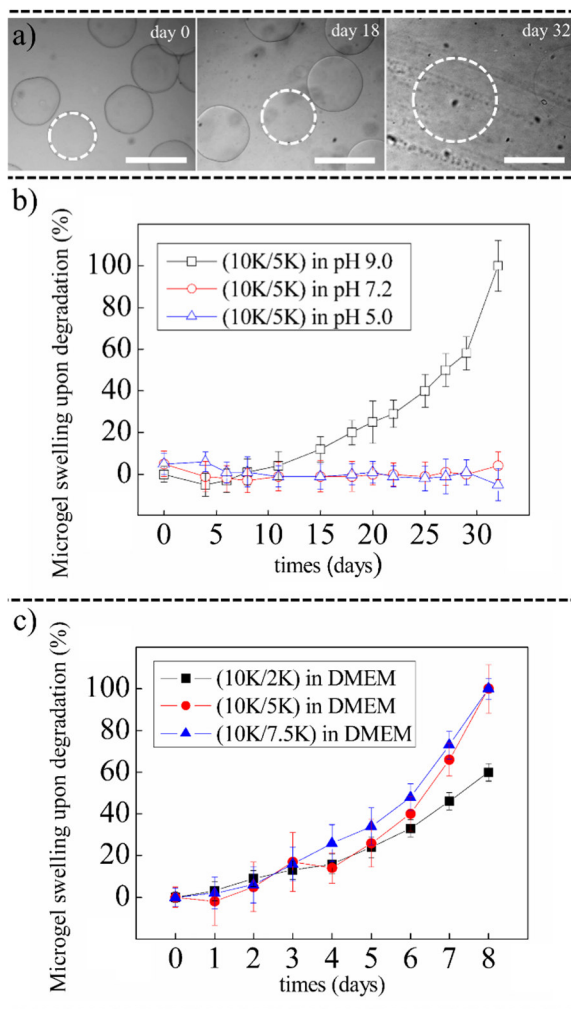


**Figure 3-10.** Degradation of microgels. (a) Stability of gels of type 10K/5K in phosphate buffer at pH 9.0 and room temperature, as observed over a period of 32 days. The increase of the degree of swelling of the gels is illustrated by the white dashed outlines. (b) Time-dependent microgel swelling in phosphate buffers at various pH values of 10K/5K microgels (all measurements are performed at room temperature; pH 9.0 (□), pH 7.2 (○), pH 5.0 (△)). (c) Time-dependent microgel swelling in culture medium (DMEM with 1% Gl, 10% FBS and 1% P/S) at physiological conditions (5% CO<sub>2</sub> and 37 °C) with microgels of the (10K/2K) (■), (10K/5K) (●), and (10K/7.5K) (▲) type. Gels show degradation in nearly one week. The measured data are linked by lines to guide the eye. Scale bars in panel (a): 300 μm.

### 3.4. Conclusion

We have developed a system that allows the combination of individual components under various conditions that can be used as a model for the formation of bone-regenerative and cell-containing materials. This model system can be used as an *in vitro* platform for the study of cellular metabolic processes in bone formation and may provide an *in vitro* foundation for novel tissue-regenerative therapies. The system uses hydrolysis-sensitive PEG-based model matrixes, formulated to monodisperse microgels to which additional components such as vaterite particles and cells are added using droplet-based microfluidics. The successful encapsulation of vaterite particles in these microgels as calcium precursors is confirmed by confocal Raman spectroscopy, and the transformation of vaterite to HCA is demonstrated using FT-IR spectroscopy measurements. Based on these results, we provide a powerful biopolymer-supported starting point for bone mineral growth and hence a basis for further investigation using this model system for tissue regeneration. Furthermore, osteoblast cells (MG-63 GFP) are successfully encapsulated into the microgels. This is demonstrated by confocal microscopy and cell studies show that these cells remain viable. Cells are present in microgels as agglomerates and show a greater viability than single cells under similar conditions. Rheological experiments demonstrate that the polymer system can be adjusted to form different network mesh sizes and to exhibit different gelation times and viscoelasticity, and that this can all result in differences in cell agglomeration and subsequent cell viability in the microgels. Initial studies with this model system have demonstrated that vaterite and cells can be co-encapsulated into the microgels and that a similar cell viability and high cell-compatibility is observed under these conditions compared to microgel containing only cells but no vaterite. Thus, this model system will be useful for examining and optimizing conditions for mineralization by osteoblasts in a microgel when a bone-forming substrate is available and for delivering bone-forming substrates to a target for tissue regeneration *in vivo*. The entire vaterite- and cell-containing microgel package becomes a model system for future *in vitro* and *in vivo* studies targeting bone tissue-regenerative applications.

### 3.5. Experimental Section

*Materials:* The precursor polymers 4-arm PEG-thiol 10K and linear PEG-acrylate 2K, 5K and 7.5K are purchased from JenKEM Technology USA. The Novec HFE-7500 fluid as well as HFE-7100 are purchased from 3M. Krytox 157-FSH is obtained from DuPont, GIPCO GlutaMAX Supplement and bovine serum albumin (BSA) labelled tetramethylrhodamine from Thermo Fisher Scientific, Optiprep from StemCell Technologies, ethylene glycol from ChemPur, 1H,1H,2H,2H-perfluoro-1-octanol, as well as 1H,1H,2H,2H-perfluorooctylsilan 97% from Alfa Aesar and sodium bicarbonate from Roth. The MG-63 GFP osteoblast cell line is obtained from the laboratory of one of the coauthors (RU). All other components such as DPBS-D8537, thionyl chloride,  $\alpha, \alpha, \alpha$ -trifluorotoluene, tris(hydroxymethylamino-methane), trypsin EDTA solution, DMEM high glucose-D5796, fetal bovine serum-F7524, Penicillin-Streptomycin-P4333, calcium chloride dihydrate and Sulforhodamine B are purchased from Sigma-Aldrich.

*Synthesis of PFPE–Tris Surfactant:* PFPE–Tris is synthesized in a two-step process using a method of Chiu et al.<sup>[39]</sup> In brief, Krytox 157-FSH (5 g, 0.69 mmol), dissolved in HFE-7100, is treated with thionyl chloride (0.81 g, 6.9 mmol) and stirred in an inert gas atmosphere at 50 °C for 24 h. The resulting mixture is concentrated using a cold distillation and then resolved in HFE-7100 (10 mL) and  $\alpha, \alpha, \alpha$ -trifluorotoluene (6 mL), followed by addition of tris(hydroxymethylaminomethane) (0.084 g, 0.69 mmol) under inert gas atmosphere. A refluxing reaction is conducted at 60 °C for 24 hours, and solvents were removed by cold distillation. The crude product is purified by dissolution in HFE-7100 and extraction against water. After cold distillation and vacuum drying, a waxy white product in a yield of 70% is obtained. The PFPE–Tris surfactant is analyzed by FT-IR spectroscopy with an FT/IR-470 instrument (JASCO Analytical Instruments). The results show a mode at 1683 cm<sup>-1</sup> that is assigned to the carboxylic acid amide, whereas the carboxylic acid tie of Krytox 157-FSH at 1683 cm<sup>-1</sup> is no longer observed. This indicates complete conversion of the Krytox 157-FSH. The intensity of both signals is weak due to the large perfluorinated residues.

*Fabrication of PDMS Devices:* Microfluidic devices are produced using photo- and soft lithography. In a first step, silicon wafers (MicroChemicals) are spin-coated (WS-650MZ-23NPP13 from Laurell) with a SU-8 2075 photoresist (MicroChem) and irradiated with UV-light (UV-Kub 2 from Kloe) to get negative reliefs of the microfluidic channels that are imprinted on to-scale photomasks. In a second step, PDMS is mixed with a crosslinker (Sylgard 184 elastomer kid from Dow Corning) at a ratio of 10:1 using a Thinky ARE-250 mixing setup, and

the mixture is applied to the patterned silicon wafer. After solidifying for 2 hours at 65 °C, devices are fabricated by peeling off the resulting relieved PDMS replica slabs and oxygen plasma bonding (electronic diener Plasma-Surface-Technology) of these onto glass slides. To increase fluorophilicity, the channels are coated with a solution of 2% 1H, 1H, 2H, 2H-perfluorooctylsilane in HFE-7100 for a few minutes and this is then removed by air-drying. The resulting channels have a uniform height of 180  $\mu\text{m}$  and a width of 150  $\mu\text{m}$  at the droplet forming cross-junction.

*Synthesis of Vaterite Particles:* Vaterite particles are synthesized using a method previously described.<sup>[19,30]</sup> Calcium chloride dihydrate (10 mM) is dissolved in ethylene glycol (100 mL) by sonication at 40 °C (Bandelin Sonorex Digitec). Sodium bicarbonate (20 mM) is dispersed in ethylene glycol (100 mL) by mechanical stirring and is added to the calcium chloride solution. The resulting dispersion is sonicated for 25 minutes at 40 °C. The precursor vaterite solution is analyzed by dynamic light scattering measurements (for details see SI **Figure S9-3**) to quantify the particle size, which denotes a polydisperse particle size distribution in the range of 200–600 nm. Subsequently, water (100 mL) is added to the vaterite precursor solution and the mixture is sonicated for another 5 minutes. Precipitated particles are separated from the turbid sol product by centrifugation (9000 rpm; 10 minutes), washed several times with water and ethanol and dried under high vacuum. The yield (60%) is determined gravimetrically.

*Vaterite-Containing Microgels:* Droplet templating is carried out with the PDMS device shown in **Figure 3-1** (on the left and right side of the scheme) by connecting the device to four syringe pumps (neMESYS Plugin) via polyethylene tubing (Intramedic Clay Adams Brand PE20) and plastic syringes. The precursor polymers 4-arm PEG-thiol 10000  $\text{g mol}^{-1}$  (300  $\text{g L}^{-1}$ ) and linear PEG-acrylate 5000  $\text{g mol}^{-1}$  (300  $\text{g L}^{-1}$ ) are dissolved in DPBS and then equally injected with a flow rate of 75  $\mu\text{L h}^{-1}$ , while 5% (w/v) of vaterite particles in ethylene glycol are injected in the middle channel with a flow rate of 25  $\mu\text{L h}^{-1}$ . The vaterite suspension is prepared with a sonotrode (Bandelin Sonopuls), whereby the mixture is homogenized for 10 minutes at an energy consumption of 19.3 kJ (ice cooling). These three fluids form a laminar co-flowing stream at the first cross-junction of the microchannel, which is broken to form monodisperse pre-microgel droplets with diameters of approximately 160  $\mu\text{m}$  in the second cross-junction by flow focusing with immiscible HFE 7500, which is injected at a flow rate of 2000  $\mu\text{L h}^{-1}$ . To stabilize the resulting droplets, 2wt% of PFPE–Tris surfactant is also added to the fluorinated oil. Droplets are purified with a 50% solution of 1H, 1H, 2H, 2H-perfluoro-1-octanol in HFE7500 in several trituration steps after 30–60 minutes. After this, the vaterite-containing microgels are transferred into phosphate buffer or water.

*Verification of Vaterite Stability in Microgels:* Confocal Raman microscopy is performed using a Witec 300 alpha R setup. Illumination of the sample is performed using a 532 nm excitation line from a single-mode frequency doubled Nd:YAG laser via a 100- $\mu\text{m}$  single-mode glass fibre. We use a Zeiss LD EC Epiplan-Neofluar 50x/0.55 objective and the laser power at the sample behind the objective is 12 mW. An edge filter is used to separate the Raman signal from the excitation line. Confocality of the Raman signal is achieved via a 50- $\mu\text{m}$  multi-mode fibre glass between microscope and the Raman spectrometer, where the fibre serves as a pin-hole. The Raman spectrometer is equipped with a holographic grating of 600 lines/mm. As detector, a Newton Andor EMCCD camera with 1600x200 pixels is used. With this configuration a spectral resolution of about 2  $\text{cm}^{-1}$  is obtained. All data sets are analyzed using Cluster Analysis and Non Negative Matrix Factorization.

*Vaterite Transformation to HCA:* The transformation of vaterite particles to HCA is analyzed using FT-IR spectroscopy. The first measurement is performed without further vaterite incubation in DPBS ( $t = 0$  h). The second measurement is performed after 48 h of vaterite incubation in DPBS (2  $\text{g L}^{-1}$ ) at 37 °C and shaking (150 rpm). Before analysis, the sample is washed three times with water and dried at high vacuum. The analysis of vaterite particles embedded in the polymer gel is carried out as follows: Two gels are prepared mixing 4arm PEG-thiol precursor polymers 10K and linear PEG-acrylate precursor polymers 5K, solved in phosphate buffer (each with a mass concentration of 300  $\text{g L}^{-1}$ ). 25wt% vaterite particles (based on the dry precursor polymer total mass) are added and mixed using a sonotrode. After 1 hour gelation time, the first gel is washed three times with water, freeze dried and analyzed with FT-IR spectroscopy. The second gel is incubated 48 hours in DPBS (2  $\text{g L}^{-1}$  vaterite in DPBS), then washed three times with water, freeze dried and analyzed with FT-IR spectroscopy. The analysis of the pure gel ensured analogue to the measurements of gels with vaterite.

*Cell-Containing Microgels:* Droplet templating is carried out with the PDMS device shown in **Figure 3-1** (on the left and right side of the scheme) by connecting the device to four syringe pumps (neMESYS Plugin) via polyethylene tubing (Intramedic Clay Adams Brand PE20) and plastic syringes. HFE 7500 and PFPE-Tris surfactant (2wt%) are mixed and injected with a flow rate of 2000  $\mu\text{L h}^{-1}$ . The precursor polymers 4-arm PEG-thiol 10000  $\text{g mol}^{-1}$  (300  $\text{g L}^{-1}$ ) and linear PEG-acrylate 2000  $\text{g mol}^{-1}$ , 5000  $\text{g mol}^{-1}$  or 7500  $\text{g mol}^{-1}$  (120  $\text{g L}^{-1}$ , 300  $\text{g L}^{-1}$  or 450  $\text{g L}^{-1}$ ) are dissolved in DPBS and then equally injected with a flow rate of 75  $\mu\text{L h}^{-1}$ . Osteoblast cells (MG-63 GFP) are also injected in the middle channel with a flow rate of 75  $\mu\text{L h}^{-1}$ . The cells are cultivated in petri dishes with an area of 11.9  $\text{cm}^2$  and are



detached from the dishes for microfluidic experiments. For that purpose, cells are rinsed with DPBS, incubated with trypsin EDTA solution to release the cells and then centrifuged for 5 minutes at 1000 rpm. The resulting cell pellet is resuspended in DMEM (1% Gl., 10% FBS, 1% P/S) and 15% OptiPrep (0.333 mL). In each experiment, four petri dishes are used with a cell population density of approximately 80%, which corresponds to  $3.13 \times 10^7$  cells per microfluidic experiment. Cell counting is performed with a Neubauer counting chamber. The cell suspension is injected in the microfluidic devices, whereby the cell containing droplets are collected at 37 °C. Depending on the polymer system, microgels are then purified after 30–60 minutes with a 50% solution of 1H, 1H, 2H, 2H-Perfluoro-1-octanol in HFE7500 in several trituration steps and then transferred into DMEM (1% Gl., 10% FBS, 1% P/S). Cell-containing microgels are incubated over several weeks at 5% CO<sub>2</sub> and 37 °C and are analyzed by optical microscopy (Zeiss Axio) and 2D, as well as 3D confocal microscopy.

*Cell- and Vaterite-Containing Microgels:* Droplet templating is carried out with the PDMS device shown in **Figure 3-1** (in the middle of the scheme) by connecting the device to five syringe pumps (neMESYS Plugin and Harvard pump) via polyethylene tubing (Intramedic Clay Adams Brand PE20) and plastic syringes. HFE 7500 and PFPE–Tris surfactant (2wt%) are mixed and injected with a flow rate of 3000  $\mu\text{L h}^{-1}$ . The precursor polymers 4-arm PEG-thiol 10000  $\text{g mol}^{-1}$  (300  $\text{g L}^{-1}$ ) and linear PEG-acrylate 2000  $\text{g mol}^{-1}$  (120  $\text{g L}^{-1}$ ) are dissolved in DPBS and then equally injected with a flow rate of 75  $\mu\text{L h}^{-1}$ . Additionally, 3.42% (w/v) of vaterite particles in ethylene glycol are injected with a flow rate of 50  $\mu\text{L h}^{-1}$  to obtain a total vaterite concentration of 3.42% (w/v) in microgels, while osteoblast cells (MG-63 GFP) in DMEM are injected with a flow rate of 75  $\mu\text{L h}^{-1}$ . The cells are cultivated in petri dishes with an area of 11.9  $\text{cm}^2$  and are detached from the dishes for microfluidic experiments. For that purpose, cells are rinsed with DPBS, incubated with trypsin EDTA solution to release the cells and then centrifuged for 5 minutes at 1000 rpm. The resulting cell pellet is resuspended in DMEM (1% Gl., 10% FBS, 1% P/S) and 15% OptiPrep (0.333 mL). In each experiment, four petri dishes are used with a cell population density of approximately 80%, which corresponds to  $3.13 \times 10^7$  cells per microfluidic experiment. Cell counting is performed with a Neubauer counting chamber. After injection, the vaterite- and cell containing droplets are collected at 37 °C and then purified after 30–60 minutes with a 50% solution of 1H, 1H, 2H, 2H-Perfluoro-1-octanol in HFE7500 in several trituration steps and then transferred into DMEM (1% Gl., 10% FBS, 1% P/S). Vaterite and cell-containing

## CHAPTER I

microgels are incubated over several weeks at 5% CO<sub>2</sub> and 37 °C and are analyzed by optical microscopy (Zeiss Axio) and 2D, as well as 3D confocal microscopy.

*Testing of Gels for the Presence of Endotoxin:* The rapid induction of E-selectin on endothelial cells in culture after exposure to endotoxin (LPS) has been shown to be a very sensitive method to detect the presence of endotoxin in solutions at femtogram levels.<sup>[31,32]</sup> This method is used to examine gels made from the individual precursor molecules to show that they are free of endotoxin. Vaterite synthesis described in this publication has been previously shown to be free of endotoxin.<sup>[17]</sup> Briefly, the individual precursors (4-arm PEG-thiol 10000 g mol<sup>-1</sup> (160 g L<sup>-1</sup>) and linear PEG-acrylate 5000 g mol<sup>-1</sup> (160 g L<sup>-1</sup>) in phosphate buffer) are combined to form a gel in a microcentrifuge tube. After polymerization, 1 mL of DPBS is added to the tube and incubated for 24 hours at 37 °C. After 24 hours, the supernatant is removed from the gels and an aliquot (20 µL) is added to HUVEC cells growing in one well of an 8-well chamber slide. The gel remaining in the tube is removed via pipetting and placed onto HUVEC cells in a second well in the chamber slide with fresh media. Cells are also exposed to 1 µg mL<sup>-1</sup> of endotoxin (LPS, Sigma) or left untreated (negative control) in additional wells. After 4 hours, cells are washed 2x with PBS and fixed with paraformaldehyde and then stained with antibody against E-selectin (1:100 E-selectin, Monosan (M6010), Netherlands). After 1 hour, cells are washed 4x with PBS and then the secondary antibody is added (1:1000, anti-mouse Alexa Fluor 488, Molecular Probes) and incubated at room temperature. After 1 hour, cells are washed and Hoechst Dye 33342 (1:10,000 in PBS, Molecular Probes) is added to stain the nuclei. After 5 minutes, cells are washed 2x with PBS, mounting medium is added (Fluoroshield, ImmunoBioScience Corp.) and cells are examined by fluorescence microscopy.

*Toxicity of Gels:* The viability of cells is measured by the addition of resazurin to cells in culture in the presence and absence of gels (4-arm PEG-thiol 10000 g mol<sup>-1</sup> (300 g L<sup>-1</sup>) and linear PEG-acrylate 5000 g mol<sup>-1</sup> (300 g L<sup>-1</sup>) in phosphate buffer). Resazurin is used to measure the metabolic activity of living cells which is converted by a redox reaction to the fluorescent compound resorufin and this can be measured in a fluorescent ELISA reader. Gels are added to wells in a 96-well plate. After polymerization, 20,000 cells/96 well (MG-63) are added to the wells and incubated for 24 hours and then 20 µL of resazurin stock solution (12 mg resazurin in 100 mL Hanks' Balanced Salt Solution with Ca<sup>2+</sup> and Mg<sup>2+</sup> (Sigma-Aldrich) is added and incubated for a further 2 hours at 37 °C. After this, 100 µL is removed from each well and placed into a new 96-well plate and examined in an ELISA reader (TECAN Spark

10M, 530–570 nm excitation and 580–100 nm emission). The amount of resorufin produced by cells exposed to gels is compared to unexposed cells set at 100%.

*Rheology Measurements:* To compare the gelation time and stiffness of the several polymer systems investigated in this study (10K/2K, 10K/5K and 10K/7.5K), time-dependent rheology measurements are carried out using an Anton Paar modular compact rheometer of type MCR 302 (Anton Paar, Graz, Austria) equipped with a plate–plate measuring system PP08, with a radius of 8 mm and a plate–plate gap distance of 0.4 mm at 21 °C. For all measurements, a solvent trap is used to suppress evaporation of the solvent. The samples are prepared by mixing the precursor polymers (4arm PEG-thiol 10K (300 g L<sup>-1</sup>) and linear PEG-acrylate 2K (120 g L<sup>-1</sup>), 5K (300 g L<sup>-1</sup>) or 7.5K (450 g L<sup>-1</sup>), dissolved in phosphate buffer, DMEM, or a mixture of both (ratio 6:1) prior to beginning the measurements. For this purpose, 18 µL of sample is applied. Experiments are carried out at a constant shear amplitude of 1% and a shearing frequency of 6.28 rad s<sup>-1</sup>. Measurements in the linear-viscoelastic (LVE) regime are confirmed by amplitude sweeps, whereby the frequency remained constant at 6.28 rad s<sup>-1</sup> and the amplitude varied between 0.01 and 100% deformation. Also, frequency sweeps are done in a frequency range of 100–0.1 rad s<sup>-1</sup>, at a fixed amplitude of 1% within the LVE regime of the sample.

*FCS:* Experiments are done with a Leica TCS-SP8 AOBS SMD microscope and a SymPhoTime 64 analysis software from PicoQuant. Measurements are performed with a HCPLAPO CS2 63x/1.20 water objective, an argon laser with 20% intensity, and an HyD SMD 1 detector. For sample preparation, gels (4-arm PEG-thiol 10000 g mol<sup>-1</sup> (300 g L<sup>-1</sup>) and linear PEG-acrylate 2000 g mol<sup>-1</sup> (120 g L<sup>-1</sup>), 5000 g mol<sup>-1</sup> (300 g L<sup>-1</sup>) and 7500 g mol<sup>-1</sup> (450 g L<sup>-1</sup>) in phosphate buffer) are prepared in an eight-well- plate (Ibidi). After gelation, gels are incubated in a dye solution at room temperature overnight. A 6-nM solution of sulforhodamine B is used, as well as a 6-nM solution of bovine serum albumin (BSA) labelled with tetramethyl rhodamine (both prepared in DPBS). All measurements are carried out in the gel volume, whereby five points for each gel are selected. For fitting with SymPhoTime 64 analysis software, the 3D-Gaussian triplet model is selected. Calibration is performed with a sulforhodamine B solution (6-nM) in phosphate buffer, with a diffusion coefficient of 440 µm<sup>2</sup> s<sup>-1</sup> (22 °C).<sup>[34]</sup>

*Swelling Measurements:* Droplet templating is carried out with the PDMS device shown in **Figure 3-1** (on the left and right side of the scheme) by connecting the device to four syringe pumps (neMESYS Plugin) via polyethylene tubing (Intramedic Clay Adams Brand PE20)

## CHAPTER I

and plastic syringes. The precursor polymers 4-arm PEG-thiol  $10000 \text{ g mol}^{-1}$  ( $300 \text{ g L}^{-1}$ ) and linear PEG-acrylate  $2000 \text{ g mol}^{-1}$ ,  $5000 \text{ g mol}^{-1}$  or  $7500 \text{ g mol}^{-1}$  ( $120 \text{ g L}^{-1}$ ,  $300 \text{ g L}^{-1}$  or  $450 \text{ g L}^{-1}$ ) are dissolved in phosphate buffer and then equally injected with a flow rate of  $75 \mu\text{L h}^{-1}$ , while pure DPBS is injected in the middle channel with a flow rate of  $25 \mu\text{L h}^{-1}$ . The microgels are then purified after 1 hour with a 50% solution of 1H, 1H, 2H, 2H-Perfluoro-1-octanol in HFE7500 in several trituration steps and then transferred into DPBS or DMEM (1% Gl, 10% FBS, 1% P/S). Microgels are incubated in diverse DPBS solutions, which differ from each other in the pH value. Phosphate buffer (pH 5) is prepared by acidifying DPBS (pH 7.2) with HCl, while phosphate buffer of pH 9 is prepared by adding aqueous NaOH solution. The swelling behavior of microgels is then observed by optical microscopy (Zeiss Axio) and ImageJ is used to determine the size of the microgels. All measurements are done at room temperature. In addition, measurements are performed at physiological conditions. For this purpose, microgels are transferred into DMEM (1% Gl, 10% FBS, 1% P/S) and then incubated for several days at 5%  $\text{CO}_2$  and  $37 \text{ }^\circ\text{C}$ . The swelling behavior of the microgels is evaluated as described above.

*Statistical Analysis:* Quantitative data and sample size of cell viability results are given as mean  $\pm$  standard deviation (SD) and numbers (n), respectively. Excel from Microsoft and Origin from OriginLab publishes are the software used for statistical analysis.

### 3.6. Literature

- [1] M. R. Iaquinta, E. Mazzoni, M. Manfrini, A. D'Agostino, L. Trevisiol, R. Nocini, L. Trombelli, G. Barbanti-Brodano, F. Martini, M. Tognon, *Int. J. Mol. Sci.* **2019**, *20*, 618.
- [2] K. Zhang, S. Wang, C. Zhou, L. Cheng, X. Gao, X. Xie, J. Sun, H. Wang, M. D. Weir, M. A. Reynolds, N. Zhang, Y. Bai, H. H. K. Xu, *Bone Res.* **2018**, *6*, 31.
- [3] Y. Zeng, J. Hoque, S. Varghese, *Acta Biomater.* **2019**, *93*, 152.
- [4] J. Scheinpflug, M. Pfeiffenberger, A. Damerau, F. Schwarz, M. Textor, A. Lang, F. Schulze, *Genes* **2018**, *9*, 247.
- [5] K. N. Tu, J. D. Lie, C. K. V. Wan, M. Cameron, A. G. Austel, J. K. Nguyen, K. Van, D. Hyun, *P T* **2018**, *43*, 92.
- [6] V. Paspaliaris, G. Kolios, *Stem Cells Int.* **2019**, *2019*, 1.
- [7] M. Dang, L. Saunders, X. Niu, Y. Fan, P. X. Ma, *Bone Res.* **2018**, *6*, 25.
- [8] X. Li, B. Cho, R. Martin, M. Seu, C. Zhang, Z. Zhou, J. S. Choi, X. Jiang, L. Chen, G. Walia, J. Yan, M. Callanan, H. Liu, K. Colbert, J. Morrissette-McAlmon, W. Grayson, S. Reddy, J. M. Sacks, H.-Q. Mao, *Sci. Transl. Med.* **2019**, *11*, 490.
- [9] Y. Wu, L. Wang, B. Guo, P. X. Ma, *J. Mater. Chem. B* **2014**, *2*, 3674.
- [10] R. Dong, X. Zhao, B. Guo, P. X. Ma, *ACS Appl. Mater. Interfaces* **2016**, *8*, 17138.
- [11] B. Guo, J. Qu, X. Zhao, M. Zhang, *Acta Biomater.* **2019**, *84*, 180.
- [12] Y. Wu, L. Wang, B. Guo, P. X. Ma, *ACS Nano* **2017**, *11*, 5646.
- [13] D. Shi, J. Shen, Z. Zhang, C. Shi, M. Chen, Y. Gu, Y. Liu, *J. Biomed. Mater. Res. - Part A* **2019**, *107*, 2040.
- [14] D. Anandan, S. M. Stella, N. Arunai Nambiraj, U. Vijayalakshmi, A. K. Jaiswal, *J. Biomed. Mater. Res., Part A* **2018**, *106*, 3267.
- [15] S. Chen, Y. Shi, X. Zhang, J. Ma, *J. Biomed. Mater. Res.*, **2019**, *107*, 2512.
- [16] W. Zheng, X. Jiang, *Acc. Chem. Res.* **2018**, *51*, 3166.
- [17] R. J. Havlik, *Plast. Reconstr. Surg.* **2002**, *110*, 1176.
- [18] R. Schröder, H. Pohlitz, T. Schüller, M. Panthöfer, R. E. Unger, H. Frey, W. Tremel, *J. Mater. Chem. B* **2015**, *3*, 7079.

## CHAPTER I

- [19] R. Schröder, L. Besch, H. Pohlit, M. Panthöfer, W. Roth, H. Frey, W. Tremel, R. E. Unger, *J. Tissue Eng. Regen. Med.* **2018**, *12*, 1754.
- [20] T. E. L. Douglas, A. Łapa, K. Reczyńska, M. Krok-Borkowicz, K. Pietryga, S. K. Samal, H. A. Declercq, D. Schaubroeck, M. Boone, P. Van der Voort, K. De Schamphelaere, C. V Stevens, V. Bliznuk, L. Balcaen, B. V Parakhonskiy, F. Vanhaecke, V. Cnudde, E. Pamula, A. G. Skirtach, *Biomed. Mater.* **2016**, *11*, 065011.
- [21] E. Kapourani, F. Neumann, K. Achazi, J. Dervede, R. Haag, *Macromol. Biosci.* **2018**, *18*, 1800116.
- [22] B. V. Slaughter, S. S. Khurshid, O. Z. Fisher, A. Khademhosseini, N. A. Peppas, *Adv. Mater.* **2009**, *21*, 3307.
- [23] R. Langer, J. P. Vacanti, *Science* **1993**, *260*, 920.
- [24] Y. Lu, W. Zhang, J. Wang, G. Yang, S. Yin, T. Tang, C. Yu, X. Jiang, *Int. J. Oral Sci.* **2019**, *11*, 17.
- [25] S. Seiffert, *ChemPhysChem* **2013**, *14*, 295.
- [26] P. De Vos, H. A. Lazarjani, D. Poncelet, M. M. Faas, *Adv. Drug Delivery Rev.* **2014**, *67–68*, 15.
- [27] T. Rossow, J. A. Heyman, A. J. Ehrlicher, A. Langhoff, D. A. Weitz, R. Haag, S. Seiffert, *J. Am. Chem. Soc.* **2012**, *134*, 4983.
- [28] S. Hackelbusch, T. Rossow, D. Steinhilber, D. A. Weitz, S. Seiffert, *Adv. Healthc. Mater.* **2015**, *4*, 1841.
- [29] D. Steinhilber, T. Rossow, S. Wedepohl, F. Paulus, S. Seiffert, R. Haag, *Angew. Chem., Int. Ed.* **2013**, *52*, 13538.
- [30] T. Schüler, W. Tremel, *Chem. Commun.* **2011**, *47*, 5208.
- [31] R. E. Unger, *Adv. Biomater. Devices Med.* **2014**, *1*, 38.
- [32] R. E. Unger, K. Peters, A. Sartoris, C. Freese, C. J. Kirkpatrick, *Biomaterials* **2014**, *35*, 3180.
- [33] S. Hackelbusch, T. Rossow, H. Becker, S. Seiffert, *Macromolecules* **2014**, *47*, 4028.
- [34] P.-O. Gendron, F. Avaltroni, K. J. Wilkinson, *J. Fluoresc.* **2008**, *18*, 1093.
- [35] J. Wu, C. Zhao, W. Lin, R. Hu, Q. Wang, H. Chen, L. Li, S. Chen, J. Zheng, *J. Mater. Chem. B* **2014**, *2*, 2983.

- [36] T. P. Kraehenbuehl, P. Zammaretti, A. J. Van der Vlies, R. G. Schoenmakers, M. P. Lutolf, M. E. Jaconi, J. A. Hubbell, *Biomaterials* **2008**, *29*, 2757.
- [37] D. Loessner, K. S. Stok, M. P. Lutolf, D. W. Hutmacher, J. A. Clements, S. C. Rizzi, *Biomaterials* **2010**, *31*, 8494.
- [38] E. E. Hui, S. N. Bhatia, *Proc. Natl. Acad. Sci. USA* **2007**, *104*, 5722.
- [39] Y.-L. Chiu, H. F. Chan, K. K. L. Phua, Y. Zhang, S. Juul, B. R. Knudsen, Y.-P. Ho, K. W. Leong, *ACS Nano* **2014**, *8*, 3913.

## 4. Chapter II

●●● ‘Rational Design of Thermoresponsive Microgel  
Templates with Polydopamine Surface Coating  
for Microtissue Applications’

The results of the following chapter (p. 88–119) and the Supporting Information (p. 148–163) were published at *Macromolecular Bioscience* on August 3, 2021.

**Elena Stengelin,<sup>1</sup>** [REDACTED]

[REDACTED]\*,

*Macromol. Biosci.* **2021**, *21*, 2100209.

<sup>1</sup> Johannes Gutenberg-University Mainz, Department of Chemistry, Duesbergweg 10–14, D-55128 Mainz, Germany

<sup>2</sup> [REDACTED]

<sup>3</sup> [REDACTED]

\* Corresponding author

Reprinted with permission from *Macromol. Biosci.* **2021**, *21*, 2100209.

© 2021 The Authors. *Macromolecular Bioscience* published by Wiley-VCH GmbH

### 4.1. Specific Summary

Analogous to the study on microtissue-based in vitro model systems for bone regeneration applications (*Chapter I: “Bone Scaffolds Based on Degradable Vaterite/PEG-Composite Microgels”*), the following study addresses the use of microscopic in vitro model platforms as potential alternatives to animal testing. The work focuses on mimicking the heterogeneous and complex nature of biological microtissues such as the blastula in embryogenesis, mammary



glands, or the alveolar epithelium using volume-switchable core–shell microgel platforms. These platforms are intended to be used for 3D cell cultivation applications and are tuned to the specific requirements of different in vivo tissues by selective tailoring the multiparametric material functionalities.

In this context, special attention is paid to the material selection in the form of thermoresponsive and long-term stable poly(*N*-isopropylacrylamide) (PNIPAAm) and its processability in microfluidics. Regarding the adaptivity, different amounts of hydrophilic *N*-hydroxyethylacrylamide are incorporated into the microgels to tune their mechanical strength. To improve the cell adhesive properties of the PNIPAAm microgels and to increase their biocompatibility, the surface of the microgels is modified with polydopamine. Finally, the use in 3D cell culture applications is demonstrated by investigating the cell growth on macroscopic hydrogels, single microgel templates as well as cell/microgel agglomerates.

The personal contribution to the publication was the project development, interdisciplinary project coordination, lab work (polymer basis development; microgel preparation by microfluidics; temperature-dependent swelling measurements of microgels; temperature-dependent rheology measurements to analyze hydrogel elasticity; analysis of microgel properties at physiological conditions; polydopamine surface coating of macro- and microgels; analysis of polydopamine surface coating by FT-IR spectroscopy measurements; collagen coating of microgels; cell experiments (cell adhesion on hydrogels and on single microgel templates); light microscopy and confocal laser scanning microscopy imaging; sample preparation for <sup>1</sup>H MAS NMR spectroscopy, SEM measurements, confocal Raman microscopy, and cell spheroid growth experiments), data analysis, writing and illustration of the manuscript.

### **Acknowledgements**

Parts of the results of this study were acquired with a confocal laser scanning microscope funded in part by the Major Research Instrumentation Program of the German Research Foundation under grant No. INST 247/878-1 FUGG. The authors wish to thank [REDACTED] [REDACTED] for providing osteoblasts expressing GFP (MG-63 GFP). Further thanks go to [REDACTED] for practical support and to [REDACTED] [REDACTED] for photography. [REDACTED] thanks the European Research Council for the ERC Starting Grant ARTIST (# 757593).

## 4.2. Introduction

Microtissue engineering is a significant development in the field of 3D cell culture technology, as the design of microtissue platforms reflects the diversity and complexity of in vivo environments, thereby providing excellent alternatives to animal testing. As animal experiments face ethical and moral concerns, they are increasingly blocked by law and need to be reduced, replaced, and refined according to the 3R concept by Russel and Burch from 1959.<sup>[1]</sup> Classical two-dimensional (2D) cell cultures may appear to be such a substitute, but they only inadequately reflect the complex in vivo conditions.<sup>[2,3]</sup> To overcome that limitation, the development of 3D cell culture in vitro models is needed, especially such models that mimic the hierarchical structure of in vivo environments in a simplifying manner.

In this context, an increasing amount of research deals with the fabrication of microtissue-based spheroidal 3D in vitro models using scaffold-free and scaffold-assisted methods. While the scaffold-free method does not require any matrix at all, the scaffold-promoted method uses additional hydrogel-based matrix elements to form cell spheroids. For this purpose, several research studies are especially focused on the encapsulation of cells in poly(ethylene glycol) (PEG)-based microgels. In these microgels, cells preferentially interact with other cells, forming cell spheroids due to the antifouling property of PEG.<sup>[4,5]</sup> Compared to 2D cell culture models, these cell spheroids effectively mimic a 3D environment by growing in a network-like structure instead of growing on a flat substrate. However, these cells also grow without control in all three dimensions, ignoring the intrinsically defined and hierarchically structured in vivo environment. In view of the general motivation of replacing animal experiments by synthetic platforms, a better-defined basis of 3D in vitro models is therefore necessary, which additionally takes into account the shape, the nature and the mechanical properties of in vivo tissues to best mimic the in vivo environment. To address this issue and to contribute to that basis, we aim at a rational design of microgel-based templates with functional and at the same time cell-adhesive properties for the engineering of complex microtissue constructs.

An appropriate material for our intent is the stimuli responsive poly(*N*-isopropylacrylamide) (PNIPAAm). Hydrogels made from this polymer exhibit a reversible volume phase transition (VPT) in the physiological temperature range and undergo changes in solubility and swelling, which facilitates the imitation of the structure, properties, and microenvironment of native tissue.<sup>[6–8]</sup> By incorporation of comonomers into the PNIPAAm network, the VPT temperature can be further tuned to higher or lower values depending on the hydrophilicity and the

amount of the comonomer.<sup>[9]</sup> Since PNIPAAm-based microgels can be easily shaped via droplet-based microfluidics, various temperature-dependent microgels can be obtained, which differ in size, mechanical strength, and opacity.<sup>[10]</sup> As a result, this approach enables the rational material design of specific and tuneable microgel-based microcarrier cores and provides a good platform for precisely directed microtissue templating.

The other key point for the successful implementation of the microgel templates is to increase their cell affinity. In general, PNIPAAm hydrogels show a temperature-dependent cell affinity, such that above the VPT temperature, cells show increased cell adhesion and proliferation on PNIPAAm-coated culture dishes, whereas when the temperature is decreased, the cells are detached from the culture dish.<sup>[11]</sup> Hence, to make the templates more versatile, temperature-independent cell adhesion on the PNIPAAm microgels needs to be supported. To address this objective, we use a polydopamine (PDA) coating, which is a cost-effective and biocompatible solution providing potentially high cell affinity and maintaining the microgels' VPT properties.<sup>[12]</sup> Moreover, PDA adheres to a variety of surfaces with strong binding forces, as Messersmith's group has demonstrated.<sup>[13,14]</sup> In a preliminary work to our study, Zhang et al. have adapted this method for producing PDA-coated PNIPAAm-based nanogels.<sup>[15]</sup> The approach translates well to PNIPAAm-based microgels, thus enabling the synthesis of highly cell-affine and multifunctional core-shell microcarriers.

Based on this strategy, this work presents the manufacturing of well-designed core-shell microgels, which are suitable templates for fine-structured microtissues mainly due to their dual functionality (VPT properties of the core and cell growth-promoting properties of the shell). Our approach involves three steps, as shown in **Figure 4-1**: The first step (1) focuses on the microgel design and synthesis, the second step (2) on the PDA surface coating of the microgels to increase their cell adhesion properties, and the third step (3) on the cell growth experiments on microgels. For this purpose, we use a systematic parameter control and enable targeted tuning of the microgel properties at multiple levels. On a nanoscopic scale, we choose temperature-sensitive and cell-affine materials, while on a microscopic level, the templating of the PNIPAAm-based microgels is performed by droplet-based microfluidics and subsequent PDA-surface coating. At the same time, the microgel core properties, such as their size and mechanical strength, are controlled at the mesoscopic level by additional incorporation of the hydrophilic comonomer *N*-hydroxyethylacrylamide (HEAM). Based on this systematic approach, our platform offers a great variety of well-designed PNIPAAm/HEAM core-shell microgel templates and provides a promising basis for complex and

advanced 3D in vitro cell culture systems with deep understanding on a conceptual and practical level as alternative for animal testing.

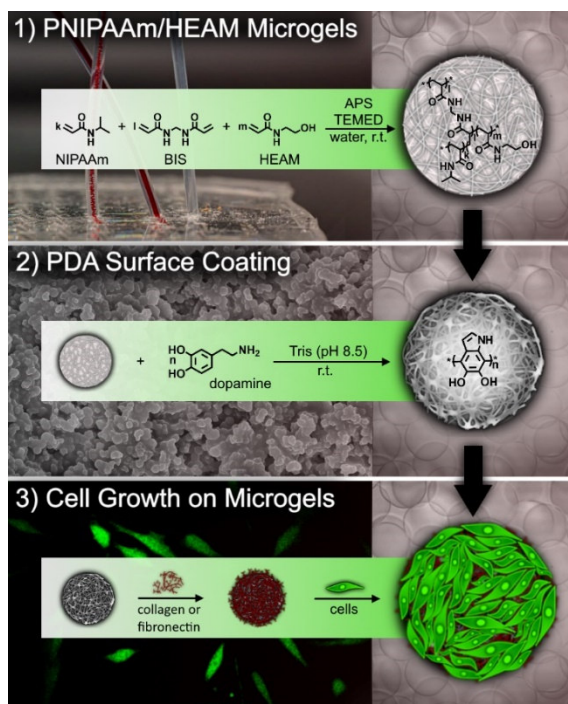


**Figure 4-1.** PDA-coated PNIPAAm/HEAM-based core-shell microgels as templates for microtissue applications in three steps: (1) PNIPAAm/HEAM microgel (core) synthesis by droplet-based microfluidics. The microgel network is based on NIPAAm, *N,N'*-methylenebisacrylamide (BIS) crosslinker and different amounts of HEAM comonomer, which react in a radical polymerization to form stable networks initiated by *N,N,N',N'*-tetramethylethylenediamine (TEMED) and ammonium persulfate (APS). (2) PDA surface modification of PNIPAAm/HEAM-based microgels (shell) to increase the microgels' cell adhesiveness. (3) Cell coating experiments of PNIPAAm/HEAM-PDA microgels improved by previous collagen or fibronectin coating of the microgels.

## 4.3. Results & Discussion

### 4.3.1. PNIPAAm/HEAM Microgels

#### 4.3.1.1. Polymer Basis

PNIPAAm is chosen to provide a suitable polymer basis for our work due to its thermoresponsiveness in water, by which PNIPAAm hydrogels exhibit temperature-dependent mechanical properties that can be further tuned by incorporating comonomers. Moreover, due to their hydrophilic nature, PNIPAAm-based materials mimic the extracellular matrix (ECM) well and provide a stable environment as a basis for potential 3D microtissue engineering. Hence, we focus on the development of PNIPAAm-based 3D templates that are designed at several levels. On a nanoscopic level, hydrogels are prepared using NIPAAm monomers and *N,N'*-methylenebisacrylamide (BIS) as a crosslinker. Dissolved in water and initiated by ammonium persulfate (APS) and *N,N,N',N'*-tetramethylethylenediamine (TEMED), these molecules react with each other in a radical polymerization and crosslink to form stable gels at room temperature.<sup>[16]</sup> Moreover, by incorporating HEAM as a comonomer into the PNIPAAm network, the mechanical properties of the PNIPAAm system can be altered. To analyze the influence of the comonomer on the thermoresponsive PNIPAAm properties, we investigate three different hydrogel systems that differ in the amount of HEAM. Specifically, 2.5 mol%, 7.5 mol%, and 12.5 mol% of HEAM content are considered, while the NIPAAm content is adjusted accordingly, and the BIS content remains constant at 1 mol%.

#### 4.3.1.2. Comonomer Content in PNIPAAm/HEAM-Based Hydrogels

To understand and analyze the HEAM influence on our thermoresponsive hydrogel properties, it is necessary to determine the actual comonomer content in the PNIPAAm networks. For this purpose, we investigate the HEAM content in the 2.5 mol%, 7.5 mol%, and 12.5 mol% PNIPAAm/HEAM polymer networks as well as the HEAM-free PNIPAAm network (0 mol%) swollen in D<sub>2</sub>O using quantitative <sup>1</sup>H Magic Angle Spinning NMR spectroscopy (<sup>1</sup>H MAS NMR). In the case of gels (as well as semisolid matrixes), the anisotropic interactions like dipole–dipole couplings, quadrupole couplings, and anisotropy of the chemical shift are partially averaged due to the limited mobility of molecules induced by the solvent in the gel. To further reduce the line-broadening, and therewith to improve the resolution,

only low spinning speeds of a few kilohertz are needed. At these conditions, the recorded  $^1\text{H}$  MAS NMR spectra mimic those obtained in solution and provide comparable resolution. The investigated polymer compositions are listed in **Table 4-1**, while the full  $^1\text{H}$  MAS NMR spectra are shown in **Figure 4-2**.

**Table 4-1.** Composition of the 0 mol%, 2.5 mol%, 7.5 mol%, and 12.5 mol% PNIPAAm/HEAM polymer networks. The amounts of NIPAAm, HEAM, and BIS in the respective systems are indicated as  $x$  in mol%. Proton ratios (proton ratio<sub>NMR</sub>) of NIPAAm (H-c) and HEAM (H-f, H-e) comonomers are calculated as proton ratio<sub>NMR</sub> =  $(A_{\text{NIPAAm}} \cdot (A_{\text{HEAM}})^{-1} \cdot 4\text{H})$ , using the proton integrals of NIPAAm ( $A_{\text{NIPAAm}}$ ) and HEAM ( $A_{\text{HEAM}}$ ), experimentally determined by  $^1\text{H}$  MAS NMR spectroscopy (**Figure S9-5** and **Table S9-1**). For comparison, the molar ratios of PNIPAAm ( $n_{\text{NIPAAm}}$ ) and HEAM ( $n_{\text{HEAM}}$ ) comonomers are calculated as molar ratio =  $(n_{\text{NIPAAm}} \cdot (n_{\text{HEAM}})^{-1})$  (**Table S9-2**).

	$x_{\text{NIPAAm}}$ [mol%]	$x_{\text{HEAM}}$ [mol%]	$x_{\text{BIS}}$ [mol%]	proton ratio <sub>NMR</sub>	molar ratio
<b>0 mol%</b>	99.0	0.0	1	-	-
<b>2.5 mol%</b>	96.5	2.5	1	30.41	40.00
<b>7.5 mol%</b>	91.5	7.5	1	13.09	13.33
<b>12.5 mol%</b>	86.5	12.5	1	8.18	8.00

There we assign the signal at 3.90 ppm to the methine proton of the isopropyl side group of PNIPAAm (H-c). The peaks at 3.67 ppm and 3.34 ppm are related to the hydroxyethyl side group of HEAM (H-f, H-e). The two resonances at 2.30–1.83 ppm and 1.83–1.32 ppm refer to the backbone protons of the polymer network (H-b, H-a), and those at 1.32–0.90 ppm to the six methyl protons of the PNIPAAm side chain (H-d).<sup>[17]</sup> Due to the small amount of BIS (1 mol%) in the polymer network, the related signals are not considered.

The quantification of the HEAM content in the PNIPAAm/HEAM networks is performed based on the H-c, H-f, and H-e proton signals, which are shown enlarged in **Figure 4-2**. In this representation, all spectra are referenced to the H-c proton of the PNIPAAm isopropyl side group. Accordingly, from the 2.5 mol% system (gray), over the 7.5 mol% system (red) up to the 12.5 mol% system (green), an increasing intensity of the H-f and H-e proton signals is observed due to the increasing amount of HEAM comonomer within the three copolymer systems. In accordance, no H-f and H-e signals are detected for the 0 mol% (black) system.

Whether the HEAM comonomer incorporation into the PNIPAAm network is stoichiometric can be assessed by determining the integral ratio (proton ratio<sub>NMR</sub>) between the H-c proton signal ( $A_{\text{NIPAAm}}$ ) and the H-f and H-e proton signals ( $A_{\text{HEAM}}$ ) of each copolymer system using the formula: proton ratio<sub>NMR</sub> =  $(A_{\text{NIPAAm}} \cdot (A_{\text{HEAM}})^{-1}) \cdot 4\text{H}$  (**Table 4-1**). Respective

$A_{\text{NIPAAm}}$  and  $A_{\text{HEAM}}$  values are obtained by deconvoluting the  $^1\text{H}$  MAS NMR spectra as shown in the Supporting Information (SI) (**Figure S9-5** and **Table S9-1**). For comparison, the theoretical molar ratios of NIPAAm ( $n_{\text{NIPAAm}}$ ) and HEAM ( $n_{\text{HEAM}}$ ) (molar ratio =  $(n_{\text{NIPAAm}} \cdot n_{\text{HEAM}})^{-1}$ ) are also analyzed (**Table S9-2**) and presented in **Table 4-1**. The values of the 12.5 mol% (proton ratio<sub>NMR</sub>: 8.18, molar ratio: 8.00), and 7.5 mol% (proton ratio<sub>NMR</sub>: 13.09, molar ratio: 13.33) systems agree well. But deviations are observed in the 2.5 mol% system (proton ratio<sub>NMR</sub>: 30.41, molar ratio: 40.00), probably due to the small amount of HEAM comonomer used. The lower the amount of comonomer, the more error-prone are the measurements.

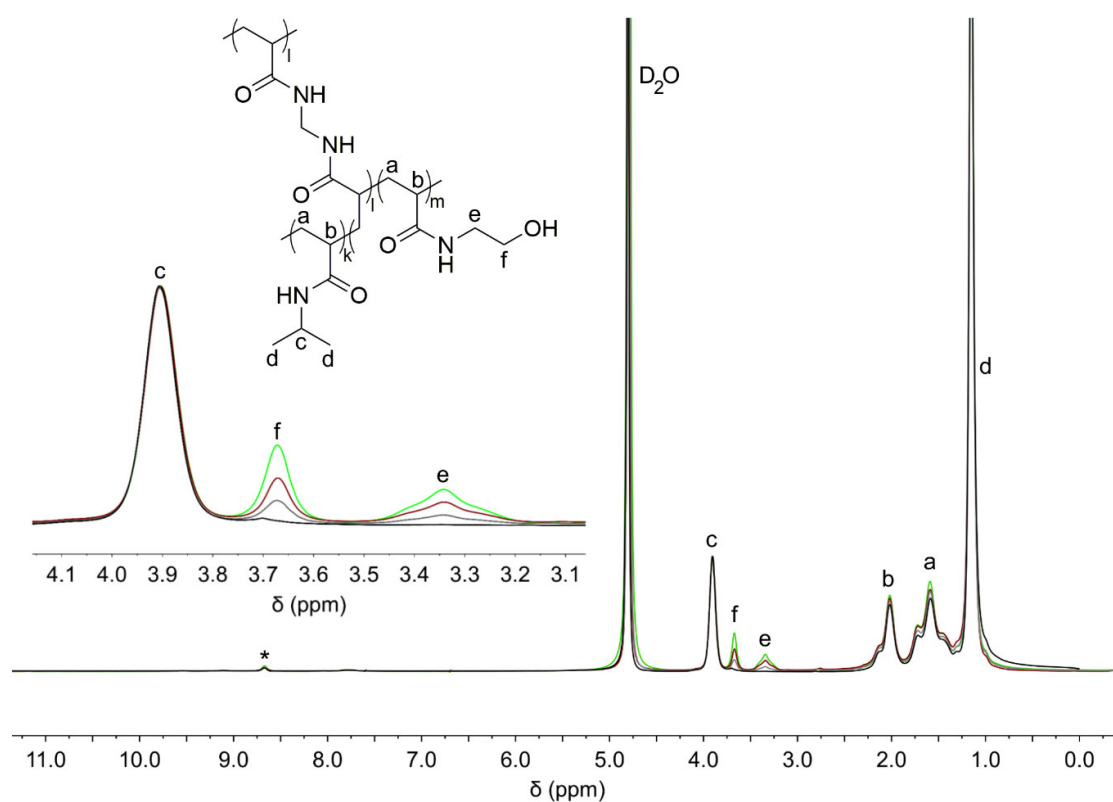


**Figure 4-2.** Full  $^1\text{H}$  MAS NMR spectra of the 0 mol% (black), 2.5 mol% (gray), 7.5 mol% (red), and 12.5 mol% (green) PNIPAAm/HEAM hydrogels and schematic structure of the polymer network with the proton species assigned. Enlarged sections of the  $^1\text{H}$  MAS NMR spectra show relevant signals for the quantification of the HEAM content in the hydrogels at 3.90 (H-c), 3.67 (H-f), and 3.34 ppm (H-e).

In conclusion, HEAM can be assumed to be stoichiometrically incorporated into the PNIPAAm/HEAM networks, as the experimentally determined proton ratios<sub>NMR</sub> agree well with the theoretically calculated values. This finding provides a fundament to classify our subsequent investigations.

#### 4.3.1.3. Microgel Synthesis via Droplet-Based Microfluidics

To make the 2.5 mol%, 7.5 mol%, and 12.5 mol% PNIPAAm/HEAM polymer systems useful for microtissue templating, they need to be shaped on a microscopic level. A suitable method to convert the polymer networks into spherical microgels is droplet-based microfluidic templating, which we use for the microgel synthesis. For this purpose, a poly(dimethylsiloxane) (PDMS) based microchannel device, fabricated by hard and soft lithography, is used as described in the SI (**Figure S9-6**). The microfluidic channel has a rectangular cross-section of 100  $\mu\text{m}$  in diameter in which the aqueous solution based on NIPAAm, HEAM, BIS, and APS is broken into monodisperse droplets by flow-focusing by an immiscible carrier fluid of fluorinated oil (Novec 7500), surfactant (Krytox), and initiator (TEMED). Stabilized by the oil–surfactant mixture, the NIPAAm, HEAM, and BIS molecules in these droplets react in a free-radical crosslinking polymerization reaction initiated by TEMED that diffuses from the surrounding oil phase into the aqueous droplet within a few minutes, thereby gelling the drops. By breaking the resulting microgel suspension using 1*H*,1*H*,2*H*,2*H*-perfluoro-1-octanol, PNIPAAm/HEAM microgels of type 2.5 mol%, 7.5 mol%, and 12.5 mol% with diameters between 160–180  $\mu\text{m}$  in water are obtained to which the following investigations refer. The size of the microgels can also be adjusted by varying the flow rates of injected fluids or by varying the microfluidics channel system width, as described in the SI (**Figure S9-7**).

#### 4.3.1.4. Temperature-Dependent Swelling Measurement

To provide a platform of well-designed microgel templates with stimuli-responsive properties, we investigate the three PNIPAAm/HEAM polymer networks and analyze the impact of the HEAM-comonomer on their temperature-dependent swelling. A characteristic quantity of thermoresponsive gels is the Volume Phase Transition Temperature (VPTT). At this temperature, the nanoscopic network-strand structure is rearranged due to changing polymer–solvent interactions, thereby causing a change of the microgel volume and elastic properties.

To study temperature as well as solvent influences on the VPTT, PNIPAAm/HEAM microgels are immersed in three different solvents. In detail, the microgels are placed in water as a standard solution and in phosphate buffer as well as Dulbecco's Modified Eagle Medium (DMEM) with 10% fetal bovine serum (FBS), 1% GlutaMAX (Gl.), and 1% Penicillin-Streptomycin (P/S), which are relevant media for applications in cell biology. While the microgels



are immersed in these different solvents, the temperature is increased from 25 °C to 50 °C at a rate of 0.1 °C per minute. At each step, images of the microgels are taken by light microscopy, and their diameters are determined using an image processing program. By plotting the microgel diameters as a function of temperature, temperature-dependent swelling curves are obtained. Such swelling curves of the microgels in water are represented in **Figure 4-3a**, while swelling curves of the same microgels in phosphate buffer and DMEM (10% FBS, 1% Gl. and 1% P/S) are shown in the SI (**Figure S9-8**). The symbols in gray (■) refer to the 2.5 mol%, in red (●) to the 7.5 mol%, and in green (▲) to the 12.5 mol% microgels. When comparing the three swelling curves of microgels in water, two observations can be identified: First, the curves shift towards higher temperatures with increasing comonomer content in the microgel polymer networks from 2.5 mol%, over 7.5 mol% up to 12.5 mol%. Second, the gradients of the respective swelling curves decrease with increasing temperature.

The shift of the swelling curves towards higher temperatures with increasing HEAM comonomer content is explainable by the more hydrophilic character of HEAM compared to that of PNIPAAm.<sup>[9]</sup> With increasing HEAM comonomer content, the PNIPAAm/HEAM networks therefore become more hydrophilic, whereby solvents can be better retained in the network at higher temperatures.

The decrease of the swelling-curve gradients of the PNIPAAm/HEAM networks is also explainable by the increasing network hydrophilicity with increasing HEAM content. The more HEAM comonomer is in the network, the less cooperative chain segments collapse in it, resulting in a more widespread VPT.<sup>[9]</sup> This trend is well known in literature for PNIPAAm microgels copolymerized to neutral or charged hydrophilic comonomers.<sup>[18]</sup>

From the inflection points of the swelling curves, we further determine the VPT<sup>\*</sup>T as a characteristic parameter. The inflection points are calculated by derivation of the swelling curves and subsequent Gaussian fitting, while the maximum of the fit curves corresponds to the inflection points. Derivations and Gaussian fittings of the swelling curves in DMEM (10% FBS, 1% Gl. and 1% P/S) are shown in the SI (**Figure S9-9**), while the estimated VPT<sup>\*</sup>T<sub>SC</sub> quantities of all three systems in water, phosphate buffer, and DMEM (10% FBS, 1% Gl. and 1% P/S) are represented in **Figure 4-3b** and in the SI (**Table S9-3**).

By comparing the VPT<sup>\*</sup>T<sub>SC</sub> values, it is noticeable that they shift to higher temperature with increasing HEAM comonomer content in all three solvents. The increasing VPT<sup>\*</sup>T<sub>SC</sub> within the three systems is explainable by the same reasons as discussed above. The more

hydrophilic HEAM comonomer is incorporated in the PNIPAAm/HEAM polymer networks, the more do the swelling curves and the  $VPTT_{SC}$  shift to higher temperatures.

Additionally, the solvent type has a significant influence on the  $VPTT_{SC}$ . Compared to the swelling measurements in water, the swelling curves in phosphate buffer and DMEM (10% FBS, 1% Gl. and 1% P/S) shift to lower temperatures. Since phosphate buffer and DMEM (10% FBS, 1% Gl. and 1% P/S) include inorganic salts, this finding is explainable with the competition for solvent molecules between the microgels and salt ions due to the osmotic pressure. This competition effectively strengthens hydrophobic interactions within the polymer network and thereby promotes a  $VPTT_{SC}$  at lower temperatures.<sup>[18]</sup> Minor differences can also be observed between the  $VPTT_{SC}$  of microgels in phosphate buffer and DMEM (10% FBS, 1% Gl. and 1% P/S), but they are small compared to the values in water. These differences may be due to the multitude of ingredients in the DMEM (10% FBS, 1% Gl. and 1% P/S), which all have an influence on the osmotic pressure and hence on the  $VPTT_{SC}$  of the polymer networks.

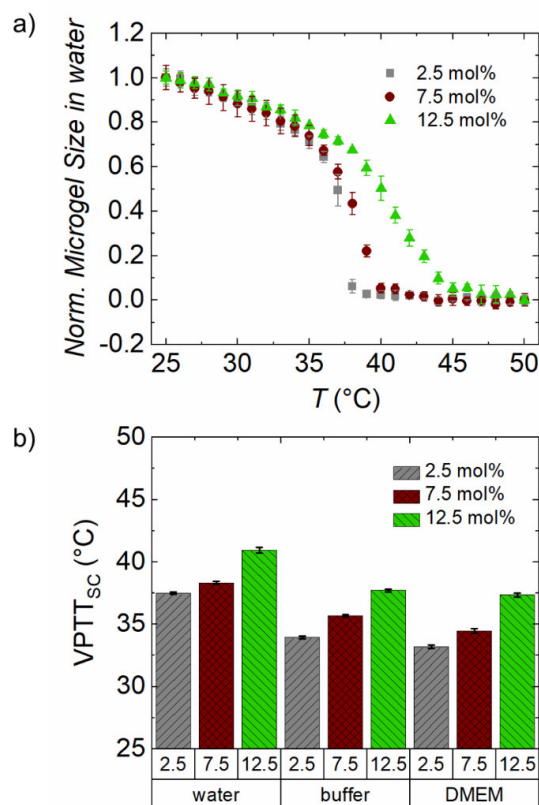


**Figure 4-3** Temperature-dependent swelling of 2.5 mol% (■), 7.5 mol% (●), and 12.5 mol% (▲) microgels. (a) Swelling curves in water. (b)  $VPTT_{SC}$  in water, phosphate buffer, and DMEM (10% FBS, 1% Gl. and 1% P/S).

#### 4.3.1.5. Hydrogel Elasticity

To achieve a general understanding of the polymer-network elasticity on a mesoscopic level, we focus on the mechanical hydrogel properties and examine temperature and solvent influences. These examinations are performed by temperature-dependent rheology measurements in water, phosphate buffer, and DMEM (10% FBS, 1% Gl. and 1% P/S). Respective data are represented in **Figure 4-4**, where the storage modulus  $G'$  is plotted against the temperature from 25 °C to 50 °C. **Figure 4-4a** displays measurements of the 2.5 mol% (■), 7.5 mol% (●), and 12.5 mol% (▲) hydrogels in plain water as the swelling medium. In all these three systems,  $G'$  increases with increasing temperature, which is due to their VPT behavior: with increasing temperature, the polymer systems collapse and expel the solvent. Thus, the hydrogels become smaller, but the amount of polymer in them remains the same, resulting in a higher concentration of the remaining polymer backbone contributing to the deformation resistance, which is why  $G'$  increases with increasing temperature.<sup>[19]</sup>

Since the three hydrogel systems differ in comonomer content and hence in the VPTT, the  $G'$  versus temperature curves increase at different temperatures.  $G'$  (2.5 mol%, ■) system with the lowest comonomer content increases first with increasing temperature,  $G'$  (7.5 mol%, ●) system increases later, and  $G'$  (12.5 mol%, ▲) with highest comonomer content increases last. For reference, a  $G'$  temperature curve of pure PNIPAAm without any comonomer (0 mol% (▼)) is also shown, with a VPT correspondingly ahead of the other three systems. **Figure 4-4b** and **c** show rheology measurements of the hydrogels in phosphate buffer and DMEM (10% FBS, 1% Gl. and 1% P/S). Again,  $G'$  of the three systems increases with increasing temperature, which is again attributed to the increasing comonomer content within these systems and thus an increasing VPT.

Since the  $G'$  versus temperature curves are similar to the swelling curves discussed in the section before,  $VPTT_{G'}$  are calculated for the three polymer networks in water, phosphate buffer, and DMEM (10% FBS, 1% Gl. and 1% P/S), and compared to the  $VPTT_{SC}$  obtained by the microgel swelling measurements. Respective analysis is shown and discussed in the SI (**Figure S9-10**, and **Table S9-3**), whereby the  $VPTT_{G'}$  and  $VPTT_{SC}$  values are found to be all in a similar range, which makes the rheology measurements a valuable complement to the swelling measurements described above.

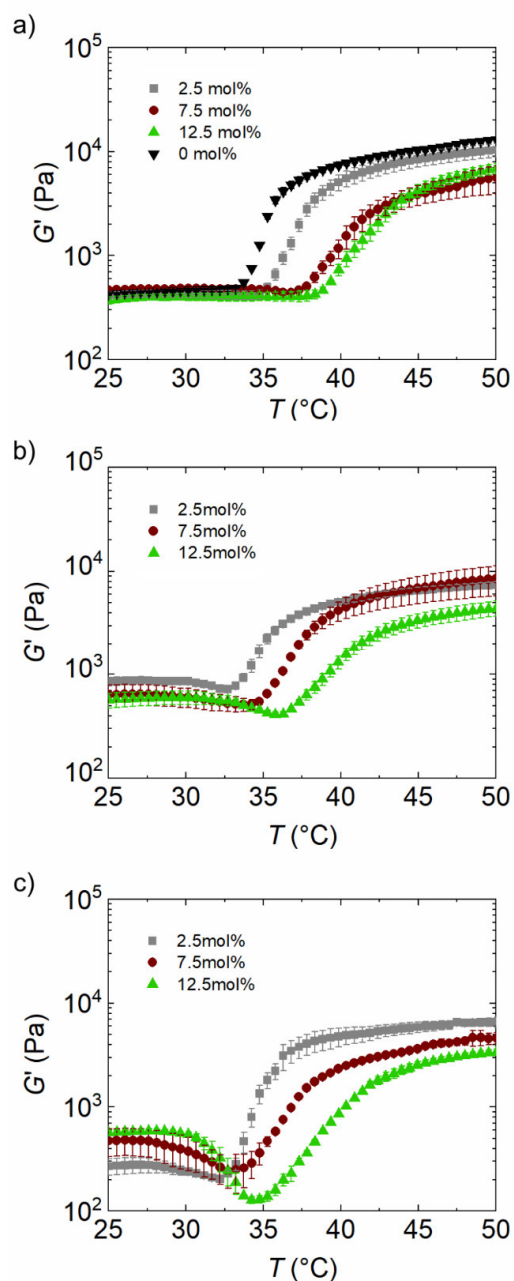


**Figure 4-4.** Temperature-dependent rheology measurements of 0 mol% ( $\blacktriangledown$ ), 2.5 mol% ( $\blacksquare$ ), 7.5 mol% ( $\bullet$ ), and 12.5 mol% ( $\blacktriangle$ ) hydrogels in (a) water, (b) phosphate buffer and (c) DMEM (10% FBS, 1% Gl. and 1% P/S).

#### 4.3.1.6. Microgel Properties at Physiological Conditions

So far, we have investigated the temperature-dependent swelling and the mechanical properties of the PNIPAAm/HEAM hydrogels. To further improve their applicability in microtissue engineering, we now focus on the microgel properties at physiological conditions, as assessed by the microgel diameter and mechanical strength in DMEM (10% FBS, 1% Gl. and 1% P/S) at 32 °C and 37 °C. As reference, also values at 25 °C are considered.

The microgel diameters ( $d_{\text{norm}}$ ) at 25 °C, 32 °C, and 37 °C in DMEM (10% FBS, 1% Gl. and 1% P/S) are obtained in the context of temperature-dependent swelling measurements and represented in a normalized form in **Figure 4-5a**, as well as in **Table S9-4**, while **Figure 4-5b** shows micrographs of single representatives of the different microgel types in DMEM (10% FBS, 1% Gl. and 1% P/S). At 25 °C, all microgel types are in a similar size range, whereas at 37 °C, the microgel diameters increase from 2.5 mol% over 7.5 mol% up to 12.5 mol%, which again can be explained by the increasing comonomer content. The more comonomer is in the polymer network, the more does the VPT shift to higher temperatures, so, microgels with a high comonomer content collapse at higher temperatures than microgels with a low comonomer content, which therefore affects the microgel diameter at given fixed temperature in the range in between. Thus, with increasing comonomer content, the microgels become larger at 37 °C. The mechanical properties are received by temperature-dependent rheology measurements (**Figure 4-4**) and represented in **Figure 4-5c**, as well as in **Table S9-4**. Corresponding values in water and phosphate buffer at 32 °C, and 37 °C are shown in the SI (**Figure S9-11**). At 25 °C and 32 °C, the storage modules  $G'$  of all three systems are in a similar order of magnitude with values around 200–600 Pa. But even here, an increase in that modules with increasing comonomer content can be observed. In contrast, at 37 °C, values increase up to  $(3474 \pm 853)$  Pa for the 2.5 mol% polymer system with less comonomer content, whereas the values decrease with increasing comonomer content up to  $(231 \pm 39)$  Pa for the 12.5 mol% polymer network. This finding again is explainable by the content of comonomer and the respective differences in the VPT. The more comonomer is in the microgels, the more does the VPT shift to higher temperatures, and so accordingly, the microgels collapse at higher temperatures. Respectively, with increasing comonomer content, microgels become larger, but the amount of polymer in them remains the same, resulting in a lower concentration of the remaining polymer backbone contributing to the deformation resistance. For that reason,  $G'$  decreases with increasing comonomer content.<sup>[19]</sup>

In conclusion, we have analyzed the microgel size of the 2.5 mol%, 7.5 mol%, and 12.5 mol% systems at 25 °C, 32 °C, and 37 °C, which fit well to the respective  $G'$  values. With increasing comonomer content, the microgels become larger, whereas the microgel stiffness decreases. This finding allows us to provide a construction kit of functional microgels with adjustable size and mechanical strength at the physiological relevant temperature range of 32–37 °C.

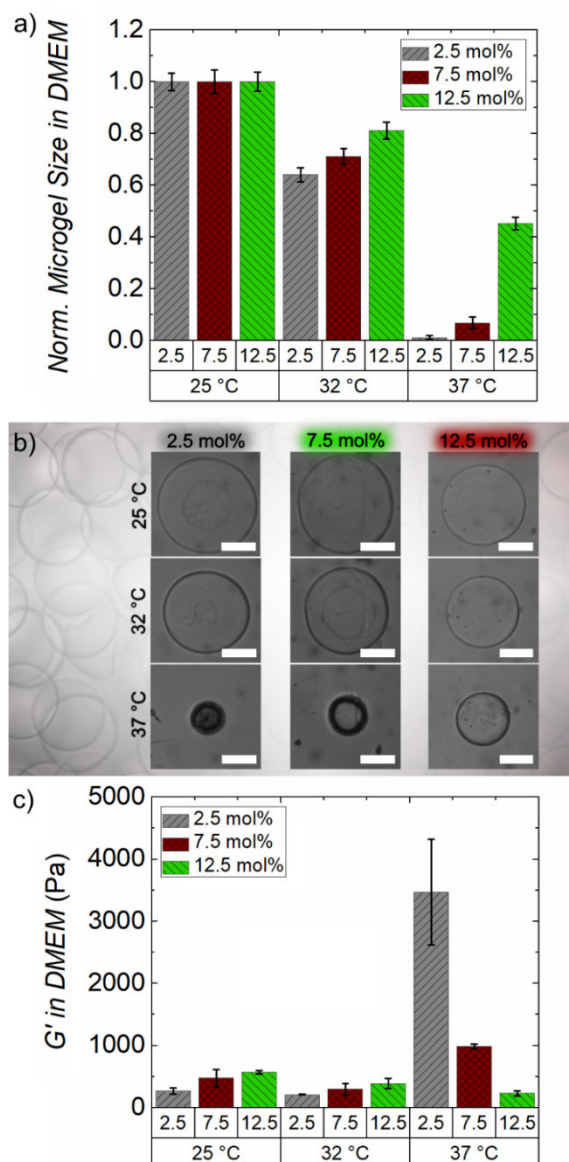


**Figure 4-5.** Microgel properties of 2.5 mol%, 7.5 mol%, and 12.5 mol% PNIPAAm/HEAM polymer networks in DMEM at 25 °C, 32 °C, and 37 °C. (a) Normalized microgel diameter. (b) Light microscopy imaging of microgels (scale bars are 50 μm). (c) Polymer stiffness.

### 4.3.2. Polydopamine Surface Coating

Having tuned and analyzed the thermoresponsive and mechanical properties of 2.5 mol%, 7.5 mol%, and 12.5 mol% PNIPAAm/HEAM-based polymer networks, we further focus on enhancing their cell-adhesiveness in the following section to make these microgels applicable for cell adhesion and cell growth. To achieve this goal, we focus on the surface modification of the microgels using PDA, as schematically shown in **Figure 4-1b** (2), since PDA demonstrates cell adhesion-promoting properties and adheres to a multitude of surfaces through physical binding forces.<sup>[20,21]</sup>

The strategy of PDA coating is inspired by mussel adhesive proteins, which are largely composed of 3,4-dihydroxy-L-phenylalanine (*L*-DOPA), whose catechol and amino groups are mainly responsible for its strong adhesive properties. Dopamine hydrochloride (DA), the precursor of PDA, contains similar catechol moieties as well as a primary amine function and exhibits analogous adhesive properties in the polymerized state. For this reason, PDA adheres to a variety of surfaces through hydrogen bonding,  $\pi$ - $\pi$ -stacking and coordination, including PNIPAAm hydrogels.<sup>[21–23]</sup> Moreover, DA polymerizes to PDA by autooxidation under mild basic conditions, providing a powerful and simple way to modify PNIPAAm/HEAM microgel surfaces with cell adhesion-promoting properties.

#### 4.3.2.1. PDA Coating of Macrogels

In a first step, we study the time-dependent PDA coating of PNIPAAm/HEAM hydrogels using the 12.5 mol% gel type. For this purpose, macrogels are synthesized and incubated in a solution of DA in Tris(hydroxymethyl)aminomethane (TRIS) buffer of pH 8.5 (1 mg mL<sup>-1</sup>) at room temperature for 0 min (PDA.0), 15 min (PDA.15), 90 min (PDA.90), 3 h (PDA.3h), and 24 h (PDA.24h) as shown in **Figure 4-6a** on the right (from the bottom to the top). PDA.0 is colorless and translucent, whereas the black coloration of the hydrogels increases with increasing PDA coating. The black coloration of PDA-coated hydrogels is described in literature and thus a good indication of the successful hydrogel coating.<sup>[24]</sup> To further examine that coating, the hydrogels are freeze dried and subsequently analyzed by Fourier-Transform Infrared Spectroscopy (FT-IR) using a FT-IR-470 instrument (JASCO Analytical Instruments), along with a reference based on pure PDA (**Figure 4-6a**, left). The spectrum of PDA.0 has characteristic signals at 3431 cm<sup>-1</sup> (O–H and N–H stretching mode), 2840–3000 cm<sup>-1</sup> (C–H stretching modes), and two signals at 1633 cm<sup>-1</sup> (C=O stretching mode) and 1538 cm<sup>-1</sup> (N–H bending mode).<sup>[25–27]</sup> With increasing PDA coating on the hydrogels, these FT-IR signals are overlaid by characteristic PDA absorbance peaks at 3172 cm<sup>-1</sup> (phenolic O–H and N–H stretching modes), 1506 cm<sup>-1</sup> (N–H bending modes), and 1273 cm<sup>-1</sup> (phenolic C–O stretching modes), also confirming the successful PDA surface coating strategy.<sup>[28,29]</sup>

#### 4.3.2.2. PDA Coating of Microgels

In a second step, the PDA coating procedure is transferred to 12.5 mol% PNIPAAm/HEAM microgels. Corresponding microgels of type PDA.0, PDA.15, PDA.90, PDA.3h, and PDA.24h suspended in isopropanol are shown in the SI (**Figure S9-12**), where

again the increased black coloration confirms PDA surface coating of microgels. Subsequently, the microgels are freeze-dried and morphologically analyzed by Field-Emission Scanning Electron Microscopy (FE-SEM), as well as pure PDA as a reference. Respective FE-SEM measurements are shown in **Figure 4-6b**, whereby the PDA.0 microgels exhibit a plain structure, while pure PDA shows a rough morphology. With increasing PDA coating time an increase of that rough morphology is observed on the microgels' surfaces. Further FE-SEM images are shown in the SI (**Figure S9-13**), along with photographs of the freeze-dried PDA.24 microgels (**Figure S9-14**).

To further investigate whether PDA preferentially accumulates on or in the microgels, microgels are analyzed by confocal Raman microscopy in the swollen state in water. Since the concentration of PDA below 90 minutes of PDA coating time is not sufficient to record clear Confocal Raman spectra and the fluorescence emitted by PDA leads to highly noisy spectra (**Figure S9-15**), we focus in the following on the PDA.90, PDA.3h, and PDA.24h systems. In **Figure 4-6c** the corresponding spectra for the PDA.3h microgels, as well as the bright-field and Raman images are shown. The PDA spectrum (green) can be clearly distinguished from the water spectrum (black) and the gel spectrum (red). For the PDA, the main bands at 1590, 1415, 1350, and 1240  $\text{cm}^{-1}$  and the broadband around 2900  $\text{cm}^{-1}$  are detected, the first four peaks correspond to the presence of aromatic rings, while the broadband is attributable to strongly hydrogen-bonded OH and NH stretching vibrations and complies to values in literature.<sup>[30]</sup> The resulting spectra indicate enhanced accumulation of PDA on the microgel surface, whereas almost no PDA can be detected inside the microgels. Further analysis also allowed the thickness of the PDA layer on the microgels to be determined (**Figure S9-16**) and revealed a thickness of approximately  $2.3 \pm 0.6 \mu\text{m}$  for the PDA.90 microgels,  $3.1 \pm 1.2 \mu\text{m}$  for the PDA.3h microgels and  $3.7 \pm 1.8 \mu\text{m}$  for the PDA.24h microgels.

Whether PDA surface coating of microgels influences temperature-dependent microgel swelling is investigated using PDA.0, PDA.15, PDA.90, PDA.3h, and PDA.24h microgels in phosphate buffer (**Figure S9-17**). All swelling curves show a similar course, indicating almost identical swelling of these microgels. Thus, PDA coating does not seem to have any influence on the microgel swelling, confirming the results of Confocal Raman spectroscopy. With increasing PDA coating, PDA accumulates on the microgel surface, but hardly any PDA is detectable inside the microgels, thus having little effect on the temperature-dependent microgel swelling.



In summary, we could demonstrate the successful PDA surface modification of 12.5 mol% PNIPAAm/HEAM macro- and microgels. Overall, hence, core-shell microgels are obtained, whereby the microgel cores are less affected from the PDA coating, providing a suitable and functional base for subsequent cell experiments.

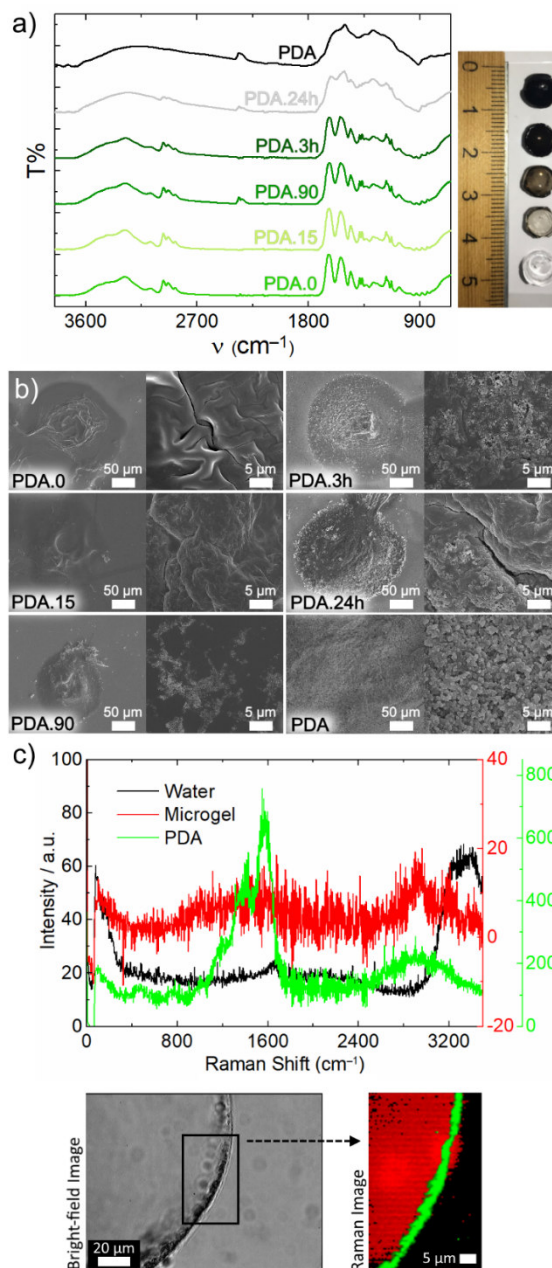


**Figure 4-6.** PDA-coated 12.5 mol% PNIPAAm/HEAM hydrogels. (a) FT-IR spectroscopy measurements of freeze-dried macrogels and pure PDA (left) and corresponding gels swollen in water (right, from the bottom to the top: PDA.0, PDA.15, PDA.90, PDA.3h, and PDA.24h). (b) FE-SEM measurements of freeze dried microgels and of pure PDA. (c) Confocal Raman microscopy measurements of PDA.3h microgels, as well as respective bright-field and Raman images.

### 4.3.3. Cell Growth on Microgels

The transfer of PDA-coated PNIPAAm/HEAM microgels to biological applications in microtissue engineering needs to be supported by cellular experiments as schematically shown in **Figure 4-1** (3). Hence, we focus in the following on homogenous cell coating of microgels.

#### 4.3.3.1. Cell-Affinity of PDA

To coat core-shell microgels homogeneously with cells, it must be first investigated whether PDA influences cell adhesion on the hydrogels in general. For this reason, we analyze cell growth on 2.5 mol%, 7.5 mol%, and 12.5 mol% PDA hydrogels with 0 (PDA.0), 15 (PDA.15), and 60 (PDA.60) minutes of PDA coating. For this purpose, macrogels are synthesized and incubated in a suspension of osteoblasts expressing GFP (MG-63 GFP) and DMEM (10% FBS, 1% Gl., 1% P/S) at 37 °C and 5% CO<sub>2</sub> for several days, whereby cell growth on the hydrogels is analyzed by Confocal Laser Scanning Microscopy (CLSM). Respective images are shown in **Figure 4-7**. As shown on the left, 2.5 mol% and 7.5 mol% hydrogels precipitate at 37 °C, since their VPTT is far below this temperature. Hence, they show a whitish, opaque haze and do not shrink in any way. Due to this reason, it is impossible to analyze the cell growth on these hydrogels since transparent materials are required for quantitative CLSM.

In contrast, 12.5 mol% hydrogels show a VPTT in the range of 37 °C, whereby they partly shrink but remain transparent, which makes CLSM possible in these cases. But again, there is a limitation in imaging. Since the intense blackish color of the PDA.60 hydrogels diminishes their transparency, imaging is poorly possible. For this reason, we concentrate on CLSM of the 12.5 mol% PDA.0 and PDA.15 hydrogels. Respective images are shown in **Figure 4-7** on the right, whereby (I) represents the cell adhesion experiments on 12.5 mol% PDA.0 hydrogels, and (II) on 12.5 mol% PDA.15 hydrogels (both: 2D fluorescence path of CLSM). In (I), large cell clusters are observed, which indicates less cell adhesion on these materials, whereby in (II), the elongated cell morphology argues for excellent cell growth. A control experiment of cells growing on plastic is also shown for comparison.

To extend the hydrogels functionality, we also perform cell experiments at 32 °C as shown in the SI (**Figure S9-18**). Since the VPTT of all hydrogels are above 32 °C, they are transparent at this temperature and hence suitable for light- and confocal microscopy. Accordingly, we detect cell growth on all three gel types at 32 °C. Thus, the 15-minute PDA coating appears to be a valuable approach to enable cell growth on hydrogels, both at 32 °C, and

37 °C. These results provide a stable basis on which to build in subsequent cell experiments on homogeneous cell coating of PDA.15 microgels.

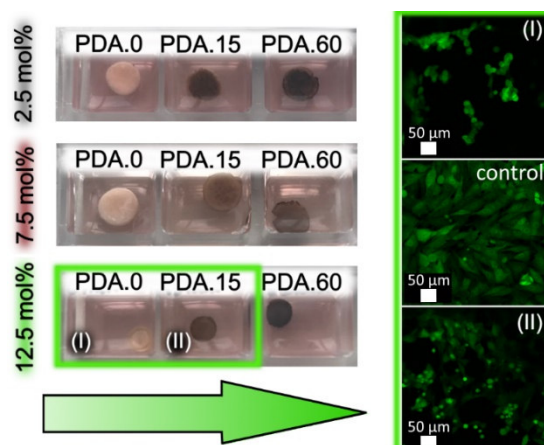


**Figure 4-7.** Cell growth on 2.5 mol%, 7.5 mol%, and 12.5 mol% PNIPAAm/HEAM-PDA hydrogels at 37 °C. Left: Hydrogels with 0-, 15-, and 60-minutes of PDA coating, incubated in DMEM (10% FBS, 1% Gl, 1% P/S) at 37 °C and 5% CO<sub>2</sub>. Right: CLSM imaging of cells (MG-63 GFP) growing on 12.5 mol% PDA.0 (I) and PDA.15 (II) hydrogels after 24h incubation time. Both images (I) and (II) are obtained by the 2D fluorescence path of the CLSM. For comparison, a control experiment of cells growing on plastic is also shown.

#### 4.3.3.2. Cell Growth on PDA.15 Microgels

To translate the microgel-templates to potential application in microtissue engineering, we need to realize a homogeneous cell coating on the microgel surfaces. In general, the PDA coating allows for good cell adhesion, but still there are some factors that complicate a homogeneous cell coating to be realized, which is why we need to develop a method to make this possible in general.

One of these factors are the adhesive properties of PDA-coated microgels, which cause microgels to stick onto a multitude of surfaces and other microgels. Corresponding preliminary experiments have been performed and are shown in the SI (**Figure S9-19**). Since the sticky behavior of PDA-coated microgels is easily circumvented by diluting the microgels in liquid-filled cell culture dishes, this problem can be easily overcome. Another major factor counteracting the homogeneous cell coating of microgels in solution is gravity, which is why cells in solution settle on the culture dish bottom over time. If that settling occurs faster than the establishment of cell–gel interactions on the microgel surface, this leads to unoccupied microgel surfaces. Hence, to enable homogeneous cell coating of our PDA.15 microgels, we need to address two aspects: (i) cell–matrix interactions must be significantly increased, and (ii) cells and microgels must be brought into spatial proximity. Taking these factors into account, we investigate in two approaches. First, we focus the nature of the microgel surfaces

to promote cell–matrix interactions. Second, we optimize the cell suspension density used in the experiment to bring cells and microgels into spatial proximity.

To investigate the influence of different microgel surfaces on cell–matrix interactions, we use two surface types. One type is based on the already characterized PDA.15 microgels, and the second type on PDA.15 microgels with additional collagen coating (PDA.15/collagen microgels). Due to its excellent cell adhesion properties, collagen represents a suitable surface modification substance for microgel coating. Moreover, PDA adheres to a variety of materials, including proteins as collagen, which essentially facilitates the respective modification of PDA microgel surfaces.<sup>[31]</sup>

To examine the effect of different cell concentrations on the homogeneous microgel cell coating, PDA.15 and PDA.15/collagen microgels are additionally incubated in two different cell concentrations each (high and low). In summary, we focus on four different cell experiments (1–4), which are schematically shown in **Figure 4-8a**. In experiments (1) and (2), PDA.15 and PDA.15/collagen microgels are incubated at low cell concentrations, respectively. In contrast, in experiments (3) and (4), the PDA.15 and PDA.15/collagen microgels are incubated at high cell concentrations.

In general, cell experiments are performed with osteoblasts expressing GFP (MG-63 GFP), which are trypsinized and detached from the culture dishes at the beginning of each experiment. For the low cell concentration experiments ((1) and (2)),  $1.57 \times 10^5$  cells  $\cdot$  mL<sup>-1</sup> suspended in DMEM (10% FBS, 1% Gl., 1% P/S) are used. An appropriate volume of cell suspension is transferred to a bioinert Petri dish and mixed with either 7.5 mol% PDA.15 or PDA.15/collagen microgels. The microgels are incubated for 24h at 32 °C and 5% CO<sub>2</sub> and subsequently analyzed by CLSM, keeping the temperature constant at 32 °C. Respective images are shown in **Figure 4-8a** ((1) and (2)). In both approaches, cells partially adhere to the microgel surfaces and form large cell–microgel clusters, resulting in inhomogeneous cell coated microgel surfaces. In conclusion both approaches (1) and (2) seem to be unsuitable for homogeneous cell coating of microgels.

In contrast, for the high cell concentration experiments ((3) and (4))  $1.57 \times 10^6$  cells  $\cdot$  mL<sup>-1</sup> in DMEM (10% FBS, 1% Gl., 1% P/S) are used. The cell suspension is transferred into 96-well plates, and either 7.5 mol% PDA.15 or PDA.15/collagen microgels are added. Leaving the microgels and cells densely packed in the culture dish, the mixture is incubated for 1 h at 32 °C, and 5% CO<sub>2</sub>. Subsequently, the microgels are transferred into bio-coated culture dishes containing DMEM (10% FBS, 1% Gl., 1% P/S) to separate them from the remaining

free cells. Due to gravity, most of the free cells settle and adhere to the bottom of the bio-coated cell culture plate, so the microgels are easily separable from the remaining cells. Again, the microgels are transferred into new bio-inert culture dish plates and analyzed by CLSM, keeping the temperature constant at 32 °C. In total, PDA.15/collagen microgels are easily coatable with cells by incubating in a highly concentrated cell suspension, while cells do not adhere to the collagen-free PDA.15 microgels. Instead, large cell–microgel agglomerates are observed. This behavior completely contradicts the cell growth on hydrogel surfaces coated with PDA shown in the previous section and is probably caused by the natural binding protein deficit in the highly concentrated cell suspensions, since these proteins are responsible for cell adhesion on PDA coated surfaces. The denser the cell suspension, the less volume of DMEM (10% FBS, 1% Gl., 1% P/S) is present, and thus fewer binding proteins are contained in the FBS. This probably results in an insufficient PDA.15 microgel surface coating with binding proteins from the FBS and prevents cells from adhering well. However, by coating the PDA.15 microgels with collagen beforehand, this problem is avoided. Respective CLSM images are shown in **Figure 4-8a** (3) and (4).

Beside 7.5 mol% PDA.15/collagen microgels, also 2.5 mol% and 12.5 mol% microgels are incubated in a highly concentrated cell suspension and subsequently analyzed by CLSM keeping the temperature constant at 32 °C as represented in **Figure 4-8b**. The CLSM images on the left show cell-coated microgels after 2 h, and those on the right after 24 h incubation in DMEM (10% FBS, 1% Gl., 1% P/S) at 32 °C and 5% CO<sub>2</sub>. The first row demonstrates transmission images, the second superposition of transmission and fluorescence images, and the third fluorescence images of the microgels. After 2 h, cells are homogeneously distributed on each microgel surface, as shown by their rounded morphology, while after 24 h, their morphology becomes more elongated. This morphology indicates viable cells, adhering and proliferating on the microgel surfaces. To demonstrate the homogeneity of cell coating on the microgels, an image stack is recorded at six levels of a cell-coated 12.5 mol% PDA.15/collagen microgel, as shown in the SI (**Figure S9-20**). The variation of the cell concentration in the cell-coating experiment, as well as different PDA coating times of the microgels showed no influence on the cell density on these microgels (**Figure S9-21**).

As all three microgel systems are incubated in DMEM (10% FBS, 1% Gl., 1% P/S) at 32 °C and 5% CO<sub>2</sub>, significant differences in the microgel size are recognizable. Overall, an increase in diameter is observed within the 2.5 mol% through 7.5 mol% up to 12.5 mol% systems, which can be attributed to the increasing comonomer content. The more comonomer, the more does the VPT shift towards higher temperatures, and the larger the microgels become.

This additionally affects the mechanical strength of the microgels, which decreases within the three systems as discussed above. However, since the cells adhere evenly distributed on all three microgel systems, no effects of the respective microgel properties on cell growth are observed.

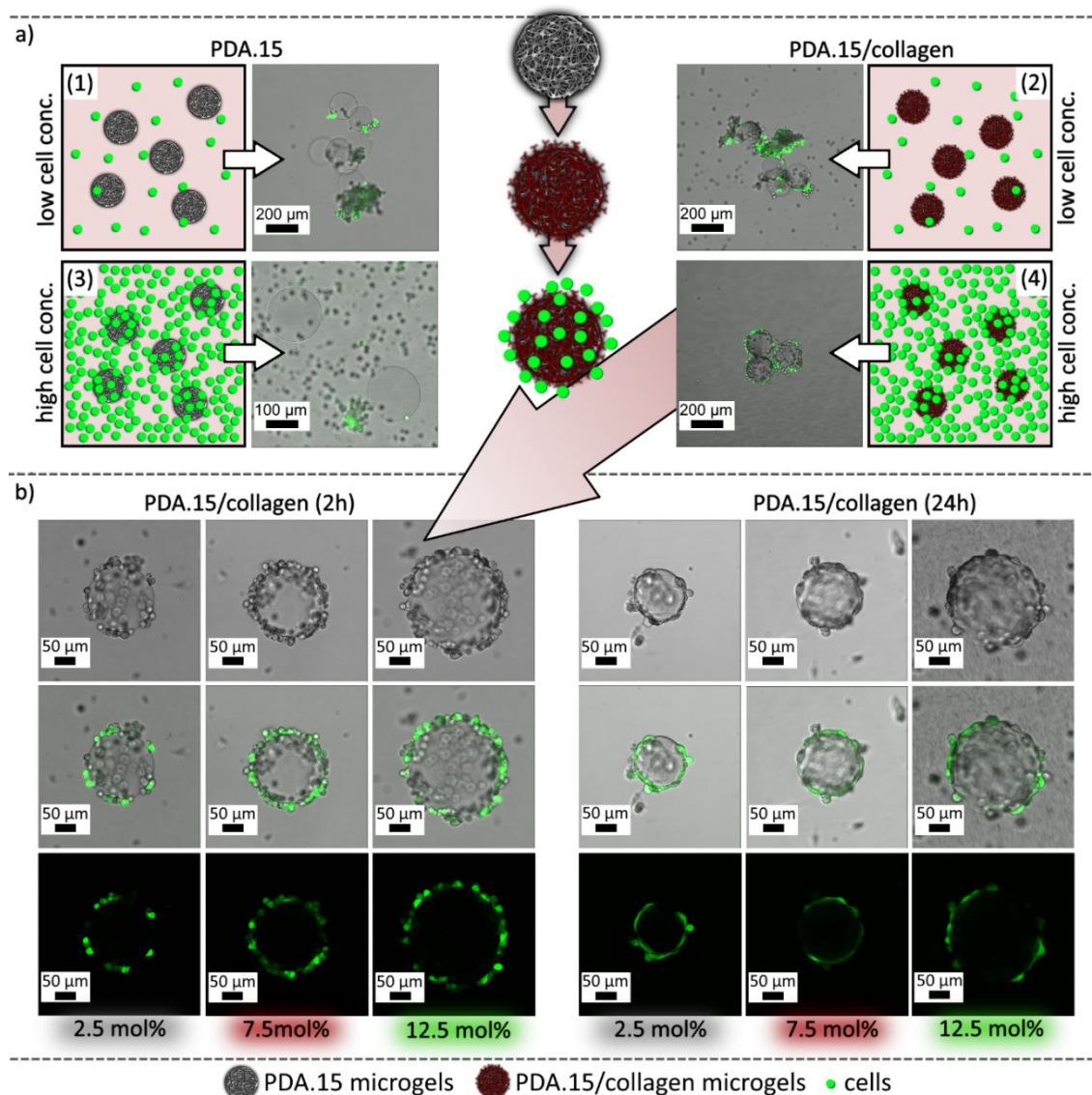


**Figure 4-8.** Cell coating of microgels. (a) CLSM imaging (superposition of transmission and fluorescence path) of 7.5 mol% PDA.15 and PDA.15/collagen microgels coated with low or high cell concentrations after 24 h incubation time in DMEM (10% FBS, 1% Gl., 1% P/S) at 32 °C and 5% CO<sub>2</sub>. (b) CLSM imaging (transmission path, fluorescence path, and superposition of both) of cell-coated 2.5 mol%, 7.5 mol%, and 12.5 mol% PDA.15/collagen microgels after 2 h and 24 h incubation time in DMEM (10% FBS, 1% Gl., 1% P/S) at 32 °C and 5% CO<sub>2</sub>.

In total, we could demonstrate the ability to obtain a homogeneous cell coating of core–shell microgels by increasing cell–matrix interactions using collagen and a high concentrated cell-suspension. Additionally, a microgel-type independent cell adhesion is observed, meaning

cells are unaffected from the 2.5 mol%, 7.5 mol%, and 12.5 mol% microgel size and mechanical strength. This finding enables a system-independent and thus universal use of the microgel templates in potential follow-up studies for microtissue engineering applications, such as mimicking the blastula in embryogenesis, breast glands, and the alveolar epithelium.<sup>[32–34]</sup>

#### 4.3.3.3. Microgels Incorporated in Cell Spheroids

Since spheroids are commonly used 3D cell culture models for microtissue engineering and drug screening applications, we investigate the mimicking of higher hierarchical spheroid structures with tunable mechanical properties using our core–shell microgel platform. Towards this end, 7.5 mol% PDA.15 microgels are coated with fibronectin to improve their cell adhesions properties. Subsequently they are added to MCF7 cells and seeded into cell spheroid cultures. After 24 h microgel-laden cell spheroids are formed at 30 °C with one to three integrated microgels (**Figure 4-9**), whereby the number of integrated microgels depends on the number of microgels added to each well.

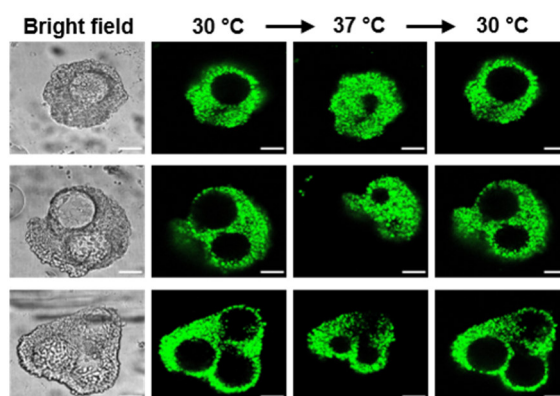


**Figure 4-9.** Fibronectin-coated 7.5 mol% PDA.15 microgels incorporated in cell spheroid structures based on MCF7 cells. On the left, bright field micrographs of spheroids at 30 °C are shown, and on the right, confocal fluorescence micrographs are added. The MCF7 cells are stained with vibrant DiO (green fluorescence). The temperature is first increased from 30 °C to 37 °C and later decreased back to 30 °C. Scale bars are 100  $\mu\text{m}$ .

The thermoresponsive microgel properties allowed altering the microgel size and analyzing the stability of microgel-laden spheroid structures. When the temperature is increased from 30 to 37 °C, the microgels within the spheroids shrink, and the cells follow the movement induced by the microgels. Next, when the temperature is decreased again to 30 °C, the spheroids recover their initial structure and the microgel swell to their initial volume. The shrinking of the microgels is fast within a few seconds, yet the reaction of the cells is slower and takes place within 20 minutes. This behavior is explainable by the strong cell–cell adhesion

and high E-cadherin expression of MCF7 cells, which presumably leads to the stability of the multicellular structure during this movement. In summary, this finding offers a temperature-sensitive cell spheroid platform with tunable mechanical properties as basis for future investigations on higher hierarchical spheroid structures.

### 4.4. Conclusion

Since 3D in vitro microtissue models offer a suitable approach to reduce and replace animal testing, we have developed microtissue systems using a core–shell micro-template platform that takes into account the complex shape, the nature, and the mechanical properties of in vivo tissues to best mimic the in vivo environment. These microgels were synthesized and analyzed with a primary focus on material design such to obtain a deep understanding at the conceptual level through (1) systematic tuning of the mechanical and functional properties of the microgel cores, (2) enhancement of their cell adhesiveness, and (3) application in cell biology.

In the first development step, by using microfluidic technology, we were able to obtain spherical cores whose mechanical properties could be tuned by choosing a thermoresponsive polymer and different proportions of hydrophilic comonomers, essentially simplifying the mimicking of natural microstructures. In the second step, we were able to increase the attractiveness of the microgel cores to cell adhesion by effective PDA surface coating, while minimizing its influence on the mechanical and functional properties of the cores. In the last step, we demonstrated the successful homogeneous cell coating of the core–shell microgels, using additional collagen surface coating, and also presented the successful embedment of fibronectin coated microgels into cell spheroid structures and their response to temperature changes.

Thus, the present core–shell microcarrier toolkit enables a multifunctional and versatile 3D microtissue platform and can be used as flexibly adjustable template for the in vitro formation and analysis of hollow spherical tissue constructs, as well as for the investigations on higher hierarchical spheroid structures.



## 4.5. Experimental Section

*Materials:* NIPAAm and APS are purchased from Acros Organics. HEAM, TEMED, SPAN 80, dopamine hydrochloride, trypsin EDTA solution, phosphate buffer (DPBS-D8537), DMEM high glucose (D5796), fetal bovine serum (FBS) (F7524), Penicillin–Streptomycin (P/S) (P4333) and Tris(hydroxymethyl)aminomethane are obtained from Sigma-Aldrich. BIS is obtained from Merck, Novoc 7500 from 3M, Krytox 157FS(L) from DuPont, 1H,1H,2H,2H-Perfluor-1-octanol from Alfa-Aesar and gibco GlutaMAX (Gl.), as well as gibco collagen I (Rat Tail) from Thermo Fisher Scientific. Deuterium oxide is purchased from deutero. Osteoblasts (MG-63 GFP) are obtained from R. E. Unger – Johannes Gutenberg University Mainz, Institute of Pathology.

*Hydrogel Synthesis:* NIPAAm is recrystallized twice from *n*-hexane before use in hydrogel synthesis. 0 mol%, 2.5 mol%, 7.5 mol%, and 12.5 mol% hydrogels are synthesized by mixing NIPAAm (0 mol%: 99.0 mg, 0.875 mmol, 0.990 eq.; 2.5 mol%: 96.5 mg, 0.853 mmol, 0.965 eq.; 7.5 mol%: 91.5 mg, 0.809 mmol, 0.915 eq.; 12.5 mol%: 86.5 mg, 0.764 mmol, 0.865 eq.), HEAM (0 mol%: 0.0 mg, 0.000 mmol, 0.000 eq.; 2.5 mol%: 2.5 mg, 0.021 mmol, 0.025 eq.; 7.5 mol%: 7.0 mg, 0.061 mmol, 0.075 eq.; 12.5 mol%: 11.0 mg, 0.096 mmol, 0.125 eq.), BIS (1.3 mg, 0.009 mmol, 0.010 eq.), APS (4.9 mg, 0.021 mmol, 0.025 eq.), and water (1 mL). Subsequently, the aqueous solution is transferred into a 96-well plate (70  $\mu$ L per well). Gelation is initiated by adding TEMED (1  $\mu$ L per well). After 10 minutes, gelation occurs, and gels are purified by incubation in water over three days while changing the water twice per day.

*Microgel Synthesis:* Droplet-based microfluidics is carried out using a poly(dimethylsiloxane) (PDMS) device fabricated by soft lithography as described in the SI (**Figure S9-6**). The PDMS device is connected to two syringe pumps (neMESYS Plugin) via polyethylene tubing (Intramedic Clay Adams Brand PE20) and plastic syringes (Becton Dickinson). NIPAAm is recrystallized twice from *n*-hexane before use in the microgel synthesis. For the synthesis of 2.5 mol%, 7.5 mol%, and 12.5 mol% microgels, NIPAAm (2.5 mol%: 96.5 mg, 0.853 mmol, 0.965 eq.; 7.5 mol%: 91.5 mg, 0.809 mmol, 0.915 eq.; 12.5 mol%: 86.5 mg, 0.764 mmol, 0.865 eq.), HEAM (2.5 mol%: 2.5 mg, 0.021 mmol, 0.025 eq.; 7.5 mol%: 7.0 mg, 0.061 mmol, 0.075 eq.; 12.5 mol%: 11.0 mg, 0.096 mmol, 0.125 eq.), BIS (1.3 mg, 0.009 mmol, 0.010 eq.) and APS (4.9 mg, 0.021 mmol, 0.025 eq.) are dissolved in water (1 mL) and injected with a flow rate of 450  $\mu$ m h<sup>-1</sup> into the PDMS device. At the cross-junction of the microchannel, the aqueous solution is broken to form monodisperse pre-

## CHAPTER II

microgel droplets by flow-focusing with an immiscible oil (Novec 7500), which is injected with a flow rate of  $1500 \mu\text{m h}^{-1}$ . To stabilize the resulting droplets, 2 wt% of Krytox and 3 wt% TEMED are added to the fluorinated oil. Resulting droplets are purified after 24 h gelation time with Novec 7500 containing 20 wt% 1*H*,1*H*,2*H*,2*H*-Perfluor-1-octanol (3x 400  $\mu\text{L}$ ), pure Novec 7500 (3x 400  $\mu\text{L}$ ), *n*-hexane containing SPAN 80 surfactant (1wt%) (3x 400  $\mu\text{L}$ ), pure *n*-hexane (3x 400  $\mu\text{L}$ ), isopropanol (3x 400  $\mu\text{L}$ ) and 1,4-dioxane (3x 400  $\mu\text{L}$ ). The microgels are cooled to 5 °C and washed with cold water. Depending on the application, the microgels are transferred into DPBS-D8537 or DMEM (10% FBS, 1% Gl., 1% P/S).

*Microgel Swelling:* Swelling measurements are carried out using microgels of type 2.5 mol%, 7.5 mol% and 12.5 mol% synthesized via microfluidics as described above. Samples are incubated in water, DPBS-D8537, and DMEM (10% FBS, 1% Gl. and 1% P/S) placed on a thermoelectric stage from Instec, while heating up from 25 °C to 50 °C in 1 °C per 10 minutes steps. After equilibration for 10 min, an optical micrograph is taken at each temperature step with a high-resolution digital camera from Carl Zeiss. The pictures are analyzed, and particle sizes are determined using the ImageJ software.

*Rheology:* For elasticity measurements of the 0 mol%, 2.5 mol%, 7.5 mol%, and 12.5 mol% systems, hydrogels of 300  $\mu\text{L}$  volume are synthesized using a rounded cap of 1.8 cm diameter for shaping, while the hydrogel compositions refer to that described above. After 10 minutes of gelation, gels are purified by incubation in water over three days while changing the water twice per day. Subsequently hydrogels are transferred into DPBS-D8537 or DMEM (10% FBS, 1% Gl., 1% P/S) and applied to rheology after incubation time of 24 h in the respective solvent. Rheological measurements are performed using an Anton Paar modular compact rheometer of type MCR 302 (Anton Paar, Graz, Austria) equipped with a plate–plate measuring system PP25 (2.5 cm diameter) and solvent trap. Temperature-dependent elasticity measurements are carried out a constant shear amplitude of 1% and a constant shearing frequency of  $1 \text{ rad s}^{-1}$  each as well as using a constant normal force of  $F_N = 1 \text{ N}$ . Measuring points are recorded while the rheometer heats up from 25 °C to 50 °C in 1 °C per 1-minute steps. Measurements in the linear-viscoelastic (LVE) regime are confirmed by amplitude sweeps, whereby the frequency remained constant at  $1 \text{ rad s}^{-1}$  and the amplitude varied between 0.01% and 100% deformation. In addition, frequency sweeps are performed in a frequency range between 100–0.01  $\text{rad s}^{-1}$  and at a fixed amplitude of 1% within the LVE regime of the sample.

*PDA Coating:* 12.5 mol% macrogels and microgels are synthesized as described above and incubated in a 1 mg mL<sup>-1</sup> solution of dopamine hydrochloride (DA) and Tris(hydroxymethyl)aminomethane (TRIS) buffer of pH 8.5 on a shaking plate at room temperature. PDA.0 macrogels and microgels are incubated for 0 min, PDA.15 for 15 min, PDA.90 for 90 minutes, PDA.3h for 3 h and PDA.24h for 24 h. After coating, macrogels are purified by incubation in water over 24 h by changing water five times. Microgels are purified by washing with water five times and using a centrifuge (10000 rpm, 5 min, 5 °C). Pure PDA as reference is synthesized by incubating 1 mg mL<sup>-1</sup> dopamine hydrochloride (DA) in a TRIS buffer solution (pH 8.5) for 24 h at room temperature. 10% acetone is added, and PDA is separated from the PDA/TRIS buffer solution by centrifugation (10000 rpm, 20 min, 5 °C). The black powder is purified by washing with water five times and using a centrifuge (10000 rpm, 5 min, 5 °C).

*FE-SEM:* FE-SEM measurements are performed on a NOVA Nano-SEM 630 with an attached Oxford Inca X-ray system for chemical analysis. Freeze-dried samples are sputtered with a gold-layer of 10 nm before analysis. Secondary and backscattered electron images are collected with an acceleration voltage of 10 keV and a spot size of 5 using a through-the-lense detector.

*MAS NMR Spectroscopy:* All NMR experiments are performed on a Bruker Avance DSX 400 NMR spectrometer operating at 399.87 MHz <sup>1</sup>H frequency. Prior to the <sup>1</sup>H NMR experiments all gels are incubated in D<sub>2</sub>O for 24 h at room temperature, while solvent is changed three times. The gel samples are measured using 4 mm rotors and inserts specially developed to investigate gels and soft matter. The <sup>1</sup>H single pulse excitation NMR spectra are recorded using a commercial three channel Bruker 4 mm probe head at 3 kHz Magic Angle Spinning (MAS), averaging 32 scans with a 20 s recycle delay.

*Confocal Raman Spectroscopy:* Confocal Raman spectroscopy are performed with a Witec 300 alpha R setup. During the measurement 12.5 mol% PDA-coated microgels are illuminated with a 532 nm and 633 nm excitation line from a single mode frequency doubled Nd:YAG laser via a 100- $\mu$ m single-mode glass fiber. Emitted light is focused on a Zeiss C-Aprocrhomat 63x/1.2 W objective, while the laser power at the sample behind the objective is 0.5 mW to avoid damage of the sample. To further separate the Raman signals from the excitation line an edge filter is installed. The confocal character of the Raman signal is achieved via a 50- $\mu$ m multi-mode fiber glass between microscope and the Raman spectrometer, where the fiber serves as a pinhole. The Raman spectrometer is equipped with a holographic grating of

## CHAPTER II

600 lines per mm. As detector, a Newton Andor EMCCD camera with  $1600 \times 200$  pixels is used. With this configuration, a spectral resolution of about  $2 \text{ cm}^{-1}$  is obtained and a spatial resolution of 270 nm (lateral). All data sets are analyzed using cluster analysis and non-negative matrix factorization. The cross sections calculation are obtained from the average of a 10mm thick line perpendicular to the PDA layer

*Cell Coating of Microgels:* Osteoblasts (MG-63 GFP) cultivated in Petri dishes with an area of  $11.9 \text{ cm}^2$  and of 80% confluency are detached from plastic by trypsinization using trypsin EDTA solution. After centrifugation (1000 rpm, 5 min), the resulting cell pellet is resuspended in DMEM (10% FBS, 1% Gl., 1% P/S) and adjusted to a specific cell concentration, while cell counting is performed using a Neubauer counting chamber. Depending on the cell experiment, different amounts of cells are used as described in the following. For the cell growth on macrogels, 2.5 mol%, 7.5 mol% and 12.5 mol% hydrogels of type PDA.0, PDA.15 and PDA.60 are synthesized as described above and incubated in DPBS-D8537. Subsequently hydrogels are transferred into 8well plates from ibidi and covered with 300  $\mu\text{L}$  of cell suspension in DMEM (10% FBS, 1% Gl., 1% P/S) at a final concentration of  $1.57 \times 10^5 \text{ cells} \cdot \text{mL}^{-1}$  each. The cell-coated hydrogels are incubated at  $37 \text{ }^\circ\text{C}$  and 5%  $\text{CO}_2$ , as well as at  $32 \text{ }^\circ\text{C}$  and 5%  $\text{CO}_2$  for several days and analyzed by optical microscopy (Zeiss Axio) and CLSM. For cell growth on microgels, 2.5 mol%, 7.5 mol% and 12.5 mol% PDA.15 microgels are synthesized as described above and transferred in DPBS-D8537. Additionally, 2.5 mol%, 7.5 mol% and 12.5 mol% PDA.15/collagen microgels are synthesized, by incubating PDA.15 microgels in a solution of  $50 \mu\text{g mL}^{-1}$  collagen in 20 mM acetic acid at room temperature for 1 h. Afterwards, microgels are purified by washing three times with DPBS-D8537 using a centrifuge (10000 rpm, 5 min,  $5 \text{ }^\circ\text{C}$ ). For the low cell concentration experiments (1) and (2),  $1.57 \times 10^5 \text{ cells} \cdot \text{mL}^{-1}$  suspended in 3 mL DMEM (10% FBS, 1% Gl., 1% P/S) are transferred to a bioinert Petri dish and mixed with 10–20 7.5 mol% PDA.15 or 7.5 mol% PDA.15/collagen microgels and incubated for 24 h at  $32 \text{ }^\circ\text{C}$  and 5%  $\text{CO}_2$ . For the high cell concentration experiments (3) and (4),  $1.57 \times 10^6 \text{ cells} \cdot \text{mL}^{-1}$  suspended in 300  $\mu\text{L}$  DMEM (10% FBS, 1% Gl., 1% P/S) are transferred into a 96-well plate and 5–10 7.5 mol% PDA.15 or 7.5 mol% PDA.15/collagen microgels are added. The mixture is incubated for 1 h at  $32 \text{ }^\circ\text{C}$  and 5%  $\text{CO}_2$  and subsequently transferred into a bio-coated culture dish containing DMEM (10% FBS, 1% Gl., 1% P/S). Again, microgels are incubated for 1 h at  $32 \text{ }^\circ\text{C}$  and 5%  $\text{CO}_2$  and subsequently transferred to a bio-inert culture dish plate. and analyzed by CLSM, keeping the temperature constant at  $32 \text{ }^\circ\text{C}$ .

*Spheroid Culture:* The MCF7 human breast cancer cells (ATCC® Cat. No. HTB-22™) are cultured in DMEM (Dulbecco's Modified Eagle Media, Gibco, 10565018), supplemented with 10% FBS (Fetal bovine serum, Sigma Aldrich, F2442) and 1% PS (Penicillin/Streptomycin, Jena Bioscience, ML-105XL) at 37 °C and 5% CO<sub>2</sub> using standard cell culture methods. The 7.5 mol% PDA.15 PNIPAAm/HEAM microgels are incubated with 10–20 µg mL<sup>-1</sup> human plasma fibronectin (Millipore Cat. # FC010) for 1 h at room temperature with mild agitation. The microgels are washed twice with PBS buffer and used immediately in cell culture. Cells are grown to 80% confluence and the cells are stained with the vybrant™ Dio cell-labeling solution (Thermo Fisher Cat. No. V22886) following the manufacturer's protocol. The cells are detached with trypsin from the flask and resuspended in spheroid media (DMEM containing 3% FBS, 1% PS and 0.6% methylcellulose (Sigma Aldrich Cat. # M7027)). The cells are counted using a cell counter (BioRad, TC20™) and diluted to 2×10<sup>3</sup> cells · mL<sup>-1</sup>. The microgels are added to the cell suspension in a 1–3 microgels per 200 cells. 100 µL of the cell-microgel mixture (200 cells, 1–3 microgels) per well is pipetted into a U-bottom 96 well plate (Greiner bio-one Cat. # 650 185). The plate is centrifuged at 200 rcf for 3 min and cultured at 30 °C for 24 h. Total internal reflections and fluorescence images (488 nm excitation laser) confocal microscopy (Leica SP8) equipped with a temperature controller. Images are acquired initially at 30 °C, then the temperature was increased to 37 °C and subsequently again at 30 °C.

*CLSM:* Experiments are performed using a Leica TCS-SP8 AOBS SMD microscope with an HCPL APO CS2 10×/0.40 DRY objective. Cells expressing GFP are excited with an argon laser (488 nm), while fluorescence is detected between 500 nm and 600 nm using a PMT2 detector. Transmission is detected using a PMT Trans detector.

## 4.6. Literature

- [1] P. Bédard, S. Gauvin, K. Ferland, C. Caneparo, È. Pellerin, S. Chabaud, S. Bolduc, *Bioengineering* **2020**, *7*, 115.
- [2] F. Fontana, M. Raimondi, M. Marzagalli, M. Sommariva, N. Gagliano, P. Limonta, *Int. J. Mol. Sci.* **2020**, *21*, 6806.
- [3] R. Edmondson, J. J. Broglie, A. F. Adcock, L. Yang, *Assay Drug Dev. Technol.* **2014**, *12*, 207.
- [4] E. Stengelin, A. Kuzmina, G. L. Beltramo, M. F. Koziol, L. Besch, R. Schröder, R. E. Unger, W. Tremel, S. Seiffert, *Adv. Healthc. Mater.* **2020**, *6*, e1901820.
- [5] T. Rossow, P. S. Lienemann, D. J. Mooney, *Macromol. Chem. Phys.* **2017**, *218*, 1600380.
- [6] J. Feng, J. Dou, Y. Zhang, Z. Wu, D. Yin, W. Wu, *Polymers* **2020**, *12*, 547.
- [7] R. Begum, Z. H. Farooqi, E. Ahmed, A. Sharif, W. Wu, A. Irfan, *RSC Adv.* **2019**, *9*, 13838.
- [8] L. Yang, X. Fan, J. Zhang, J. Ju, *Polymers* **2020**, *12*, 389.
- [9] H. L. Judah, P. Liu, A. Zarbakhsh, M. Resmini, *Polymers* **2020**, *12*, E2590.
- [10] S. Seiffert, *Macromol. Rapid Commun.* **2011**, *32*, 1600.
- [11] K. Nagase, M. Yamato, H. Kanazawa, T. Okano, *Biomaterials* **2018**, *153*, 27.
- [12] N. Kaushik, L. Nhat Nguyen, J. H. Kim, E. H. Choi, N. Kumar Kaushik, *Int. J. Mol. Sci.* **2020**, *21*, 6544.
- [13] J. H. Ryu, P. B. Messersmith, H. Lee, *ACS Appl. Mater. Interfaces* **2018**, *10*, 7523.
- [14] H. Lee, S. M. Dellatore, W. M. Miller, P. B. Messersmith, *Science* **2007**, *318*, 426.
- [15] L. Zhang, Z. Liu, L.-Y. Liu, J.-L. Pan, F. Luo, C. Yang, R. Xie, X.-J. Ju, W. Wang, L.-Y. Chu, *ACS Appl. Mater. Interfaces* **2018**, *10*, 44092.
- [16] M. Seuss, W. Schmolke, A. Drechsler, A. Fery, S. Seiffert, *ACS Appl. Mater. Interfaces* **2016**, *8*, 16317.
- [17] G. Fundueanu, M. Constantin, I. Asmarandei, S. Bucatariu, V. Harabagiu, P. Ascenzi, B. C. Simionescu, *Eur. J. Pharm. Biopharm.* **2013**, *85*, 614.
- [18] J. Es Sayed, C. Lorthioir, P. Perrin, N. Sanson, *Soft Matter* **2019**, *15*, 963.
- [19] N. Adrus, M. Ulbricht, *React. Funct. Polym.* **2013**, *73*, 141.

- [20] J. Lin, W. Wang, J. Cheng, Z. Cui, J. Si, Q. Wang, W. Chen, *J. Appl. Polym. Sci.* **2020**, *137*, 49252.
- [21] H. A. Lee, E. Park, H. Lee, *Adv. Mater.* **2020**, *32*, e1907505.
- [22] J. Saiz-Poseu, J. Mancebo-Aracil, F. Nador, F. Busqué, D. Ruiz-Molina, *Angew. Chem., Int. Ed.* **2019**, *58*, 696.
- [23] C.-T. Kao, C.-C. Lin, Y.-W. Chen, C.-H. Yeh, H.-Y. Fang, M.-Y. Shie, *Mater. Sci. Eng. C* **2015**, *56*, 165.
- [24] Y. Wu, C. Yu, M. Xing, L. Wang, G. Guan, *J. Biomed. Mater. Res., Part B* **2020**, *108*, 117.
- [25] X. Zhang, W. Shen, J. Dou, Y. Meng, S. Fang, R. Liu, *J. Appl. Polym. Sci.* **2020**, *137*, 48486.
- [26] M. H. Futscher, M. Philipp, P. Müller-Buschbaum, A. Schulte, *Sci. Rep.* **2017**, *7*, 17012.
- [27] X. Xu, B. Bai, H. Wang, Y. Suo, *ACS Appl. Mater. Interfaces* **2017**, *9*, 6424.
- [28] F. Xu, S. Xie, R. Cao, Y. Feng, C. Ren, L. Wang, *Sens. Actuator, B* **2017**, *243*, 609.
- [29] X. Liu, J. Cao, H. Li, J. Li, Q. Jin, K. Ren, J. Ji, *ACS Nano* **2013**, *7*, 9384.
- [30] M. L. Alfieri, R. Micillo, L. Panzella, O. Crescenzi, S. L. Oscurato, P. Maddalena, A. Napolitano, V. Ball, M. D'Ischia, *ACS Appl. Mater. Interfaces* **2018**, *10*, 7670.
- [31] J.-L. Wang, K.-F. Ren, H. Chang, F. Jia, B.-C. Li, Y. Ji, J. Ji, *Macromol. Biosci.* **2013**, *13*, 483.
- [32] C. Spiteri, V. Caprettini, C. Chiappini, *Biomater. Sci.* **2020**, *8*, 6992.
- [33] A. Gaiko-Shcherbak, G. Fabris, G. Dreissen, R. Merkel, B. Hoffmann, E. Noetzel, *PLoS One* **2015**, *10*, e0145174.
- [34] K. J. R. Lewis, M. W. Tibbitt, Y. Zhao, K. Branchfield, X. Sun, V. Balasubramaniam, K. S. Anseth, *Biomater. Sci.* **2015**, *3*, 821.

# 5. Chapter III

●●● “Cell Adhesion on UV-Crosslinked Polyurethane  
Gels with Adjustable Mechanical Strength  
and Thermoresponsiveness”

<p>The results of the following chapter (p. 120–135) and the Supporting Information (p. 164–208) were published at <i>Macromolecular Rapid Communications</i> on September 25, 2021. In this thesis, the publication has been supplemented by an additional excursus.</p>
<p>■† <u>Elena Stengelin</u>,<sup>1†</sup> ■          ■          ■*,  <i>Macromol. Rapid Commun.</i> <b>2021</b>, 2100505.</p>
<p><sup>1</sup>Johannes Gutenberg University Mainz, Department of Chemistry, Duesbergweg 10–14, D-55128 Mainz, Germany          † Author 1 and Author 2 contributed equally to this work          * Corresponding author</p>
<p>Reprinted with permission from <i>Macromol. Rapid Commun.</i> <b>2021</b>, 2100505.          © 2021 The Authors. <i>Macromolecular Rapid Communications</i> published by Wiley-VCH GmbH</p>

## 5.1. Specific Summary

In addition to the two previously described publications (*Chapter I: “Bone Scaffolds Based on Degradable Vaterite/PEG-Composite Microgels”* and *Chapter II: “Rational Design of Thermoresponsive Microgel Templates with Polydopamine Surface Coating for Microtissue Applications”*), the following publication also pursues the overall goal of replacing animal testing by combining the experiences of the first two projects to provide a new microtissue platform from scratch. Accordingly, this project is mainly focused on the synthesis of new polymer materials with customizable properties. For this purpose, hydrolysis-sensitive precursor polymers based on



polyurethane (PU) are synthesized, whose thermoresponsive properties can be adjusted by the amphiphilic equilibrium of comonomers in the polymer framework. Furthermore, gel formation is achieved by incorporating dimethylmaleimide units in the backbone of the precursor polymers, which are covalently crosslinkable by UV irradiation. Depending on the amount of crosslinking units and the concentration of the precursor polymer, the mechanical strength of the gels can be adapted to the requirements of natural tissue. Due to the high poly(ethylene glycol) content in the PU-based networks, the hydrogels exhibit intrinsically low cell-adhesive properties, which is why their biocompatibility is promoted by incorporating catechol biolinkers into the networks. The corresponding biocompatibility is investigated in cell culture experiments. In an excursus, the transfer of the PU material platform to potential applications in microtissue engineering is additionally demonstrated by microfluidic experiments.

The personal contribution to the publication was the project development, interdisciplinary project coordination, lab work (cell experiments; confocal laser scanning microscopy imaging), data analysis, writing and illustration of the manuscript. The results of the excursus were developed in collaboration with [REDACTED] (Bachelor thesis: [REDACTED], Biokompatible Hydrogele mit einstellbarer Volumenphasenübergangstemperatur, Johannes Gutenberg-Universität Mainz, 2021.).

### **Acknowledgements**

Parts of the results of this study were acquired with a Confocal Laser Scanning Microscope funded in part by the Major Research Instrumentation Program of the German Research Foundation under grant No. INST 247/878-1 FUGG. The authors wish to thank [REDACTED] [REDACTED] for providing osteoblasts expressing GFP (MG-63 GFP).

## 5.2. Introduction

Thermoresponsive hydrogels are one of the most promising material platforms for modern biomedical applications with a scope ranging from nanomedical drug carriers to 3D in vitro models and tissue engineering applications.<sup>[1,2]</sup> Especially in the latter cases, it is crucial to provide soft materials which resemble the biological extracellular matrix (ECM). To ensure an efficient nutrient and waste transport as well as tissue-like mechanical properties, this requires hydrogels with swelling ratios between 50–85 wt%.<sup>[3,4]</sup> Depending on the respective application, the adaptive hydrogels should further be cell adhesive, biodegradable, and exhibit robust and distinct thermoresponsive properties.

While natural hydrogels such as proteins usually fulfill the bio-related requirements, their weak mechanical properties as well as the batch-to-batch variations resulting from their animal-based origins limit the application scope.<sup>[5,6]</sup> In contrast, the chemical and mechanical properties of synthetic hydrogels are by far easier to adjust to the application specific demands. However, synthetic materials are usually bioinert, and cell-adhesion must be enabled through additional bio-linkers or coatings that allow interactions with cell surface receptors.<sup>[7–10]</sup> Due to these complementary properties, the development of hydrogel platforms that combine the advantages of natural and synthetic materials is an ongoing challenge for materials scientists.

Regarding the thermal adaptivity of responsive hydrogels, poly(*N*-isopropylacrylamide) (PNIPAAm) is still the most common polymer backbone due its sharp volume phase transition (VPT) close to the physiological temperature range in aqueous media. Nevertheless, it has drawbacks. Although much progress was achieved with respect to the often insufficient mechanical performance of PNIPAAm-based hydrogels,<sup>[11]</sup> fundamental issues such as the non-degradability of the vinyl backbone remain.<sup>[12]</sup> To provide versatile alternatives, thermoresponsive polyurethane (PU) hydrogels received increasing interest. The general biocompatibility of PU materials is widely established and enabled various medical applications ranging from controlled drug delivery carriers<sup>[13–15]</sup> to promising or already commercialized materials for blood contacting devices like prosthetic heart valves.<sup>[16]</sup> In these materials, the urethane groups in the polymer backbone are not only responsible for the often superior mechanical strength of PU networks but are also intrinsically hydrolysable.<sup>[14,17–19]</sup>

To obtain thermoresponsive PUs, the combination of a hydrophilic oligomeric diol (soft segment) and a hydrophobic diisocyanate (hard segment) has been established as versatile design approach. Due to its commercial availability, pronounced hydrophilicity and

nontoxicity, poly(ethylene glycol) (PEG) became the most commonly applied soft segment. As shown by Fu et al., the variation of the polyether molar mass and thus the molar ratio of hydrophilic and hydrophobic segments allows for an easy variation of the lower critical solution temperature (LCST) of such amphiphilic PUs in aqueous solution.<sup>[18]</sup> Nevertheless, it should be noted that their turbidity measurements showed a rather broad ( $\approx 10$  °C) and partially incomplete LCST transition in comparison to PNIPAAm. This has been strongly improved through the introduction of charged comonomers, which further allowed an even more flexible variation of the LCST, as demonstrated by Sardon et al.<sup>[13,20]</sup>

To transfer the obtained insights from linear chains to 3D crosslinked networks, PU hydrogels have either been obtained in a crosslinking polymerization in the presence of a trifunctional comonomer<sup>[17,21,22]</sup> or through the consecutive crosslinking of linear precursor polymers with reactive side-groups.<sup>[20,23]</sup> As shown in the studies of Frydrych et al. and Li et al., the absolute swelling ratio of such PU gels can be varied through the molar mass of the polyether soft segment in both cases. The comparison of the equilibrium swelling ratios  $Q$  (in wt%) at 4 and 40 °C demonstrates a  $Q_{4^\circ\text{C}}/Q_{40^\circ\text{C}}$  switching around 100% in a purely PEG based system<sup>[17]</sup> while up to 600% can be achieved through the implementation of oligo(ethylene glycol) side chains as demonstrated by Aoki and Ajiro.<sup>[22]</sup>

Despite the numerous improvements achieved with respect to the processability, mechanical performance, and thermal adaptivity of PEG-based PU hydrogels, strategies to achieve cell adhesion have been rarely implemented. To overcome this limitation, in the present work, we apply the modular design principles established for thermoresponsive PUs to create hydrogels with adjustable mechanical strength and thermoresponsiveness that can additionally be bio-activated through the covalent attachment of cell-adhesive groups. As a consecutive crosslinking strategy provides a greater flexibility with respect to the material's processability, we focus on the synthesis of linear PUs based on PEG and isophorone diisocyanate (IPDI). To avoid unspecific crosslinking, toxic catalysts or a strong pH dependency, an uncharged dimethylmaleimide (DMMI) comonomer is incorporated as reactive side-group which undergoes a dimerization reaction in the presence of a photosensitizer and UV light.<sup>[24]</sup> To improve the cell adhesion on these gels, we further attach arginine-glycine-aspartate- (RGD) amino acid sequences and catechol groups to the network through the identical DMMI dimerization reaction.

## 5.3. Results & Discussion

### 5.3.1. Thermoresponsive, UV-Crosslinkable Polyurethanes

Linear PUs are synthesized in a prepolymer procedure starting from PEG diols with differing molar masses ( $M_n \approx 1.0$  (**1a**), 1.5 (**1b**), 2.0 (**1c**) and 4.0 (**1d**)  $\text{kg}\cdot\text{mol}^{-1}$ ) that are added to the asymmetric isophorone diisocyanate (IPDI) **2** and converted into the corresponding macrodiisocyanates (PEG/IPDI) **3a–d** by reaction with the cycloaliphatic, secondary isocyanate group under organo-tin catalysis (**Figure 5-1a**).<sup>[25–27]</sup> To incorporate dimerizable DMMI-groups, 2,3-dimethyl maleic anhydride **10** is first attached to a hydrophilic triethylene glycol linker **9**, which is coupled with the acetonide protected 2,2-bis(hydroxymethyl)propionic acid **14** as shown in **Scheme S9-1** in the Supporting Information (SI). The deblocked DMMI-diol **4** is then applied as chain extender for the PEG diisocyanates **3a–d**. Size exclusion chromatography (SEC) measurements of the PEG diols **3a–d** and the obtained linear PUs **5a–e** demonstrate moderately effective but sufficient chain elongation efficiencies as summarized in **Table 5-1** and **Figure S9-23**.

**Table 5-1.** PEG diols applied in the polymerization. Characterization of the synthesized PUs.

#	$M_n$ (PEG diol) [ $\text{kg}\cdot\text{mol}^{-1}$ ] <sup>a)</sup>	$M_w$ [ $\text{kg}\cdot\text{mol}^{-1}$ ] <sup>a)</sup>	$D$ <sup>a)</sup>	$n_{\text{EG}}/n_{\text{IPDI}}/n_{\text{DMMI}}$ <sup>b)</sup>	$T_{\text{cp}}$ [°C]
<b>5a</b> - PU-1.0k	0.88	6.3	1.5	29:2.7:1	5
<b>5b</b> - PU-1.5k <sup>0.6</sup>	1.24	12.0	1.9	36:2.8:1	18
<b>5c</b> - PU-1.5k	1.24	12.4	1.8	47:3.3:1	28
<b>5d</b> - PU-2.0k	1.95	14.6	1.6	61:3.2:1	52
<b>5e</b> - PU-4.0k	4.22	30.3	1.5	140:4.5:1	> 90

<sup>a)</sup> SEC (DMF, PEG calibration); <sup>b)</sup> <sup>1</sup>H-NMR analysis (EG: 3.76–3.40 ppm, 4H; IPDI: 1.19–0.06 ppm, 15H; DMMI: 1.89 ppm, 6H).

The molar ratios between the hydrophilic ethylene glycol (EG) units of the PEG backbone and the hydrophobic IPDI-DMMI blocks are investigated by <sup>1</sup>H-NMR spectroscopy. Comparing the characteristic signals of the DMMI methyl groups (1.89 ppm), the IPDI cycloaliphatic methylene- and methyl-groups (1.19–0.06 ppm) and the PEG backbone (3.76–3.40 ppm) reveals the intended increase of the molar content of hydrophilic EG groups with the molar mass of the polyether (**Table 5-1**, **Figure S9-(41–46)**). To enable an even finer variation of the hydrophilic-to-hydrophobic balance than accessible through the commercially available PEG diols, the molar feed ratio between PEG and DMMI is additionally varied from 1:1 to 1:2.3 for PEG-1.5k (**5b** - PU-1.5k<sup>0.6</sup>). The <sup>1</sup>H-NMR analysis verifies that

this approach is another facile option to alter the PU composition. All experimental details and full characterizations can be found in the SI.

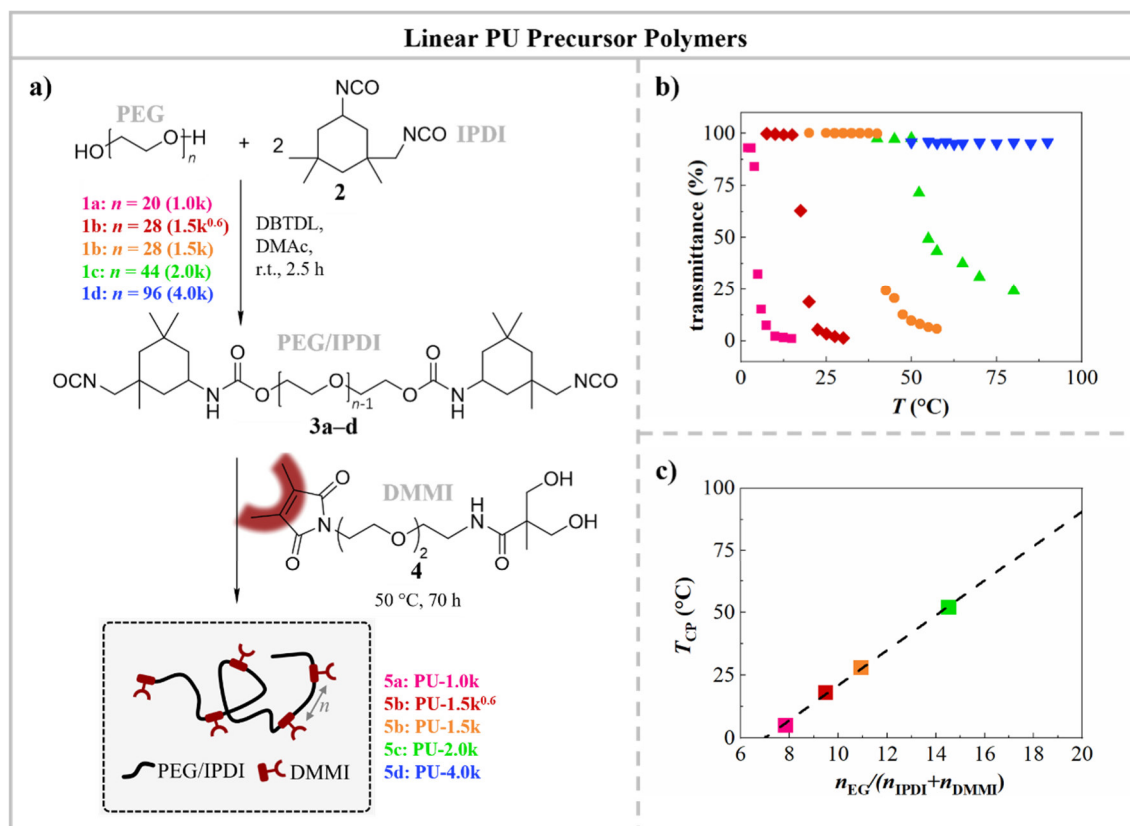


**Figure 5-1.** (a) Synthesis of linear PEG/IPDI-based PUs with DMMI pendant groups (**5a–e**). (b) Turbidity measurements of **5a** - PU-1.0k (■), **5b** - PU-1.5k<sup>0.6</sup> (◆), **5c** - PU-1.5k (●), **5d** - PU-2.0k (▲) and **5e** - PU-4.0k (▼) in water (5 g·L<sup>-1</sup>). (c) Cloud point temperatures as a function of the molar ratio between EG, IPDI and DMMI with linear regression (dashed line).

To investigate how the variation of the amphiphilic balance influences the thermoresponsivity, the cloud point temperatures  $T_{CP}$  are determined through UV-Vis transmittance measurements in dilute aqueous solutions (**Figure 5-1b**). As shown in **Figure 5-1b**, the cloud point temperatures depend linearly on the molar ratio between hydrophilic EG and hydrophobic IPDI and DMMI groups and can be varied from 5 to over 90 °C. In accordance with the observations reported by Li et al. and Ronco et al., the turbidity curves depicted in **Figure 5-1b** also reveal a sharper and more pronounced LCST transition for the more hydrophobic PU compositions.<sup>[20,23]</sup>

### 5.3.2. Gelation and Mechanical Properties

Further on, the UV-induced crosslinking of the linear precursor polymer solutions in the presence of the photosensitizer thioxanthone disulfonate (TXS) is investigated by linear shear rheological experiments. Applying **5e** - PU-4.0k ( $\rho_{\text{PU}} = 100 \text{ g}\cdot\text{L}^{-1}$ ) as a representative example, the gelation time in terms of the  $G'$ - $G''$  crossover is determined as  $t_{\text{gel}} = 8 \text{ min}$  at a TXS concentration of 1 mM and an irradiation aperture of 1%, and is shown to be temperature independent between 5–20 °C (**Figure S9-24**). When the TXS concentration is reduced to 0.1 mM while the irradiation intensity is kept constant at 1%, the gelation time increases to 68 min while the obtained gel strength remains constant. The gelation time at the lower TXS concentration (0.1 mM) can however be reduced to 7 min if the irradiation aperture is increased to 10%. This qualitative parameter screening demonstrates how the gelation time of the DMMI crosslinked hydrogels can be readily adjusted by these two external parameters.

Next, we investigate how the gel strength in terms of the plateau modulus depends on the precursor polymer concentration of **5e** - PU-4.0k ( $T = 5 \text{ }^\circ\text{C}$ ). As indicated in **Figure 5-2a**, no stable gel is obtained below a concentration of  $\rho_{\text{PU}} = 100 \text{ g}\cdot\text{L}^{-1}$ . Above this gelation threshold, the plateau moduli increase approximately linearly from 200 to 3900 Pa with the polymer concentration (**Figure 5-2b**), as expected for affine and phantom networks. It should be noted though, that the precursor solutions then become increasingly viscous (**Figure 5-2a**) which leads to inhomogeneities and handling difficulties.

Further on, we compare the mechanical properties of hydrogels obtained from the different precursor polymers ( $\rho_{\text{PU}} = 100 \text{ g}\cdot\text{L}^{-1}$ ). **5a** - PU-1.0k is excluded from all further experiments due to its incomplete dissolution in water at higher polymer contents. As shown in **Figure 5-2c**, the time-dependent plateau moduli clearly demonstrate the dependency of the gel strength on the average sticker spacing, which is mainly determined by the PEG molar mass (**Figure 5-2d**). As expected, the **5b** - PU-1.5k<sup>0.6</sup> hydrogel shows the highest plateau modulus (1200 Pa), which decreases with the PEG content and molar mass to 990 Pa (**5c** - PU-1.5k), 370 Pa (**5d** - PU-2.0k), and finally 200 Pa (**5e** - PU-4.0). In summary, the concentration and precursor polymer dependent mechanical properties are qualitatively consistent with the expected structure–property relations and allow an easy adjustment of the gel strength between 200–4000 Pa though the precursor polymer concentration and average sticker density.

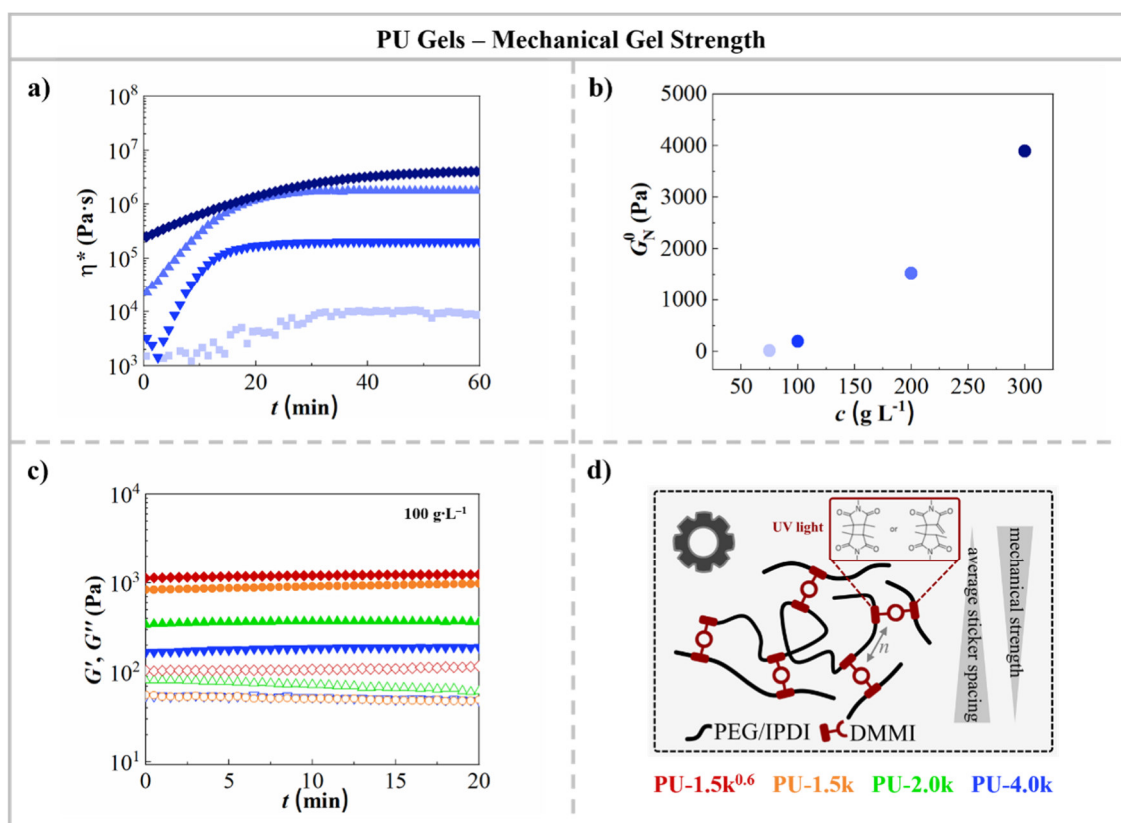


**Figure 5-2.** (a) Time-dependent complex viscosity of **5e** PU-4.0k solutions under UV irradiation at a concentration of 75 ( $\blacksquare$ ), 100 ( $\blacktriangledown$ ), 200 ( $\blacktriangle$ ), and 300 g·L<sup>-1</sup> ( $\blacklozenge$ ). Gelation occurs at a TXS concentration of 1 mM, an irradiation aperture of 1% (320–500 nm), and at a temperature of 5 °C. (b) Plateau moduli as a function of the PU-4k concentration. (c) Time-dependent storage  $G'$  (closed symbols) and loss  $G''$  moduli (open symbols) of **5b** PU-1.5k<sup>0.6</sup> ( $\blacklozenge$ ), **5c** PU-1.5k ( $\bullet$ ), **5d** PU-2.0k ( $\blacktriangle$ ) and **5e** PU-4.0k ( $\blacktriangledown$ ) hydrogels at a concentration of 100 g·L<sup>-1</sup> ( $T = 5$  °C). (d) Schematic representation of the DMMI crosslinked PU networks.

### 5.3.3. Swelling Properties of PU Hydrogels

To investigate the temperature-dependent hydration behavior (**Figure 5-3a**), the swelling degrees of PU gels crosslinked at  $c_{PU} = 100$  g·L<sup>-1</sup> are measured at 5, 20, and 40 °C after equilibration for 12 h at each temperature. Note that the synthesized hydrogels are thoroughly dialyzed beforehand to avoid interferences with a potentially occurring sol fraction. It can first be observed that the swelling degrees of the fully hydrated networks at 5 °C show the same crosslinking-density dependency as the gel strength and increase from 2700% (PU-1.5k<sup>0.6</sup>) over 4100% (PU-1.5k) and 5000% (PU-2.0k) to 7800% (PU-4.0k) with increasing soft segment length (**Figure 5-3b**). This tendency is in accordance with the findings reported by Li et al. and Frydrych et al. who also varied the PEG molar mass in chemically cross-linked PU hydrogels and investigated their temperature-dependent equilibrium swelling.<sup>[17,23]</sup>

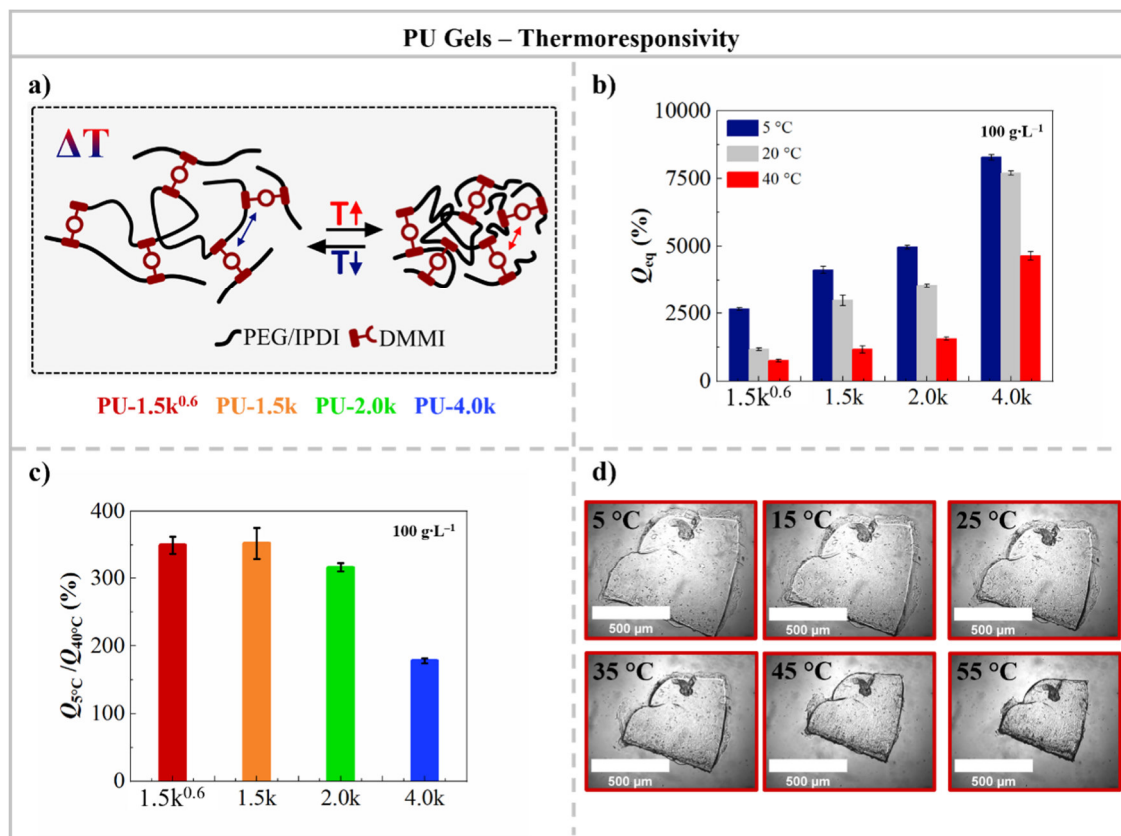


**Figure 5-3.** (a) Schematic representation of the temperature-induced hydrogel deswelling. (b) Equilibrium swelling degrees and (c) swelling degree switches between 5 and 40 °C of **5b** - PU-1.5k<sup>0.6</sup> (—), **5c** - PU-1.5k (—), **5d** - PU-2.0k (—) and **5e** - PU-4.0k (—) hydrogels crosslinked at a concentration of  $100 \text{ g}\cdot\text{L}^{-1}$  and equilibrated for 12 h at 5, 20 and 40 °C. (d) Microscope images of **5b** - PU-1.5k<sup>0.6</sup> gels at increasing temperatures.

The thermal responsiveness of the hydrogels is further evaluated by comparing the equilibrium swelling degrees at 5 and 40 °C. As depicted in **Figure 5-3c**, the temperature induced volume switch decreases around a factor two from  $(350 \pm 12)\%$  (**5b** - PU-1.5k<sup>0.6</sup>) to  $(180 \pm 4)\%$  (**5e** - PU-4.0k) from the most hydrophobic to the most hydrophilic PU composition. This trend qualitatively reflects the LCST behavior of the dilute precursor polymer solutions which was shown to depend linearly on the balance between hydrophilic EG and hydrophobic DMMI- and IPDI-monomers (**Figure 5-1c**). However, within the crosslinked gels this dependency is not as clearly pronounced and the volume switches of the PU-1.5k<sup>0.6</sup> and PU-1.5k gels even coincide within the margin of error. Note, that the considerable weighing error and small sample number (performed in triplicate) limit the accuracy of the swelling degree determinations in contrast to the turbidity measurements. Nonetheless, in comparison to the formerly mentioned studies on similar PU hydrogels, it can be observed that the volume switches between 5 and 40 °C of the PEG-2.0k- ( $(320 \pm 7)\%$ ) and PEG-1.5k- ( $(350 \pm 12)\%$ ) based hydrogels significantly exceed those reported by Li et al. (PEG-2.0k,  $\approx 100\%$ )<sup>[23]</sup> and



Frydrych et al. (PEG-1.5k,  $\approx 200\%$ ).<sup>[17]</sup> This is likely caused by the additionally incorporation of the hydrophobic DMMI-groups and generally depends on the overall amphiphilic balance. As exemplarily shown for PU-1.5k<sup>0.6</sup>, the temperature-induced deswelling is also accompanied by a significant size reduction corresponding to 83% (25 °C), 69% (45 °C) and finally 63% (55 °C) of the initial diameter at 5 °C (**Figure 5-3d**).

### 5.3.4. Bio-Linker Attachment and Cell Adhesion

To generate bio-adhesive hydrogel surfaces, we further investigated the possibility to incorporate integrins such as catechol groups or RGD sequences into the PU networks, since both groups are known to promote cell adhesion. To keep the polymer design simple, the initially incorporated DMMI side-groups are also used for the attachment of these bio-linkers. For this purpose, 3,4-(dihydroxyphenyl)propionic acid **16** is coupled with a DMMI functionalized triethylene glycol linker **12** in an HATU mediated amidation to obtain the DMMI-functionalized catechol **6** (**Figure 5-4a, Scheme S9-2**). Analogously, the RGD-alkyne derivate **23** synthesized by solid phase peptide synthesis is coupled with a triethylene glycol-DMMI azide linker **22** in a copper catalyzed azide-alkyne cycloaddition (**Figure 5-4a, Scheme S9-3**). The triethylene glycol linker ensures the water solubility of both bio-linkers. The schematic incorporation of RGD-DMMI units in the PU gel is shown in **Scheme S9-5**. To further ensure the mechanical integrity of the hydrogels and to allow good material handling in the cell adhesion test, we changed the polymer concentration from 100 to 200 g·L<sup>-1</sup>.

Analytical evidence of the bio-linker incorporation into the PU gels is provided by <sup>1</sup>H magic angle spinning (MAS) NMR spectroscopy (**Figure 5-4b**). The <sup>1</sup>H MAS NMR spectra of thoroughly dialyzed PU-2.0k (200 g·L<sup>-1</sup>) gels with 0 mol% RGD (i) and 25 mol% RGD (ii) (compared to the PU-DMMI groups) are analyzed and compared to the one of pure RGD-DMMI **7** (iii). As shown in **Figure 5-4b** (ii) the <sup>1</sup>H NMR spectrum is dominated by the PU backbone resonances, but the additionally occurring signals at 7.87 ppm (triazole-CH), 4.58 ppm (triazoleN-CH<sub>2</sub>), 3.22 ppm (arginine NHCH), 3.06 ppm (triazoleC-CH<sub>2</sub>CH<sub>2</sub>), and 2.73 ppm (triazoleC-CH<sub>2</sub>CH<sub>2</sub>) can be assigned to the RGD-DMMI and indicate the successful incorporation into the network. An especially clearly visible example is the resonance of the triazole proton at  $\delta = 7.82$  ppm. The weak, low field-shoulder observed the reference spectrum in aqueous solution is presumably caused by a second tautomeric of the triazole.<sup>[28,29]</sup> Nonetheless, it can be noted that the signal of the RGD-DMMI linker is shifted to

$\delta = 7.87$  ppm inside the gel and significantly broadened as shown by the increased full width at half height fwhh (solution: fwhh = 2.42 Hz; gel: fwhh = 9.05 Hz). A similar broadening is observed for all related signals and can be explained by the confinement in the gel pores resulting in reduced chain dynamics. An analogous measurement with 5 mol% RGD showing the same characteristic signals with lower intensities is provided in the SI (Figure S9-25).

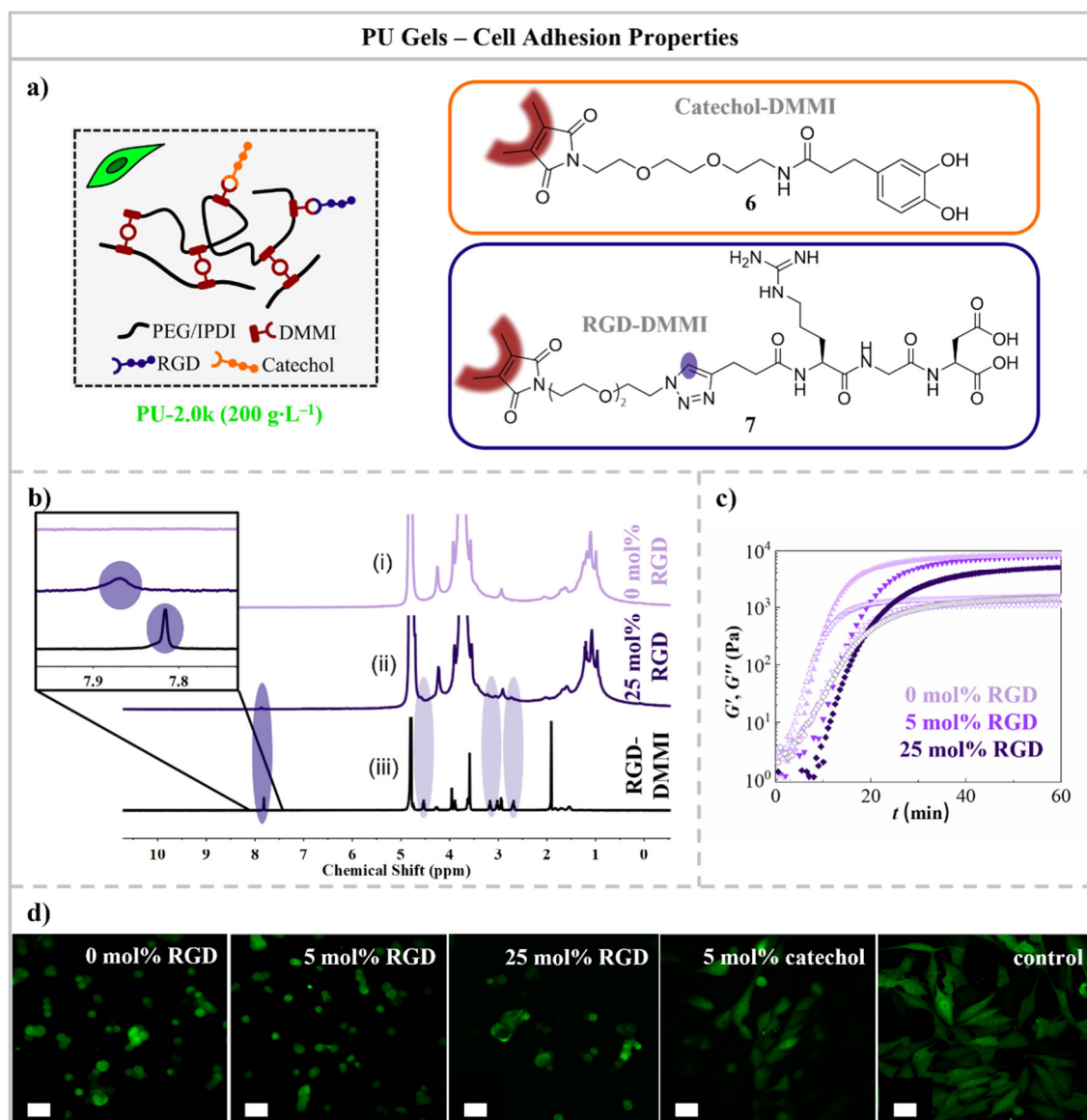


**Figure 5-4.** (a) Scheme for the incorporation of RGD-DMMI (highlighted in purple) or catechol-DMMI (highlighted in orange) groups into the PU networks to increase their cell adhesive properties. (b)  $^1\text{H}$  MAS NMR spectra of PU-2.0k gels ( $200\text{ g}\cdot\text{L}^{-1}$ ) containing 0 mol% (i) and 25 mol% RGD-DMMI (ii) in  $\text{D}_2\text{O}$  and  $^1\text{H}$  solution NMR spectrum of DMMI-RGD (iii) in  $\text{D}_2\text{O}$ . (c) Mechanical strength of PU-2.0k gels ( $200\text{ g}\cdot\text{L}^{-1}$ ) with 0, 5, and 25 mol% RGD-DMMI bio-linker. (d) CLSM imaging of green-fluorescent cells (MG-63 GFP) after 24 h incubation ( $37^\circ\text{C}$  and  $5\%\text{ CO}_2$ ) on PU-2.0k gels ( $200\text{ g}\cdot\text{L}^{-1}$ ) with 0, 5, and 25 mol% RGD, and 5 mol% catechol. For comparison, a control experiment with cells growing on polystyrene-based petri dishes with cell adhesive properties is also shown. The scale bars refer to  $50\ \mu\text{m}$ .

Since the DMMI groups that react with a linker molecule cannot contribute to the 3D cross-linking reaction, it is further investigated how the attachment of RGD sequences influences the gelation of the PU-2.0k gels ( $200 \text{ g}\cdot\text{L}^{-1}$ ). As shown in **Figure 5-4c**, the addition of 5 mol% RGD to the precursor solution does not significantly affect the plateau modulus. If the concentration is however increased to 25 mol%, a 40% lower plateau modulus results. In addition to this investigation during the gelation process, it is also probed how the incorporation of the catechol linker influences the mechanical properties of the purified gels under equilibrium swelling conditions (**Figure S9-26**). The results coincide with the former findings and demonstrate that the applicable concentration range of the bio-linkers is limited by the accessible number of DMMI groups in the PU chains.

To analyze the cell adhesive properties of PU gels with RGD or catechol bio-linkers, cell experiments are performed (**Figure 5-4**). For this purpose, green-fluorescent osteoblasts (MG-63 GFP) are cultured on PU-2k gels ( $200 \text{ g}\cdot\text{L}^{-1}$ ) with 0 and 5 mol% RGD and catechol. After 24 h, the gels are analyzed by Confocal Laser Scanning Microscopy (CLSM). The cells on the 0 and 5 mol% RGD gels show a spherical morphology, indicating a low cell adhesion capacity. By contrast, the cells on the 5 mol% catechol gels show an elongated morphology comparable to the control experiment, indicating a pronounced cell adhesion. Consequently, the question arises as to why the cells adhere to the catechol-based but not to the RGD-based PU-2k hydrogels. This is likely due to the insufficient amount of integrins in the RGD-based polymer, as the cells require a certain concentration of integrins to adhere.<sup>[30,31]</sup> Although the same concentration of RGD and catechol units was used, the total integrin density in catechol is higher because serum proteins from the culture medium adhere to the catechol units, which have a higher number of integrin binding sites than single amino acid sequences such as RGD.<sup>[32,33]</sup> To probe whether an analogous behavior can be achieved at a higher RGD concentration, the experiment is repeated with a 25 mol% RGD containing gel. However, as can be seen in **Figure 5-4d**, this increase in concentration is still insufficient, which can be explained by the decreasing mechanical gel strength. The more RGD sequences are incorporated into the network, the fewer network junctions can be formed which increases the swelling degree of the corresponding hydrogels. Due to this counteracting behavior, an increase of the RGD concentration does not efficiently increase the RGD density in the network and thus prevents an improvement of the cell attachment. Beyond that, sufficiently stable gels are not obtained above 25 mol% RGD. Hence, it is not practicable to improve the cell adhesion by a further increase of the RGD concentration. Based on this comparison,

the catechol linkers are found to be a suitable way to increase the biocompatibility of the PU hydrogels.

### 5.3.5. Excursus: Microgel Preparation via Microfluidics

Since microgels are valuable tools for microtissue applications, PU microgels of type **5b** - PU-1.5k<sup>0.6</sup>, **5c** - PU-1.5k, and **5d** - PU-2.0k are synthesized using a polydimethylsiloxane (PDMS)-based microfluidic setup as shown in **Figure 5-5a**. For this purpose, monodisperse droplets based on an aqueous PU precursor/TXS-photosensitizer solution are prepared by flow focusing at the intersection of the PDMS-channel system with an immiscible carrier fluid (Novec 7500/Krytox). The PU precursor polymers are covalently connected via UV irradiation inside the monodisperse droplets to form stable microgels. After removal of the carrier fluid and surfactant (Krytox), microgels are transferred to water, and microgel diameters between 171–182  $\mu\text{m}$  (20  $^{\circ}\text{C}$ ) are obtained (**Figure 5-5b**).

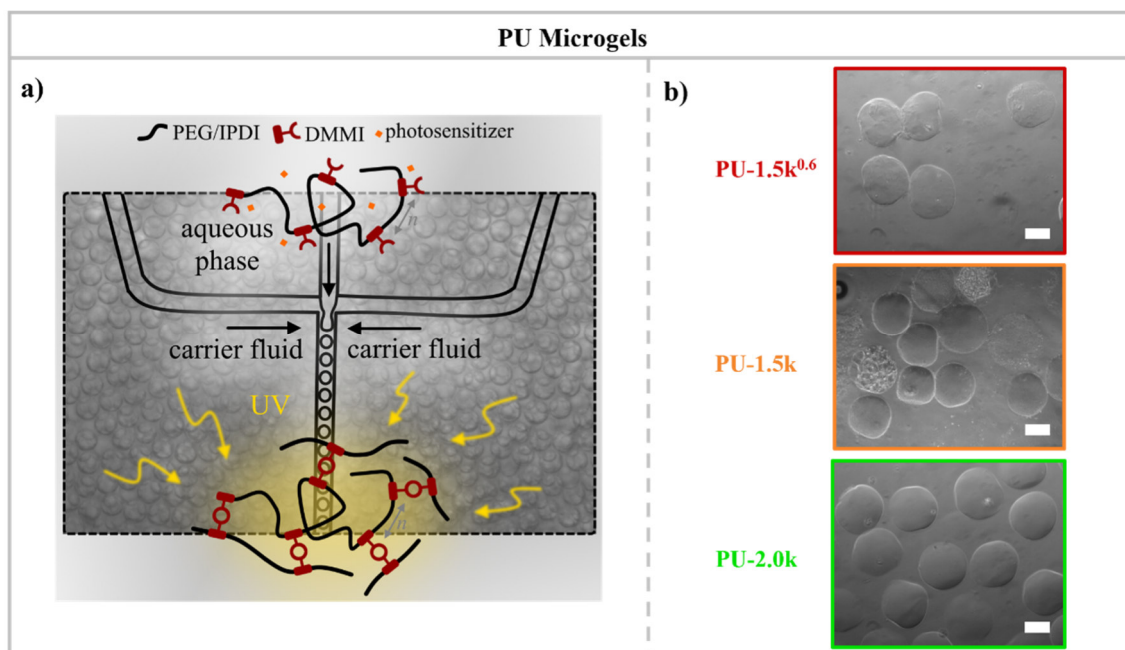


**Figure 5-5.** **5b** - PU-1.5k<sup>0.6</sup>, **5c** - PU-1.5k, and **5d** - PU-2.0k microgels synthesized by microfluidics. a) Schematic of the microfluidic setup. (b) Photographs of microgels at 20  $^{\circ}\text{C}$  in water. The scale bars refer to 100  $\mu\text{m}$ .

While microgels from the **5d** - PU-2.0k system have a stable and monodisperse spherical structure, microgels from the **5b** - PU-1.5k<sup>0.6</sup> and **5c** - PU-1.5k systems are less stable and polydisperse. These differences can be caused by phase separation processes during droplet formation, which lead to inhomogeneities in the polymer network. Due to the cloud point temperatures close to room temperature (**5b** - PU-1.5k<sup>0.6</sup> (18  $^{\circ}\text{C}$ ); **5c** - PU-1.5k (28  $^{\circ}\text{C}$ )), partial precipitation of the precursor polymers is likely. By using UV irradiation to crosslink the

precursor polymers, the temperature inside the droplets can be additionally increased, which also affects the phase separation process. This behavior is less pronounced in the **5d** - PU-2.0k system due to the higher cloud point temperature of 52 °C. In summary, this leads to monodisperse microgels with homogeneously pronounced swelling behavior. Microgels of type **5d** - PU-2.0k therefore have the greatest potential for microtissue engineering applications. To expand the toolbox of microgels and to realize their full potential, the microfluidic conditions need to be improved.

## 5.4. Conclusion

In this study, thermoresponsive PEG-IPDI-based PUs with dimerizable DMMI side groups are synthesized. The cloud point temperatures of the dilute aqueous PU solutions depend linearly on the molar ratio between hydrophilic EG and hydrophobic IPDI and DMMI groups and can be varied from 5 to above 90 °C. Soft hydrogels are obtained by UV light-induced crosslinking of the precursor polymers in the presence of a photosensitizer. Both the equilibrium swelling ratio ( $Q_{5^{\circ}\text{C}} = 2700\text{--}7800\%$ ) and the gel strength in terms of plateau modulus ( $G' = 200\text{--}4000$  Pa) are determined by the precursor polymer concentration and the average DMMI density. The changes in the swelling ratio of the hydrogels ( $Q_{5^{\circ}\text{C}}/Q_{40^{\circ}\text{C}}$ ) reflect the dependence of the cloud point temperature on the amphiphilic equilibrium, increasing from 180% to 350% for the more hydrophobic PU compositions. Moreover, the cell adhesive properties of these PU gels can be significantly improved by incorporating low concentrations of a catechol biolinker via DMMI side groups without significantly affecting the mechanical properties. In microfluidic experiments, microgels with homogeneous size distributions were synthesized using the precursor PU polymers with cloud point temperatures of about 50 °C. Below this temperature, the size distribution was quite inhomogeneous and needs to be improved in further studies.

## 5.5. Literature

- [1] F. Doberenz, K. Zeng, C. Willems, K. Zhang, T. Groth, J. Mater. Chem. B 2020, 8, 607.
- [2] L. Klouda, A. G. Mikos, *Eur. J. Pharm. Biopharm.* **2008**, 68, 34.
- [3] H. Fan, J. P. Gong, *Macromolecules* **2020**, 53, 2769.
- [4] C. A. Deforest, K. S. Anseth, *Annu. Rev. Chem. Biomol. Eng.* **2012**, 3, 421.
- [5] J. J. Rice, M. M. Martino, L. De Laporte, F. Tortelli, P. S. Briquez, J. A. Hubbell, *Adv. Healthcare Mater.* **2013**, 2, 57.
- [6] D. Dippold, A. Cai, M. Hardt, A. R. Boccaccini, R. E. Horch, J. P. Beier, D. W. Schubert, *Mater. Sci. Eng. C* **2019**, 95, 217.
- [7] Y. Zhang, J. Hu, X. Zhao, R. Xie, T. Qin, F. Ji, *ACS Appl. Bio Mater.* **2019**, 2, 1056.
- [8] K. Wei, X. Chen, P. Zhao, Q. Feng, B. Yang, R. Li, Z.-Y Zhang, L. Bian, *ACS Appl. Mater. Interfaces* **2019**, 11, 16328.
- [9] T. J. Dennes, J. Schwartz, *Soft Matter* **2008**, 4, 86.
- [10] E. Stengelin, B. N. Mombo, M. Mondeshki, G. L. Beltramo, M. A. Lange, P. Schmidt, H. Frerichs, S. V Wegner, S. Seiffert, *Macromol. Biosci.* **2021**, 21, 2100209.
- [11] A. Bin Imran, K. Esaki, H. Gotoh, T. Seki, K. Ito, Y. Sakai, Y. Takeoka, *Nat. Commun.* **2014**, 5, 5124.
- [12] V. Pertici, C. Pin-barre, C. Rivera, C. Pellegrino, D. Gimes, T. Trimaille, *Biomacromolecules* **2019**, 20, 149.
- [13] H. Sardon, J. P. K. Tan, J. M. W. Chan, D. Mantione, D. Mecerreyes, J. L. Hedrick, Y. Y. Yang, *Macromol. Rapid Commun.* **2015**, 36, 1761.
- [14] L. Polo Fonseca, R. B. Trinca, M. I. Felisberti, *Int. J. Pharm.* **2018**, 546, 106.
- [15] M. Ding, N. Song, X. He, J. Li, L. Zhou, H. Tan, Q. Fu, Q. Gu, *ACS Nano* **2013**, 7, 1918.
- [16] F. Oveissi, S. Naficy, A. Lee, D. S. Winlaw, F. Dehghani, *Mater. Today Bio* **2020**, 5, 100038.
- [17] M. Frydrych, S. Román, N. H. Green, S. Macneil, B. Chen, *Polym. Chem.* **2015**, 6, 7974.
- [18] H. Fu, H. Gao, G. Wu, Y. Wang, Y. Fan, J. Maa, *Soft Matter* **2011**, 7, 3546.

- [19] J. P. Santerre, K. Woodhouse, G. Laroche, R. S. Labow, *Biomaterials* **2005**, *26*, 7457.
- [20] L. I. Ronco, A. Basterretxea, D. Mantione, R. H. Aguirresarobe, R. J. Minari, L. M. Gugliotta, D. Mecerreyes, H. Sardon, *Polymer* **2017**, *122*, 117.
- [21] D. Aoki, H. Ajiro, *Macromol. Rapid Commun.* **2018**, *39*, 1800239.
- [22] D. Aoki, H. Ajiro, *Macromol. Rapid Commun.* **2021**, *42*, 2100128.
- [23] K. Li, C. Zhou, S. Liu, F. Yao, G. Fu, L. Xu, *React. Funct. Polym.* **2017**, *117*, 81.
- [24] S. Seiffert, W. Oppermann, K. Saalwächter, *Polymer* **2007**, *48*, 5599.
- [25] S. V. Karpov, V. P. Lodygina, V. V. Komratova, A. S. Dzhalmukhanova, G. V. Malkov, E. R. Badamshina, *Kinet. Catal.* **2016**, *57*, 422.
- [26] H.-K. Ono, F. N. Jones, S. P. Pappas, *J. Polym. Sci. Polym. Lett. Ed.* **1985**, *23*, 509.
- [27] K. Breul, S. Seiffert, *Polym. Chem.* **2021**, *12*, 2305.
- [28] L. Lunazzi, F. Parisi, D. Macciantelli, *J. Chem. Soc. Perkin Trans. 2* **1984**, 1025.
- [29] J. R. Cox, S. Woodcock, I. H. Hillier, M. a Vincent, *J. Phys. Chem.* **1990**, 5499.
- [30] J. A. Rowley, D. J. Mooney, *J. Biomed. Mater. Res.* **2002**, *60*, 217.
- [31] J. A. Burdick, K. S. Anseth, *Biomaterials* **2002**, *23*, 4315.
- [32] S. Spaans, P. P. K. H. Fransen, B. D. Ippel, D. F. A. De Bont, H. M. Keizer, N. A. M. Bax, C. V. C. Bouten, P. Y. W. Dankers, *Biomater. Sci.* **2017**, *5*, 1541.
- [33] W.-B. Tsai, W.-T. Chen, H.-W. Chien, W.-H. Kuo, M.-J. Wang, *Acta Biomater.* **2011**, *7*, 4187.

## 6. Summary & Conclusion

In this work, three separate studies are presented that focus on the development of adaptive and smart synthetic materials for potential applications in microtissue engineering. The major goal of each section is to develop new *in vitro* models that can replace animal experiments based on the 3R principles in the long term. All the individual studies combine into a toolbox that offers new strategies for replacing animal experiments in science. Particular attention is paid to the materials used and their properties such as processability, adaptivity, biocompatibility, and stability/degradability, as well as their shaping by droplet-based microfluidics. The investigations are additionally complemented by cell experiments to demonstrate the biotechnological applicability of the materials.

The first study addresses potential *in vitro* model systems as promising material platforms to study cellular metabolic processes in bone formation. Droplet-based microfluidics is used to produce microgel systems with embedded living cells, vaterite particles, or a combination of both. It is demonstrated that by using poly(ethylene glycol) (PEG)-based precursor polymers and varying their molar masses, microgels with tunable gelation times and viscoelastic properties can be generated. Their respective influence on the viability of the encapsulated cells is shown in 3D cell studies. In addition, confocal Raman microscopy measurements show successful conversion of the embedded vaterite to hydroxycarbonate apatite. The stable triple combination of microgels, vaterite particles, and cells demonstrates a well-designed and analyzed microgel composite system with a cell viability comparable to that of the dual combination of microgels and cells. Finally, the degradation potential of the hydrolysis-sensitive microgel systems is demonstrated. Overall, this results in a high-performance composite material that can support the bone growth process due to its specific material properties and also serves as a model system for future microtissue-based *in vitro* bone mineralization studies. The methods and findings obtained from the material design and cell experiments also provide a valuable basis for further projects.

In a second study, novel core–shell microtemplate platforms are presented for *in vitro* fabrication and analysis of hollow, spherical tissue constructs, mainly to mimic the blastula in embryogenesis, mammary glands, or the alveolar epithelium. For this purpose, the synthesis of thermoresponsive and long-term stable microgel cores based on poly(N-



isopropylacrylamide) (PNIPAAm) and various amounts of a hydrophilic comonomer using droplet-based microfluidics is demonstrated. Microgels, that differ significantly in size and mechanical strength in the physiological temperature range, are obtained. In addition, the biocompatibility of the microgel cores is improved by a homogeneous surface coating with polydopamine as well as collagen or fibronectin, without affecting the mechanical microgel properties. Corresponding results are provided through 3D cell culture experiments, which show comparable, homogeneous cell growth on the surface of all microgel types. Further cell experiments also show the formation of microgel-based cell agglomerates that respond volumetrically to temperature changes. Overall, multifunctional core–shell microcarrier systems provide a powerful platform for further and more intense research and development of *in vitro* microtissue-based structures.

The third study presented in this work, focuses on the development of polyurethane (PU)-based polymers as potential materials for future *in vitro* studies on microtissues. The successful design and synthesis of hydrolysis-sensitive PEG-based PU precursor polymers with dimerizable crosslinking units are presented. The resulting polymers exhibit a lower critical solution temperature, which can be tuned by the amphiphilic balance of the used comonomers. UV irradiation dimerizes the crosslinking units of the polymers, resulting in hydrogels, whose degree of swelling and mechanical strength can be varied by the amount of precursor polymers and dimerizable crosslinking units. The biocompatibility of the hydrogels is significantly improved through the incorporation of catechol biolinkers, as proven by cell studies. Successful microgel formation using microfluidics can be demonstrated for PU precursor polymers with cloud point temperatures around 50 °C, providing an excellent basis for further studies on microtissues.

In summary, three interdependent and consecutive studies on defined and functional microgels as *in vitro* models are reported. The spectrum of applications covered by the projects ranges from mimicking natural *in vivo* processes (bone regeneration) to modelling the highly complex functionality of *in vivo* tissues, and up to providing a promising new polymer platform for microtissue applications. The results within this thesis show, that these highly functional material platforms provide a valuable basis for further investigations and make an important contribution to the field of sustainable avoidance of animal testing.

## 7. Additional Projects

Through the work on microtissue-based in vitro model systems, methods and strategies have been developed that are also transferable to other application areas outside microtissue engineering. Accordingly, the knowledge gained from both the material design and the cell studies has also been applied to other projects, which were carried out in collaboration with research groups from other fields such as supramolecular and inorganic chemistry. These projects focus on research topics from a wide variety of life science fields, such as tissue engineering, biomimetic heterogeneous catalysis, and sustainable water treatment. Overall, these collaborations demonstrate that there is a variety of useful application areas for the methods and systems described and developed in this thesis.

●●● *“Thermal Programming of Multidomain Supramolecular Copolymers into Injectable Soft Hydrogel Scaffolds”*







Manuscript in preparation.
<p>██████████ <u>Elena Stengelin</u>,<sup>1</sup> ██████████          ██████████*</p>
<p><sup>1</sup> Johannes Gutenberg-University Mainz, Department of Chemistry, Duesbergweg 10–14, D-55128 Mainz, Germany</p> <p><sup>2</sup> ██████████</p> <p><sup>3</sup> ██████████          ██████████</p> <p><sup>4</sup> ██████████</p> <p style="text-align: center;">* Corresponding author</p>

**Personal Contributions:** Cell experiments; confocal laser scanning microscopy.

**Abstract:** In vitro tests are important tools for drug development in the pharmaceutical industry. However, due to the use of animal-derived scaffolds, the accuracy and reproducibility

of test results are often not guaranteed. To enable more precise results, this project aims to develop synthetic 3D hydrogels which mimic the fibrous extracellular matrix and can be used as an advanced in vitro model. To this end, thermo-induced hydrogelation on the basis of a modular supramolecular copolymer system of C<sub>3</sub>-symmetric peptide amphiphiles is investigated with respect to the self-assembly, viscoelastic properties and shape stability. Further investigations are performed to test the biocompatibility of the material in cell studies with human primary osteoblasts (hOB) and osteosarcoma cells (SaOS-2), as well as the potential application in bioprinting.

●●● *“Quorum Quenching Induced Biofilm Inhibition  
by CeO<sub>2-x</sub> Containing Paints”*

Manuscript in preparation.
 <b>Elena Stengelin,<sup>1</sup></b>  
<sup>1</sup> Johannes Gutenberg-University Mainz, Department of Chemistry, Duesbergweg 10–14, D-55128 Mainz, Germany <sup>2</sup>   <sup>3</sup> 
<sup>‡</sup> Author 1 and Author 2 contributed equally to this work <sup>*</sup> Corresponding author

**Personal contributions:** Cell experiments; confocal laser scanning microscopy.

**Abstract:** The formation of biofilms on ship hulls is one of the largest cost factors in the marine industry due to the additional energy consumption. To reduce costs, there is a great interest in developing strategies to prevent these biofilms. This project therefore investigates possible interventions in the biofilm formation process. Since the main cause of biofilms is the accumulation of bacteria and their growth, the signal transmission between individual bacteria should be inhibited. This can be achieved through coatings, which contain cerium oxide (IV) particles. These nanoparticles are expected to catalyze the bromination of signaling molecules and thus restrict signaling pathways between bacteria by Quorum Quenching.

## ADDITIONAL PROJECTS

For the studies, paints based on  $\text{CeO}_{2-x}$  particles are synthesized, analyzed and their influence on bacterial and cell growth/viability is investigated.

● ● ● *“Porous Alginate- $\text{CeO}_{2-x}$  Composite Hydrogels  
for Water Treatment Applications”*

Manuscript in preparation.
[REDACTED] <a href="#">Elena Stengelin</a> , <sup>1</sup> [REDACTED] [REDACTED]
<sup>1</sup> Johannes Gutenberg-University Mainz, Department of Chemistry, Duesbergweg 10–14, D-55128 Mainz, Germany * Corresponding author

**Personal contributions:** Project idea, initiation, development, and interdisciplinary project coordination; lab work (degradation studies); supervision of [REDACTED] in research module and Master thesis (Master thesis: [REDACTED], Synthese und Strukturaufklärung von porösen, alginatbasierten Filtrationseinheiten zur selektiven Filtration von Farbstoffen aus Wasser, Johannes Gutenberg-Universität Mainz, 2021).

**Abstract:** Clean drinking water is the basis of human existence. Due to climate change, however, its availability will become one of the greatest global challenges. As a contribution to this, a possible model system for hydrogel-based drinking water treatment is investigated. Special attention is paid to the microscopic material design of the porous alginate-based hydrogel matrix and its nano- and mesoscopic structural properties. To investigate the filtration potential of the alginate matrix, differently charged organic dyes are used as model pollutants, whose intense colorations and electrostatic properties allow a simple analysis of the interaction mechanisms between matrix and dye molecules.  $\text{CeO}_{2-x}$  nanoparticles are another key component whose potential for photocatalytic degradation of dyes is exploited for water treatment. Therefore, a beneficial combination with the results from previously described project (*“Quorum Quenching Induced Biofilm Inhibition by  $\text{CeO}_{2-x}$  Containing Paints”*) is possible.

# 8. Indexes

## List of Figures

FIGURE 1-1. ....	5
FIGURE 1-2. ....	10
FIGURE 1-3. ....	15
FIGURE 1-4. ....	19
FIGURE 1-5. ....	24
FIGURE 1-6. ....	26
FIGURE 2-1. ....	46
FIGURE 3-1. ....	54
FIGURE 3-2. ....	56
FIGURE 3-3. ....	59
FIGURE 3-4. ....	60
FIGURE 3-5. ....	62
FIGURE 3-6. ....	64
FIGURE 3-7. ....	66
FIGURE 3-8. ....	70
FIGURE 3-9. ....	74
FIGURE 3-10. ....	76
FIGURE 4-1. ....	92
FIGURE 4-2. ....	95
FIGURE 4-3. ....	98
FIGURE 4-4. ....	100
FIGURE 4-5. ....	102
FIGURE 4-6. ....	105
FIGURE 4-7. ....	107
FIGURE 4-8. ....	110
FIGURE 4-9. ....	111
FIGURE 5-1. ....	125
FIGURE 5-2. ....	127
FIGURE 5-3. ....	128
FIGURE 5-4. ....	130
FIGURE 5-5. ....	132

## List of Tables

TABLE 1-1. ....	9
TABLE 1-2. ....	29
TABLE 3-1. ....	65
TABLE 4-1. ....	94
TABLE 5-1. ....	124

## List of Abbreviations and Symbols

<b>APS</b>	ammonium persulfate	<b>GelMa</b>	gelatin methacrylate
<b>RGD</b>	arginine-glycine-aspartate	<b>Gl.</b>	GlutaMAX
<b>N<sub>A</sub></b>	Avogadro constant	<b>GFP</b>	green fluorescent protein
<b>k<sub>B</sub></b>	Boltzmann constant	<b>R<sub>H</sub></b>	hydrodynamic radius
<b>BSA</b>	bovine serum albumin	<b>HA</b>	hydroxyapatite
<b>CLSM</b>	confocal laser scanning microscopy	<b>HCA</b>	hydroxycarbonate apatite
<b>D</b>	diffusion coefficient	<b>IPDI</b>	isophorone diisocyanate
<b>DMMI</b>	dimethylmaleimide	<b>G'</b>	loss modulus
<b>DA</b>	dopamine hydrochloride	<b>LCST</b>	lower critical solution temperature
<b>DMEM</b>	Dulbecco's Modified Eagle Medium	<b>MAS</b>	magic angle spinning
<b>DPBS</b>	Dulbecco's phosphate buffered saline	<b>ξ</b>	mesh size
<b>DLS</b>	dynamic light scattering	<b>TEMED</b>	<i>N,N,N',N'</i> -tetramethyl- ethylenediamine
<b>E</b>	elastic modulus	<b>BIS</b>	<i>N,N'</i> -methylenebis- acrylamide
<b>EG</b>	ethylene glycol	<b>HEAM</b>	<i>N</i> -hydroxyethylacrylamide
<b>EDTA</b>	ethylenediaminetetraacetic acid	<b>NMR</b>	nuclear resonance spectroscopy
<b>ECM</b>	extracellular matrix	<b>P/S</b>	penicillin-streptomycin
<b>FBS</b>	fetal bovine serum	<b>ν</b>	Poissons ratio
<b>FT-IR</b>	fourier-transform infrared spectroscopy	<b>PEG</b>	poly(ethylene glycol)
<b>f</b>	functionality of cross-links	<b>PNIPAAm</b>	poly( <i>N</i> -isopropylacrylamide)

<b>PDMS</b>	polydimethylsiloxane
<b>PDA</b>	polydopamine
<b>PU</b>	polyurethane
<b>SEM</b>	scanning-electron microscopy
<b>SEC</b>	size exclusion chromato- graphy
<b><math>G'</math></b>	storage modulus
<b><math>A</math></b>	structure factor
<b>SI</b>	Supporting Information
<b><math>T</math></b>	temperature
<b>TXS</b>	thioxanthone disulfonate
<b>TRIS</b>	tris(hydroxymethyl)-amino- methane
<b>R</b>	universal gas constant
<b>UCST</b>	upper critical solution tem- perature
<b><math>\eta</math></b>	viscosity
<b>VPT</b>	volume phase transition
<b>VPTT</b>	volume phase transition temperature

# 9. Appendix

## 9.1. Chapter I

### 9.1.1. Microfluidic devices

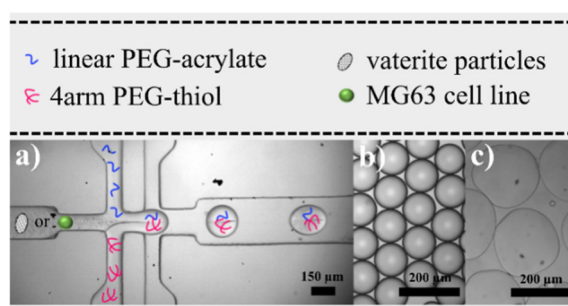


**Figure S9-1.** Fabrication of cell- or vaterite-containing microgels by microfluidics. (a) Microfluidic device overlaid by schematics for the injected linear PEG-acrylate precursors (blue), star-shaped 4-arm PEG-thiols (red), vaterite particles (gray), or cells (green). The device channel system consists of two rectangular cross-sections. At the first intersection, precursor polymer solutions along with cells or vaterite particles are injected in order to form a laminar co-flowing stream. At the second intersection the fluid stream is transformed into droplets by a flow focusing process with a non-miscible fluid. (b) The resulting droplets are then stored in an immiscible carrier fluid until the reaction between the precursor polymers is complete. (c) Afterwards, the generated microgels are transferred into phosphate buffer, where they swell to uniform sizes in the range of 200 to 300 μm.

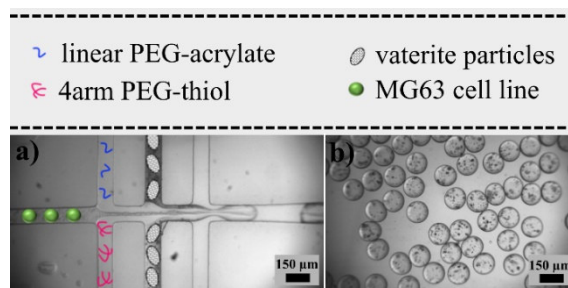


**Figure S9-2.** Fabrication of cell- and vaterite-containing microgels by microfluidics. (a) Microfluidic channel system, overlaid by schematics of the injected linear PEG-acrylate precursors (blue), star-shaped 4-arm PEG-thiols (red), vaterite particles (gray), and cells (green). The device channel system is composed of three rectangular intersections. In the first intersection, precursor polymers and cells are injected. At the second intersection, vaterite particles suspended in ethylene glycol are injected. In the third intersection, the fluid stream is broken into droplets by flow focusing with a non-miscible fluid. (b) Templated droplets are then stored in an immiscible carrier fluid until the reaction between the precursor polymers is complete.



immiscible carrier fluid until the reaction between the precursor polymers inside is complete. 2D confocal imaging of microgels confirm the presence of MG-63 cells expressing GFP and vaterite agglomerates.

### 9.1.2. Dynamic Light Scattering measurements

DLS measurements are performed using a uniphase He/Ne laser ( $\lambda = 632.8$  nm, 22 mW), an ALV-SP125 goniometer, an ALV/High QE APD-avalanche photo diode with fiber optical detection, an ALV 5000/E/PCI-correlator, and a Lauda RC-6 thermostat unit at 20 °C. Angular dependent measurements of typically 10° steps are carried out in the range  $30^\circ \leq \Theta \leq 150^\circ$ . For data evaluation, experimental intensity correlation functions are transformed into amplitude correlation functions through the Siegert relation extended to include negative values after baseline subtraction by calculation according to  $g_1(t) = \text{SIGN}(G_2(t)) \cdot \text{SQRT}(\text{ABS}((G_2(t) - A)/A))$ .

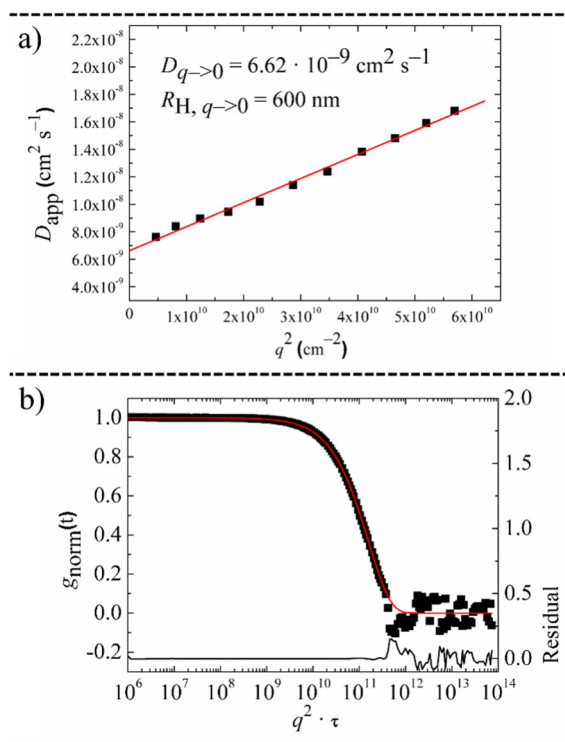


**Figure S9-3.** DLS results of the vaterite/ethylene glycol mixture.

All field correlation functions usually show monomodal decay and are fitted by a sum of two exponentials  $g_1(t) = a \cdot \exp(-t/b) + c \cdot \exp(-t/d)$  to take polydispersity into account. Average apparent diffusion coefficients  $D_{app}$  are calculated by applying  $q^2 \cdot D_{app} = (a \cdot b - 1 + c \cdot d - 1)/(a + c)$ , resulting in an angular-dependent diffusion coefficient  $D_{app}$  or a reciprocal hydrodynamic radius  $\langle 1/R_H \rangle_{app}$ , according to formal application of the Stokes–Einstein law. By extrapolation of  $\langle 1/R_H \rangle_{app}$  to  $q = 0$ , z-average hydrodynamic

radii  $R_h = \langle 1/R_H \rangle_{z-1}$  are obtained (uncorrected for concentration-dependency). The measurements are performed in methanol and denoted polydisperse nanometer sized particles in the range of 200 to 600 nm, as the  $\mu^2$ -value of 0.229 at  $90^\circ$  shows.

### 9.1.3. Scanning electron microscopy (SEM)

Vaterite particles are observed with a Fei Phenom SEM, as they are applied on transmission electron microscopy grids by dissolving in isopropanol. To increase the contrast, the samples are coated with 7.6 nm gold with a BAL-TEC/MED020 sputtering system.

### 9.1.4. Confocal Raman spectroscopy

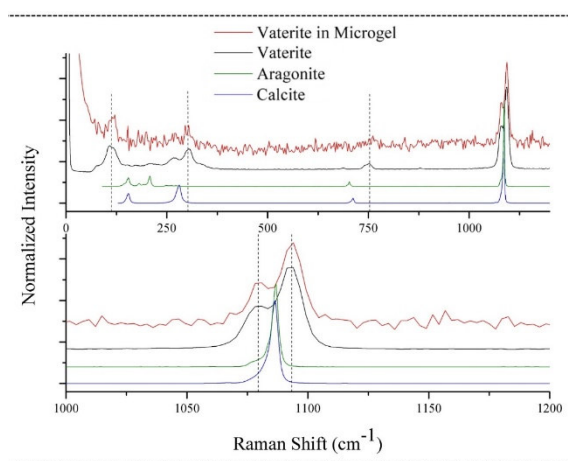


**Figure S9-4.** Comparison of vaterite-Raman spectra measured in PEG microgel (red), vaterite (black), aragonite (green) and calcite (blue). Dashed lines are for reference.<sup>[1]</sup>

### 9.1.5. Confocal microscopy

Experiments are done with a Leica TCS-SP8 AOBS SMD microscope with an HCPL APO CS2  $10\times/0.40$  DRY objective. For sample preparation, cell-containing and vaterite-containing microgels, respectively, are transferred in phosphate buffer into 8-well plates (300  $\mu\text{L}$  each well). To distinguish between the gel matrix and the encapsulated components, 20  $\mu\text{L}$  of 2  $\mu\text{M}$  sulforhodamine B solution are added. The dye molecules adhere to the polymer scaffold, which leads to an increased contrast, whereby the microgels become clearly visible. The excitation takes place with a DPSS laser (561 nm), and a detection range between 570 and 650 nm is used. In addition, vaterite-containing microgels are stained with calcium staining tetracycline dye. For this purpose, 1  $\mu\text{L}$  of 1 mM tetracycline, dissolved in methanol, is added to the samples in 8-well dishes. Here, excitation takes place with a UV diode (405 nm),

and a detection range between 500 and 550 nm is used. The osteoblast cell line expressing GFP is excited with an argon laser (488 nm), and fluorescence is detected in a range between 500 and 550 nm. As detectors, a PMT and a HyD SMDs are used. To obtain 3D confocal images of the stained microgels, z-stacks are recorded with a line average of 1, frame average of 1, line accumulation of 1 and frame accumulation of 1.

## 9.2. Chapter II

### 9.2.1. HEAM Comonomer Content in PNIPAAm/HEAM Hydrogels

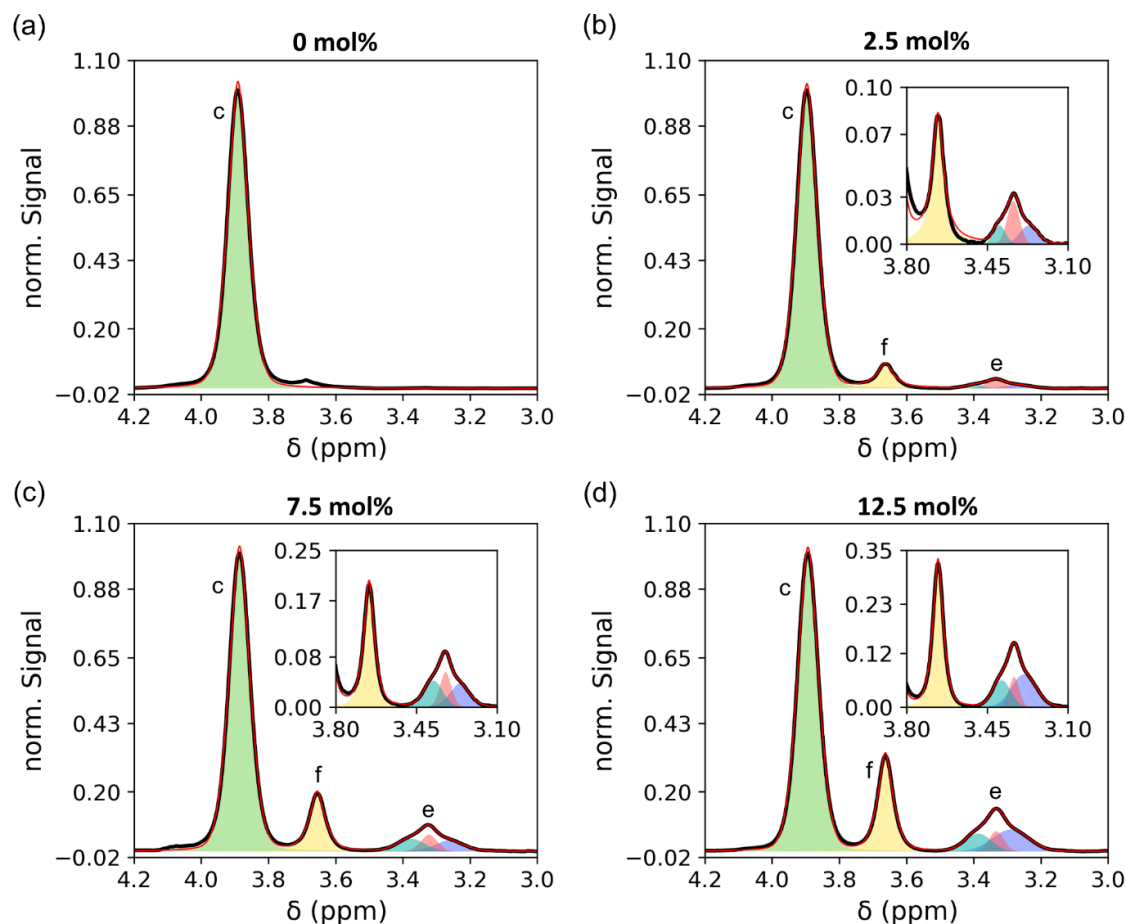


**Figure S9-5.** Deconvolution of the  $^1\text{H}$  MAS NMR spectra of a) 0 mol%, (b) 2.5 mol%, c) 7.5 mol%, and d) 12.5 mol% PNIPAAm/HEAM hydrogels. For the evaluation of the proton integrals A (H-c), A (H-f) and A (H-e) a preliminary data processing is performed using Mestrenova (v 11.0.4-18998). All spectra are shifted against the reference of  $\text{D}_2\text{O}$  (4.8 ppm) for standardization. The region from 3.0–4.2 ppm is extracted and a baseline fit using a 3-point cubic spline interpolation is performed. Each spectrum is normalized afterwards (with respect to the highest signal at around 3.9 ppm (H-c)) and fitted using the Python modules SciPy (1.6.2) and Scikit-learn (0.24.1) via a pseudo Voigt-like function (formula 1) in the range of 3.0–4.2 ppm. The areas of the fitted signals are then determined using the trapezoidal method (Scikit-learn) and placed in relation to each other.

$$\sum_{i=1}^n (1 - \tau_i) \cdot \left( A_{Gi} \cdot \exp\left(-\frac{(x-\mu_i)^2}{(2 \cdot \sigma_i)^2}\right) \right) + \tau_i \cdot \left( \frac{A_{Li} \cdot \sigma_i}{\pi \cdot ((x-\mu_i)^2 + \sigma_i^2)} \right) \quad (1)$$

**Table S9-1.** Proton ratios (proton ratio<sub>NMR</sub>) of NIPAAm (H-c) and HEAM (H-f, H-e) comonomers are calculated as  $\text{proton ratio}_{\text{NMR}} = (A_{\text{NIPAAm}} \cdot (A_{\text{HEAM}})^{-1} \cdot 4H)$ , using the proton integrals of NIPAAm ( $A_{\text{NIPAAm}} = A$  (H-c)) and HEAM ( $A_{\text{HEAM}} = A$  (H-f) +  $A_1$  (H-e) +  $A_2$  (H-e) +  $A_3$  (H-e)), experimentally determined by <sup>1</sup>H MAS NMR spectroscopy.

	$A$ (H-c)	$A$ (H-f)	$A_1$ (H-e)	$A_2$ (H-e)	$A_3$ (H-e)	proton ratio <sub>NMR</sub>
0 mol%	0.085	-	-	-	-	-
2.5 mol%	0.083	0.007	0.001	0.002	0.001	30.410
7.5 mol%	0.084	0.014	0.004	0.004	0.004	13.088
12.5 mol%	0.084	0.022	0.010	0.004	0.006	8.184

**Table S9-2.** Molar ratios of PNIPAAm and HEAM comonomers are calculated as  $\text{molar ratio} = (n_{\text{NIPAAm}} \cdot (n_{\text{HEAM}})^{-1})$  using NIPAAm ( $n_{\text{NIPAAm}}$ ) and HEAM ( $n_{\text{HEAM}}$ ) quantities.

	$n_{\text{NIPAAm}}$ [mmol]	$n_{\text{HEAM}}$ [mmol]	proton ratio <sub>NMR</sub>
2.5 mol%	0.853	0.021	40.000
7.5 mol%	0.809	0.061	13.333
12.5 mol%	0.764	0.096	8.000

### 9.2.2. Droplet-Based Microfluidics

Spherical shaped PNIPAAm/HEAM microgels of type 2.5 mol%, 7.5 mol%, and 12.5 mol% are synthesized using droplet-based microfluidics. For this purpose, we employ a poly(dimethylsiloxane) (PDMS) channel system as shown in **Figure S9-6**, which is fabricated by photo- and soft lithography. For photo lithography, silicon wafers (Micro-Chemicals) are spin-coated (WS-650MZ-23NPP13 from Laurell) with a 100  $\mu\text{m}$  layer of 3050 photoresist (MicroChem) and subsequently irradiated with UV-light (UVKub 2 from Kloé). To obtain negative reliefs of the microfluidic channels, to-scale photomasks are applied during UV irradiation on the photoresist-coated silicon wafer. For soft lithography, PDMS is mixed with a crosslinker (Sylgard 184 Elastomer Kid from Dow Corning) in a 10:1 ratio using a mixer (Thinky ARE-250) and applied to the silicon wafer placed in a Petri dish. Any air bubbles are removed from the liquid PDMS by placing the Petri dish in a desiccator and, in an alternating fashion, evacuating and venting it. After curing at 65  $^{\circ}\text{C}$  for 2 h, the resulting relief PDMS replica plates are peeled off, and holes for the inlets and outlets are created using a 1 mm biopsy punch. Subsequently, the PDMS device is covalently bonded to glass slides by oxygen-plasma bonding (electronic Diener Plasma-Surface-Technology). The channels are conditioned with 2% 1H,1H,2H,2H-perfluorooctylsilane (Alfa-Aesar) in Novec 7100 (3M) for 10 minutes at room temperature making them fluorophilic, while the residues are removed by  $\text{N}_2$  drying.

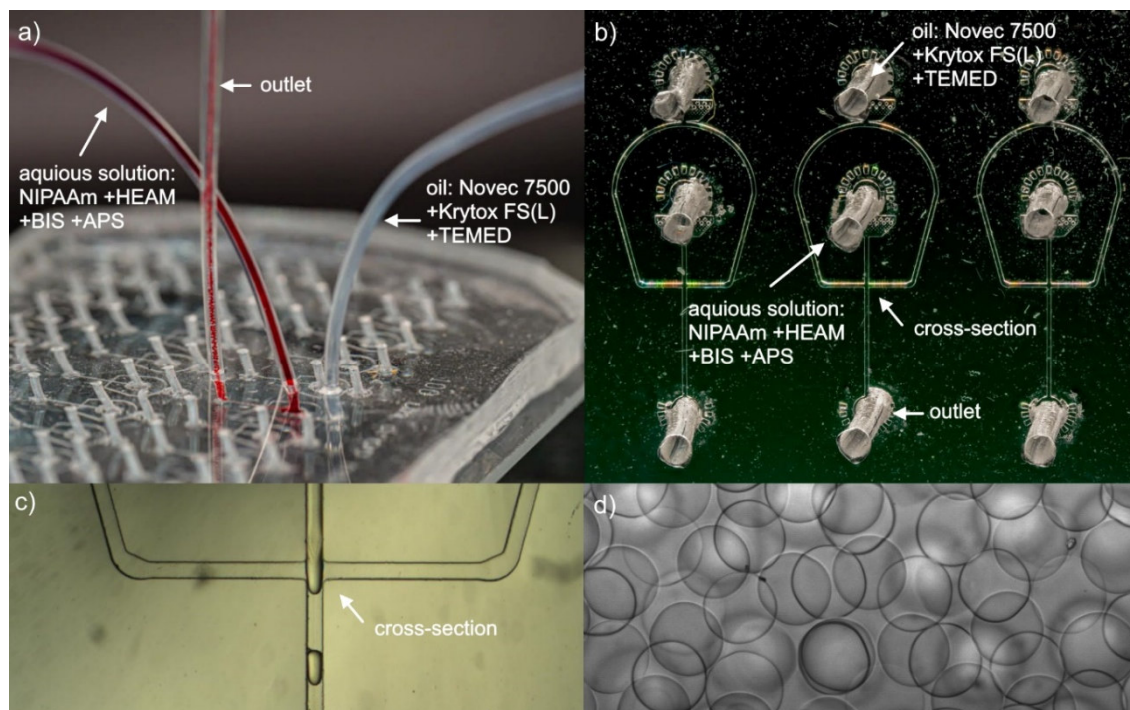


**Figure S9-6.** PDMS microfluidic setup. (a) PDMS device connected to syringe pumps via polyethylene tubing. The colorless tube represents the oil inlet, the red tube the injection of the aqueous solution, and the tube with

small red droplets represents the outlet. (b) Section of the PDMS template with three microfluidic channels. The microfluidic channels exhibit a rectangular cross-section of 100  $\mu\text{m}$  diameter, where the aqueous solution based on NIPAAm, HEAM, BIS, and APS is broken into monodisperse droplets by flow-focusing with an immiscible carrier fluid composed of fluorinated oil (Novec 7500), surfactant (Krytox FS(L)) and initiator (TEMED). (c) Enlarged view of the cross-section of a microfluidic channel. (d) Microgels in water.

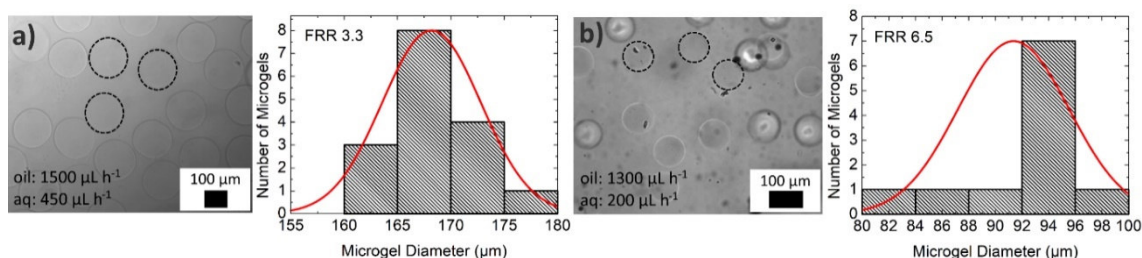


**Figure S9-7.** 12.5 mol% PNIPAAm/HEAM microgels in water at room temperature. Due to the weak contrast of the microgels in water, the contour of some microgels is visually highlighted by dashed lines. The microgel size can be adjusted by varying the Flow Rate Ratio (FRR) between the oil and the aqueous phase during the microfluidics experiment. The larger FRR, the smaller the microgel diameter become.<sup>[2]</sup> (a) Flow rate oil: 1500  $\mu\text{L h}^{-1}$ , flow rate aqueous phase (aq): 450  $\mu\text{L h}^{-1}$ , FRR: 3.3; mean microgel diameter:  $168 \pm 4 \mu\text{m}$ . (b) Flow rate oil: 1300  $\mu\text{L h}^{-1}$ , flow rate aqueous phase (aq): 200  $\mu\text{L h}^{-1}$ , FRR: 6.5; mean microgel diameter:  $91 \pm 4 \mu\text{m}$ . Another way to vary the microgel size is to use microfluidic channel systems with smaller channel widths, as shown in previous work.<sup>[3]</sup>

### 9.2.3. Volume Phase Transition Temperature (Swelling Measurements)

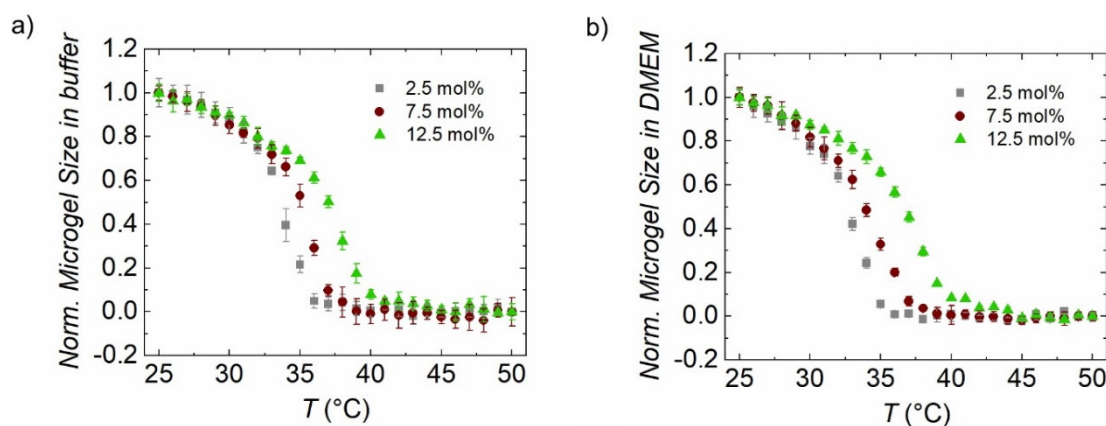


**Figure S9-8.** Swelling measurements of 2.5 mol% (■), 7.5 mol% (●), and 12.5 mol% (▲) PNIPAAm/HEAM microgels in (a) phosphate buffer and (b) DMEM (10% FBS, 1% Gl. and 1% P/S).

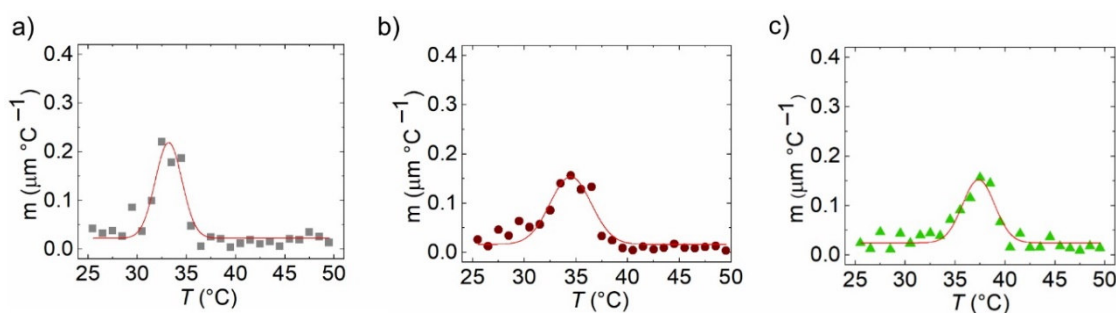


**Figure S9-9.** Derivations (symbols) and Gaussian fitting (red curves) of microgel swelling curves in DMEM (10% FBS, 1% Gl. and 1% P/S) of (a) 2.5 mol% (■), (b) 7.5 mol% (●), and (c) 12.5 mol% (▲) type. The derivations are determined by plotting the slope between two measuring points of the respective swelling curves against the average temperature of these two points. By Gaussian fitting, the maximum of these curves is determined, which corresponds to the inflection point of the swelling curves and thus to the respective  $VPT_{SC}$ .



### 9.2.4. Volume Phase Transition Temperature (Rheology)

Since the  $G'$  versus temperature curves (**Figure 4-4**) are similar to the swelling curves (**Figure 4-3**, and **Figure S9-8**,  $VPTT_{G'}$  are calculated for the three polymer networks in water, phosphate buffer, and DMEM (10% FBS, 1% Gl. and 1% P/S) (**Figure S9-10**) and compared to the  $VPTT_{SC}$  obtained by the microgel swelling measurements. By derivation of the  $G'$  versus temperature curves, inflection points are determined, which results in the  $VPTT$  values listed in **Table S9-3**. The 0 mol% ( $\blacktriangledown$ ) system as reference has a  $VPTT_{G'}$  of  $(35.0 \pm 0.0)$  °C which is comparable to values in literature.<sup>[4]</sup> The  $VPTT_{G'}$  and  $VPTT_{SC}$  values of the 2.5 mol% ( $\blacksquare$ ) polymer network in water, phosphate buffer, and DMEM (10% FBS, 1% Gl. and 1% P/S) complement each other well within the scope of error. In contrast, the  $VPTT_{G'}$  and  $VPTT_{SC}$  values of the 7.5 mol% ( $\bullet$ ) polymer network differ slightly, whereby the  $VPTT_{G'}$  are shifted to higher temperatures compared to the  $VPTT_{SC}$  values. In case of the 12.5 mol% ( $\blacktriangle$ ) systems the values diverge even further, while the  $VPTT_{G'}$  are shifted to even higher temperatures compared to the  $VPTT_{SC}$  values. The deviations between the  $VPTT_{SC}$  and  $VPTT_{G'}$  values are explainable by small differences in the swelling and rheology curves. In case of the swelling curves, the microgel diameter decreases continuously up to the VPT area with increasing temperature, then drops sharply in the VPT area, and subsequently remains constant in the smallest possible microgel state. In case of the  $G'$  versus temperature curves,  $G'$  remains constant up to the VPT area with increasing temperature, then increases sharply in the VPT area, and subsequently continues to increase smoothly. But with increasing comonomer content,  $G'$  does not remain constant but drops *before* increasing sharply in the VPT area. This we observe less in water, but more in phosphate buffer and DMEM (10% FBS, 1% Gl. and 1% P/S), indicating first a decrease and then an increase of gel elasticity. That finding can be explained by taking into consideration that hydrogels gain hydrophilicity with increasing comonomer content, whereby their network strands less cooperatively collapse with increasing temperature.<sup>[5,6]</sup> Thereby, aqueous solutions are inhomogeneously expelled from the polymer networks with increasing temperature and collects on the hydrogel surface, which is detected by the rheometer as viscous hydrogel fraction. This artefact results in a decrease of the  $G'$  versus temperature curves just before the VPT is detected and causes a  $VPTT_{G'}$  shift to slightly higher temperatures compared to the  $VPTT_{SC}$  values. Since this finding occurs more strongly in phosphate buffer and even more strongly in DMEM (10% FBS, 1% Gl. and 1% P/S), salts and further ingredients seem to promote such a less cooperative collapse of the network strands with increasing temperature as well.

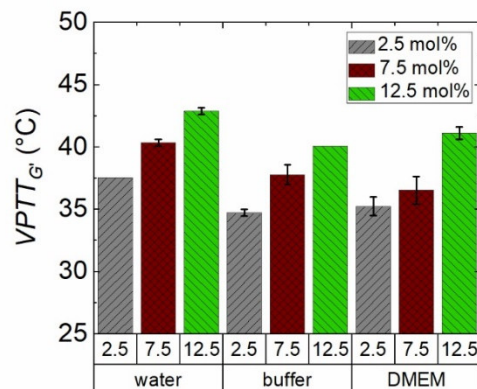


**Figure S9-10.** VPTT<sub>G</sub> of 2.5 mol%, 7.5 mol%, and 12.5 mol% hydrogels in water, phosphate buffer, and DMEM (10% FBS, 1% Gl. and 1% P/S), determined by derivation of the  $G'$  versus temperature curves shown in **Figure 4-4**. The derivations are obtained by plotting the slope between two measuring points of the respective  $G'$  versus temperature curves against the average temperature of these two points. The maximum of the resulting derivations corresponds to the inflection points of the  $G'$  versus temperature curves and thus to the respective VPTT<sub>G</sub>.

**Table S9-3.** VPTT of 2.5 mol% (■), 7.5 mol% (●), and 12.5 mol% (▲) microgels in water, phosphate buffer, and DMEM (10% FBS, 1% Gl. and 1% P/S) calculated by swelling measurements (VPTT<sub>sc</sub>) and rheology (VPTT<sub>G</sub>).

(°C)	2.5 mol%		7.5 mol%		12.5 mol%	
	VPTT <sub>sc</sub>	VPTT <sub>G</sub>	VPTT <sub>sc</sub>	VPTT <sub>G</sub>	VPTT <sub>sc</sub>	VPTT <sub>G</sub>
water	37.5 ± 0.1	37.6 ± 0.0	39.1 ± 0.1	40.4 ± 0.3	39.9 ± 0.2	42.9 ± 0.3
buffer	35.1 ± 0.1	34.7 ± 0.3	36.2 ± 0.1	37.8 ± 0.8	38.6 ± 0.1	40.1 ± 0.0
DMEM	34.2 ± 0.1	35.3 ± 0.8	36.0 ± 0.1	36.5 ± 1.1	37.4 ± 0.1	41.1 ± 0.5

### 9.2.5. Microgel Properties at Physiological Conditions

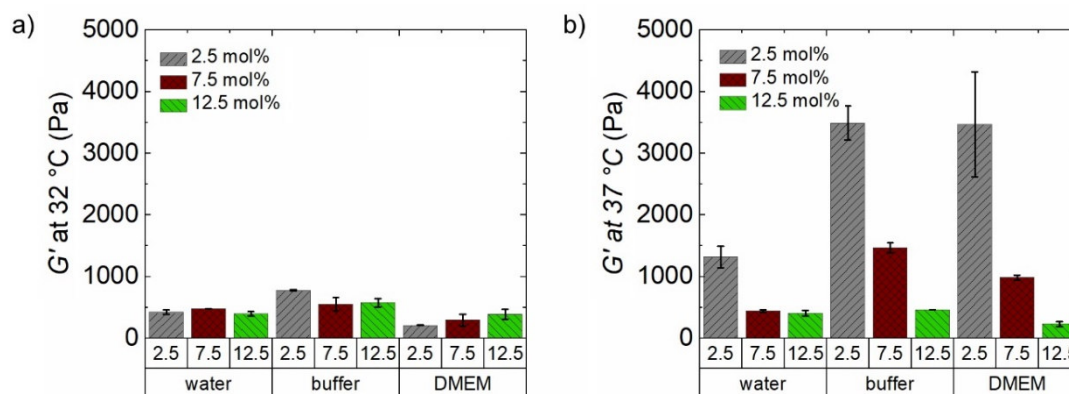


**Figure S9-11.** Microgel stiffness of the 2.5 mol%, 7.5 mol%, and 12.5 mol% systems in water, phosphate buffer, and DMEM (10% FBS, 1% Gl. and 1% P/S) at (a) 32 °C, and (b) 37 °C obtained by rheology.

**Table S9-4.** Normalized microgel size ( $d_{norm} = (d - d_{min}) \cdot (d_{max} - d_{min})^{-1}$ , with microgel diameter  $d$ , minimum microgel diameter  $d_{min}$  and maximum microgel diameter  $d_{max}$ ) and mechanical strength ( $G'$ ) of 2.5 mol%, 7.5 mol%, and 12.5 mol% networks at 25 °C, 32 °C, and 37 °C in DMEM (10% FBS, 1% Gl. and 1% P/S).

	2.5 mol%		7.5 mol%		12.5 mol%	
	$G'$ [Pa]	$d_{norm}$	$G'$ [Pa]	$d_{norm}$	$G'$ [Pa]	$d_{norm}$
25 °C	270 ± 49	1.00 ± 0.03	475 ± 140	1.00 ± 0.05	570 ± 26	1.00 ± 0.04
32 °C	209 ± 4	0.64 ± 0.03	296 ± 94	0.71 ± 0.03	386 ± 81	0.81 ± 0.03
37 °C	3474 ± 853	0.01 ± 0.01	985 ± 41	0.07 ± 0.02	231 ± 39	0.45 ± 0.02

### 9.2.6. PDA Coating of Microgels

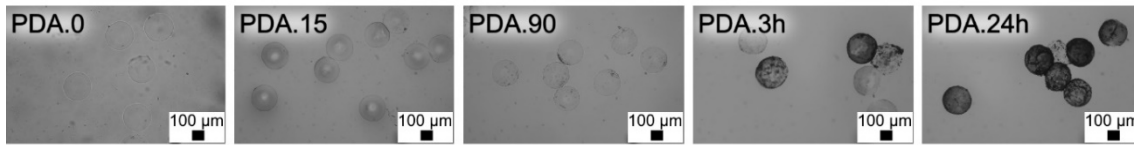


**Figure S9-12.** Light microscopy imaging of 12.5 mol% PNIPAAm/HEAM microgels with 0 min (PDA.0), 15 min (PDA.15), 90 min (PDA.90), 3h (PDA.3h) and 24h (PDA.24) PDA coating, suspended in isopropanol.

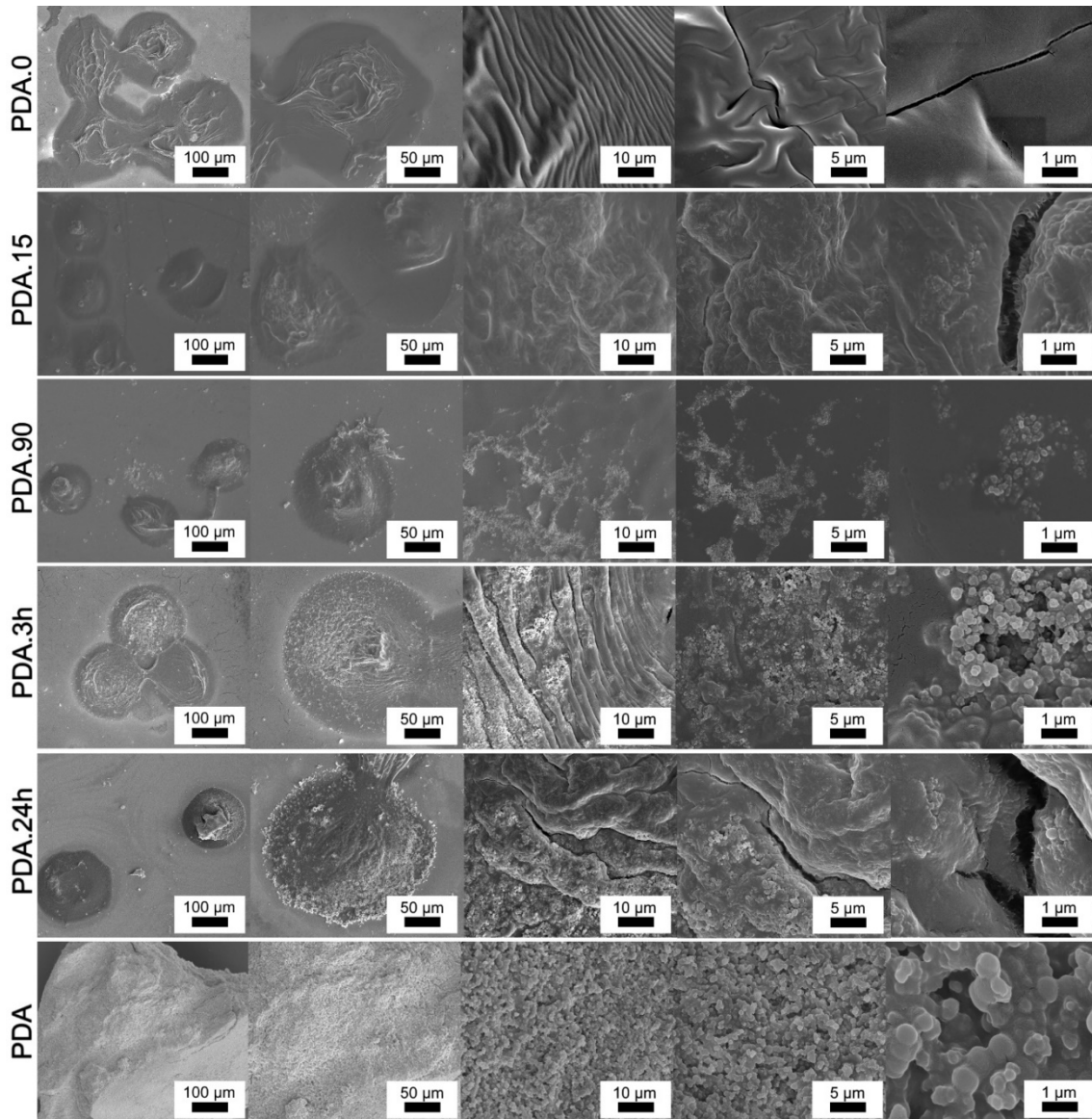


**Figure S9-13.** FE-SEM measurements of freeze-dried 12.5 mol% PNIPAAm/HEAM microgels with 0 min (PDA.0), 15 min (PDA.15), 90 min (PDA.90), 3h (PDA.3h), and 24h (PDA.24) PDA coating. Samples are sputtered with gold (10 nm) before analysis.

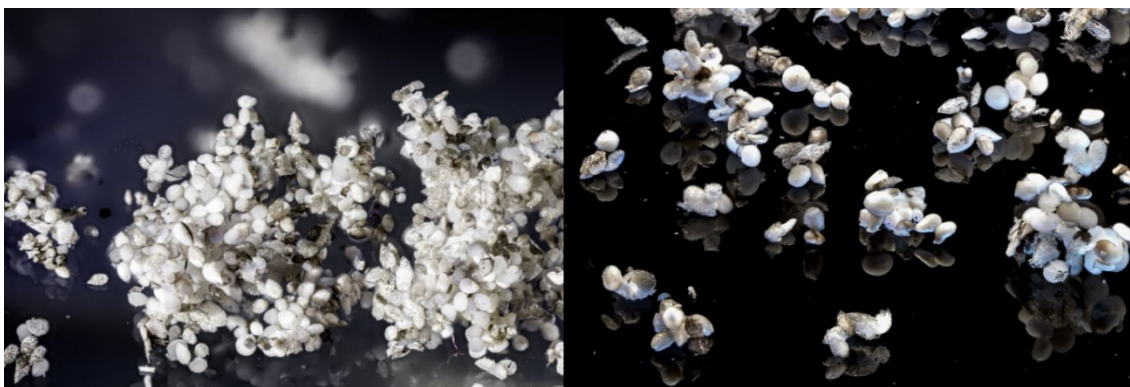


Figure S9-14. Photographs of freeze-dried PDA.24 microgels.

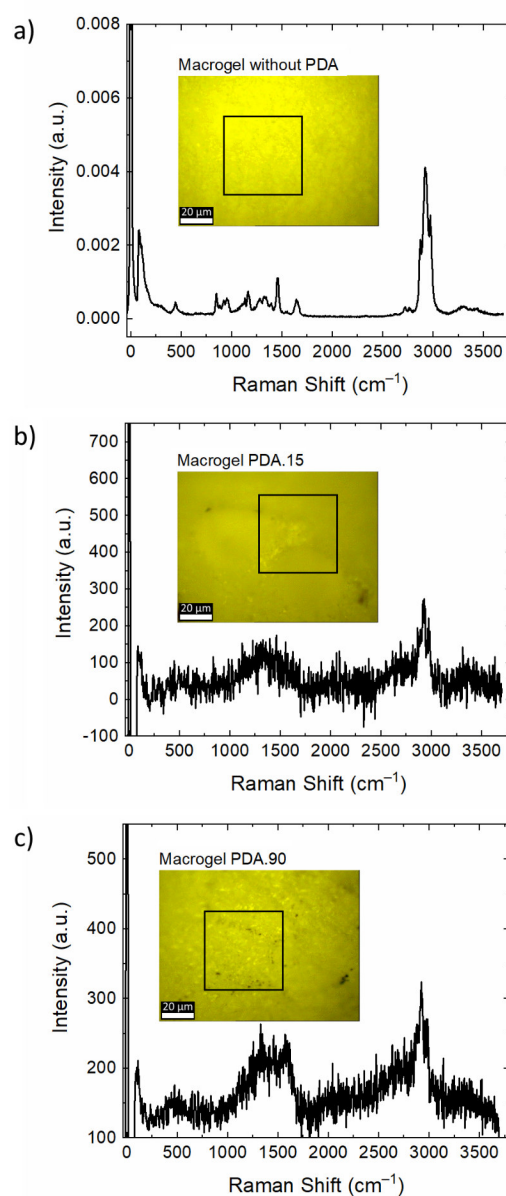
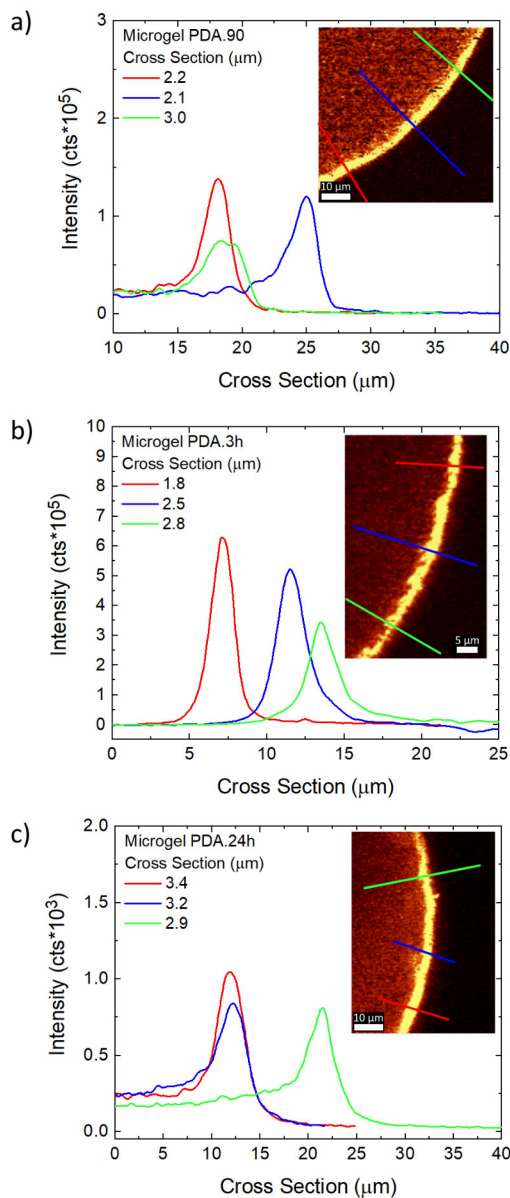


Figure S9-15. Confocal Raman spectroscopy measurements of freeze-dried (a) PDA.0, (b) PDA.15, and (c) PDA.90 macrogels and respective bright-field imaging. The gel without PDA coating shows a clear spectrum, whereas the PDA.15 gel shows a comparable but noisy spectrum due to fluorescence emitted by PDA,

## APPENDIX

indicating PDA coating in general. Since the PDA concentration is probably insufficient, no clear PDA signals are detectable in this spectrum. Confocal Raman measurement of the PDA.90 gel shows the same noisy spectrum, but PDA-specific bands are observed between 1000 and 1750  $\text{cm}^{-1}$ . Based on this finding, further confocal Raman studies will be performed on microgels containing PDA.90, PDA.3h and PDA.24h microgels.



**Figure S9-16.** Confocal Raman measurements to determine the thickness of PDA coating on 12.5 mol% PNIPAAm/HEAM microgels swollen in water with (a) 90 minutes (PDA.90), (b) 3h (PDA.3h), and (c) 24h (PDA.24h) PDA coating time. The insert shows the peak integral at  $1590\text{cm}^{-1}$  of the scanned area for each microgel. The cross-section of the PDA was calculated averaging the intensities along a  $10\ \mu\text{m}$  line (some depicted in the insert). For all measured microgels, the mean values of the calculated cross-section give approximately  $2.3\pm 0.6\ \mu\text{m}$  for the PDA.90 microgels,  $3.1\pm 1.2\ \mu\text{m}$  for the PDA.3h microgels, and  $3.7\pm 1.8\ \mu\text{m}$  for the PDA.24h microgels.

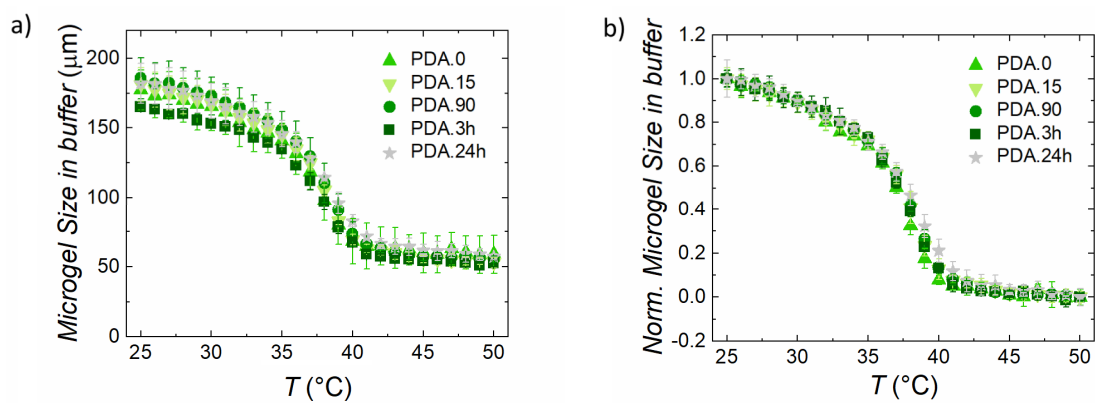


**Figure S9-17.** Temperature-dependent swelling measurements of 12.5 mol% PNIPAAm/HEAM PDA.0 ( $\blacktriangle$ ), PDA.15 ( $\blacktriangledown$ ), PDA.90 ( $\bullet$ ), PDA.3h ( $\blacksquare$ ) and PDA.24h ( $\star$ ) microgels in phosphate buffer. (a) Absolute, and (b) normalized microgel diameters.

### 9.2.7. Cell-Affinity of PDA

To extend the hydrogels functionality, we also perform cell experiments at 32 °. Since the VPTT of the 2.5 mol%, 7.5 mol%, and 12.5 mol% PNIPAAm/HEAM hydrogels are above 32 °C, they are transparent at this temperature and hence suitable for light- and confocal microscopy. Accordingly, hydrogels are synthesized and incubated in a suspension of MG-63 GFP in DMEM (10% FBS, 1% Gl., 1% P/S) at 32 °C and 5% CO<sub>2</sub> for several days. Respective images are presented in **Figure S9-18**, whereby in (I) the light microscopy images of the PDA.0 hydrogels and in (II) the CLSM images (fluorescence path) of the PDA.15 hydrogels are shown.

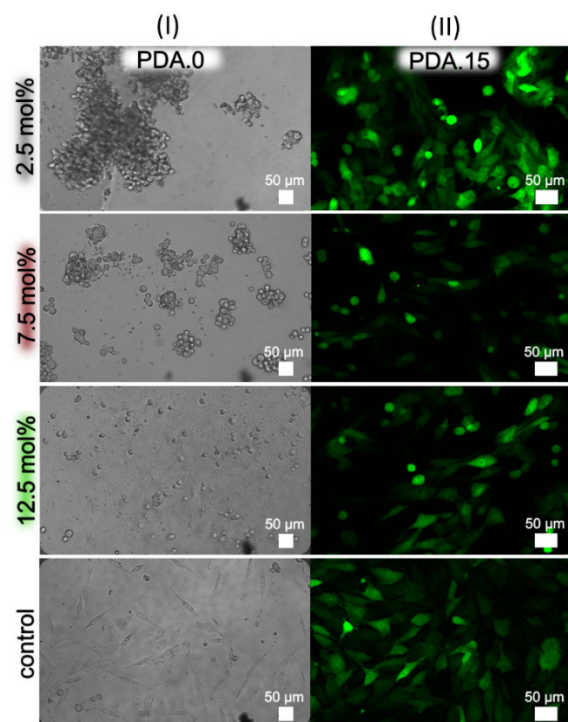


**Figure S9-18.** Cell growth on 2.5 mol%, 7.5 mol%, and 12.5 mol% hydrogels at 32 °C. (I) Light microscopy imaging of PDA.0 hydrogels, and (II) 2D CLSM imaging of PDA.15 hydrogels.

Additionally, control experiments of cells growing on plastic are presented. In (I), cells do not adhere to the PDA.0 hydrogels as indicated by their rounded cell morphology, which confirms the previous results at 37 °C. Furthermore, differences in cell cluster growth are observed on the 2.5 mol%, 7.5 mol%, and 12.5 mol% PDA.0 hydrogels. On the 2.5 mol% hydrogel cells form larger clusters compared to the 7.5 mol%, and 12.5 mol% PDA.0 hydrogels, which is justified by the increasing comonomer content within the three systems from 2.5 mol% through 7.5 mol% up to 12.5 mol%. The larger the comonomer content, the more does the VPTT shift to higher temperatures. As a result, the 2.5 mol% PDA.0 hydrogel contracts stronger and becomes smaller compared to the other two hydrogels. Hence, cells are



brought into spatial proximity and cluster on the hydrogels due to less cell–material interactions. In contrast, cells adhere well to the PDA.15 hydrogels (II), as indicated by their elongated morphology. Thus, the 15-minute PDA coating appears to be a valuable approach to enable cell growth on PNIPAAm/HEAM hydrogels, both at 32 °C, and 37 °C.

## 9.2.8. Cell Growth on PDA.15 Microgels

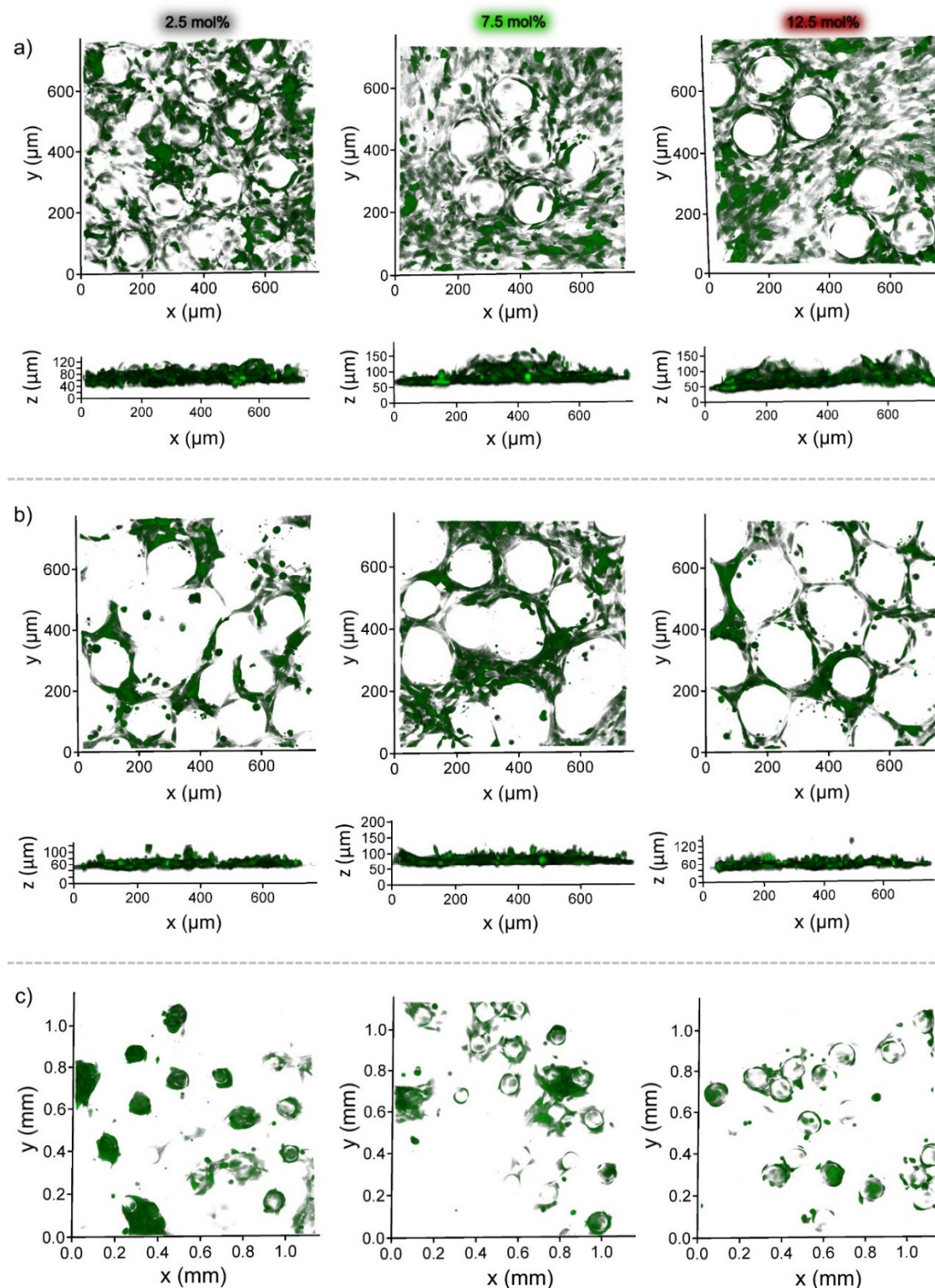


**Figure S9-19.** 3D CLSM imaging (fluorescence path) of culture dishes coated with 2.5 mol% (left), 7.5 mol% (middle), and 12.5 mol% (right) PNIPAAm/HEAM microgels. Microgels are suspended in isopropanol and applied to the culture dish surfaces, whereby isopropanol is subsequently removed by evaporation (2 h at room temperature). Microgels are coated with MG-63 GFP osteoblasts ( $1.57 \times 10^5 \text{ cells} \cdot \text{mL}^{-1}$ ) and incubated in

DMEM (10% FBS, 1% Gl. and 1% P/S) at 37 °C and 5% CO<sub>2</sub>. (a) PDA.15 microgels coated on bio-coated culture plates after 72 h incubation (x-y and z-y level). Cells grow on the bio-coated culture plates, as well as on the PDA coated microgels, demonstrated by green-fluorescent cells on the culture dish and the microgel surfaces. (b) PDA.0 microgels coated on bio-coated culture plates after 72 h incubation (x-y and z-y level). Cells grow on plastic but avoid microgels (c) PDA.15 microgels coated on bio-inert culture plates after 48h (x-y level). Cells grow on PDA coated microgels, demonstrated by green-fluorescent cells on the culture dish and the microgel surfaces, but avoid growth on bioinert culture plates.

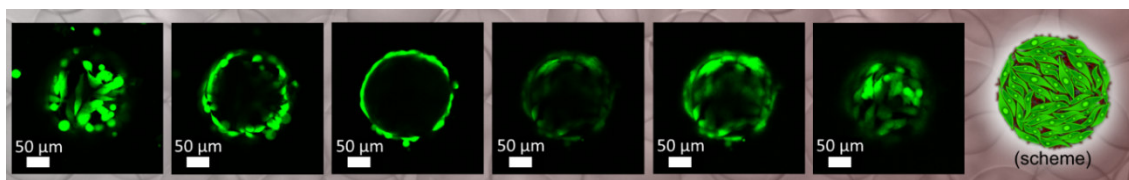


**Figure S9-20.** Cell growth on 12.5 mol% microgels after 24 h incubation in DMEM (10% FBS, 1% Gl., 1% P/S) at 32 °C and 5% CO<sub>2</sub>, analyzed by CLSM (fluorescence mode). From left to the right, the microgel section-plane levels shift from lower to upper parts on z-axis, whereby a complete cell coated microgel is demonstrated. The schematic on the right shows a cell-coated microgel.

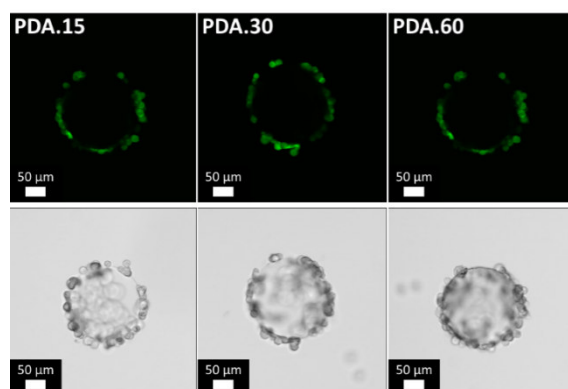


**Figure S9-21.** CLSM images (top: fluorescence path; bottom: transmission path) of cell-coated (MG-63 GFP) 12.5 mol% PDA.15/collagen, PDA.30/collagen and PDA.60/collagen microgels after 2 h incubation time in DMEM (10% FBS, 1% Gl., 1% P/S) at 32 °C and 5% CO<sub>2</sub>. They show no significant increase in microgel cell coating with increasing PDA surface coating. By increasing the cell concentration in the 12.5 mol% PDA.15/collagen cell-coating experiment, no significant increase in cells on the microgel surface is observed either. Instead, more cell agglomerates form in the cell culture dish, as the denser cell suspension also increases the probability of cell-cell interactions.

## 9.3. Chapter III

### 9.3.1. Materials

O-(7-Aza-1H-benzotriazol-1-yl)-*N,N,N',N'*-tetramethyluronium hexafluorophosphate (HATU, Alfa Aesar, 99%), 2,2-bis(hydroxymethyl)propionic acid (Aldrich, 98%), copper(II) sulfate (Sigma, 98%), *N,N*-diisopropylethylamine (DIPEA, Aldrich, 99.5%), 3,4-dihydroxyhydrocinnamic acid (Aldrich, 98%), 2,2-dimethoxypropane (DMP, Merck, 98%), 2,3-dimethylmaleic anhydride (Alfa Aesar, 97%), di-*n*-butyltin dilaurate (DBTDL, 98%, Alfa Aesar), di-*tert*-butyl dicarbonate (Merck Millipore, 98%), hydrogen chloride solution (4.0 m in dioxane, TCI), *p*-toluenesulfonic acid monohydrate (PTSA, TCI, 98%), (+)-Sodium L-ascorbate (Acros Organics, 99%), sodium azide (Alfa Aesar, 99%), triphenylphosphine (Alfa Aesar, 99%), tris[(1-benzyl-1*H*-1,2,3-triazol-4-yl)methyl]amine (TBTA, TCI, 97%) and trifluoroacetic acid (TFA, Alfa Aesar, 99%) are purchased from commercial resources and used without further purification. DOWEX X50W-X8 and Chelex 100 resin are thoroughly washed with MeOH prior to use. Isophorone diisocyanate (IPDI, mixture of *cis/trans* isomers (72:28), 98%, Acros Organics) and 1,2-bis(2-chloroethoxy)ethane (Aldrich, 97%) are freshly distilled prior to use. The poly(ethylene glycol)s (Sigma Aldrich) are first purified by precipitation into diethyl ether, freeze dried from benzene and further dried in high vacuum prior to polymerization. Cyclohexan (CHex), ethylacetate (EA), dichloromethane (DCM), 1,4-dioxane, and methanol (MeOH) are used as received. Anhydrous toluene, acetone, dimethyl sulfoxide (DMSO), *N,N*-dimethylformamid (DMF), and *N,N*-dimethylacetamide (DMAc) are purchased from Acros Organics and used as received. For cell experiments: Phosphate buffer (DPBS)-D8537 (Sigma-Aldrich), Dulbecco's Modified Eagle Medium (DMEM) high glucose-D5796 (Sigma-Aldrich), fetal bovine serum (FBS)-F7524 (Sigma-Aldrich), GlutaMAX (Gl.) (Thermo Fisher Scientific), Penicillin-Streptomycin (P/S)-P4333 (Sigma-Aldrich), trypsin EDTA solution (Sigma-Aldrich), Osteoblasts (MG-63 GFP obtained from R. E. Unger – Johannes Gutenberg University Mainz, Institute of Pathology).

### 9.3.2. Chromatography

Thin-layer chromatography is performed on F<sub>254</sub> silica gel 60 (Merck) or silica gel 60 RP-18 (Merck, coated plates. Spots are detected with UV-light ( $\lambda = 254$  nm), iodine or ninhydrin (0.2 g in 100 mL EtOH) solution. Flash chromatography is performed on silica gel 60 (40–63  $\mu$ m, Merck Millipore) and LiChroprep® RP-18 (40–63  $\mu$ m, Merck Millipore. Size

exclusion chromatography (SEC) measurements are performed at 60 °C in DMF (+ 1 g L<sup>-1</sup> LiCl) using a 1260 Infinity GPC/SEC-system from Agilent (PSS SECcurity pump, VWR Elite Chrom RI detector) equipped with a PSS GRAM guard column, two PSS GRAM 1000 Å and one PSS GRAM 100 Å columns at a flow rate of 1 mL min<sup>-1</sup>. All data are analyzed with the software PSS WinSEC provided by PSS. The number- and weight average molecular weight ( $M_n$ ,  $M_w$ ) and dispersity ( $D$ ) are calculated with a PEG calibration (calibration standards provided by PSS). Samples (2 g L<sup>-1</sup>) are filtered through a Chromafil PET-45/15 MS syringe filter prior to injection. Analytical and semipreparative HPLC were performed on a JASCO (Tokyo, Japan) LC-4000 system equipped with a binary pump system, an in-line degasser, dynamic mixer and a UV/VIS-detector. Signals were detected in a range from 400–200 nm. The system was operated by the software ChromNAV by JASCO in its version 2.00.02. For analytical purpose, a reverse phase Luna C18(2) (250 × 4.6 mm), 100 Å pore size, 10 µm particle size, by Phenomenex (Torrance, USA) was used as stationary phase, operated at 20 °C with a flow rate of 1.5 mL/min. Semipreparative HPLC was performed on a reverse phase Macherey-Nagel Nucleodur C18 Pyramid (250 × 21 mm), 100 Å pore size, 5 µm particle size with a flow rate of 18.9 mL/min. The fractions were collected automatically by a CHF122SC fraction collector (Advantec MFC Inc., Dublin, USA). Acetonitrile (B) and ultrapure water (A), each with 0.1% TFA, were used as eluents. Analytical gradient: 5% B (1 min) → 30% B (in 15 min) → 30% B (3 min) → 50% B (in 5 min); Semi-preparative gradient: 15% B (1 min) → 50% B (in 24 min) → 100% B (3 min).

### 9.3.3. Instrumentation

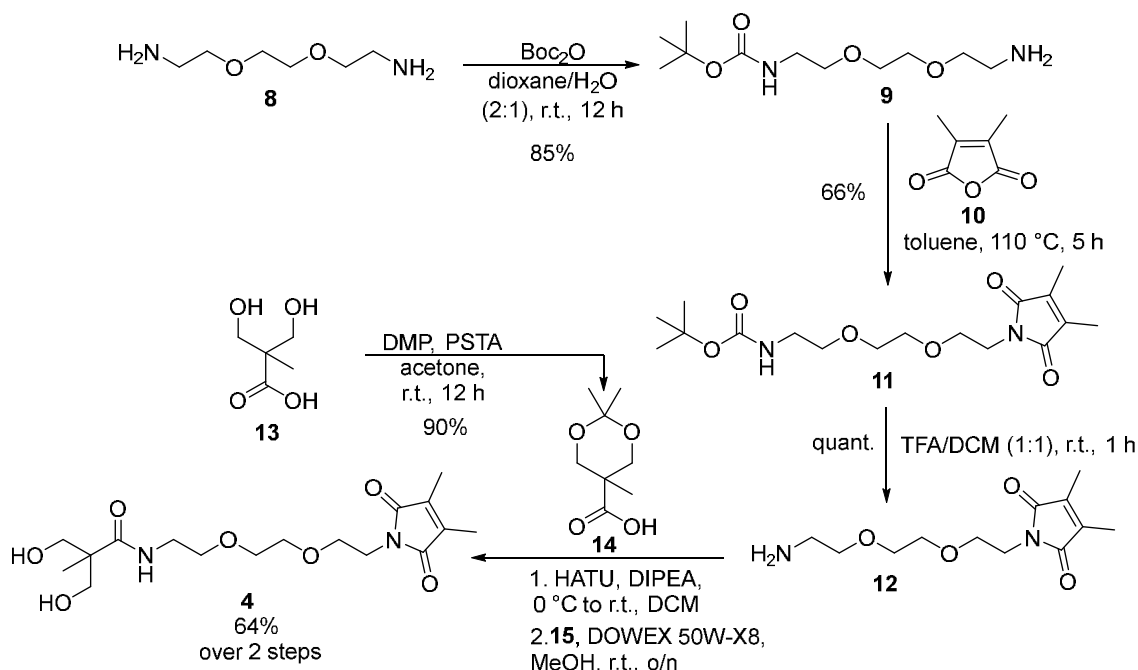
NMR spectra are recorded on a Bruker Avance-II HD 400 instrument at 20 °C. The chemical shift  $\delta$  is given in ppm by using tetramethylsilane as internal standard ( $\delta = 0$  ppm) and deuterated solvents (CDCl<sub>3</sub>, DMSO-*d*<sub>6</sub>) as internal reference. The reported signal splittings are abbreviated as follows: s = singlet, d = doublet, t = triplet). Coupling constants  $J$  are reported in Hz. High resolution electron spray mass spectra (HR-ESI MS) are measured with an Agilent 6545 QTOF-instrument. Turbidity measurements are performed on a Jasco UV-Vis V-760 Spectrophotometer equipped with a mechanical stirrer and external thermostat using 1 cm quartz class cuvettes. Optical swelling measurements are performed using a Zeiss Primovert inverted microscope with a 4x objective. Images are recorded using a ABS UK155m microscope camera. The samples immersed in water are sealed between two microscope cover slides divided by a silicon isolator before they are placed in an Instec TSA12Gi thermal stage controlled by a mK2000 temperature controller equipped with an external industrial

## APPENDIX

chiller (C500WU) (all components by Instec). UV-irradiations are performed with the UV lamp OmniCure, Series 1500 (Model No. S1500A, 200 Watt Mercury Arc, 320–500 nm) from Lumen Dynamics Group Inc equipped with a fiber optic light guide. Linear shear rheology is performed on a stress-controlled modular compact rheometer of the type MCR 302 (Anton Paar, Graz, Austria) equipped with UV-transparent lower glass plate, a stainless-steel cone–plate geometry and a solvent trap. The temperature is controlled by a Peltier plate. Motor adjustment and inertial calibration are performed before each measurement.  $^1\text{H}$  MAS NMR spectroscopy measurements are performed on a Bruker Avance DSX 400 NMR spectrometer operating at 399.87 MHz  $^1\text{H}$  frequency using 4 mm rotors and inserts specially developed to investigate gels and soft matter. The  $^1\text{H}$  single pulse excitation NMR spectra are recorded using a commercial three channel Bruker 4 mm probe head at 4 kHz Magic Angle Spinning (MAS), averaging 512 scans with a 5 s recycle delay. Confocal Laser Scanning Microscopy (CLSM) is performed using a Leica TCS-SP8 AOBS SMD microscope with an HCPL APO CS2 10 $\times$ /0.40 DRY objective. GFP expressing cells are excited with 488 nm (argon laser), while their green fluorescence is detected between 500 nm and 600 nm (PMT2 detector).

### 9.3.4. Synthesis

#### 9.3.4.1. DMMI-<sup>T</sup>EG diol (4)



Scheme S9-1. Synthesis of DMMI-<sup>T</sup>EG diol 4.

#### *tert*-Butyl-(2-(2-(2-aminoethoxy)ethoxy)ethyl)carbamate (9)

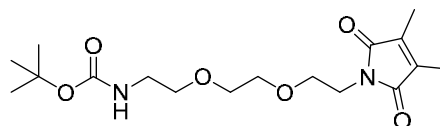
According to a literature procedure, 1,8-Diamino-3,6-dioxoctan (**8**) (30.0 g, 202 mmol, 1 eq.) is dissolved in a 1,4-dioxane/water mixture ( $v/v = 2:1$ , 300 mL) in a 500 mL Schlenk flask under Argon atmosphere and cooled in a water-ice-bath (2–5 °C).<sup>[7]</sup> A solution of di-*tert*-butyl dicarbonate (14.5 g, 66.4 mmol, 0.33 eq.) in 1,4-dioxane (100 mL) is added dropwise over 5 h. Afterwards, the ice-bath is removed and the reaction mixture is stirred for 17 h at r.t. before the turbid solution is concentrated under reduced pressure. After dilution with brine (200 mL), the pH is adjusted to 3 with an aqueous citric acid solution (3%) under ice-cooling (1.2 L). The aqueous phase is washed with DCM (3 x 200 mL) and the pH is adjusted to 10 with sodium carbonate (190 g). Finally, the basic aqueous phase is extracted with DCM (5 x 300 mL) before the organic layer is dried over sodium sulfate and the solvent is removed under reduced pressure. Amine **9** is obtained as colorless liquid (14.1 g, 56.9 mmol, 85%).

**Molecular formula:** C<sub>11</sub>H<sub>24</sub>N<sub>2</sub>O<sub>4</sub>. **TLC:** R<sub>f</sub> = 0.33 (DCM:MeOH = 10:3; SiO<sub>2</sub>). **ESI-HRMS (m/z):** Calculated for [M+H]<sup>+</sup>: 249.181, found: 249.181 **<sup>1</sup>H-NMR, COSY** (300 MHz, DMSO-*d*<sub>6</sub>, δ): 6.78 (t, 1H, C(=O)NH), 3.47 (m, 4H, OCH<sub>2</sub>CH<sub>2</sub>O), 3.40–3.28 (m, 6H, H<sub>2</sub>NCH<sub>2</sub>CH<sub>2</sub>O, OCH<sub>2</sub>CH<sub>2</sub>NHC(=O)), 3.05 (q, 2H, CH<sub>2</sub>NHC(=O)), 2.63 (t, 2H, NH<sub>2</sub>),

1.37 (s, 9H, CH<sub>3</sub>) ppm. **<sup>13</sup>C-NMR, HMBC, HSQC** (75 MHz, DMSO-*d*<sub>6</sub>, δ): 155.6 (OC(=O)NH), 77.6 (C(CH<sub>3</sub>)<sub>3</sub>), 73.1 (CH<sub>2</sub>O), 69.6 (CH<sub>2</sub>O), 69.5 (CH<sub>2</sub>O), 69.1 (CH<sub>2</sub>O), 41.4 (CH<sub>2</sub>NH<sub>2</sub>), 39.7 (CH<sub>2</sub>NHC(=O)), 28.3 (CH<sub>3</sub>) ppm.

### ***DMMI-<sup>T</sup>EG tert-butyl amine (11)***

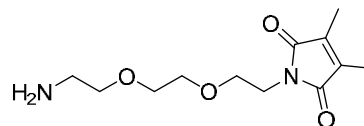
*tert*-Butyl-(2-(2-(2-aminoethoxy)ethoxy)ethyl)carbamate (**9**) and 2,3-dimethyl maleic anhydride (**10**) are dissolved in toluene (95 mL each) and added to a



250 mL two-neck flask equipped with a Dean-Stark apparatus. The colorless solution is heated under reflux for 11 h before the solvent is removed under reduced pressure and the crude product is obtained as orange liquid. After chromatographical purification (<sup>C</sup>Hex/EA = 3:2, SiO<sub>2</sub>), DMMI-TEG BOC-protected amine **11** is obtained as slightly yellow, viscose liquid (13.5 g, 37.8 mmol, 66%). **Molecular formula:** C<sub>17</sub>H<sub>28</sub>N<sub>2</sub>O<sub>6</sub>. **TLC:** R<sub>f</sub> = 0.25 (<sup>C</sup>Hex/EA = 3:2, SiO<sub>2</sub>). **ESI-HRMS (*m/z*):** Calculated for [M+H]<sup>+</sup>: 357.2025, [M+Na]<sup>+</sup>: 379.1840, found: [M+H]<sup>+</sup>: 357.2018, [M+Na]<sup>+</sup>: 379.1836 **<sup>1</sup>H-NMR, COSY** (300 MHz, CDCl<sub>3</sub> δ): 5.05 (s, 1H, C(=O)NH), 3.72–3.66 (m, 2H, NCH<sub>2</sub>), 3.6–3.50 (m, 8H, CH<sub>2</sub>O), 3.28 (q, <sup>3</sup>J = 5.1 Hz, 2H, CH<sub>2</sub>NH(C=O)), 1.95 (s, 6H, (C=C)CH<sub>3</sub>), 1.44 (s, 9H, OCCH<sub>3</sub>) ppm. **<sup>13</sup>C-NMR, HMBC, HSQC** (75 MHz, CDCl<sub>3</sub> δ): 172.2 (C(=O)N), 156.2 (OC(=O)NH), 137.4 (CH<sub>3</sub>C=CCH<sub>3</sub>), 77.3 (C(CH<sub>3</sub>)<sub>3</sub>), 70.4 (CH<sub>2</sub>O), 69.9 (CH<sub>2</sub>O), 68.3 (CH<sub>2</sub>O), 40.5 (CH<sub>2</sub>NH(C=O)), 37.1 (NCH<sub>2</sub>), 28.6 (C(CH<sub>3</sub>)<sub>3</sub>), 8.9 (C=C)CH<sub>3</sub>) ppm.

### ***DMMI-<sup>T</sup>EG amine (12)***

DMMI-TEG BOC-protected amine **11** (13.1 g, 36.8 mmol, 1.0 eq.) is dissolved in DCM (18.5 mL) under inert atmosphere before trifluoro acetic acid (TFA) (18.4 mL,

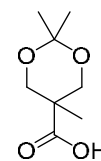


239 mmol, 6.5 eq.) and triethylsilane (0.37 mL, 1 vol%) are added. After stirring at r.t. for 60 min, TFA and solvent are removed under reduced pressure. The yellow residue is repeatedly re-dissolved in toluene which is then removed under reduced pressure (6 x) before the highly viscous TFA salt is finally dried under high vacuum for 48 h. **Molecular formula:** C<sub>12</sub>H<sub>20</sub>N<sub>2</sub>O<sub>4</sub>. **TLC:** R<sub>f</sub> = 0.44 (DCM/MeOH = 10:3, SiO<sub>2</sub>). **ESI-HRMS (*m/z*):** Calculated for [M+H]<sup>+</sup>: 257.1501, found: [M+H]<sup>+</sup>: 257.1500 **NMR, COSY** (300 MHz, CDCl<sub>3</sub> δ): 7.26 (*s<sub>br</sub>*, 3H, NH<sub>3</sub>), 3.76–3.57 (m, 10H, CH<sub>2</sub>O), 3.22 (m, 2H, CH<sub>2</sub>NH<sup>+</sup>), 1.94 (s, 6H, CH<sub>3</sub>) ppm. **<sup>13</sup>C-NMR, HMBC, HSQC** (75 MHz, CDCl<sub>3</sub> δ): 172.6 (C(=O)N), 137.6 (CH<sub>3</sub>C=CCH<sub>3</sub>), 70.2 (CH<sub>2</sub>O), 68.8 (CH<sub>2</sub>O), 66.6 (CH<sub>2</sub>O), 40.0 (CH<sub>2</sub>NH<sub>3</sub><sup>+</sup>), 37.5 (NCH<sub>2</sub>), 8.8 (CH<sub>3</sub>) ppm.

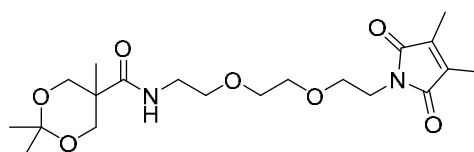


**2,2,5-trimethyl-1,3-dioxane-5-carboxylic acid (14)**

According to a literature procedure, 2,2-bis(hydroxymethyl)propionic acid **13** (10 g, 74.5 mmol, 1.0 eq.), 2,2-dimethoxypropan (13.8 mL, 113 mmol, 1.5 eq.) and *p*-toluenesulfonic acid monohydrate (0.78 g, 4.1 mmol, 0.05 eq.) are dissolved in anhydrous acetone and stirred at r.t. for 16 h under inert atmosphere.<sup>[8]</sup> Afterwards, a 1:1 mixture of EtOH and 37% ammonia solution (1 mL) is added and the solvent is removed under reduced pressure. The residue is dissolved in DCM (150 mL) and washed with water (3 x 30 mL) before the organic phase is dried over sodium sulfate. Removal of the solvent yields 2,2,5-trimethyl-1,3-dioxane-5-carboxylic acid (**14**) as colorless solid (11.6 g, 67.0 mmol, 90%). **Molecular formula:** C<sub>8</sub>H<sub>14</sub>O<sub>4</sub>. **TLC:** R<sub>f</sub> = 0.70 (EA, SiO<sub>2</sub>). **ESI-HRMS (m/z):** Calculated for [M]: 173.0814, found: 173.0820. **<sup>1</sup>H-NMR, COSY** (300 MHz, DMSO-*d*<sub>6</sub>, δ): 4.00 (d, 2H, <sup>2</sup>J = 11.6 Hz, CH<sub>2</sub>'), 3.55 (d, 2H, <sup>2</sup>J = 11.6 Hz, CH<sub>2</sub>''), 3.35 (s, 1H, C(=O)OH), 1.34 (s, 3H, CH<sub>3</sub>), 1.26 (s, 3H, CH<sub>3</sub>), 1.07 (s, 3H, CH<sub>3</sub>) ppm. **<sup>13</sup>C-NMR, HMBC, HSQC** (75 MHz, DMSO-*d*<sub>6</sub>, δ): 175.6 (C(=O)OH), 97.3 (OC<sub>q</sub>O), 65.2 (CH<sub>2</sub>), 40.7 (C<sub>q</sub>(CH<sub>2</sub>)<sub>2</sub>), 24.7 (CH<sub>3</sub>), 22.7 (CH<sub>3</sub>), 18.4 (CH<sub>3</sub>) ppm.

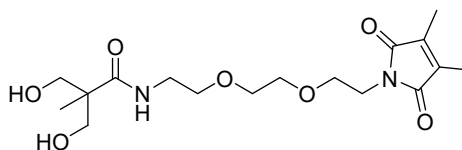
**DMMI-TEG diol acetonide (15)**

DMMI-TEG amine **12**\*TFA (1.00 g, 2.7 mmol, 1 eq.) is dissolved in anhydrous DMF (15 mL) in a 100 mL Schlenk flask under inert atmosphere before 2,2,5-trimethyl-1,3-dioxane-5-carboxylic acid (**14**) (0.57 g, 3.24 mmol, 1.2 eq.) is added. The solution is cooled in an ice-bath and a solution of HATU (1.23 g, 3.24 mmol, 1.2 eq.) in DMF (12 mL) and DIPEA (1.85 mL, 10.5 mmol, 3.9 eq.) are slowly added. After stirring for 3 h at r.t., the solvent is distilled off under high vacuum (40 °C oil bath) and the residue is dissolved in DCM (150 mL). After washing the organic phase with a saturated sodium bicarbonate solution (3 x 50 mL) and water (1 x 50 mL) and drying over sodium sulfate, the solvent is removed under reduced pressure. The crude product is chromatographically purified (ACN/H<sub>2</sub>O = 1:1, RP<sub>18</sub> silica gel) and compound **15** is obtained as colorless, highly viscous oil (749 mg, 1.82 mmol, 67%) after lyophilization. **Molecular formula:** C<sub>20</sub>H<sub>32</sub>N<sub>2</sub>O<sub>7</sub>. **TLC:** R<sub>f</sub> = 0.47 (ACN/H<sub>2</sub>O = 1:1, RP<sub>18</sub> silica gel). **ESI-HRMS (m/z):** Calculated for [M+H]<sup>+</sup>: 413.2288, [M+Na]<sup>+</sup>: 435.2107; found: [M+H]<sup>+</sup>: 413.2293, [M+Na]<sup>+</sup>: 435.2105. **<sup>1</sup>H-NMR, COSY** (400 MHz, DMSO-*d*<sub>6</sub>, δ): 7.57 (t, <sup>3</sup>J = 5.5 Hz, NHC(=O)), 3.90 (d, 2H, <sup>2</sup>J = 11.8 Hz, OCH<sub>2</sub>'C<sub>q</sub>), 3.61 (d, 2H, <sup>2</sup>J = 11.8 Hz, OCH<sub>2</sub>''C<sub>q</sub>), 3.53–3.44 (m, 8H, CH<sub>2</sub>O), 3.38 (t, <sup>3</sup>J = 5.8 Hz, 2H, CH<sub>2</sub>N), 3.21 (m, 2H, CH<sub>2</sub>NH(C=O)), 1.89 (s, 6H, (C=C)CH<sub>3</sub>), 1.35 (s, 3H, CH<sub>3</sub>), 1.28 (s, 3H, CH<sub>3</sub>), 1.00 (s, 3H, CH<sub>3</sub>) ppm.

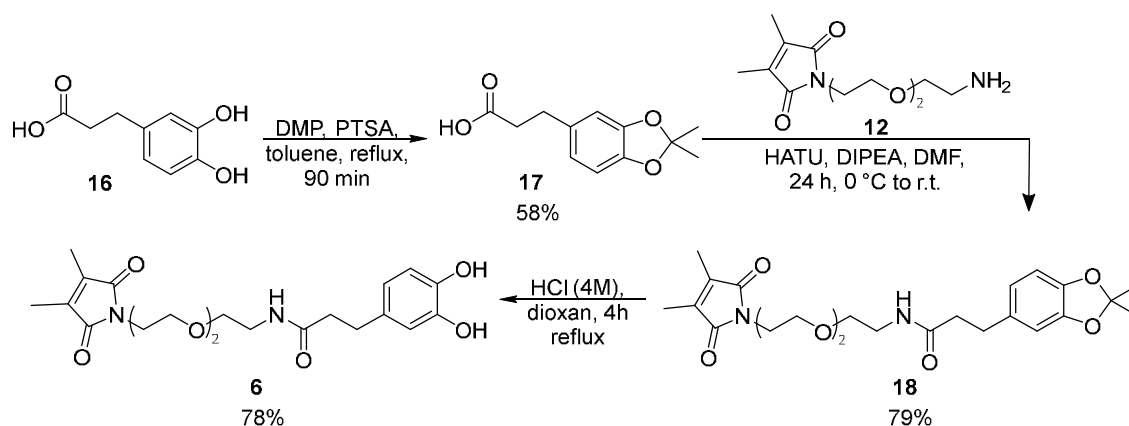


**DMMI-<sup>T</sup>EG diol (4)**

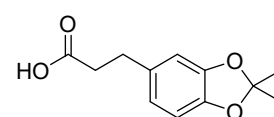
DMMI-<sup>T</sup>EG diol acetonide **15** (1.11 g, 2.69 mmol) is dissolved in MeOH (220 mL) before DOWEX X50W-X8 (5.28 g, 4.8 wt%) is



added and the colorless suspension is stirred for 19 h at r.t.. The solvent is removed under reduced pressure and the diol is obtained as slightly yellow, highly viscous oil (0.969 g, 2.58 mmol, 96%). **Molecular formula:** C<sub>17</sub>H<sub>28</sub>N<sub>2</sub>O<sub>7</sub>. **TLC:** R<sub>f</sub> = 0.44 (ACN/H<sub>2</sub>O = 1:1, RP<sub>18</sub> silica gel). **ESI-HRMS (m/z):** Calculated for [M+Na]<sup>+</sup>: 395.1794; found: [M+Na]<sup>+</sup>: 395.1793. **<sup>1</sup>H-NMR, COSY** (300 MHz, CDCl<sub>3</sub>, δ): 7.49 (*s<sub>br</sub>*, 1H, C(=O)NH), 3.63–3.49 (m, 14H, CH<sub>2</sub>CH<sub>2</sub>O, CH<sub>2</sub>OH), 3.44 (m, 2H, CH<sub>2</sub>NH(C=O)), 3.23 (*s<sub>br</sub>*, 2H, OH), 1.94 (s, 6H, CH<sub>3</sub>), 1.11 (s, 3H, CH<sub>3</sub>) ppm. **<sup>13</sup>C-NMR, HMBC, HSQC** (75 MHz, CDCl<sub>3</sub>, δ): 177.0 (C(=O)NH), 172.4 (C(=O)N), 137.5 (CH<sub>3</sub>C=CCH<sub>3</sub>), 70.3 (CH<sub>2</sub>O), 70.1 (CH<sub>2</sub>O), 69.6 (CH<sub>2</sub>OH), 68.3 (CH<sub>2</sub>O), 67.9 (CH<sub>2</sub>O), 47.8 (CH<sub>2</sub>NHC(=O)), 39.1 (C<sub>q</sub>(CH<sub>2</sub>)<sub>2</sub>), 37.3 (NCH<sub>2</sub>), 18.14 (CH<sub>3</sub>), 8.8 ((C=C)CH<sub>3</sub>) ppm.

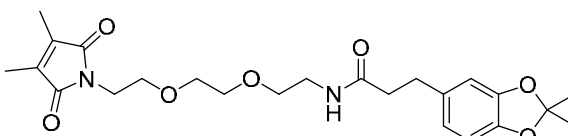
9.3.4.2. **DMMI-<sup>T</sup>EG-Catechol (6)**Scheme S9-2. Synthesis of DMMI-<sup>T</sup>EG-Catechol (6).**2,2-Dimethyl-1,3-benzodioxole-5-propanoic acid (17)**

2,2-Dimethyl-1,3-benzodioxole-5-propanoic acid (**17**) is synthesized according to a modified procedure by Liu et al.<sup>[9]</sup> 3,4-(Dihydroxyphenyl)propionic acid (**16**) (1.05 g, 5.76 mmol, 1.0 eq) is dissolved in anhydrous toluene (100 mL) in a flame-dried 250 mL two neck-flask equipped with reflux condenser and septum. 2,2-dimethoxypropan (2.2 mL, 22 mmol, 3.8 eq.) and *p*-toluenesulfonic acid monohydrate (50 mg, 0.26 mmol, 0.05 eq.) are added and the reaction mixture is refluxed for 90 min under nitrogen atmosphere. After cooling to r.t., the organic phase is washed with water (3 x 25 mL), dried over sodium sulfate before the solvent is removed under reduced pressure. The yellow residue is recrystallized from <sup>C</sup>Hex (15 mL) to yield (**17**) as colorless crystalline solid (708 mg, 58%). **Molecular formula:** C<sub>12</sub>H<sub>14</sub>O<sub>4</sub>. **TLC:** R<sub>f</sub> = 0.27 (ACN:H<sub>2</sub>O = 2:1, RP<sub>18</sub> silica gel). **ESI-HRMS (m/z):** Calculated for [M+H]<sup>+</sup>: 223.097, found: 223.090 **<sup>1</sup>H-NMR, COSY** (400 MHz, DMSO-*d*<sub>6</sub>, δ): 12.09 (s, 1H, C(=O)OH), 6.70 (m, 2H, Catechol: C<sub>3</sub>H/C<sub>6</sub>H), 6.60 (m, 1H, Catechol: C<sub>5</sub>H), 2.71 (t, 2H, <sup>3</sup>J = 7.6 Hz, CH<sub>2</sub>-Ar), 2.47 (t, 2H, <sup>3</sup>J = 7.6 Hz, CH<sub>2</sub>C(=O)OH), 1.66 (s, 6H, CH<sub>3</sub>) ppm. **<sup>13</sup>C-NMR, HMBC, HSQC** (101 MHz, DMSO-*d*<sub>6</sub>, δ): 173.8 (C(=O)OH), 146.8 (Catechol: C<sub>1</sub>), 145.1 (Catechol: C<sub>2</sub>), 134.1 (Catechol: C<sub>4</sub>), 120.5 (Catechol: C<sub>5</sub>H), 117.5 (OC<sub>q</sub>O), 108.5 (Catechol: C<sub>3</sub>H), 107.8 (Catechol: C<sub>6</sub>H), 35.6 (CH<sub>2</sub>C(=O)OH), 30.2 (CH<sub>2</sub>-Ar), 25.6 (CH<sub>3</sub>) ppm.



***DMMI-<sup>T</sup>EG-Catechol Acetonide (18)***

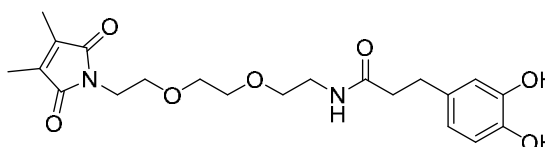
DMMI-triEG amine\*<sup>T</sup>FFA **12** (600 mg, 1.62 mmol, 1.2 eq.) is dried under high vacuum at r.t. in a 25 mL Schlenk flask for



4 h and afterwards dissolved in anhydrous DMF (2 mL) under nitrogen atmosphere before 2,2-dimethyl-1,3-benzodioxole-5-propanoic acid (**17**) (301.6 mg, 1.35 mmol, 1.0 eq) is added. Under ice cooling, a solution of HATU (770 mg, 2.0 mmol, 1.5 eq.) in DMF (2 mL) and finally DIPEA (0.92 mL, 5.40 mmol, 4.0 eq) are added dropwise and the reaction mixture is stirred for 1 h at 0 °C and another 23 h at r.t. Afterwards, the solvent is removed under reduced pressure and the residue is dissolved in DCM (80 mL). The organic phase is washed with saturated sodium carbonate solution (2 x 50 mL) and Brine (2 x 50 mL) before it is dried over sodium sulfate and the solvent is removed under reduced pressure. The residue is purified by column chromatography (ACN/H<sub>2</sub>O = 1:1, RP<sub>18</sub> silica gel) and the product is isolated as colorless oil after lyophilization (490 mg, 79%). **Molecular formula:** C<sub>24</sub>H<sub>32</sub>N<sub>2</sub>O<sub>7</sub>. **TLC:** R<sub>f</sub> = 0.25 (ACN:H<sub>2</sub>O = 1:1, RP<sub>18</sub> silica gel). **ESI-HRMS (m/z):** Calculated for [M+H]<sup>+</sup>: 461.2288, found: 461.227. **<sup>1</sup>H-NMR, COSY** (400 MHz, CDCl<sub>3</sub>, δ): 6.61 (m, 3H, Catechol: C<sub>3</sub>H, C<sub>5</sub>H, C<sub>6</sub>H), 6.20 (s, 1H, (C=O)NH), 3.57 (m, 12H, (CH<sub>2</sub>CH<sub>2</sub>O)<sub>2</sub>CH<sub>2</sub>CH<sub>2</sub>), 2.86 (m, 2H, CH<sub>2</sub>-Ar), 2.49 (m, 2H, NHC(=O)CH<sub>2</sub>), 1.94 (s, 6H, (C=C)CH<sub>3</sub>), 1.65 (s, 6H, OC<sub>q</sub>CH<sub>3</sub>) ppm. **<sup>13</sup>C-NMR, HMBC, HSQC** (101 MHz, CDCl<sub>3</sub>, δ): 172.7 (C(=O)NH), 172.6 (C(=O)N), 147.9 (Catechol: C<sub>1</sub>), 145.8 (Catechol: C<sub>2</sub>), 137.4 (CH<sub>3</sub>C=CCH<sub>3</sub>), 134.3 (Catechol: C<sub>4</sub>), 120.7 (Catechol: C<sub>5</sub>), 117.7 (OC<sub>q</sub>O), 108.8 (Catechol: C<sub>3</sub>), 108.1 (Catechol: C<sub>6</sub>), 70.4 (CH<sub>2</sub>O), 70.1 (CH<sub>2</sub>O), 69.9 (NCH<sub>2</sub>CH<sub>2</sub>O), 68.3 (CH<sub>2</sub>O), 39.6 (CH<sub>2</sub>NH(C=O)), 39.1 (CH<sub>2</sub>O), 37.6 (NH(C=O)CH<sub>2</sub>), 32.0 (CH<sub>2</sub>-Ar), 26.3 (OCCH<sub>3</sub>), 9.2 (CH<sub>3</sub>) ppm.

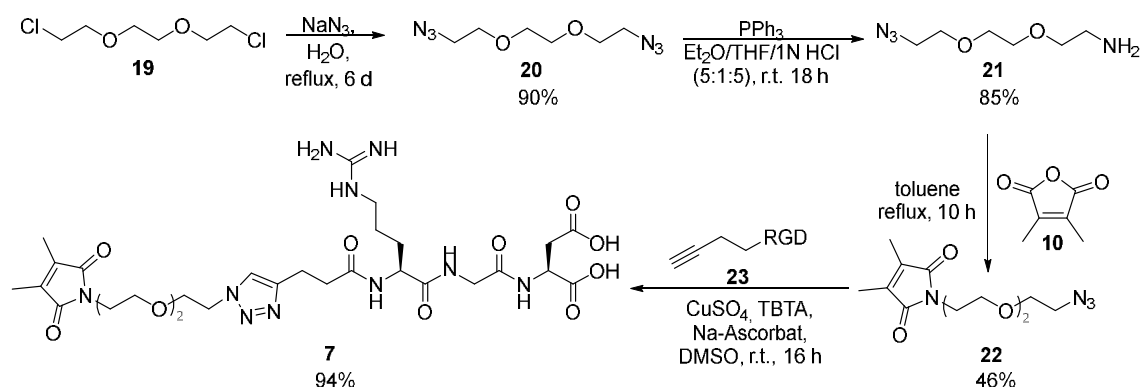
***DMMI-Catechol (6)***

DMMI-Catechol-acetonide **18** (473 g, 1.03 mmol, 1.0 eq.) is dissolved in HCl in dioxane



(4M, 10 mL) and heated under reflux in a nitrogen atmosphere for 10 h. After lyophilization of the reaction mixture, the product is purified by column chromatography (ACN/H<sub>2</sub>O = 2:1, RP<sub>18</sub> silica gel) and isolated as highly viscous, yellow oil (327 mg, 78%). **Molecular formula:** C<sub>21</sub>H<sub>28</sub>N<sub>2</sub>O<sub>7</sub>. **TLC:** R<sub>f</sub> = 0.55 (ACN:H<sub>2</sub>O = 2:1, RP<sub>18</sub> silica gel). **ESI-HRMS (m/z):** Calculated for [M+H]<sup>+</sup>: 421.19 found: 421.197. **<sup>1</sup>H-NMR, COSY** (400 MHz, DMSO-*d*<sub>6</sub>, δ): 8.69 (s, 1H, -OH), 8.59 (s, 1H, OH), 7.81 (t, <sup>3</sup>J = 5.7 Hz, 1H, (C=O)NH), 6.59 (d, <sup>3</sup>J = 7.9 Hz, 1H, Catechol: C<sub>6</sub>H), 6.55 (d,

$^4J = 2.1$  Hz, 1H, Catechol: C<sub>3</sub>H), 6.41 (dd,  $^3J = 7.9$  Hz,  $^4J = 2.1$  Hz, 1H, Catechol: C<sub>5</sub>H), 3.47 (m, 8H, CH<sub>2</sub>OCH<sub>2</sub>CH<sub>2</sub>OCH<sub>2</sub>), 3.31 (m, 2H, NCH<sub>2</sub>), 3.14 (m, 2H, CH<sub>2</sub>NH(C=O)), 2.60 (m, 2H, CH<sub>2</sub>-Ar), 2.26 (m, 2H, NHC(=O)CH<sub>2</sub>), 1.89 (s, 6H, CH<sub>3</sub>) ppm. **<sup>13</sup>C-NMR, HMBC, HSQC** (101 MHz, DMSO-*d*<sub>6</sub>, δ): 171.62 (C(=O)NH), 171.5 (C(=O)N), 144.9 (Catechol: C<sub>1</sub>), 143.3 (Catechol: C<sub>2</sub>), 136.7 (CH<sub>3</sub>C=CCH<sub>3</sub>), 132.2 (Catechol: C<sub>4</sub>), 118.7 (Catechol: C<sub>5</sub>), 115.6 (Catechol: C<sub>3</sub>), 115.4 (Catechol: C<sub>6</sub>), 69.5 (CH<sub>2</sub>O), 69.3 (CH<sub>2</sub>O), 69.2 (NCH<sub>2</sub>CH<sub>2</sub>O), 67.1 (CH<sub>2</sub>O), 38.46 (CH<sub>2</sub>NH(C=O)), 37.9 (NH(C=O)CH<sub>2</sub>), 37.4 (CH<sub>2</sub>O), 30.6 (CH<sub>2</sub>-Ar), 1, 8.4 (CH<sub>3</sub>) ppm.

9.3.4.3. **DMMI-<sup>T</sup>EG-RGD (7)**Scheme S9-3. Synthesis of DMMI-<sup>T</sup>EG RGD 7.**1,2-Bis(2-azidoethoxy)ethane (20)**

According to a literature procedure, freshly distilled 1,2-bis(2-chloroethoxy)ethane (**19**) (6.00 mL, 38.4 mmol, 1 eq.) is dissolved in water (100 mL) before sodium azide (13.8 g, 212 mmol, 5.5 eq.) is added and the colorless emulsion is heated under reflux for 6 days. After cooling to r.t., the aqueous phase is extracted with DCM (3 x 100 mL) and the combined organic phases are dried over sodium sulfate. 1,2-Bis(2-azidoethoxy)ethane (**20**) (6.90 g, 34.5 mmol, 90%) is obtained as colorless liquid after removal of the solvent under reduced pressure. **Molecular formula:** C<sub>6</sub>H<sub>12</sub>N<sub>6</sub>O<sub>2</sub>. **TLC:** R<sub>f</sub> = 0.19 (ACN/H<sub>2</sub>O = 1:1, RP<sub>18</sub> silica gel). **ESI-HRMS (m/z):** Calculated for [M+Na]<sup>+</sup>: 223.0919, found: 223.0914 **<sup>1</sup>H-NMR, COSY** (300 MHz, CDCl<sub>3</sub>, δ): 3.74–3.65 (m, 8H, CH<sub>2</sub>O), 3.40 (t, <sup>3</sup>J = 5.0 Hz, 4H, CH<sub>2</sub>N<sub>3</sub>) ppm. **<sup>13</sup>C-NMR, HMBC, HSQC** (75 MHz, CDCl<sub>3</sub>, δ): 70.9 (OCH<sub>2</sub>CH<sub>2</sub>O), 70.3 (CH<sub>2</sub>CH<sub>2</sub>N<sub>3</sub>), 50.8 (CH<sub>2</sub>N<sub>3</sub>) ppm.

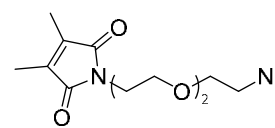
**2-[2-(2-Azidoethoxy)ethoxy]ethan-1-amine (21)**

According to a literature procedure, 1,2-bis(2-azidoethoxy)ethane (**20**) (4.15 g, 20.7 mmol, 1.0 eq.) is dissolved in a mixture of Et<sub>2</sub>O, THF and 1N HCl<sub>aq</sub> (5:1:5, 57.5 mL) in a 100 mL two-neck flask equipped under inert atmosphere.<sup>[10]</sup> Triphenylphosphine (5.42 g, 20.7 mmol, 1.0 eq.) is dissolved in Et<sub>2</sub>O (30 mL) and added over 3 h under vigorous stirring over a dripping funnel before the reaction mixture is stirred for 18 h at r.t.. Afterwards, the organic phase is separated and extracted with 4N HCl<sub>aq</sub> (100 mL). Both aqueous phases are combined and washed with Et<sub>2</sub>O (4 x 100 mL) and toluene (2 x 100 mL) before the pH is adjusted to 14 by addition of sodium hydroxide. Finally, the basic aqueous phase is extracted with DCM (2 x 100 mL) and the organic phase is dried over sodium sulfate before the solvent is removed under reduced

pressure. 2-[2-(2-Azidoethoxy)ethoxy]ethan-1-amine (**21**) is obtained as colorless liquid (3.06 g, 17.5 mmol, 85%). **Molecular formula:** C<sub>6</sub>H<sub>14</sub>N<sub>4</sub>O<sub>2</sub>. **TLC:** R<sub>f</sub>= 0.63 (ACN/H<sub>2</sub>O = 10:1, RP<sub>18</sub> silica gel). **ESI-HRMS (*m/z*):** Calculated for [M+H]<sup>+</sup>: 175.1195, found: 175.1189. Calculated for [M+Na]<sup>+</sup>: 197.1014, found: 197.1004. **<sup>1</sup>H-NMR, COSY** (300 MHz, CDCl<sub>3</sub>, δ): 3.82–3.59 (m, 6H, CH<sub>2</sub>O), 3.53 (t, <sup>3</sup>J = 5.2 Hz, 2H, CH<sub>2</sub>CH<sub>2</sub>NH<sub>2</sub>), 3.40 (t, <sup>3</sup>J = 5.0 Hz, 2H, CH<sub>2</sub>N<sub>3</sub>), 2.88 (t, <sup>3</sup>J = 5.2 Hz, 2H, CH<sub>2</sub>NH<sub>2</sub>), 1.74 (s, 2H, NH<sub>2</sub>) ppm. **<sup>13</sup>C-NMR, HMBC, HSQC** (75 MHz, CDCl<sub>3</sub>, δ): 73.44 (CH<sub>2</sub>CH<sub>2</sub>NH<sub>2</sub>), 70.81 (CH<sub>2</sub>O), 70.45 (CH<sub>2</sub>O), 70.21 (CH<sub>2</sub>O), 50.81 (CH<sub>2</sub>N<sub>3</sub>), 41.85 (CH<sub>2</sub>NH<sub>2</sub>) ppm.

### ***DMMI-TEG-azide (22)***

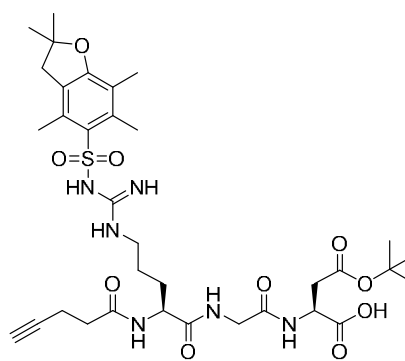
2-[2-(2-Azidoethoxy)ethoxy]ethan-1-amine (**21**) (1.59g, 9.1 mmol, 1.0 eq.) and 2,3-dimethyl maleic anhydride (**10**) (1.15 mg, 9.1 mmol, 1.0 eq.) are dissolved in toluene (50 mL)



and a 100 mL two-neck flask equipped with a Dean-Stark apparatus. The colorless solution is heated under reflux for 10 h under inert atmosphere. After removal of the solvent under reduced pressure, the obtained orange oil is purified by column chromatography (C<sub>6</sub>Hex/EA = 3:2, SiO<sub>2</sub>). DMMI-TEG-azide **22** (1.18 g, 4.2 mmol, 46%) is obtained as colorless viscous liquid. **Molecular formula:** C<sub>12</sub>H<sub>18</sub>N<sub>4</sub>O<sub>4</sub>. **TLC:** R<sub>f</sub>= 0.39 (C<sub>6</sub>Hex/EA = 3:2, SiO<sub>2</sub>). **ESI-HRMS (*m/z*):** Calculated for [M+Na]<sup>+</sup>: 305.1226, found: 305.1222 **<sup>1</sup>H-NMR, COSY** (300 MHz, CDCl<sub>3</sub>, δ): 3.71–3.60 (m, 10H, CH<sub>2</sub>O), 3.36 (m, 2H, CH<sub>2</sub>N<sub>3</sub>), 1.95 (s, 6H, CH<sub>3</sub>) ppm. **<sup>13</sup>C-NMR, HMBC, HSQC** (75 MHz, CDCl<sub>3</sub>, δ): 172.2 (C(=O)N), 137.3 (CH<sub>3</sub>C=CCH<sub>3</sub>), 70.79 (CH<sub>2</sub>O), 70.20 (CH<sub>2</sub>O), 70.16 (CH<sub>2</sub>O), 68.33 (CH<sub>2</sub>O), 50.80 (CH<sub>2</sub>N<sub>3</sub>), 37.21 (CH<sub>2</sub>N), 8.83 (CH<sub>3</sub>) ppm.

**Protected-RGD-alkyne (23a)**

The peptide is synthesized on solid support. *Loading of the resin:* 2-Chloro-tritylchloride polystyrene resin (loading = 1.60 mmol/g 2-chloro-tritylchloride, 1.00 g, 1.60 mmol) is placed in a Merrifield-reactor. A solution of Fmoc-L-Asp(O<sup>t</sup>Bu)-OH (1.32 g, 3.20 mmol, 2.0 eq.) in DCM (10 mL) with a small amount of DMF is added to the resin. After the addition of DIPEA (0.56 mL, 3.20 mmol, 2.0 eq.), the mixture is shaken for 5 min. DIPEA (0.84 mL, 4.80 mmol, 3.0 eq.) is added and the mixture agitated for 1 h. MeOH (1 mL) is added, the mixture shaken for 15 min before draining the reactor. The resin is washed consecutively with DCM (3 × 10 mL), DMF (3 × 10 mL), DCM (3 × 10 mL) and MeOH (3 × 10 mL). The resin is transferred in an automated peptide synthesizer and swollen by shaking it in DCM/DMF (1:1) for 15 min. The *N*-terminal *Fmoc*-group is removed by the treatment of the resin with piperidine in DMF (20 v% in DMF) for 5 min and subsequently for 20 min. The liquid is removed by suction and the resin washed with DMF (2×), DCM (2×) and DMF (2×). The *coupling of the following amino acid* is performed by treating the growing peptide with a solution of the Fmoc-Amino acid (4.0 eq.), HBTU (4.0 eq.), HOBT (4.4 eq.) and DIPEA (6.0 eq.) in DMF. After 1 h of shaking, the reactor is drained and the resin washed with DMF twice. The procedure is repeated for the third amino acid. After the final removal of Fmoc, the peptide was capped by shaking the resin in a solution of 4-pentynoic acid (314 mg, 3.2 mmol, 2.0 eq.), HATU (791 mg, 3.2 mmol, 2.0 eq.), HOAt (436 mg, 3.2 mmol, 2.0 eq.) and DIPEA (1.11 mL, 6.4 mmol, 4.0 eq.) for 2 h. The *peptide is cleaved* from the resin by shaking it in TFE in DCM (20 vol%, 3×20 mL) for 2 h. The cleavage cocktail is concentrated under reduced pressure and precipitated into cold water (45 mL). The residue is washed with water twice and subjected to lyophilization. The crude is purified by flash chromatography (EA/MeOH (+0.1% AcOH) = 5:1→1:1, SiO<sub>2</sub>) and the product isolated as colorless solid after lyophilization (988 mg, 1.34 mmol, 84% relative to resin loading capacity). **Molecular formula:** C<sub>54</sub>H<sub>50</sub>N<sub>6</sub>O<sub>10</sub>S. **TLC:** R<sub>f</sub> = 0.43 (EA/MeOH (+0.1% AcOH) = 3:1, SiO<sub>2</sub>). **ESI-HRMS (m/z):** Calculated for [M+H]<sup>+</sup>: 735.3387, [M+Na]<sup>+</sup>: 757.3207, found: [M+H]<sup>+</sup>: 735.3366, [M+Na]<sup>+</sup>: 757.3188. **<sup>1</sup>H-NMR, COSY** (400 MHz, DMSO-*d*<sub>6</sub>, δ): 12.82 (*s<sub>br</sub>*, 1H, **D**: C(=O)OH), 8.25 (m, 1H, **G**: NH), 8.12 (d, <sup>3</sup>*J* = 7.5 Hz, 1H, **R**: C(=O)NH), 8.03 (m, 1H, **D**: C(=O)NH), 7.19–6.21 (2× *s<sub>br</sub>*, 3H, **R**: NH), 4.50 (m, 1H, **D**: CH), 4.20 (m, 1H, **R**: CH), 3.69 (m, 2H, **G**: CH<sub>2</sub>), 3.02 (m, 2H, **R**: NHCH<sub>2</sub>), 2.96 (s, 2H, CH<sub>2</sub>(Pbf)), 2.74 (s, 1H, C≡CH), 2.64 (dd, <sup>1</sup>*J* = 16.0 Hz, <sup>3</sup>*J* = 6.1

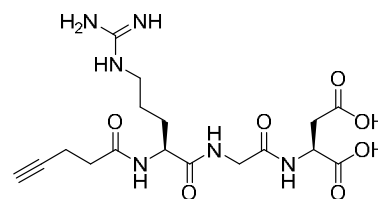




Hz, 1H, **D**: CH<sub>2</sub>'), 2.53 (dd, <sup>1</sup>J = 16.0 Hz, <sup>3</sup>J = 7.1 Hz, 1H, **D**: CH<sub>2</sub>''), 2.47 (s, 3H, **R**: CH<sub>3</sub>(Pbf)), 2.42 (s, 3H, **R**: CH<sub>3</sub>(Pbf)), 2.34 (m, 4H, HC≡CCH<sub>2</sub>CH<sub>2</sub>), 2.01 (s, 3H, **R**: CH<sub>3</sub>(Pbf)), 1.65 (m, 1H, **R**: NHCH<sub>2</sub>CH<sub>2</sub>CH<sub>2</sub>'), 1.52–1.38 (m, 9H, **R**: NHCH<sub>2</sub>CH<sub>2</sub>CH<sub>2</sub>'', NHCH<sub>2</sub>CH<sub>2</sub>, OC(CH<sub>3</sub>)<sub>2</sub>(Pbf)), 1.37 (s, 9H, **D**: OC(CH<sub>3</sub>)<sub>3</sub>). <sup>13</sup>C-NMR, HMBC, HSQC (101 MHz, DMSO-*d*<sub>6</sub>, δ): 172.2 (**D**: C(=O)OH), 171.8 (**R**: C(=O)NH), 170.6 (CH<sub>2</sub>CH<sub>2</sub>C(=O)NH), 169.2 (**D**: C(=O)O(CH<sub>3</sub>)<sub>3</sub>), 168.4 (**G**: C(=O)NH), 157.4 (C-7a(Pbf)), 156.1 (**R**: NHC(=NH)), 137.3 (C-6(Pbf)), 134.2 (C-5(Pbf)), 131.4, (C-4(Pbf)), 124.3 (C-3a(Pbf)), 116.3 (C-7(Pbf)), 86.3 (C-2(Pbf)), 83.7 (C≡CH), 80.3 (C(CH<sub>3</sub>)<sub>3</sub>), 71.3 (C≡CH), 52.5 (**R**: CH), 49.0 (**D**: CH), 42.5 (C-3(Pbf)), 41.7 (**G**: CH<sub>2</sub>), 40.1 (**R**: NHCH<sub>2</sub>), 37.3 (**D**: CH<sub>2</sub>), 33.9 (HC≡CCH<sub>2</sub>CH<sub>2</sub>), 29.4 (**R**: NHCH<sub>2</sub>CH<sub>2</sub>CH<sub>2</sub>), 28.3 (C-2-(CH<sub>3</sub>)<sub>2</sub>(Pbf)), 27.7 (C(CH<sub>3</sub>)<sub>3</sub>), 25.5 (**R**: NHCH<sub>2</sub>CH<sub>2</sub>), 19.0 (C-4-CH<sub>3</sub> (Pbf)), 17.6 (C-6-CH<sub>3</sub> (Pbf)), 14.1 (HC≡CCH<sub>2</sub>CH<sub>2</sub>), 12.30 (C-7-CH<sub>3</sub> (Pbf)) ppm.

### ***RGD-alkyne (23)***

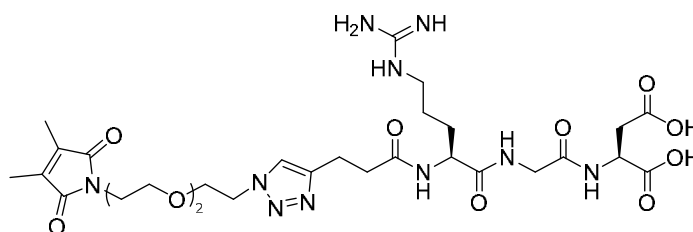
Protected RGD-alkyne **23a** (988 mg, 1.34 mmol) is dissolved in a mixture of TFA (9.0 mL), TIPS (0.5 mL) and H<sub>2</sub>O (0.5 mL) and agitated for 1.5 h at room temperature. The mixture is concentrated under reduced pressure and subsequently precipitated into cold Et<sub>2</sub>O (45 mL).



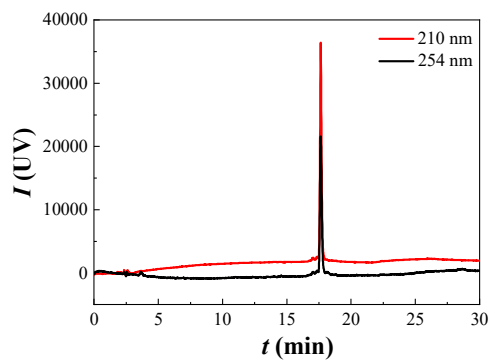
The precipitate is washed with Et<sub>2</sub>O (45 mL) twice, dried under reduced pressure, taken up in water and subjected to lyophilization to yield the product as colorless solid (TFA salt, 720 mg, 1.33 mmol, 99%). **Molecular formula:** C<sub>17</sub>H<sub>26</sub>N<sub>6</sub>O<sub>7</sub>. **TLC:** R<sub>f</sub> = 0.08 (Hex/EA = 1:1, SiO<sub>2</sub>). **ESI-HRMS (m/z):** Calculated for [M+H]<sup>+</sup>: 427.1941, found: 427.1934. <sup>1</sup>H-NMR, COSY (400 MHz, DMSO-*d*<sub>6</sub>, δ): 8.27 (t, <sup>3</sup>J = 5.8 Hz, **G**: C(=O)NH), 8.17 (d, <sup>3</sup>J = 8.2 Hz, 1H, **R**: C(=O)NH), 8.09 (d, <sup>3</sup>J = 8.1 Hz, 1H, **D**: C(=O)NH), 7.87 (m, 1H, **R**: NH), 7.16 (*s<sub>br</sub>*, 4H, **R**: NH/NH<sub>2</sub>), 4.46 (m, 1H, **D**: CH), 4.25 (m, 1H, **R**: CH), 3.71 (m, 2H, **G**: CH<sub>2</sub>), 3.08 (m, 2H, **R**: NHCH<sub>2</sub>), 2.74 (s, 1H, C≡CH), 2.59 (m, 2H, **D**: CH<sub>2</sub>), 2.35 (m, 4H, HC≡CCH<sub>2</sub>CH<sub>2</sub>), 1.72 (m, 1H, **R**: NHCH<sub>2</sub>CH<sub>2</sub>CH<sub>2</sub>''), 1.50 (m, 3H, **R**: NHCH<sub>2</sub>CH<sub>2</sub>'CH<sub>2</sub>') ppm. <sup>13</sup>C-NMR, HMBC, HSQC (101 MHz, DMSO-*d*<sub>6</sub>, δ): 172.6 (**D**: CHC(=O)OH), 172.1 (**D**: CH<sub>2</sub>C(=O)OH), 171.8 (**R**: C(=O)NH), 170.7 (CH<sub>2</sub>CH<sub>2</sub>C(=O)NH), 168.5 (**G**: C(=O)NH), 156.80 (**R**: NH<sub>2</sub>C(=NH)), 83.8 (C≡CH), 71.4 (C≡CH), 52.3 (**R**: CH), 48.7 (**D**: CH), 41.7 (**G**: CH<sub>2</sub>), 40.46 (**R**: NHCH<sub>2</sub>), 36.69 (**D**: CH<sub>2</sub>), 34.0 (HC≡CCH<sub>2</sub>CH<sub>2</sub>), 29.2 (**R**: NHCH<sub>2</sub>CH<sub>2</sub>CH<sub>2</sub>), 24.96 (**R**: NHCH<sub>2</sub>CH<sub>2</sub>), 14.2 (HC≡CCH<sub>2</sub>CH<sub>2</sub>) ppm.

**DMMI-<sup>T</sup>EG-RGD (7)**

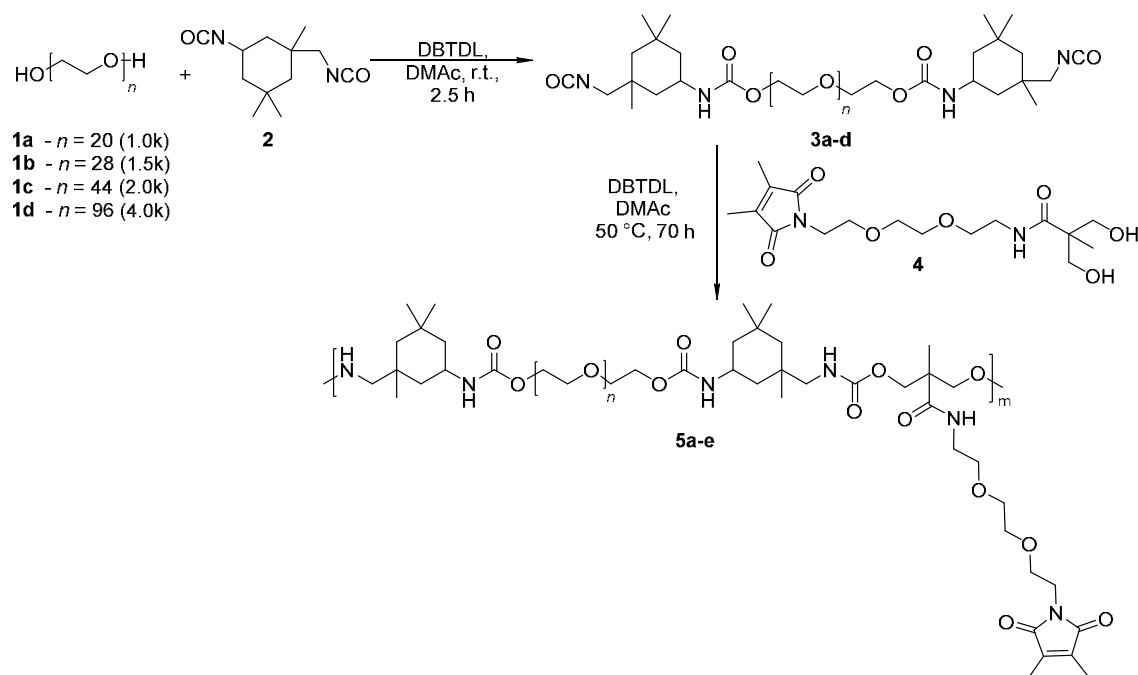
RGD-azide **23** (100 mg, 0.23 mmol, 1.0 eq.) and DMMI-TEG-azide **22** (99.3 mg, 0.35 mmol, 1.5 eq.) are dissolved in DMSO (3 mL) and oxygen is re-



moved by three consecutive freeze-pump thaw cycles. A solution of tris[(1-benzyl-1H-1,2,3-triazol-4-yl)methyl]amine (TBTA, 37.9 mg, 0.07 mmol, 0.3 eq.) and CuSO<sub>4</sub>·5H<sub>2</sub>O (11.2 mg, 0.07 mmol, 0.3 eq.) in DMSO (1 mL) is inserted before sodium ascorbate (35.8 mg, 0.18 mmol, 0.8 eq.) is added in a argon counter flow one minute later which changes the color from blue to colorless. The solution is stirred for 16 h at r.t. before the solvent is distilled off under high vacuum and the residue is dissolved in water (50 mL). After washing with Et<sub>2</sub>O (2 x 100 mL) and EA (2 x 50 mL), Chelex 100 resin is added to the blue solution, stirred at r.t. for 12 h and filtered off. After two additional Chelex treatments, DMMI-TEG-RGD **7** (156 mg) is obtained as colorless solid by lyophilization. Further purification is performed by semi-preparative HPLC (acetonitrile (B) and ultrapure water (A), each with 0.1% TFA, gradient: 15% B (1 min) → 50% B (in 24 min) → 100% B (3 min)). **Molecular formula:** C<sub>29</sub>H<sub>44</sub>N<sub>10</sub>O<sub>11</sub>. **TLC:** R<sub>f</sub> = 0.60 (ACN, RP<sub>18</sub> silica gel). **MALDI-MS (CHCA, m/z):** Calculated for [M+H]<sup>+</sup>: 709.327, found: 709.742; Calculated for [M+Na]<sup>+</sup>: 731.309, found: 731.738. **<sup>1</sup>H-NMR, COSY** (400 MHz, D<sub>2</sub>O, δ): 7.81 (s, 1H, triazole: CH), 4.75 (m, 1H, D: CH), 4.53 (t, <sup>3</sup>J = 5.0 Hz, 2H, triazoleN-CH<sub>2</sub>), 4.26 (m, 1H, R: CH), 3.95 (s, 2H, G: CH<sub>2</sub>), 3.88 (t, <sup>3</sup>J = 5.0 Hz, 2H, triazoleN-CH<sub>2</sub>CH<sub>2</sub>), 3.64–3.56 (m, 8H, CH<sub>2</sub>O, CH<sub>2</sub>NC(=O)), 3.16 (m, 2H, R: NHCH), 3.01 (m, triazoleC-CH<sub>2</sub>CH<sub>2</sub>), 2.92 (m, 2H, D: CH<sub>2</sub>), 2.68 (m, 2H, triazoleC-CH<sub>2</sub>CH<sub>2</sub>), 1.90 (s, 6H, CH<sub>3</sub>), 1.80 (m, 1H, R: NHCH<sub>2</sub>CH<sub>2</sub>'), 1.67 (m, 1H, R: NHCH<sub>2</sub>CH<sub>2</sub>CH<sub>2</sub>'), 1.52 (m, 2H, R: NHCH<sub>2</sub>CH<sub>2</sub>'CH<sub>2</sub>') ppm. **<sup>13</sup>C-NMR, HMBC, HSQC** (101 MHz, DMSO-*d*<sub>6</sub>/D<sub>2</sub>O, δ): 175.3 (R: C(=O)NH), 174.3 (DMMI: C=O), 174.2 (D: CHC(=O)OH), 174.1 (D: C(=O)OH), 170.8 (G: C(=O)NH), 156.7 (R: NH<sub>2</sub>C(=NH)), 146.2 (triazole: C=CCH<sub>2</sub>), 137.7 (DMMI: C=C), 123.7 (triazole: C=CCH<sub>2</sub>), 69.6 (CH<sub>2</sub>O), 69.2 (CH<sub>2</sub>O), 68.7 (triazoleN-CH<sub>2</sub>CH<sub>2</sub>), 67.7 (CH<sub>2</sub>O), 53.6 (R: CH), 50.7 (triazoleN-CH<sub>2</sub>), 49.2 (D: CH), 42.2 (G: CH<sub>2</sub>), 40.4 (R: NHCH<sub>2</sub>), 37.0 (DMMI-CH<sub>2</sub>), 35.6 (D: CH<sub>2</sub>), 34.6 (triazoleC-CH<sub>2</sub>CH<sub>2</sub>), 27.9 (R: NHCH<sub>2</sub>CH<sub>2</sub>CH<sub>2</sub>), 24.2 (R: NHCH<sub>2</sub>CH<sub>2</sub>CH<sub>2</sub>), 20.7 (triazoleC-CH<sub>2</sub>), 7.8 (CH<sub>3</sub>) ppm.



**Figure S9-22.** Chromatogram of Compound 7 (acetonitrile (B) and ultrapure water (A), each with 0.1% TFA; gradient: 5% B (1 min) à 30% B (in 15 min) à 30% B (3 min) à 50% B (in 5 min)).

9.3.4.4. **Linear PEG-IPDI-DMMI Polyurethanes**

**Scheme S9-4.** Synthesis of linear PEG/IPDI PUs with pendant DMMI groups.

**SOP**

All reaction steps are carried out under Argon atmosphere in flame dried glassware. An IPDI **2** stock solution in DMA (2.0 eq., 0.95 M) is added to a 100 mL three-neck flask with dripping funnel, valve and septum. Poly(ethylene glycol) **1a–d** (500 mg, 1.0 eq) of the appropriate molar mass is freshly freeze-dried from benzene and dissolved in DMA (3 mL) and transferred to the dripping funnel with a syringe. After addition of one drop DBTDL to the IPDI, the PEG solution is added over 15–30 min and the reaction mixture is stirred for another 2 h. Afterwards, the DMMI diol **4** (1.0 eq, 0.45 M) is added as a stock solution in DMA and the reaction mixture is heated to 50 °C. After 48 h, an additional portion of IPDI (0.1 eq.) is added and the solution is stirred for another 24 h. Next, the reaction is quenched with MeOH (2 mL) and cooled to r.t.. The polymer solution is precipitated into ice-cold Et<sub>2</sub>O (160 mL) and reprecipitated one time from DCM. Finally, the PU is isolated by lyophilization from ACN/H<sub>2</sub>O. All polymerizations are carried out according to this SOP.

**PU-1.0k (5a)**

The polymerization is carried out with PEG-1.0k ( $M_n = 0.88 \text{ kg mol}^{-1}$ , 401 mg, 1.0 eq.), and IPDI (stock solution: 0.94 M, 0.85 mL, 2.0 eq.) and DMMI (stock solution: 0.45 M, 0.89 mL, 1.0 eq.). **Yield:** 0.528 mg (71%). **SEC:**  $M_n = 4.15 \text{ kg mol}^{-1}$ ,  $M_w = 6.28 \text{ kg mol}^{-1}$ ,  $D = 1.5$  **<sup>1</sup>H-NMR** (400 MHz, DMSO-*d*<sub>6</sub>,  $\delta$ ): 7.55 (m, 1.1H, C(=O)NH), 7.12 (m, 2H, OC(=O)NH), 5.69

(m, 2H, OC(=O)NH), 4.87 (m, 1H, CH), 4.03 (m, 6H, NH(C=O)O-CH<sub>2</sub>), 3.50 (m, 90H, CH<sub>2</sub>O), 2.73 (m, 4H, O(C=O)NH-CH<sub>2</sub>), 1.89 (s, 4.5H, (C=C)CH<sub>3</sub>), 1.60–0.72 (m, 36H, CH<sub>3</sub>/CH<sub>2</sub>) ppm.

**<sup>13</sup>C-NMR** (101 MHz, DMSO-*d*<sub>6</sub>, δ): 173.7 (C(=O)NH), 171.6 (DMMI: C(=O)N), 158.5 (OC(=O)NH), 156.5 (OC(=O)NH), 155.4 (OC(=O)NH), 136.8 (CH<sub>3</sub>C=CCH<sub>3</sub>), 69.5 (CH<sub>2</sub>O), 69.3 (CH<sub>2</sub>O), 68.9 (CH<sub>2</sub>O), 62.9 (CH<sub>2</sub>O), 54.4 (IPDI), 47.2 (CH<sub>2</sub>NHC(=O)), 45.5 (IPDI), 43.9 (IPDI), 41.6 (IPDI), 38.6 (IPDI), 36.9 (IPDI), 36.0 (IPDI), 35.0 (IPDI), 31.4 (IPDI), 27.5 (IPDI: CH<sub>3</sub>), 23.2 (IPDI: CH<sub>3</sub>), 17.4 (CH<sub>3</sub>), 8.5 (DMMI: CH<sub>3</sub>) ppm.

Peak assignment according to literature reports and comparison with educt spectra.<sup>[11]</sup>

### ***PU-1.5k<sup>0.6</sup> (5b)***

The polymerization is carried out with PEG-1.5k ( $M_n = 1.24 \text{ kg mol}^{-1}$ , 301 mg, 0.6 eq.), and IPDI (2.0 eq., stock solution: 0.43 M, 1.13 mL) and DMMI (stock solution: 0.21 M, 1.35 mL, 1.4 eq.). **Yield:** 0.417 mg (89%). **SEC:**  $M_n = 6.55 \text{ kg mol}^{-1}$ ,  $M_w = 12.0 \text{ kg mol}^{-1}$ ,  $D = 1.9$ . **<sup>1</sup>H-NMR** (400 MHz, DMSO-*d*<sub>6</sub>, δ): 7.60 (m, 1.1H, C(=O)NH), 7.13 (m, 2.2H, OC(=O)NH), 5.84 (m, 1.8H, OC(=O)NH), 4.89 (m, 1H, CH), 4.02 (m, 6.1H, NH(C=O)O-CH<sub>2</sub>), 3.34 (m, 113H, CH<sub>2</sub>O), 2.72 (m, 3.6H, O(C=O)NH-CH<sub>2</sub>), 1.89 (s, 4.8H, (C=C)CH<sub>3</sub>), 1.55–0.81 (m, 38.5H, CH<sub>3</sub>/CH<sub>2</sub>) ppm. **<sup>13</sup>C-NMR** (101 MHz, DMSO-*d*<sub>6</sub>, δ): 173.8 (C(=O)NH), 171.7 (DMMI: C(=O)N), 158.5 (OC(=O)NH), 157.0 (OC(=O)NH), 156.9 (OC(=O)NH), 155.4 (OC(=O)NH), 136.8 (CH<sub>3</sub>C=CCH<sub>3</sub>), 69.6 (CH<sub>2</sub>O), 68.9 (CH<sub>2</sub>O), 67.1 (CH<sub>2</sub>O), 62.9 (CH<sub>2</sub>O), 53.4 (IPDI), 46.7 (CH<sub>2</sub>NHC(=O)), 45.5 (IPDI), 43.9 (IPDI), 41.6 (IPDI), 38.6 (IPDI), 36.9 (IPDI), 36.0 (IPDI), 35.0 (IPDI), 31.5 (IPDI), 27.5 (IPDI: CH<sub>3</sub>), 23.2 (IPDI: CH<sub>3</sub>), 17.5 (CH<sub>3</sub>), 8.5 (DMMI: CH<sub>3</sub>) ppm.

### ***PU-1.5k (5c)***

The polymerization is carried out with PEG-1.5k ( $M_n = 1.24 \text{ kg mol}^{-1}$ , 500 mg, 1.0 eq.), IPDI (stock solution: 0.94 M, 0.71 mL, 2.0 eq.) and DMMI (stock solution: 0.45 M, 0.74 mL, 1.0 eq.). **Yield:** 0.566 mg (73%). **SEC:**  $M_n = 7.02 \text{ kg mol}^{-1}$ ,  $M_w = 12.4 \text{ kg mol}^{-1}$ ,  $D = 1.8$ . **<sup>1</sup>H-NMR** (400 MHz, DMSO-*d*<sub>6</sub>, δ): 7.56 (m, 1H, C(=O)NH), 7.12 (m, 2H, OC(=O)NH), 5.74 (m, 2.6H, OC(=O)NH), 4.87 (m, 1H, CH), 4.03 (m, 6H, NH(C=O)O-CH<sub>2</sub>), 3.51 (m, 113H, CH<sub>2</sub>O), 2.72 (m, 4.1H, O(C=O)NH-CH<sub>2</sub>), 1.89 (s, 3.6H, (C=C)CH<sub>3</sub>), 1.61–0.73 (m, 34H, CH<sub>3</sub>/CH<sub>2</sub>) ppm. **<sup>13</sup>C-NMR** (101 MHz, DMSO-*d*<sub>6</sub>, δ): 173.7 (C(=O)NH), 171.61 (DMMI: C(=O)N), 156.8 (OC(=O)NH), 155.4 (OC(=O)NH), 136.8 (CH<sub>3</sub>C=CCH<sub>3</sub>), 69.7 (CH<sub>2</sub>O), 69.5 (CH<sub>2</sub>O), 69.3 (CH<sub>2</sub>O), 68.9 (CH<sub>2</sub>O), 67.1 (CH<sub>2</sub>O), 66.2 (CH<sub>2</sub>O), 63.1 (CH<sub>2</sub>O), 62.9

## APPENDIX

(CH<sub>2</sub>O), 60.2 (CH<sub>2</sub>O), 47.0 (CH<sub>2</sub>NHC(=O)), 46.6 (IPDI), 45.5 (IPDI), 43.9 (IPDI), 38.6 (IPDI), 36.9 (IPDI), 36.3 (IPDI), 36.0 (IPDI), 35.0 (IPDI), 31.4 (IPDI), 27.5 (IPDI: CH<sub>3</sub>), 23.2 (IPDI: CH<sub>3</sub>), 17.5 (CH<sub>3</sub>), 8.5 (DMMI: CH<sub>3</sub>) ppm.

### **PU-2.0k (5d)**

The polymerization is carried out with PEG-2k ( $M_n = 1.95 \text{ kg mol}^{-1}$ , 502 mg, 1.0 eq.), IPDI (stock solution: 0.95 M, 0.53 mL, 2.0 eq.) and DMMI (stock solution: 0.46 M, 0.55 mL, 1.0 eq.). **Yield:** 0.522 mg (74%). **SEC:**  $M_n = 8.93 \text{ kg mol}^{-1}$ ,  $M_w = 14.62 \text{ kg mol}^{-1}$ ,  $D = 1.6$ . **<sup>1</sup>H-NMR** (400 MHz, DMSO-*d*<sub>6</sub>,  $\delta$ ): 7.55 (m, 0.8H, C(=O)NH), 7.14 (m, 2H, OC(=O)NH), 5.69 (m, 2H, OC(=O)NH), 4.86 (m, 0.6H, CH), 4.03 (m, 5.2H, NH(C=O)O-CH<sub>2</sub>), 3.51 (m, 175H, CH<sub>2</sub>O), 2.73 (m, 4.3H, O(C=O)NH-CH<sub>2</sub>), 1.89 (s, 4.3H, (C=C)CH<sub>3</sub>), 1.61–0.72 (m, 41.3H, CH<sub>3</sub>/CH<sub>2</sub>) ppm. **<sup>13</sup>C-NMR** (101 MHz, DMSO-*d*<sub>6</sub>,  $\delta$ ): 173.7 (C(=O)NH), 171.61 (DMMI: C(=O)N), 158.5 (OC(=O)NH), 158.4 (OC(=O)NH), 156.8 (OC(=O)NH), 155.4 (OC(=O)NH), 136.8 (CH<sub>3</sub>C=CCH<sub>3</sub>), 70.0 (CH<sub>2</sub>O), 69.3 (CH<sub>2</sub>O), 68.9 (CH<sub>2</sub>O), 67.9 (CH<sub>2</sub>O), 63.1 (CH<sub>2</sub>O), 62.9 (CH<sub>2</sub>O), 54.4 (IPDI: CH<sub>2</sub>NHC(=O)O), 53.4 (IPDI), 46.6 (IPDI), 45.5 (IPDI), 43.9 (IPDI), 38.6 (IPDI), 36.9 (IPDI), 36.0 (IPDI), 35.0 (IPDI), 31.4 (IPDI), 30.0 (IPDI), 27.5 (IPDI: CH<sub>3</sub>), 23.0 (IPDI: CH<sub>3</sub>), 17.5 (CH<sub>3</sub>), 8.5 (DMMI: CH<sub>3</sub>) ppm.

### **PU-4.0k (5e)**

The polymerization is carried out with PEG-4k ( $M_n = 4.22 \text{ kg mol}^{-1}$ , 485 mg, 1.0 eq.) IPDI (stock solution: 0.95 M, 0.25 mL, 2.0 eq.) and DMMI (stock solution: 0.46 M, 0.26 mL, 1.0 eq.). **Yield:** 0.436 mg (72%). **SEC:**  $M_n = 20.03 \text{ kg mol}^{-1}$ ,  $M_w = 30.27 \text{ kg mol}^{-1}$ ,  $D = 1.5$ . **<sup>1</sup>H-NMR** (400 MHz, DMSO-*d*<sub>6</sub>,  $\delta$ ): 7.55 (m, 0.8H, C(=O)NH), 7.14 (m, 2H, OC(=O)NH), 5.69 (m, 2H, OC(=O)NH), 4.88 (m, 0.3H, CH), 4.03 (m, 4.8H, NH(C=O)O-CH<sub>2</sub>), 3.51 (m, 381H, CH<sub>2</sub>O), 2.92–2.60 (m, 4H, O(C=O)NH-CH<sub>2</sub>), 1.89 (s, 4.1H, (C=C)CH<sub>3</sub>), 1.78–0.63 (m, 53H, CH<sub>3</sub>/CH<sub>2</sub>) ppm. **<sup>13</sup>C-NMR** (101 MHz, DMSO-*d*<sub>6</sub>,  $\delta$ ): 176.8 (C(=O)NH), 171.6 (DMMI: C(=O)N), 158.5 (OC(=O)NH), 157.6 (OC(=O)NH), 156.8 (OC(=O)NH), 155.4 (OC(=O)NH), 136.8 (CH<sub>3</sub>C=CCH<sub>3</sub>), 69.8 (CH<sub>2</sub>O), 68.9 (CH<sub>2</sub>O), 67.1 (CH<sub>2</sub>O), 63.1 (CH<sub>2</sub>O), 62.9 (CH<sub>2</sub>O), 47.0 (IPDI), 45.6 (IPDI), 43.9 (IPDI), 38.6 (IPDI), 36.9 (IPDI), 36.1 (IPDI), 35.0 (IPDI), 31.4 (IPDI), 31.3 (IPDI), 27.5 (IPDI: CH<sub>3</sub>), 23.0 (IPDI: CH<sub>3</sub>), 8.4 (DMMI: CH<sub>3</sub>) ppm.

### 9.3.5. Molar Mass Distributions

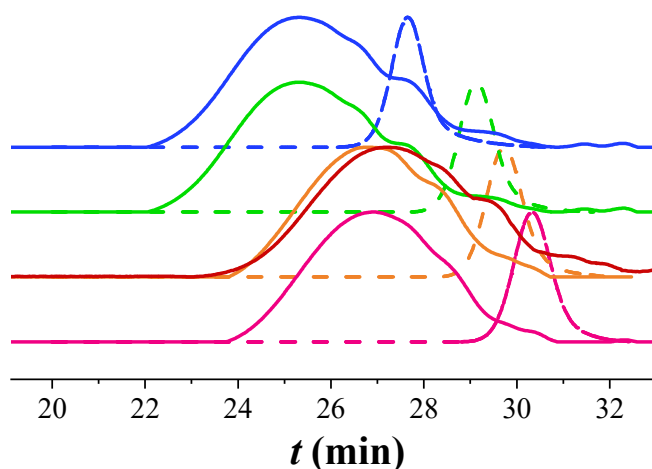


**Figure S9-23.** SEC elugrams of PEG-diols **1a–d** (dashed) and the corresponding PEG/IPDI/DMMI PUs (PU-1.0k **5a** (—), 1.5k<sup>0.6</sup> **5b** (—), PU-1.5k **5c** (—), PU-2.0k **5d** (—) and PU-4.0k **5e** (—) (measured in DMF + LiCl 1 g·L<sup>-1</sup>).

### 9.3.6. Turbidity Measurements

The PUs are dissolved in MilliQ water (3 mL) to a concentration of  $\rho_{\text{PU}} = 5 \text{ g}\cdot\text{L}^{-1}$ . Afterwards, the solutions are transferred to a quartz glass cuvette equipped with a stirring bar. For the turbidity measurements, a wavelength of 550 nm is chosen and a dark measurement is performed, before a baseline measurement is conducted with pure water. Then the PU-cuvette is placed in the spectrometer and equilibrated for 10 min at each temperature under vigorous stirring before the measurement is started. After another 10 min at the same temperature, a further measurement is performed and if both values coincide the temperature is increased (5 °C or 2.5 °C steps). Otherwise, the equilibration is continued at the same temperature. The cloud point temperatures are determined from the inflection points of the recorded curves shown in **Figure 5-1b**.

### 9.3.7. Rheological Measurements

The PUs are dissolved to the appropriate concentration in an aqueous thioxanthone disulfonate (TXS) solution (0.1 or 1 mM). For gelation experiments, 80  $\mu\text{L}$  of this solution are placed on the rheometer (plate-plate geometry, diameter: 25 mm) and the sample is equilibrated for 5 min at 5 °C at a constant shear amplitude and frequency ( $\gamma = 0.1\%$ ;  $\omega = 1 \text{ rad}\cdot\text{s}^{-1}$ ). Afterwards, the UV irradiation (1 or 10% aperture) is started through the transparent

lower glass plate and a time dependent measurement is started ( $\gamma = 0.1\%$ ;  $\omega = 1 \text{ rad}\cdot\text{s}^{-1}$ ) at  $5^\circ\text{C}$ .

### 9.3.8. Gelation Time Measurements

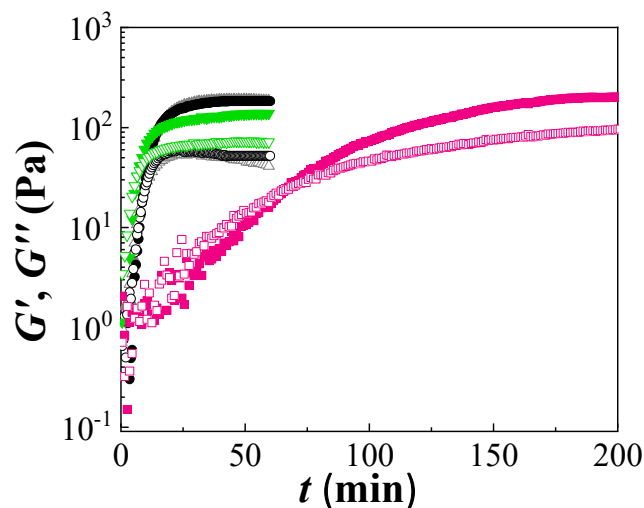


**Figure S9-24.** Time-dependent storage  $G'$  (closed symbols) and loss  $G''$  (open symbols) moduli of PU-4k ( $100 \text{ g}\cdot\text{L}^{-1}$ ) in an aqueous thioxanthone disulfonate (TXS) solution under UV irradiation at a TXS concentration of  $1 \text{ mM}$  and a light aperture of  $1\%$  at  $20^\circ\text{C}$  ( $\bullet$ ) and  $5^\circ\text{C}$  ( $\blacktriangle$ ) as well as at a TXS concentration of  $0.1 \text{ mM}$  and a light aperture of  $1\%$  ( $\blacksquare$ ) and  $10\%$  ( $\blacktriangledown$ ) at  $5^\circ\text{C}$ .

### 9.3.9. Equilibrium Swelling Experiments

Around  $10 \text{ mg}$  precursor polymer are dissolved to a concentration of  $100 \text{ g}\cdot\text{L}^{-1}$  in aqueous thioxanthone disulfonate solution ( $1 \text{ mM}$ ) and irradiated with UV light for  $60 \text{ min}$ . The obtained gels are dialyzed against MeOH (2 x) and water (4 x) to remove a potential sol fraction. The gels are then immersed in water ( $5 \text{ mL}$ ) and kept in a  $5$ ,  $20$  or  $40^\circ\text{C}$  water bath for  $12 \text{ h}$  before the gel is removed from the water and weighed ( $m_T$ ). Finally, the gels are freeze dried and the dry mass ( $m_{\text{dry}}$ ) is determined by difference weighing. The swelling degree  $Q_T$  is calculated as  $Q_T = 100\% \cdot (m_T - m_{\text{dry}}) / m_{\text{dry}}$ . Each measurement is performed at least in duplicate.

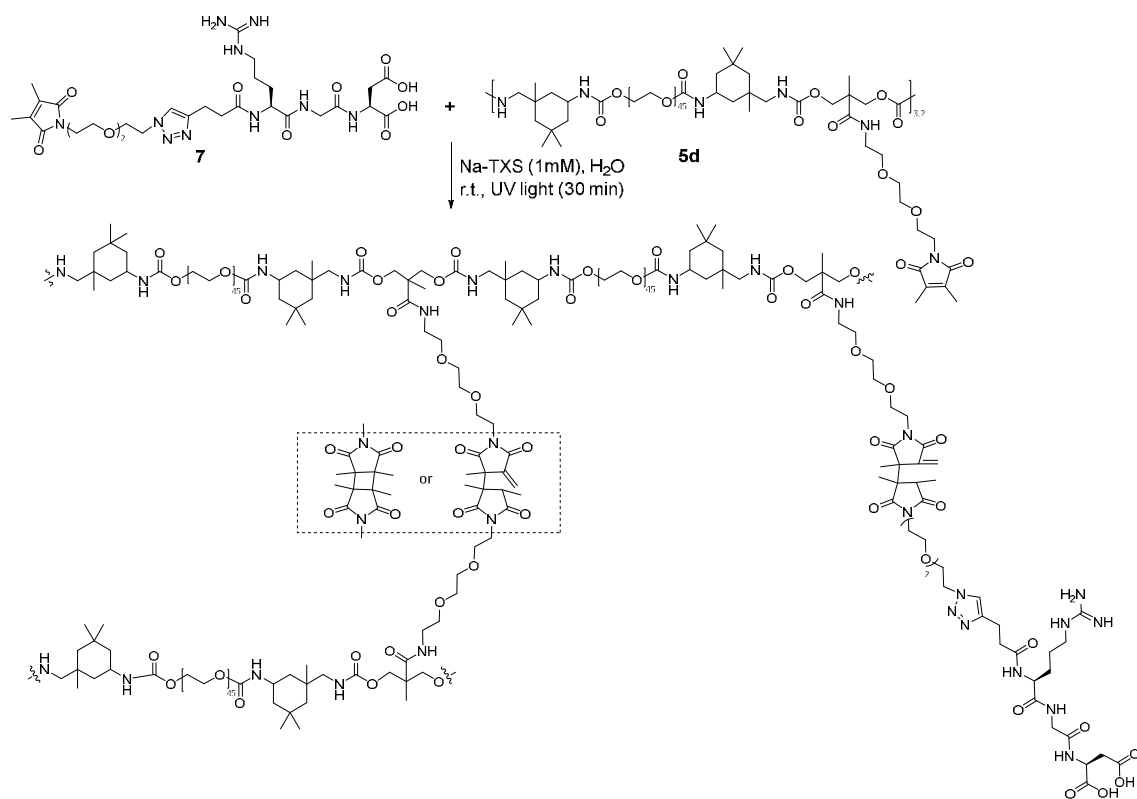


### 9.3.10. Temperature Induced Volume Change

A PU-1.5k<sup>0.6</sup> gel piece of  $\approx 2$  mm size is cut from the macroscopic gel, immersed in water and sealed between two microscopy slides. After placing the sample on an Instec Thermo-stage under an optical microscope (4x objective), a temperature ramp from 5 to 61 °C is started. During this, the temperature is increased in 2 °C steps and the samples are equilibrated for 10 min at each temperature. The diameter of the gel piece is measured at three different positions at each temperature using the software ImageJ. The measured distances are normalized to the one measured at 5 °C and an average of the normalized values from the three different positions is calculated.

### 9.3.11. Gel Preparation for MAS-NMR and Cell Experiments

The schematic gelation reaction is shown in **Scheme S9-5**. Stock solutions of the Catechol-**6** or RGD-**7** DMMI (50 mM) are prepared in MilliQ water. Afterwards, a volume portion containing 0, 5 or 25 mol% of the respective bio-linker in comparison to the DMMI groups in the PU ( $n_{\text{DMMI}} = f_{\text{DMMI}} \cdot N_x \cdot n_{\text{PU}}$  with the DMMI functionalization degree  $f_{\text{DMMI}} = 0.78$  derived from the <sup>1</sup>H NMR analysis ( $f_{\text{DMMI}} = \text{integral}(1.89 \text{ ppm}^{\text{exp}}) / \text{integral}(1.89 \text{ ppm})^{\text{theo}}$ ), the average number of repeating units per chain  $N_x = M_n(\text{PU}) / M_n(\text{repeating unit}) = 8.9 \text{ kg} \cdot \text{mol}^{-1} / 2.8 \text{ kg} \cdot \text{mol}^{-1} = 3.2$ , and the molar amount of the PU  $n_{\text{PU}} = m_{\text{PU}} / M_n(\text{PU})$ ) are added to in a previously weighed amount of PU-2k **5d** (10–20 mg). An aqueous thioxanthone disulfonate solution (1 mM) is added to obtain a polymer concentration of 200 g·L<sup>-1</sup>. After dissolution overnight, the solution is irradiated with UV light for 30 min. Afterwards, the obtained gel is dialyzed against DMSO (2 x 12 h), MeOH (2 x 12 h) and water (4 x 12 h) to remove any excess of bio-linker and photosensitizer. For <sup>1</sup>H MAS NMR measurements, the gels are then freeze-dried and immersed in D<sub>2</sub>O for at least 12 h prior to measurement. For cell tests, the gels are transferred into phosphate buffer and purified over 3 days, while changing the buffer every day.



**Scheme S9-5.** Schematic incorporation of RGD-DMMI units into the PU gel.

### 9.3.12. $^1\text{H}$ MAS NMR Spectroscopy

PU-2k **5d** gels with 0 mol% RGD (i), 5 mol% RGD (ii), and 25 mol% RGD (iii) are analyzed by  $^1\text{H}$  MAS NMR spectroscopy (**Figure S9-25**). Subsequent peak assignments are made according to literature reports and comparison with educt spectra.<sup>[37]</sup>

0 mol% RGD (i):  $^1\text{H}$  MAS NMR (400 MHz,  $\text{D}_2\text{O}$ ,  $\delta$ ): 4.25 (PU:  $\text{NH}(\text{C}=\text{O})\text{O}-\text{CH}_2$ ), 3.75 (PU:  $\text{CH}_2\text{O}$ ), 2.93 (PU:  $\text{O}(\text{C}=\text{O})\text{NH}-\text{CH}_2$ ), 2.17–0.72 (PU:  $(\text{C}=\text{C})\text{CH}_3$ ,  $\text{CH}_3/\text{CH}_2$ ) ppm.

5 mol% RGD (ii) and 25 mol% RGD (iii):  $^1\text{H}$  MAS NMR (400 MHz,  $\text{D}_2\text{O}$ ,  $\delta$ ): 7.87 (s, RGD: triazole-CH), 4.58 (RGD: triazoleN- $\text{CH}_2$ ), 4.23 (PU:  $\text{NH}(\text{C}=\text{O})\text{O}-\text{CH}_2$ ), 3.73 (PU:  $\text{CH}_2\text{O}$ ), 3.22 (RGD: **R**:  $\text{NHCH}$ ), 3.06 (RGD: triazoleC- $\text{CH}_2\text{CH}_2$ ), 2.98 (PU:  $\text{O}(\text{C}=\text{O})\text{NH}-\text{CH}_2$ ), 2.73 (RGD: triazoleC- $\text{CH}_2\text{CH}_2$ ), 2.17–0.72 (PU:  $(\text{C}=\text{C})\text{CH}_3$ ,  $\text{CH}_3/\text{CH}_2$ ) ppm.

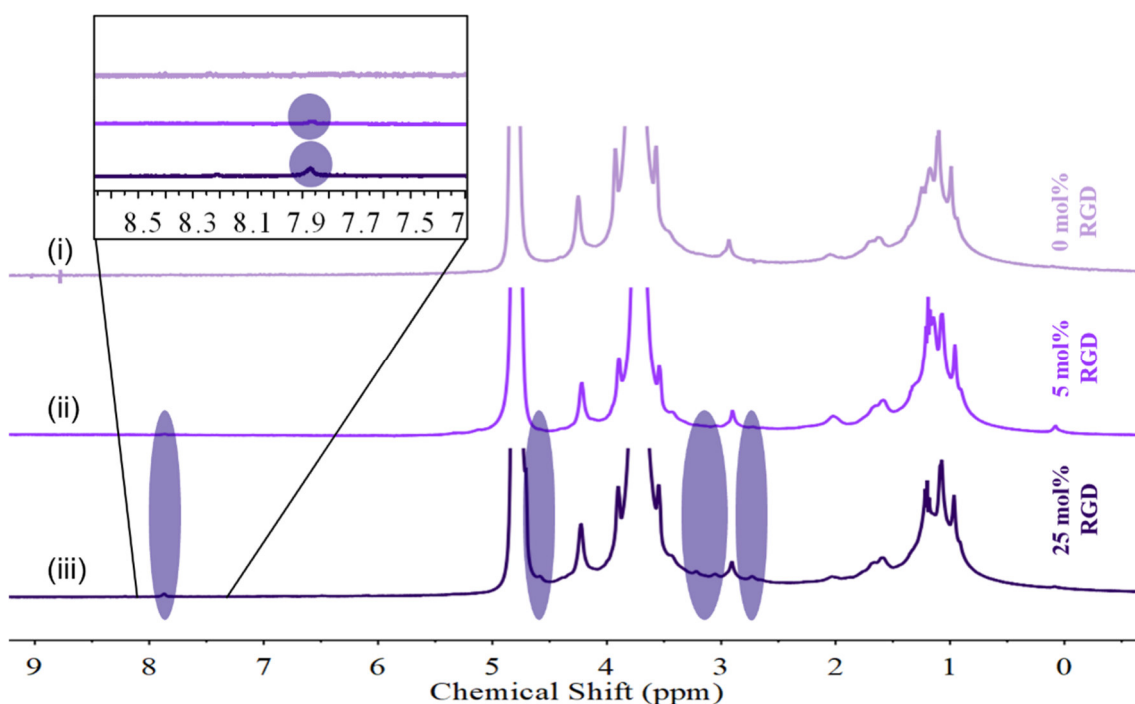


**Figure S9-25.**  $^1\text{H}$  MAS NMR spectroscopy measurements in  $\text{D}_2\text{O}$  of PU-2.0k gels ( $200\text{ g}\cdot\text{L}^{-1}$ ) containing 0 mol% (i), 5 mol% (ii), and 25 mol% RGD-DMMI (iii). Respective RGD-DMMI signals in (i) and (ii) are highlighted in purple.

### 9.3.13. Mechanical Properties

Correspondingly synthesized and purified PU-2k 5 hydrogels with 0, 5 and 25 mol% incorporated catechol-linker are immersed in water at  $5\text{ }^\circ\text{C}$  for 24 h and probed by linear shear rheology (cone-plate geometry, diameter: 7 mm).

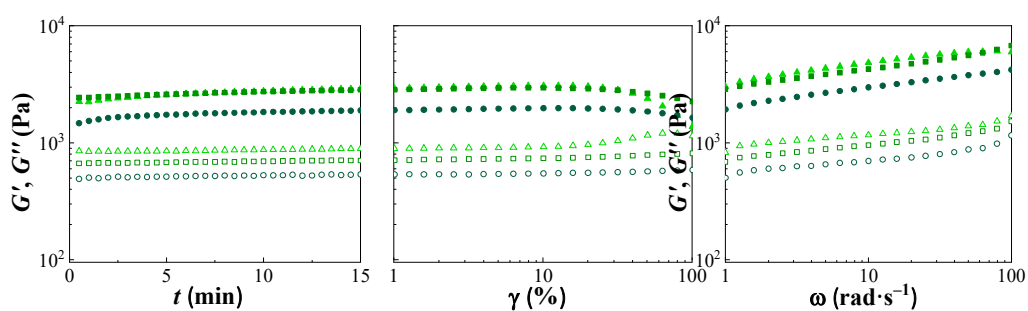


**Figure S9-26.** Time-, amplitude- and frequency sweeps of dialyzed and fully hydrated PU-2k hydrogels ( $200\text{ g}\cdot\text{L}^{-1}$ ) crosslinked in the presence of 0 mol% ( $\blacktriangle$ ), 5 mol% ( $\blacksquare$ ) and 25 mol% ( $\bullet$ ) catechol-DMMI ( $\gamma = 1\%$ ,  $\omega = 1\text{ rad}\cdot\text{s}^{-1}$ ,  $G'$ : closed symbols,  $G''$ : open symbols,  $T = 20\text{ }^\circ\text{C}$ ).

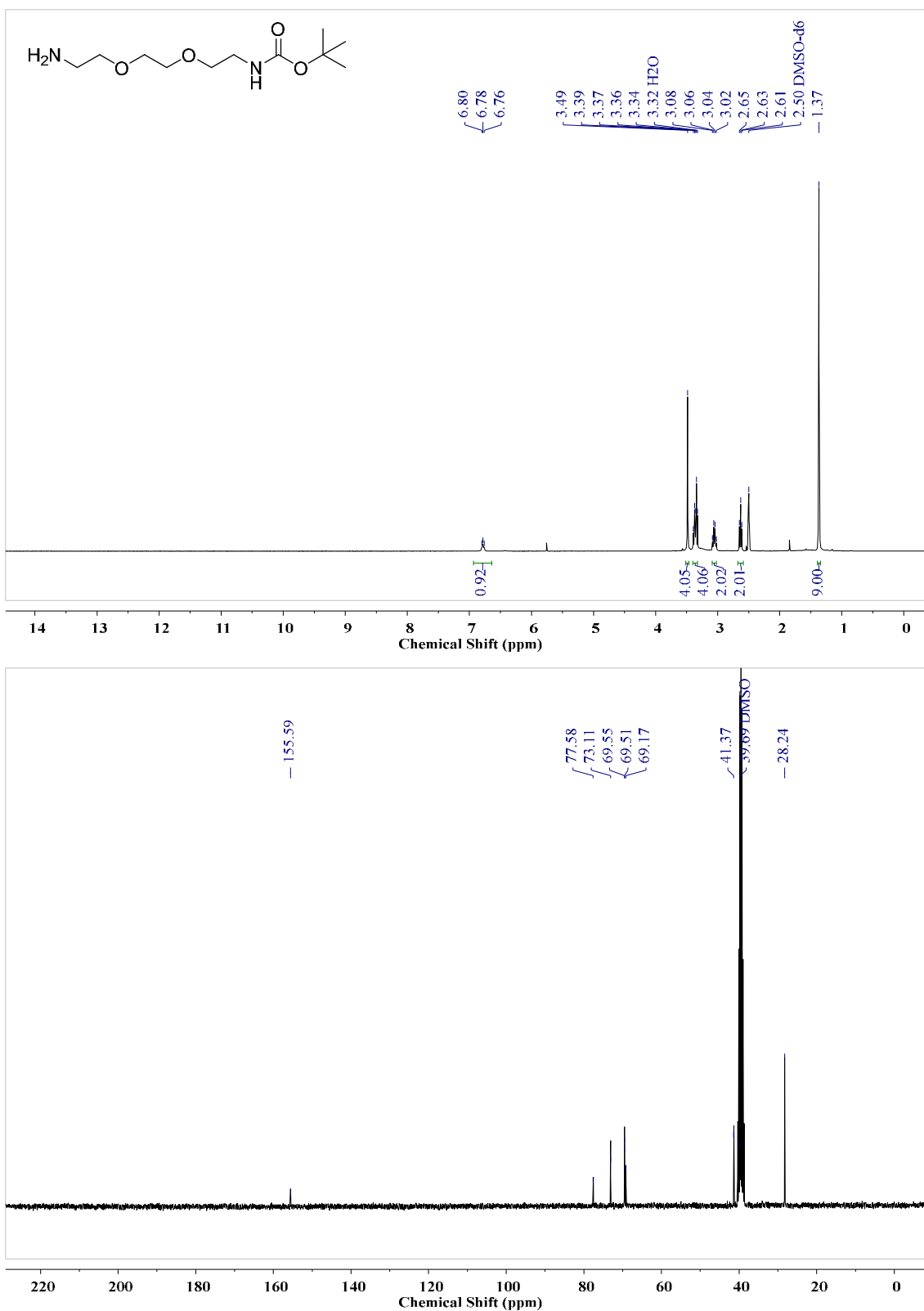
Consistent with previous findings on 5 and 25 mol% RGD hydrogels, the plateau moduli of the 0 and 5 mol% catechol-containing gels are in agreement, while the incorporation of 25 mol% results in a 35% lower plateau modulus.

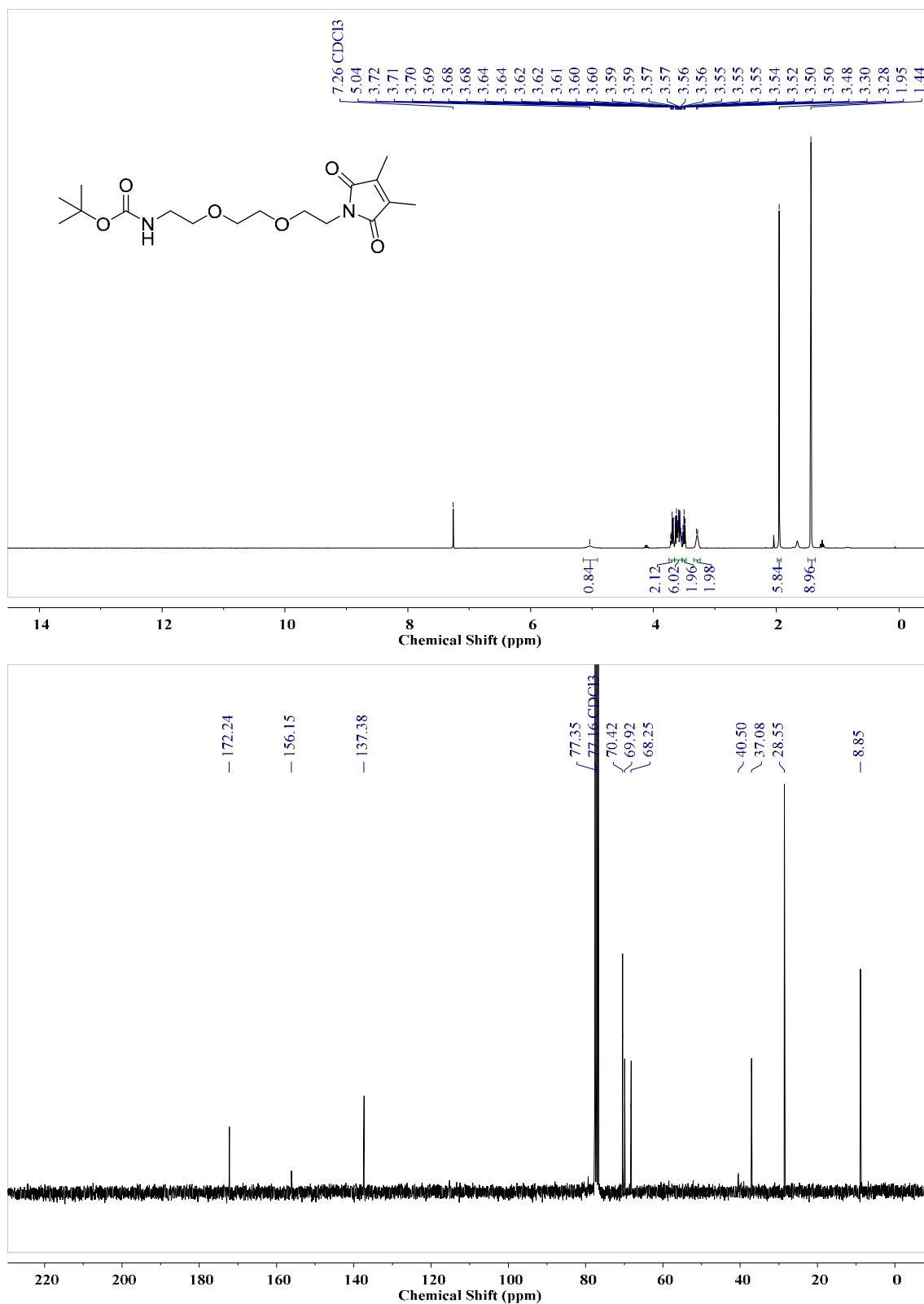
### 9.3.14. Cell Experiments

Osteoblasts (MG-63 GFP) are cultured on polystyrene (11.9 cm<sup>2</sup>) in DMEM (10% FBS, 1% Gl., 1% P/S) at 37 °C and 5% CO<sub>2</sub> using standard cell culture methods. For the cell experiments cells are detached from plastic by trypsinization with trypsin EDTA solution. After centrifugation (1000 rpm, 5 min), the resulting cell pellet is resuspended in DMEM (10% FBS, 1% Gl., 1% P/S) and adjusted to  $1.5 \times 10^5$  cells · mL<sup>-1</sup> (cell counting by Neubauer counting chamber). PU-2k gels with 0, 5, and 25 mol% RGD, as well as 5 mol% catechol, are transferred into 8well plates from ibidi and covered with 300 μL of cell suspension. After 24 h cell-coated hydrogels are analyzed by CLSM.

### 9.3.15. Microfluidics

Microgels of type **5b** - PU-1.5k<sup>0.6</sup>, **5c** - PU-1.5k, and **5d** - PU-2.0k are synthesized by droplet-based microfluidics (**Figure S9-6**). Microgel preparation is enabled by injecting two immiscible liquids into the microfluidic device and flow focusing them at the cross-section. As substrate stream, the precursor polymers **5b** - PU-1.5k<sup>0.6</sup>, **5c** - PU-1.5k, or **5d** - PU-2.0k (100g L<sup>-1</sup>) dissolved in an aqueous NaTXS (1 mM) solution are injected at a flow rate of 450 μL hr<sup>-1</sup>. As carrier stream Novec 7500 and Krytox (2 wt%) are injected at a flow rate of 900 μL hr<sup>-1</sup>. The resulting droplets are irradiated with UV light (120 min), which initiates the gelation process. The obtained microgels are purified with 20 wt% 1H,1H,2H,2H-Perfluor-1-octanol solution in Novec 7500, pure Novec 7500, isopropanol, 1,4-dioxane and transferred to water.

9.3.16.  $^1\text{H}$ - and  $^{13}\text{C}$ -NMR spectra*tert*-Butyl-(2-(2-(2-aminoethoxy)ethoxy)ethyl)carbamate (**9**)Figure S9-27.  $^1\text{H}$ - and  $^{13}\text{C}$ -NMR of compound (**9**) (300 MHz, 75 MHz, DMSO- $d_6$ ).

*DMMI-<sup>T</sup>EG tert-butyl amine (11)*

**Figure S9-28.** <sup>1</sup>H- and <sup>13</sup>C-NMR of compound (11) (300 MHz, 75 MHz, CDCl<sub>3</sub>).

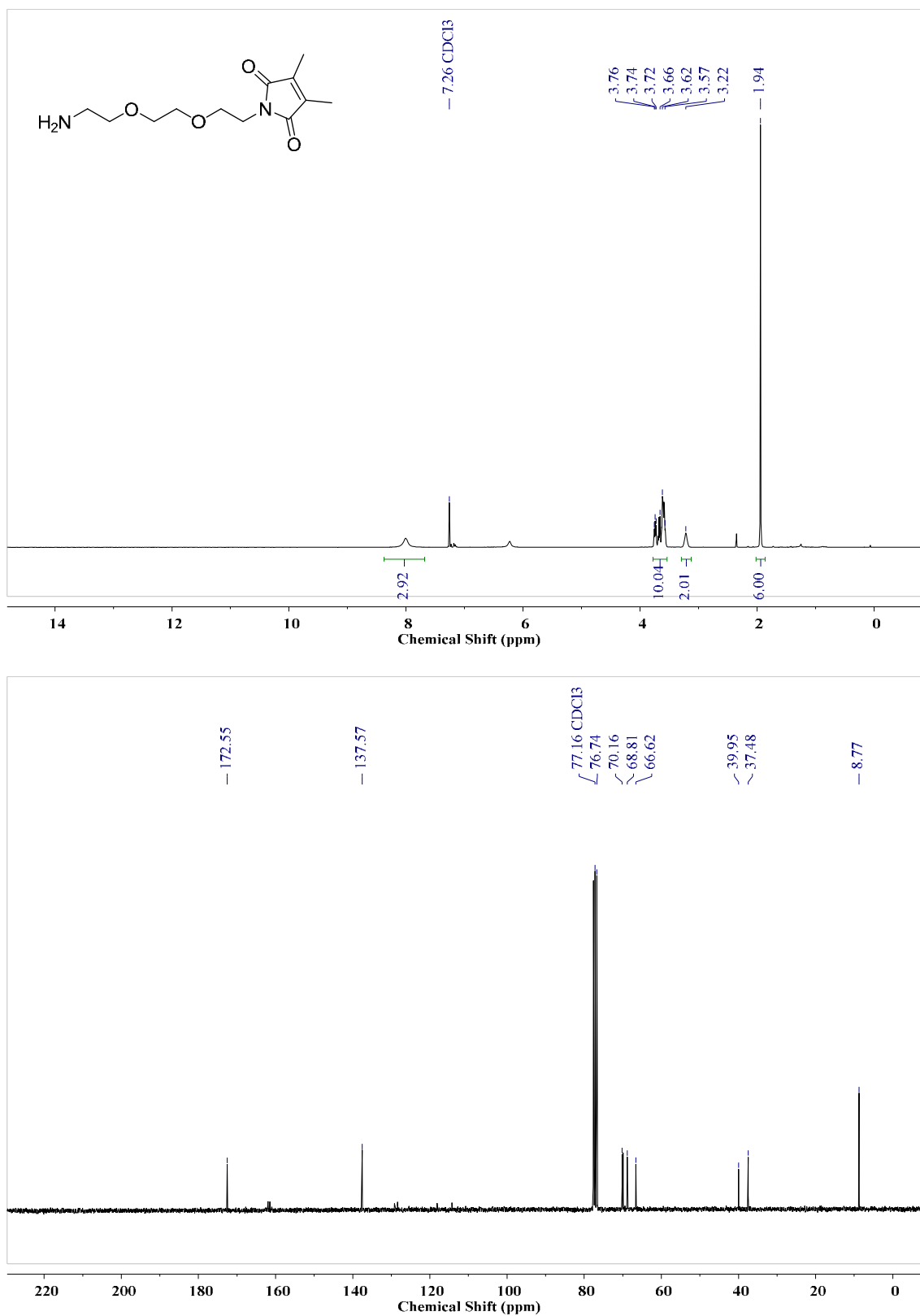
*DMMI-TEG amine (12)*

Figure S9-29.  $^1\text{H}$ - and  $^{13}\text{C}$ -NMR of compound (12) (300 MHz, 75 MHz,  $\text{CDCl}_3$ ).

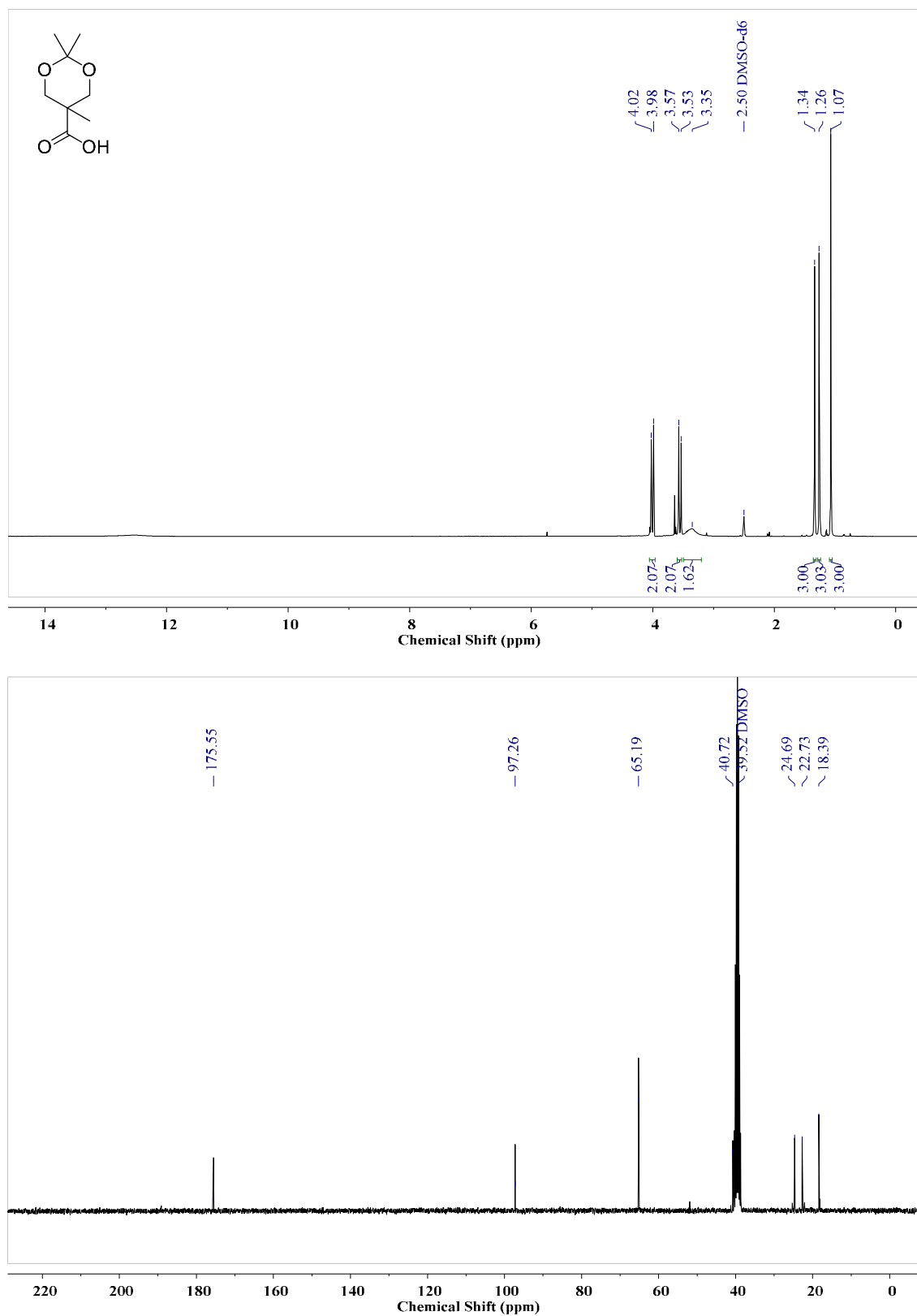
*2,2,5-trimethyl-1,3-dioxane-5-carboxylic acid (14)*

Figure S9-30. <sup>1</sup>H- and <sup>13</sup>C-NMR of compound (14) (300 MHz, 75 MHz, DMSO-*d*<sub>6</sub>).



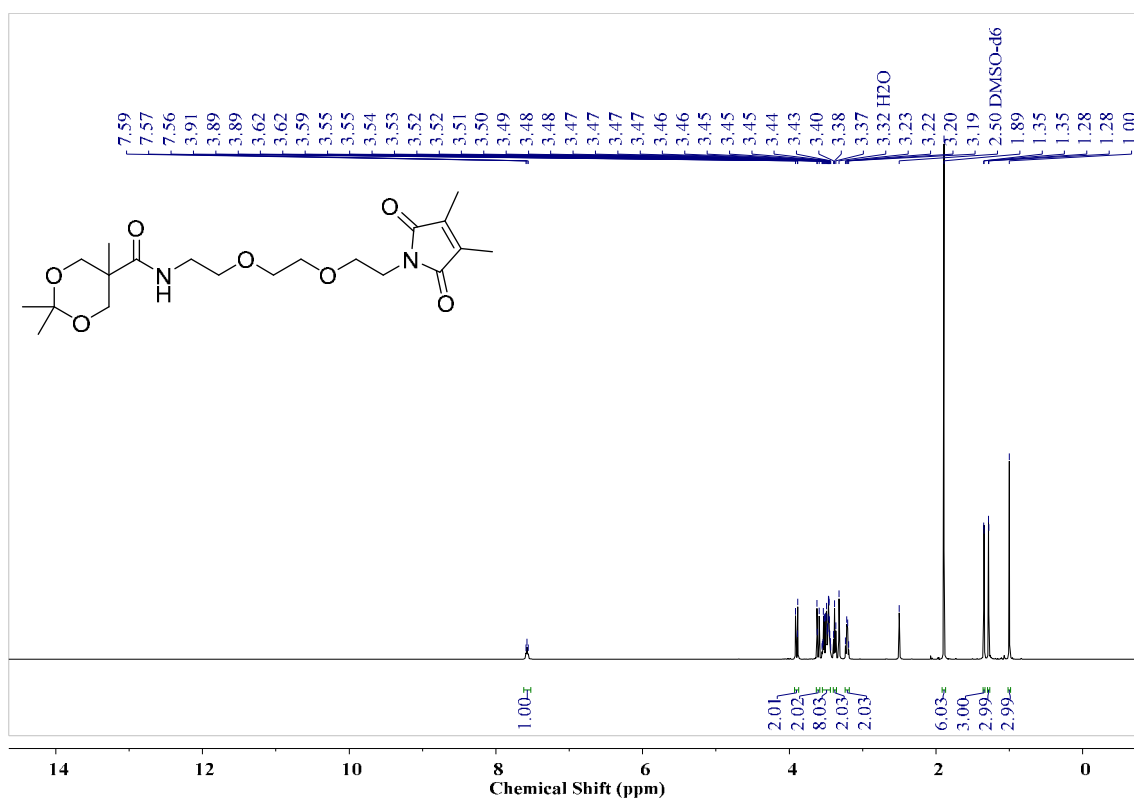
*DMMI-TEG diol acetonide (15)*

Figure S9-31. <sup>1</sup>H-NMR of compound (15) (400 MHz, DMSO-d<sub>6</sub>).

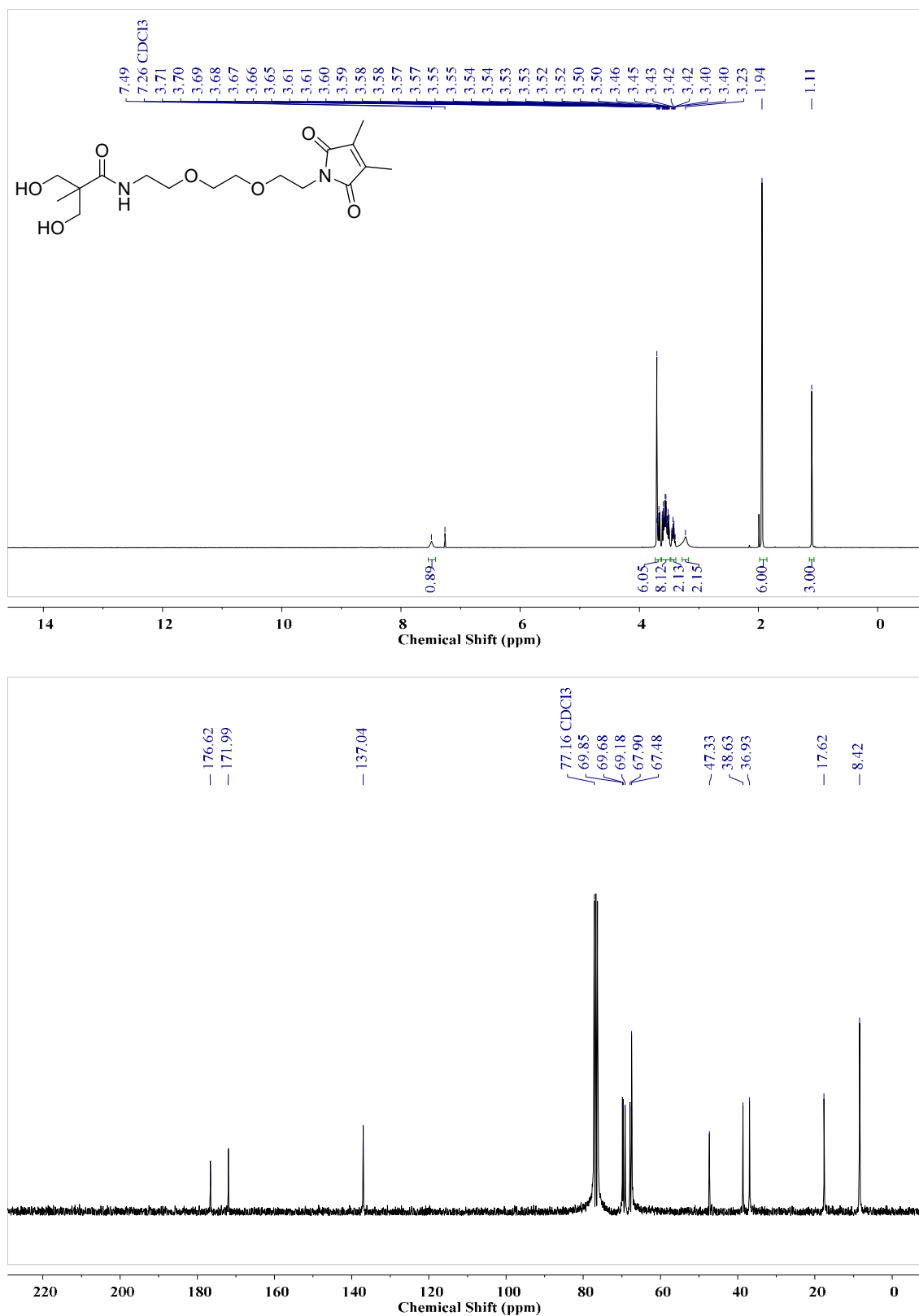
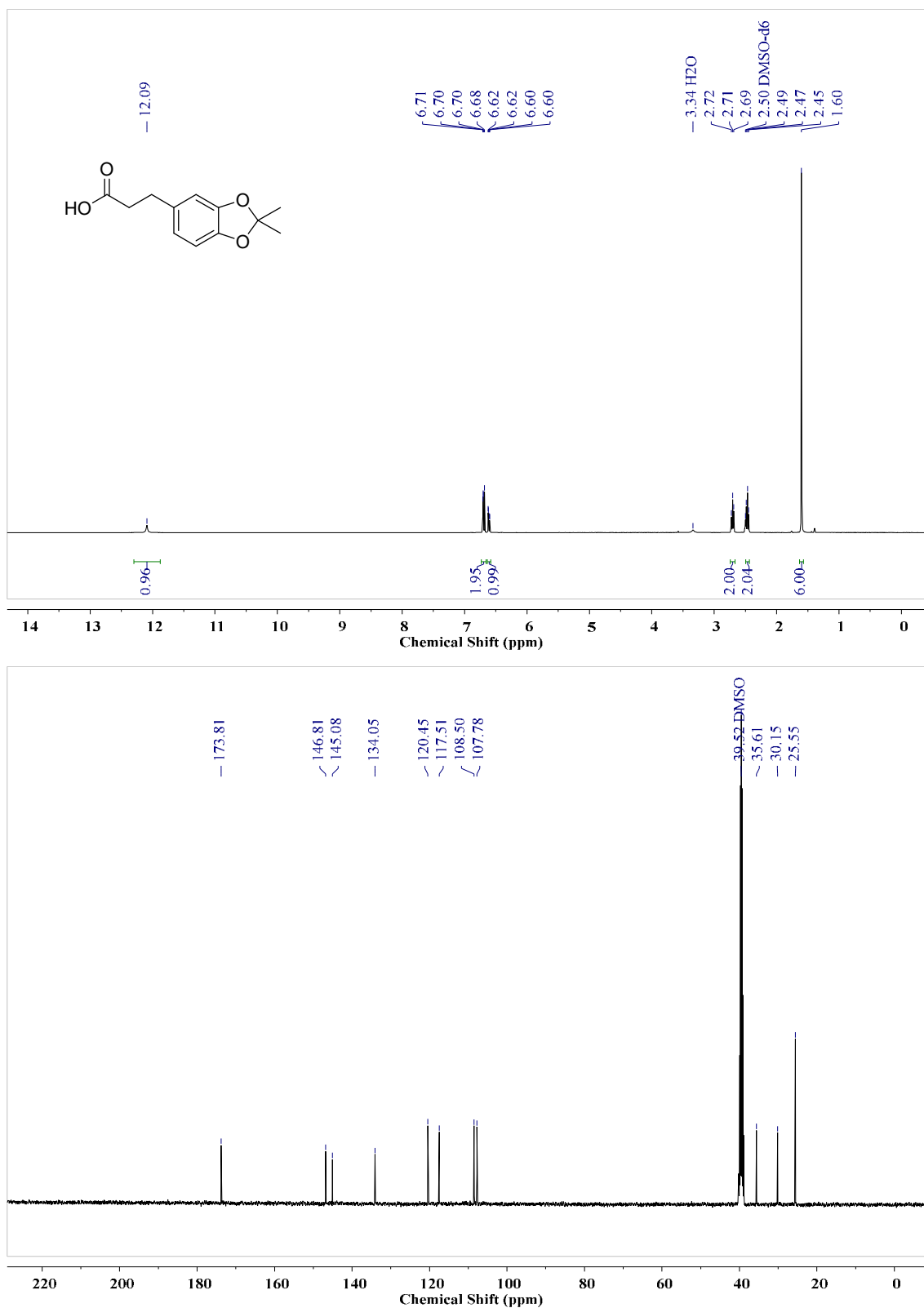
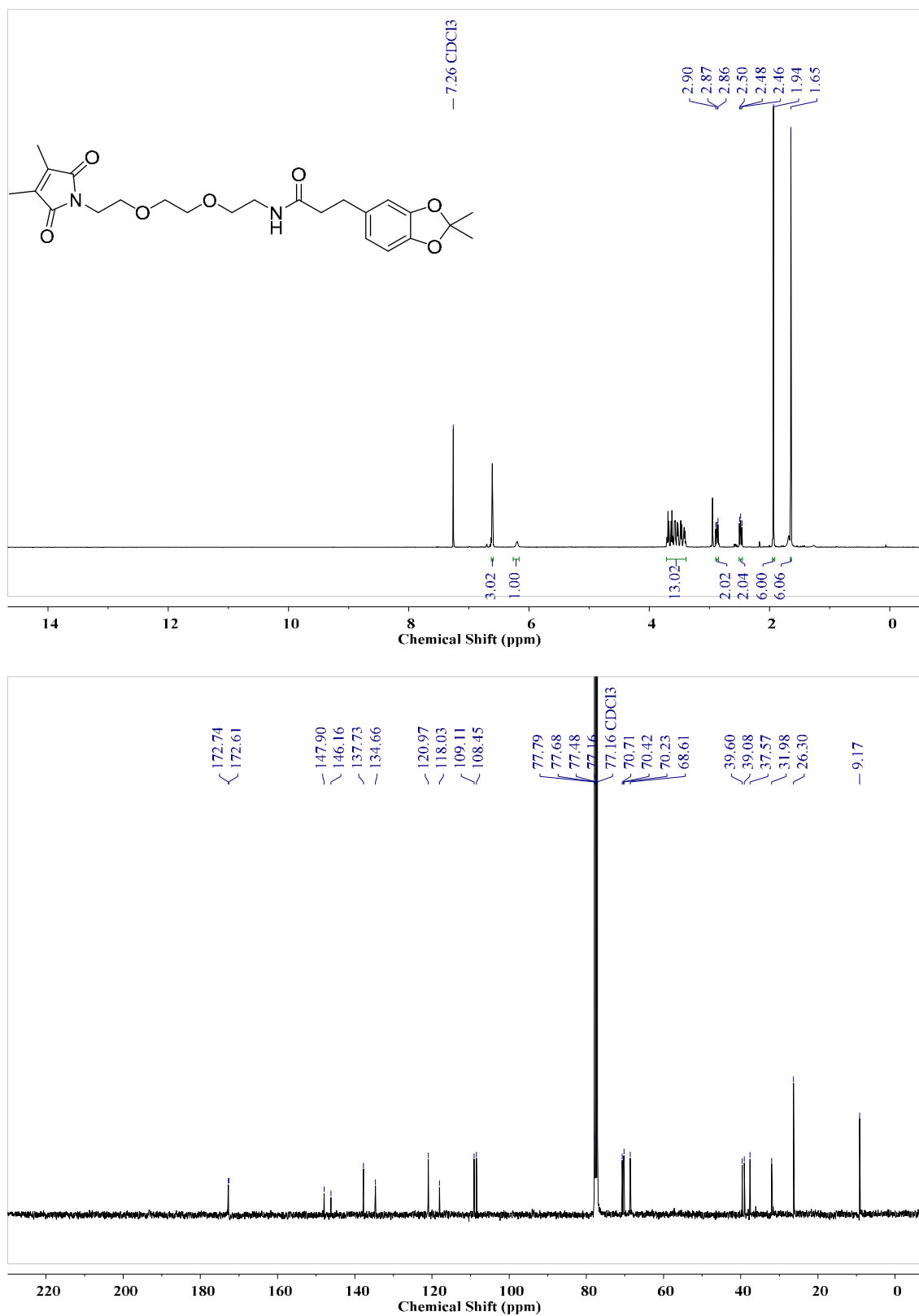
*DMMI-TEG diol (4)*

Figure S9-32. <sup>1</sup>H- and <sup>13</sup>C-NMR of compound (4) (400 MHz, 101 MHz, CDCl<sub>3</sub>).

*2,2-Dimethyl-1,3-benzodioxole-5-propanoic acid (17)*

**Figure S9-33.** <sup>1</sup>H- and <sup>13</sup>C-NMR of compound (17) (400 MHz, 101 MHz, DMSO-*d*<sub>6</sub>).

**DMMI-Catechol-Acetonide (18)****Figure S9-34.** <sup>1</sup>H- and <sup>13</sup>C-NMR of compound (18) (400 MHz, 101 MHz, CDCl<sub>3</sub>).

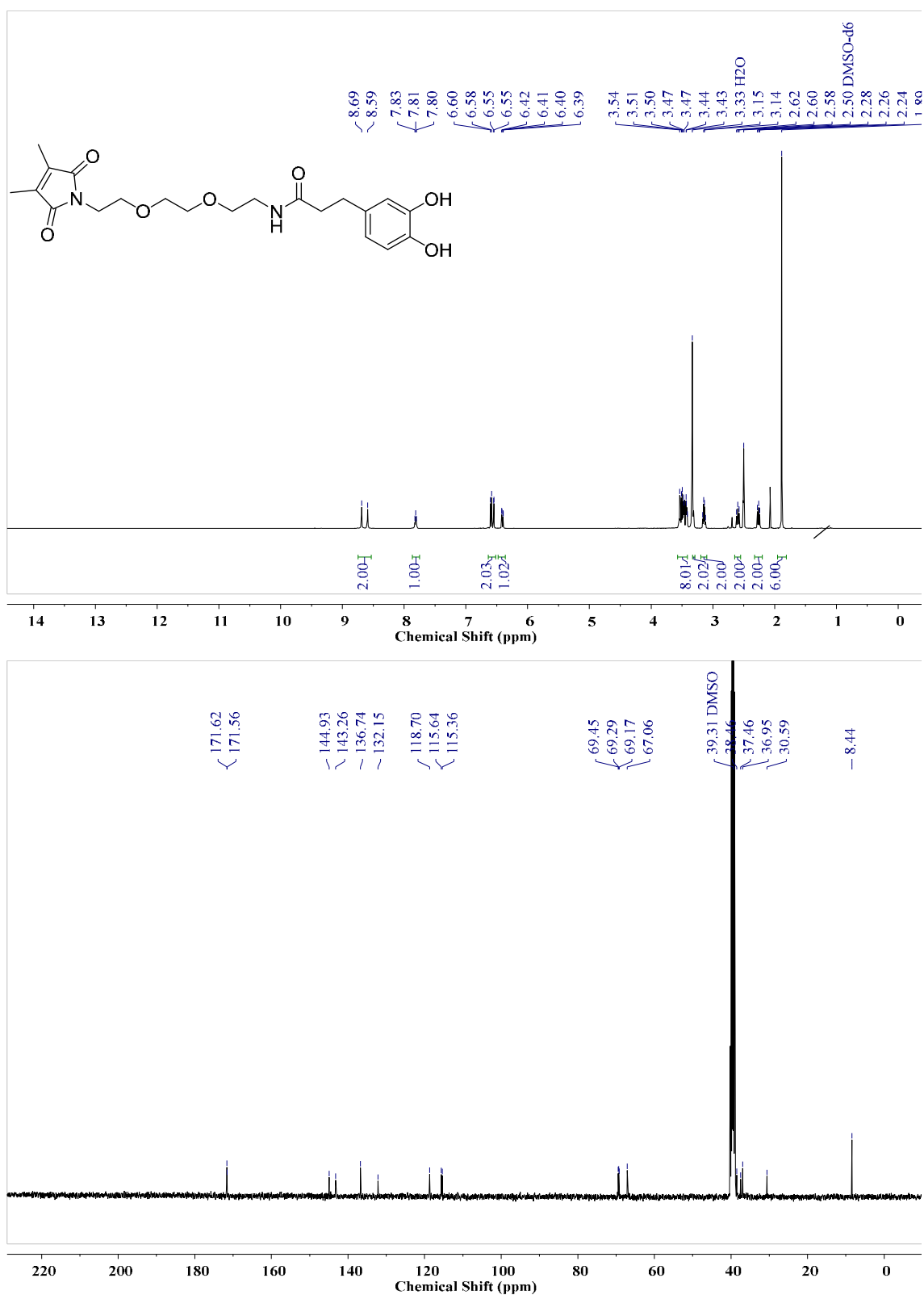
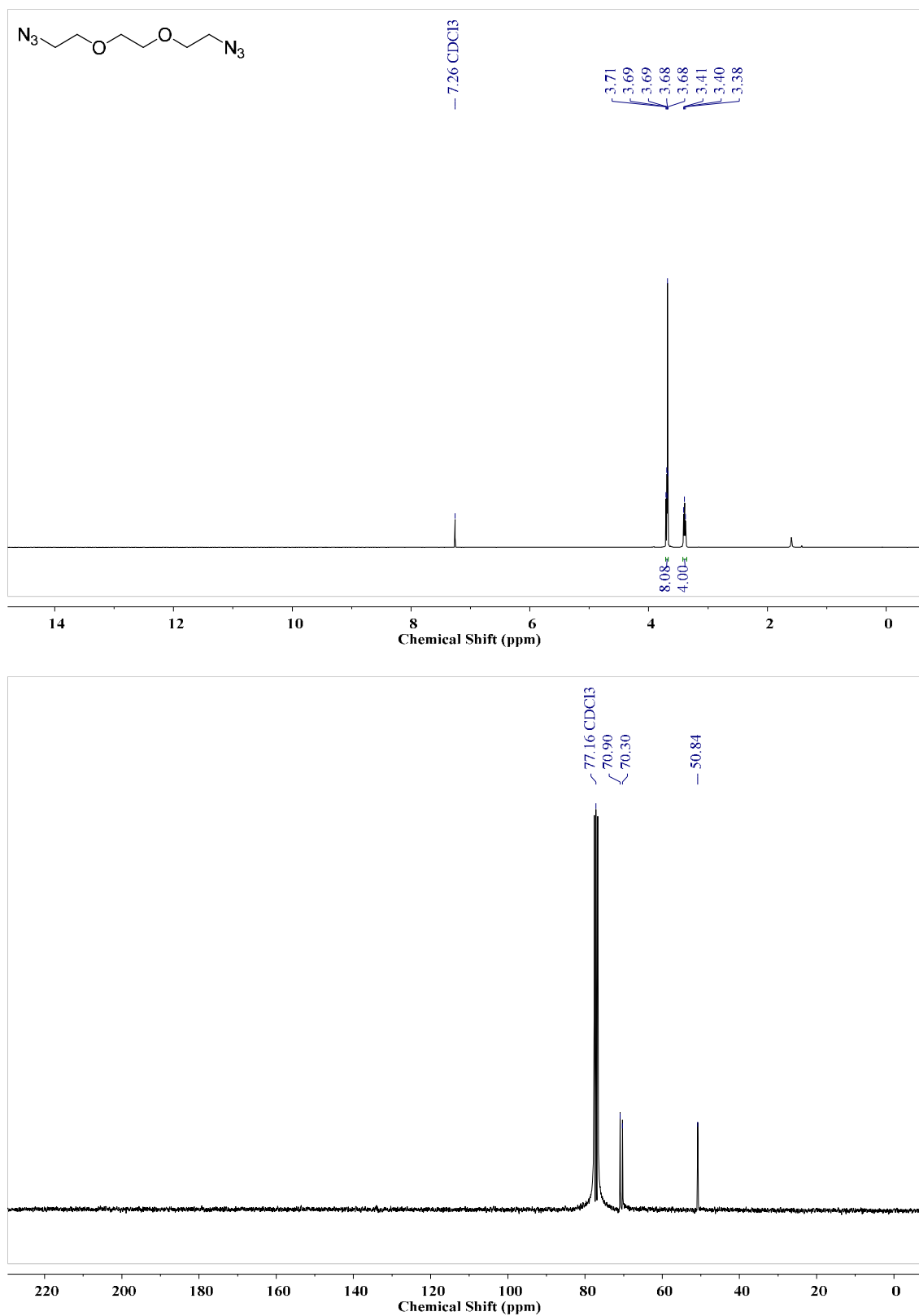
*DMMI-Catechol (6)*

Figure S9-35. <sup>1</sup>H- and <sup>13</sup>C-NMR of compound (6) (400 MHz, 101 MHz, DMSO-d<sub>6</sub>).

*1,2-Bis(2-azidoethoxy)ethane (20)*

**Figure S9-36.**  $^1\text{H}$ - and  $^{13}\text{C}$ -NMR of compound (20) (300 MHz, 75 MHz,  $\text{CDCl}_3$ ).

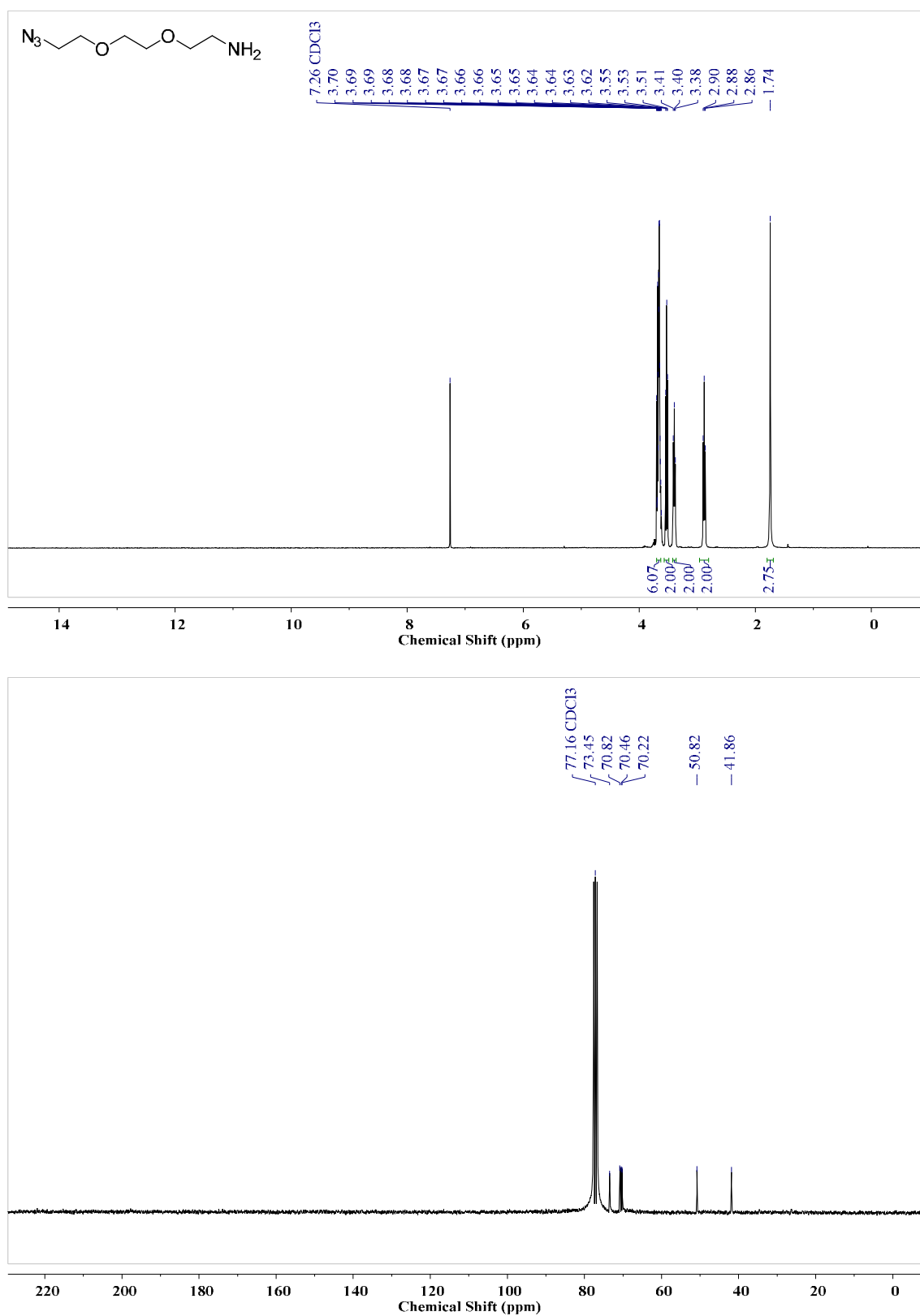
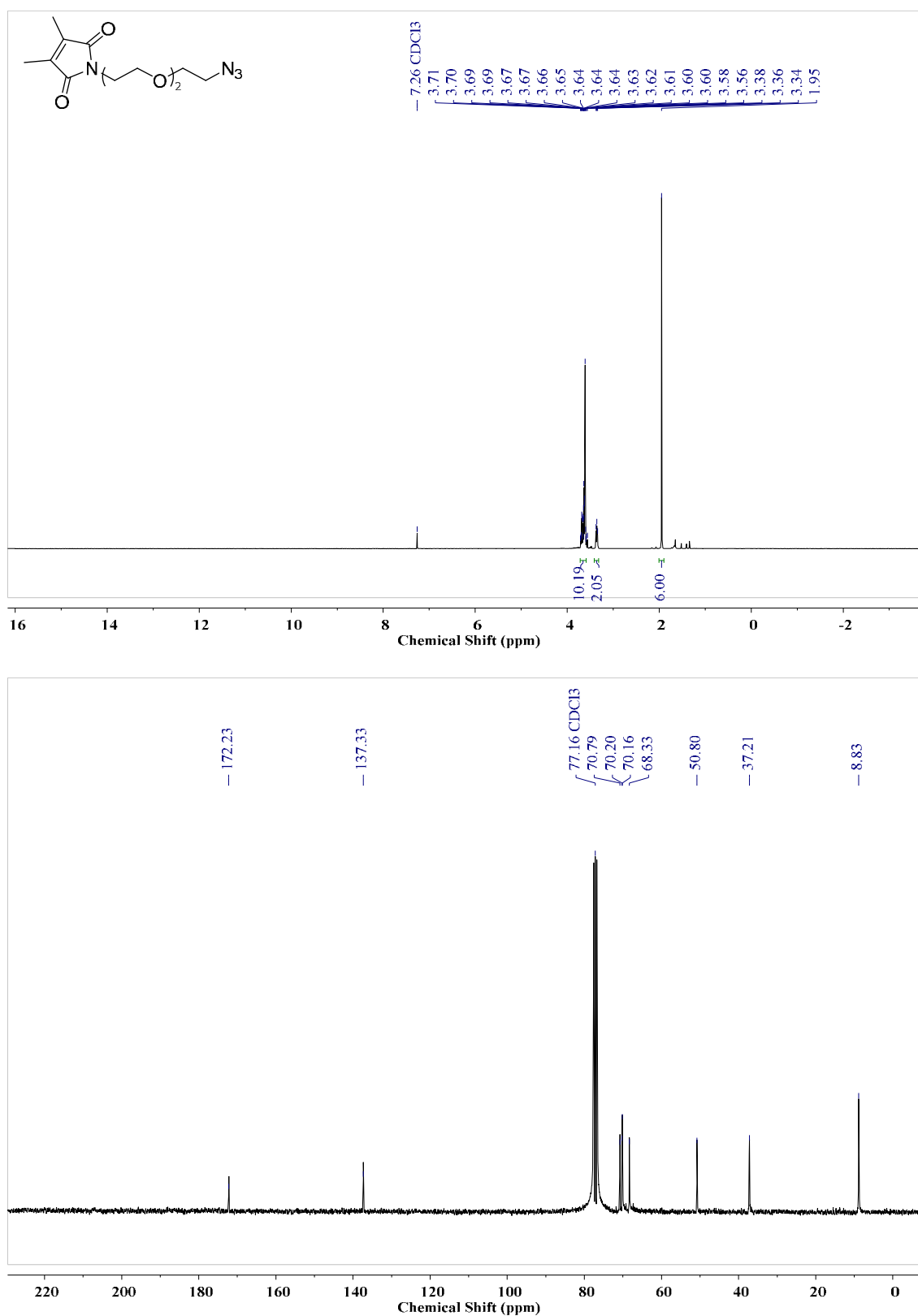
*2-[2-(2-Azidoethoxy)ethoxy]ethan-1-amine (21)*

Figure S9-37.  $^1\text{H}$ - and  $^{13}\text{C}$ -NMR of compound (21) (300 MHz, 75 MHz, CDCl<sub>3</sub>).

*DMMI-<sup>T</sup>EG-azide (22)*

**Figure S9-38.** <sup>1</sup>H- and <sup>13</sup>C-NMR of compound (22) (300 MHz, 75 MHz, CDCl<sub>3</sub>).



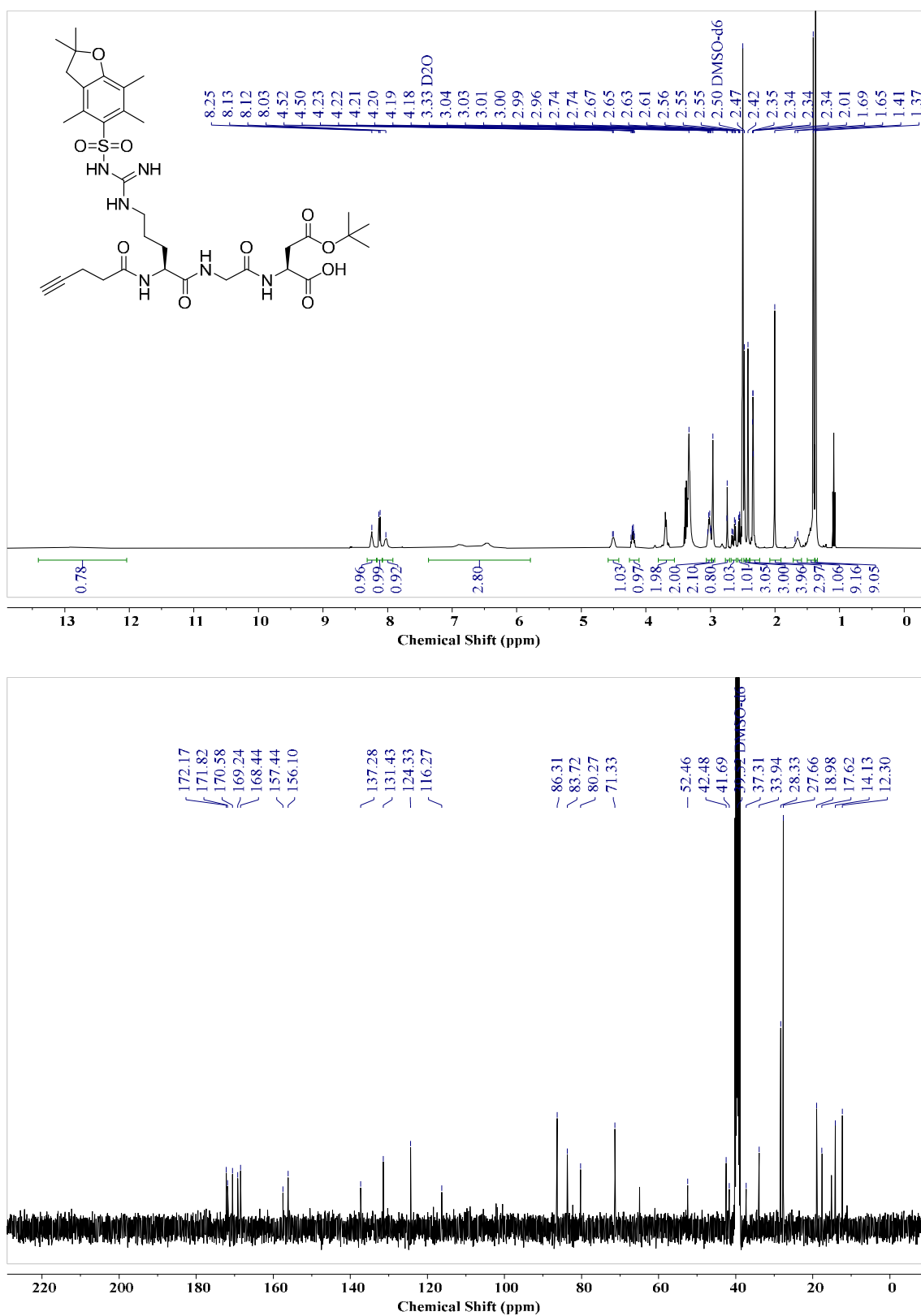
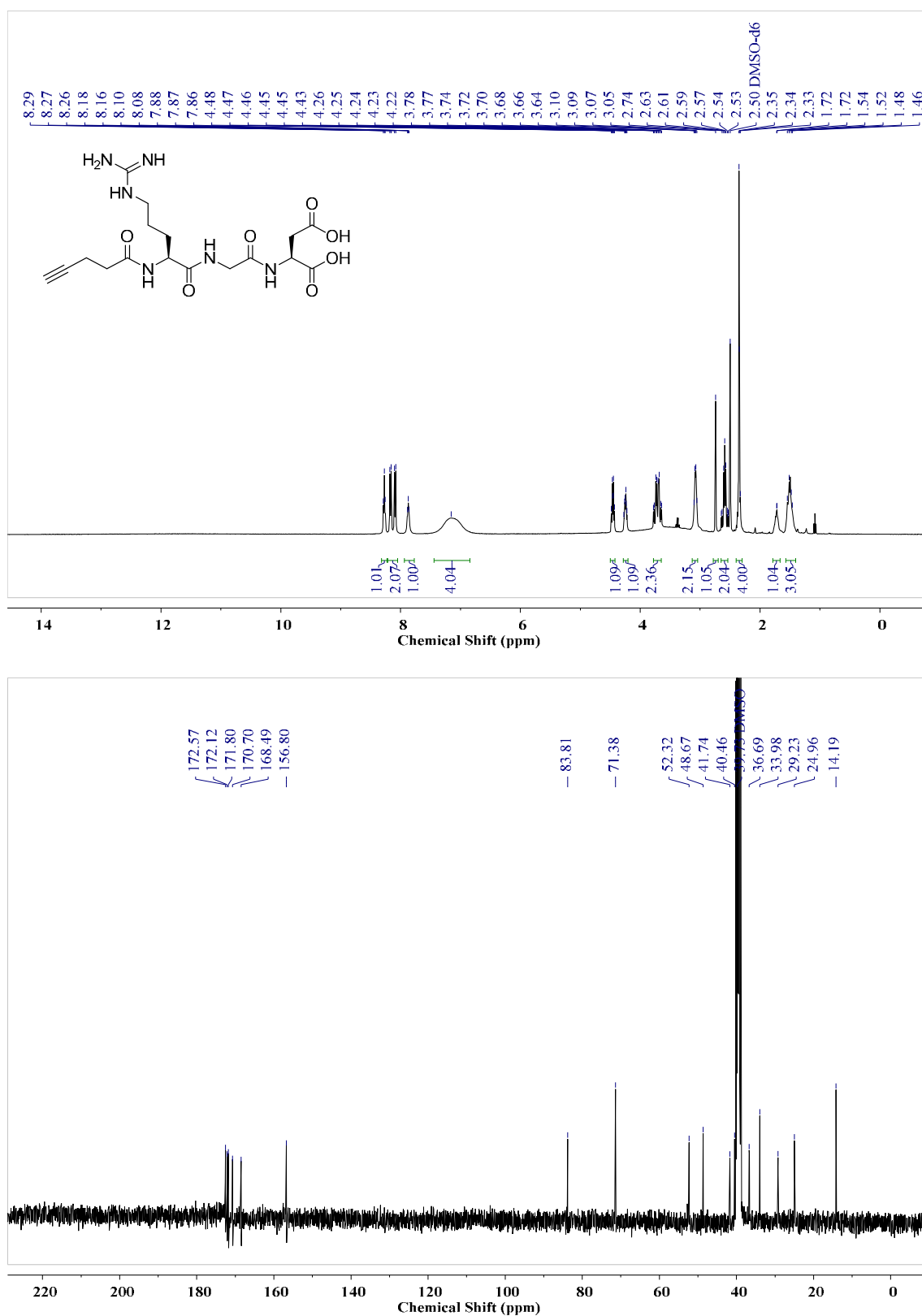
*Protected RGD-alkyne (23a)*

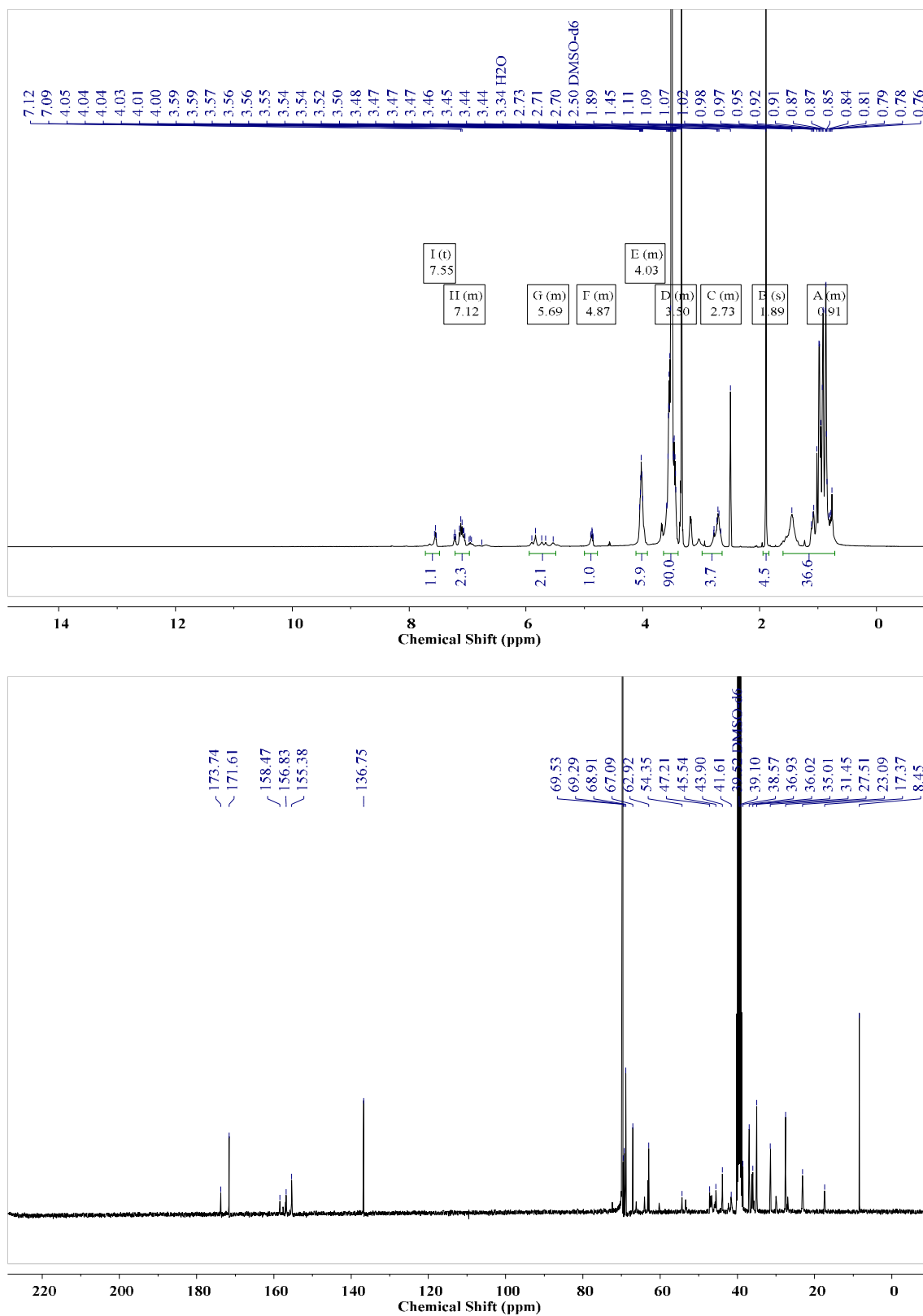
Figure S9-39. <sup>1</sup>H- and <sup>13</sup>C-NMR of compound (23a) (400 MHz, 101 MHz, DMSO-*d*<sub>6</sub>).

***RGD-alkyne (23)***

**Figure S9-40.** <sup>1</sup>H- and <sup>13</sup>C-NMR of compound (23) (400 MHz, 101 MHz, DMSO-*d*<sub>6</sub>).

***DMMI-<sup>T</sup>EG-RGD (7)***

**Figure S9-41.** <sup>1</sup>H- and <sup>13</sup>C-NMR of compound (7) (400 MHz, 101 MHz, D<sub>2</sub>O).

**PU-1.0k (5a)****Figure S9-42.** <sup>1</sup>H- and <sup>13</sup>C-NMR of compound (5a) (400 MHz, 101 MHz, DMSO-*d*<sub>6</sub>).

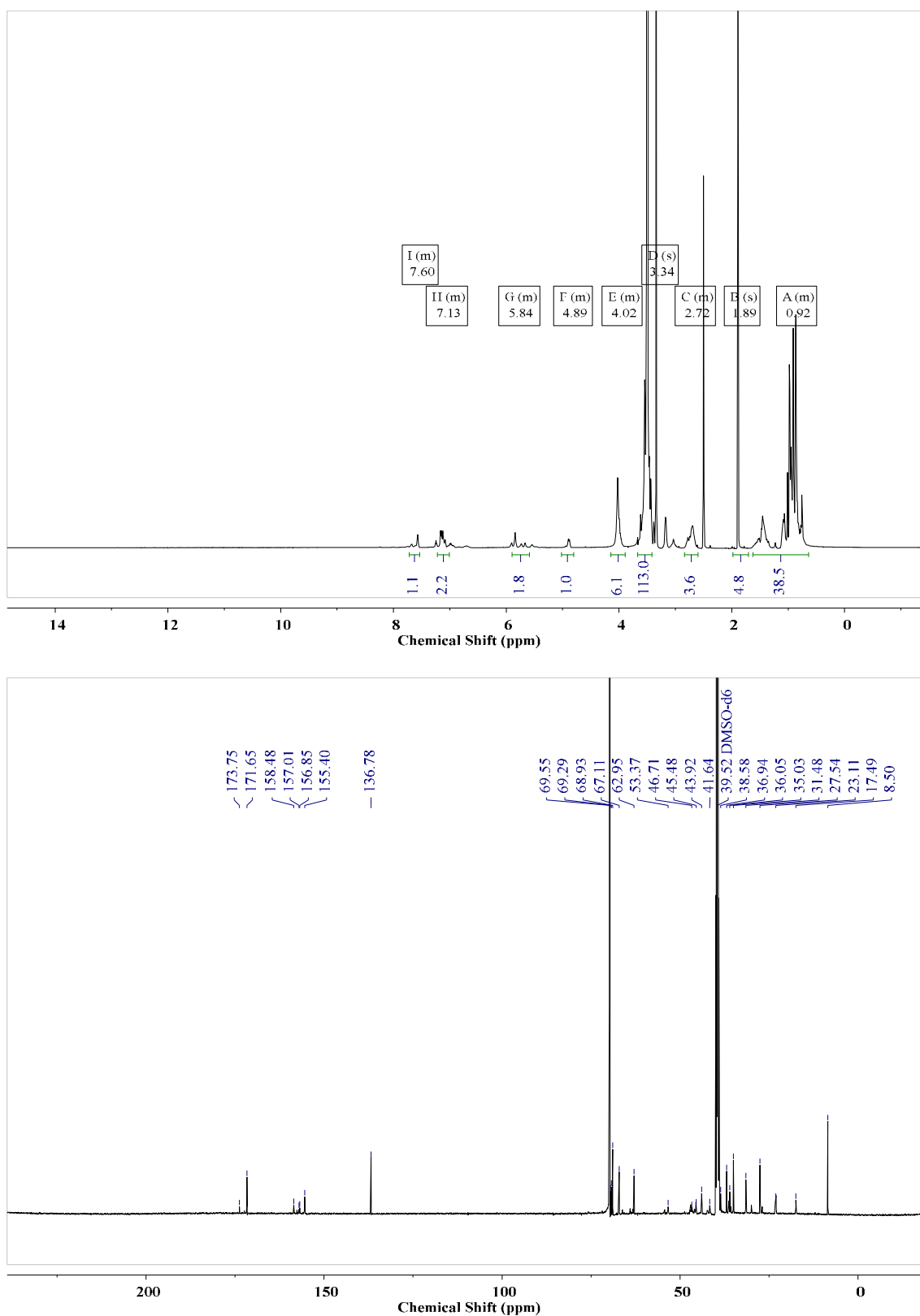
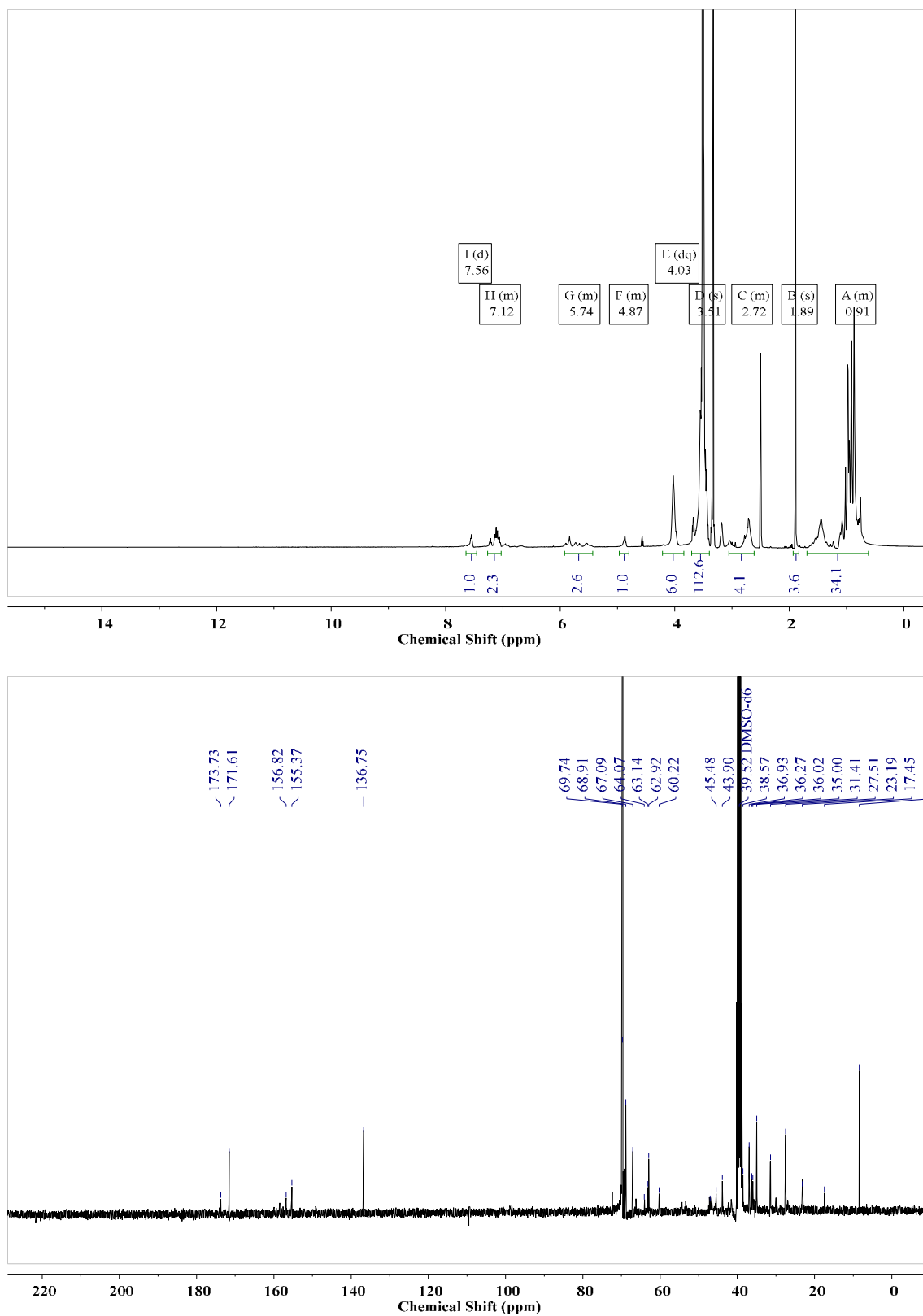
*PU-1.5k<sup>0.6</sup> (5b)*

Figure S9-43. <sup>1</sup>H- and <sup>13</sup>C-NMR of compound (5b) (400 MHz, 101 MHz, DMSO-d<sub>6</sub>).

*PU-1.5k (5c)*

**Figure S9-44.** <sup>1</sup>H- and <sup>13</sup>C-NMR of compound (5c) (400 MHz, 101 MHz, DMSO-*d*<sub>6</sub>).

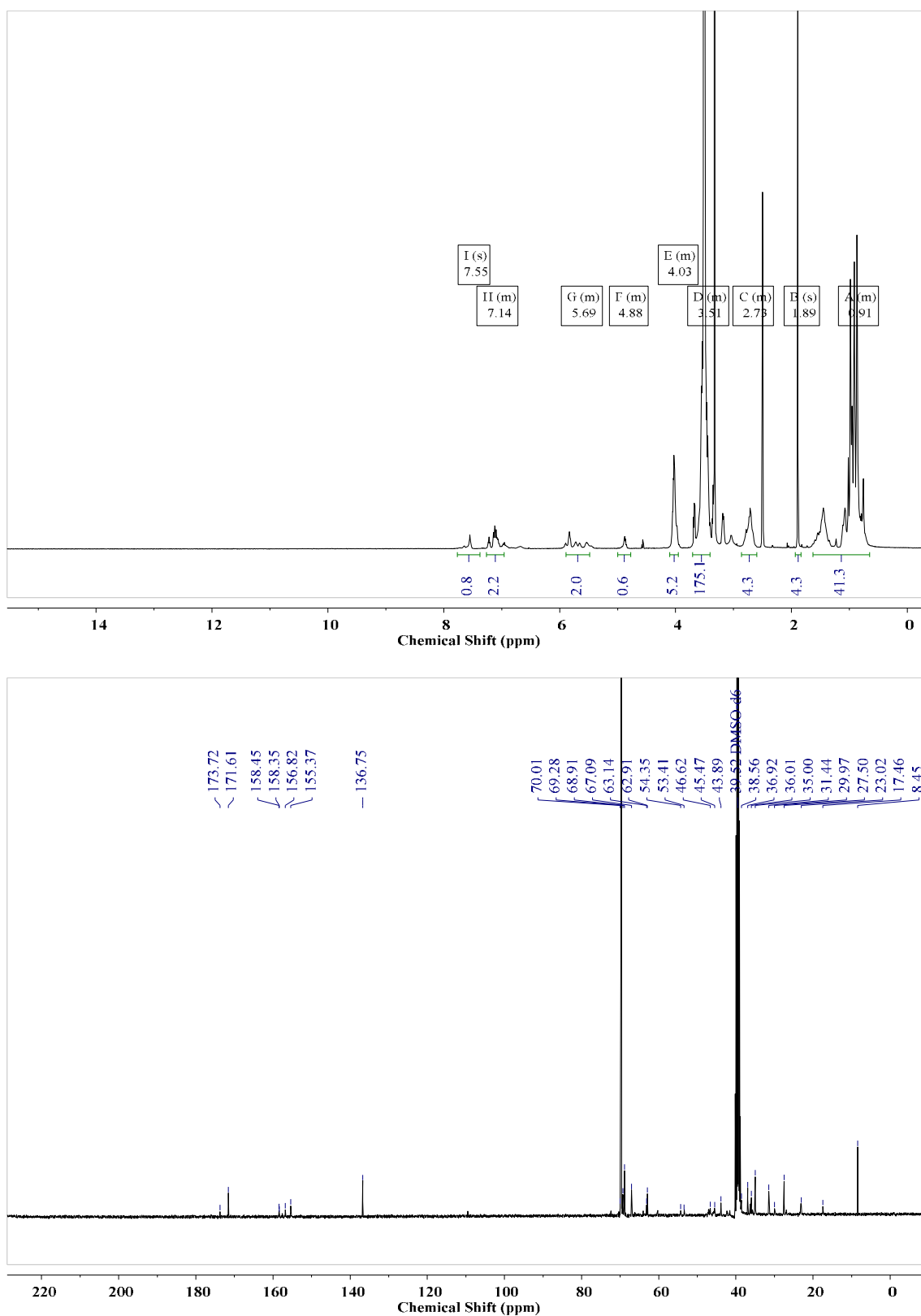
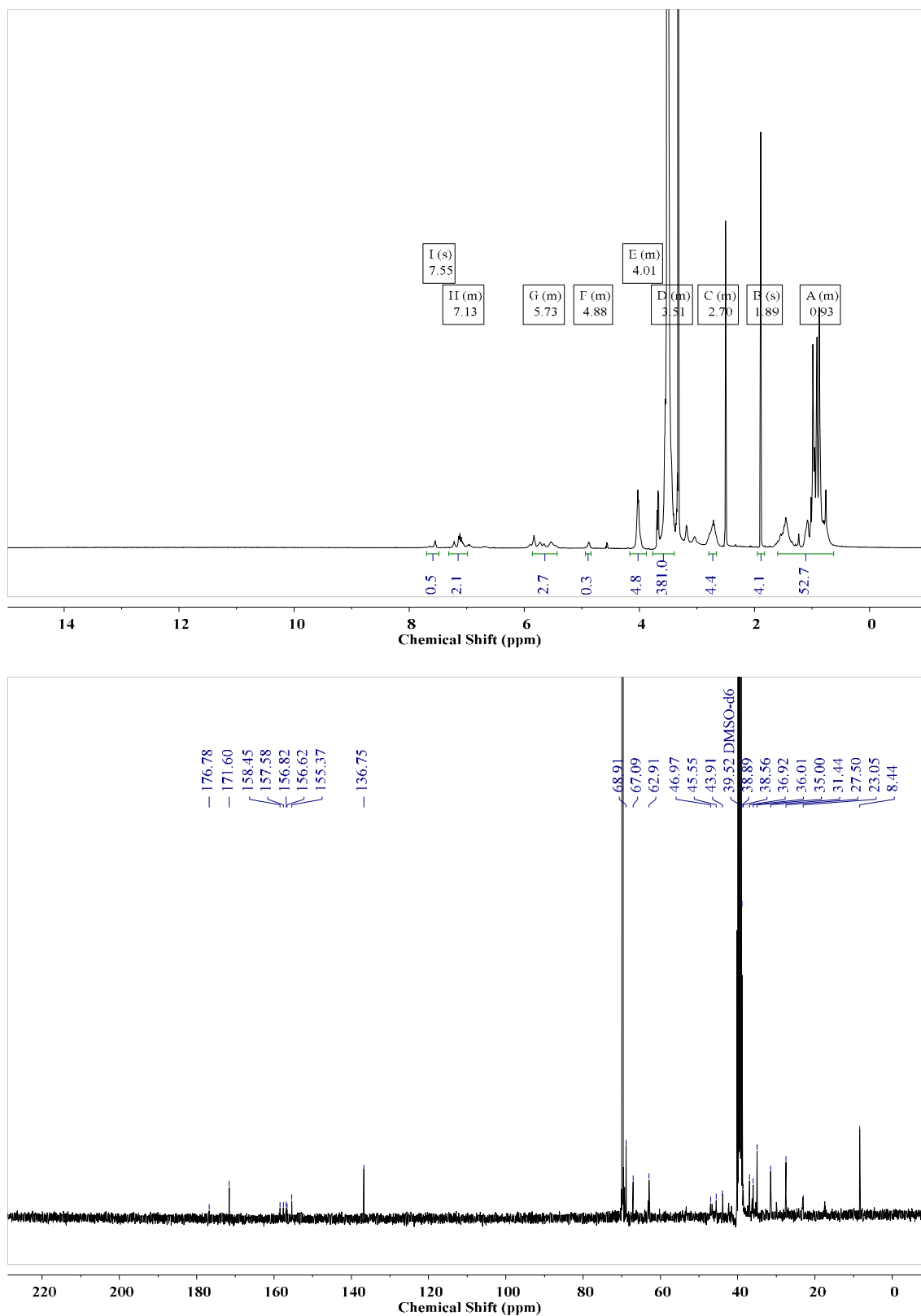
*PU-2.0k (5d)*

Figure S9-45. <sup>1</sup>H- and <sup>13</sup>C-NMR of compound (5d) (400 MHz, 101 MHz, DMSO-*d*<sub>6</sub>).

**PU-4.0k (5e)**



**Figure S9-46.** <sup>1</sup>H- and <sup>13</sup>C-NMR of compound (5e) (400 MHz, 101 MHz, DMSO-*d*<sub>6</sub>).



## 9.4. Literature

- [1] B. Lafuente, R. T. Downs, H. Yang, N. Stone, in *Highlights Mineral. Crystallogr.*, DE GRUYTER, **2015**, pp. 1–30.
- [2] S. Seiffert, J. Thiele, *Microfluidics: Theory and Practice for Beginners*, De Gruyter, **2019**.
- [3] F. Di Lorenzo, S. Seiffert, *Macromol. React. Eng.* **2016**, *10*, 201.
- [4] Z. Ahmed, E. A. Gooding, K. V. Pimenov, L. Wang, S. A. Asher, *J. Phys. Chem. B* **2009**, *113*, 4248.
- [5] H. L. Judah, P. Liu, A. Zarbakhsh, M. Resmini, *Polymers* **2020**, *12*, 2590.
- [6] J. Es Sayed, C. Lorthioir, P. Perrin, N. Sanson, *Soft Matter* **2019**, *15*, 963.
- [7] C. Wendeln, S. Rinnen, C. Schulz, T. Kaufmann, H. F. Arlinghaus, B. J. Ravoo, *Chem. - A Eur. J.* **2012**, *18*, 5880.
- [8] L. I. Ronco, A. Basterretxea, D. Mantione, R. H. Aguirresarobe, R. J. Minari, L. M. Gugliotta, D. Mecerreyes, H. Sardon, *Polymer* **2017**, *122*, 117.
- [9] Z. Liu, B. H. Hu, P. B. Messersmith, *Tetrahedron Lett.* **2010**, *51*, 2403.
- [10] E. Klein, S. DeBonis, B. Thiede, D. A. Skoufias, F. Kozielski, L. Lebeau, *Bioorganic Med. Chem.* **2007**, *15*, 6474.
- [11] A. Prabhakar, D. K. Chattopadhyay, B. Jagadeesh, K. V. S. N. Raju, *J. Polym. Sci. Part A Polym. Chem.* **2005**, *43*, 1196.